

ELECTROMAGNETIC SUSPENSIONS FOR GROUND TRANSPORTATION

by

MARC STEVEN WEINBERG

S.B., S.M., Massachusetts Institute of Technology  
1971

M.E., Massachusetts Institute of Technology  
1973

SUBMITTED IN PARTIAL FULFILLMENT  
OF THE REQUIREMENTS FOR THE  
DEGREE OF DOCTOR OF  
PHILOSOPHY  
at the  
MASSACHUSETTS INSTITUTE OF TECHNOLOGY

DECEMBER 1973, *i.e. Feb. 1974*

Signature redacted

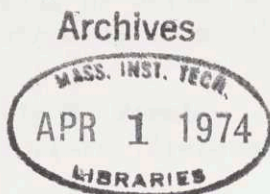
Signature of Author.....  
Department of Mechanical Engineering

Signature redacted

Certified by.....  
Thesis Supervisor

Signature redacted

Accepted by.....  
Chairman, Departmental Committee  
on Graduate Students



# ELECTROMAGNETIC SUSPENSIONS FOR GROUND TRANSPORTATION

by

Marc Steven Weinberg

Submitted to the Department of Mechanical Engineering  
in partial fulfillment of the requirements for the  
degree of Doctor of Philosophy

## ABSTRACT

A detailed model of an electromagnetic suspension operating in the heave mode is developed. The model is experimentally verified for zero forward speed.

The heave models study force-current-gap relationships, leakage fluxes, eddy currents induced by vertical motion, the effects of magnet length, and feedback control. The performance of the model is determined for stochastic road inputs. Compared to models which neglected leakage flux, magnetic flux leakage reduces the magnet's maximum lift and increases the required voltage. Increasing the magnet's length filters road irregularities so that high frequency inputs to the system are reduced. For most practical systems, the eddy currents induced by vertical motion have negligible effects on system dynamics. Current control with feedback of the average relative displacement and absolute velocity is identified as a rational control strategy.

The heave model was verified in experiments where a 13 lb. vehicle which was geometrically and dynamically scaled to represent full size systems was levitated beneath a ferromagnetic shaker programmed to simulate road inputs.

Preliminary investigations of models with heave and pitch degrees of freedom and lateral guidance are conducted.

The heave model is used to generate guidelines and sample designs for full size systems. For full size suspensions, air gaps of 0.4 to 0.6 inches are feasible. For a system with simple secondary suspension and magnets which weigh 10 to 15% of the vehicle's total weight, ride comfort and other constraints are satisfied at 300 mph. with track roughness similar to that of welded steel rails and are satisfied at 100 mph. with track roughness comparable to that of aircraft runways.

Thesis Supervisor: David N. Wormley

Title: Associate Professor of Mechanical Engineering

TABLE OF CONTENTS

	<u>Page</u>
ABSTRACT.....	2
ACKNOWLEDGMENTS.....	4
LIST OF TABLES.....	5
LIST OF FIGURES.....	6
LIST OF SYMBOLS.....	12
I. INTRODUCTION AND PRINCIPAL RESULTS.....	18
1. Introduction.....	18
2. Summary of Analytical Design.....	27
3. Experimental Program.....	64
4. Suspension Design.....	116
II. ANALYTICAL MODELS FOR HEAVE MOTION.....	162
5. Static Relations for Magnet.....	162
6. Magnet Control for Simple Suspensions.....	170
7. Finite Magnet Length.....	184
8. Nonlinear Simulations.....	194
9. Passive Secondary Suspension.....	213
10. Eddy Currents Induced by Vertical Motion.....	218
III. PRELIMINARY INVESTIGATIONS OF RELATED TOPICS.....	234
11. Optimum Suspensions for a Heave-Pitch Model.....	234
12. Lateral Motion.....	253
IV. CONCLUSIONS AND RECOMMENDATIONS.....	278
13. Conclusions and Recommendations.....	278
REFERENCES.....	282
APPENDICES .....	288
A.1 Estimated Wind Drag .....	288
A.2 Magnet Permeances with End Effects .....	288
A.3 Conversion of Voltage Control to Current Control ....	291
A.4 Vehicle Length's Filtering of Wind .....	295
A.5 Control Circuitry for Experimental Magnet.....	299
A.6 Computer Programs.....	304
BIOGRAPHICAL SKETCH .....	324

#### ACKNOWLEDGMENTS

I thank Professors Frazier, Paynter, Richardson, and Smith, my thesis committee, for their guidance and encouragement throughout this work. I am especially grateful to Professor Wormley, my thesis advisor, whose constant dedication has contributed significantly to this document.

I appreciate the stimulation received from coworkers in the suspension group. In particular, I thank Doug Limbert, Ashok Boghani, and Larry Sweet.

The fine work and suggestions of Ray Johnson and the M.E. Machine Shop is deeply appreciated. I thank Bruce Shannon, Ken Haskell, Howard Watson, and the Electromagnetic Engineering Section of Draper Labs for aiding the construction of the magnet and rail used in the experiments. I am indebted to Dick Smythe of the Draper Labs for his heat treating of the magnetic materials.

Special thanks are given to Sandy Williams and Maureen Rush who transformed my hieroglyphics into a readable manuscript.

I thank my mother and father who "made me a mensch".

I am particularly grateful to my wife Judith whose understanding and support enabled me to overcome the pressures involved in this effort.

The financial support of the National Science Foundation and the U.S. Department of Transportation is gratefully acknowledged.

LIST OF TABLES

<u>Table</u>		<u>Page</u>
1	Dimensionless Terms	74
2	Scaling of Model	78
3	Parameters and Constraints on System Design	132
4	Sample Designs	133
5	Effects of $f_1$ in Basic Suspension	137
6	Effects of $\zeta_1$ in Basic Suspension	137
7	Effects of Unsprung Mass Natural Frequency ( $f_1$ ) with Secondary Suspension	139
8	Effects of Primary Damping Ratio ( $\zeta_1$ ) with Secondary Suspension	140
9	Effects of Secondary Suspension Natural Frequency ( $f_2$ )	140
10	Effects of Secondary Suspension Damping Ratio ( $\zeta_2$ )	141
11	Effects of Velocity on Finite Length Filtering	143
12	Effects of Magnet Length	144
13	Designs for $V = 100, 300$ mph, $h_{10} = 0.4, 0.6$ in	146
14	Sample Data Based on Eddy Current Analysis, Ferromagnetic Rail	231
15	Sample Data Based on Eddy Current Analysis, Nonmagnetic Rail	232
16	Parameter Values for Sample Designs for Lateral Motion	268
A.1	Experimental Natural Frequencies, Damping, and Pot Settings	303

LIST OF FIGURES

<u>Figure</u>		<u>Page</u>
1.1	Schematic of Electromagnetic Suspension	22
2.1	Symbols for Magnet Design	28
2.2	Cross Section of Magnet Depicting Flux Paths	30
2.3	Circuit Diagrams of Flux Paths	30
2.4	Simple Heave Model of Magnetic Suspension	35
2.5	Filtering of Guideway Irregularities by Magnet's Length	42
2.6	Averaging a Sine Wave Over One Pole Face	42
2.7	Finite Magnet Length Filtering	44
2.8	Lumped Model of Electromagnet with Secondary Suspension	47
2.9	Coordinates for Discussion of Eddy Currents	47
2.10	Configuration for Analysis of Eddy Currents in Rail	53
2.11	Magnet's Representation as Periodic Structure	53
2.12	Flux Density Ratio vs. Current Frequency and Magnet Wave Length	56
2.13	Phase between Current and Flux in Rail vs. Current Frequency and Magnet Wavelength	57
2.14	Flux Density Ratio vs. Current Frequency and Air Gap	58
2.15	Phase between Current and Flux in Rail vs. Current Frequency and Air Gap	59
2.16	The Heave-Pitch Model without Secondary Suspension	61
2.17	Acceleration Spectrum in Heave-Pitch Model	62
3.1	Assembly Drawing of Magnetic Suspension Experiment	65
3.2	Magnetic Suspension Experiment	66
3.3	Magnet, Rail, Vehicle Assembly	66

<u>Figure</u>		<u>Page</u>
3.4	Magnet and Shaker	67
3.5	Control Panel	67
3.6	End View with Lateral Force Transducer	68
3.7	Magnet Parameters	78
3.8	Positions of Search Coils for Flux Measurement	82
3.9	Total Flux and Leakage Coefficients vs. Air Gap	86
3.10	Flux Paths as Air Gap Changes	88
	a. Small Gap (used in theoretical model)	
	b. Large Gap	
3.11	Static Force Tests	91
3.12	Acceleration Gain vs. Frequency $\tilde{\omega}_1 = 0.4, \zeta_1 = 0.707$	95
3.13	Acceleration Gain vs. Frequency for Laminated and Solid Rail $\tilde{\omega}_1 = 1.0, \zeta_1 = 0.2$	96
3.14	Acceleration Gain vs. Frequency $\tilde{\omega}_1 = 1.0, \zeta_1 = 0.707$	97
3.15	Acceleration Gain vs. Frequency $\tilde{\omega}_1 = 1.0, \zeta_1 = 2.0$	98
3.16	Acceleration Gain vs. Frequency $\tilde{\omega}_1 = 1.5, \zeta_1 = 0.707$	99
3.17	Displacement Gain vs. Frequency $\tilde{\omega}_1 = 1.0, \zeta_1 = 0.707$	100
3.18	Current Gain vs. Frequency $\tilde{\omega}_1 = 1.0, \zeta_1 = 0.707$	101
3.19	Voltage Gain vs. Frequency $\tilde{\omega}_1 = 1.0, \zeta_1 = 0.707$	102

<u>Figure</u>		<u>Page</u>
3.20	Average Air Gap vs. Frequency $\tilde{\omega}_1 = 1.0, \zeta_1 = 0.707$	107
3.21	Average Current vs. Frequency $\tilde{\omega}_1 = 1.0, \zeta_1 = 0.707$	108
3.22	Flux in Rail vs. Frequency	110
3.23	Phase Angle between Flux in Rail and Current vs. Frequency	111
3.24	Flux in Magnet vs. Frequency	112
3.25	Phase Angle between Flux in Magnet and Current vs. Frequency	113
4.1	Electric Circuit Analog for Magnet Heating by Ohmic Losses in Coil	120
4.2	Calculation of $A_{dis}$ . Areas shown do not contact air since magnet must be fastened to vehicle	122
4.3	Weight of Magnets and Coils vs. $l_p$ and $w_1$	124
4.4	Rail Weight vs. $l_p$ and $w_1$	124
4.5	Magnet Length vs. $l_p$ and $w_1$	125
4.6	Ohmic Losses in Coil vs. $l_p$ and $w_1$	125
4.7	Passenger Comfort: Acceleration Spectral Density vs. Natural Frequency of Basic Suspension without Secondary Suspension	150
4.8	Passenger Comfort: Acceleration Spectral Density vs. Damping Ratio of Basic Suspension without Secondary Suspension	151
4.9	Passenger Comfort: Acceleration Spectral Density vs. Primary Suspension Natural Frequency	152
4.10	Passenger Comfort: Acceleration Spectral Density vs. Primary Suspension Damping Ratio	153

<u>Figure</u>		<u>Page</u>
4.11	Passenger Comfort: Acceleration Spectral Density vs. Secondary Suspension Natural Frequency	154
4.12	Passenger Comfort: Acceleration Spectral Density vs. Secondary Suspension Damping Ratio	155
4.13	Passenger Comfort: Acceleration Spectral Density vs. Finite Length Filtering at Different Speeds	156
4.14	Passenger Comfort: Acceleration Spectral Density vs. Magnet Length	157
4.15	Passenger Comfort: Acceleration Spectral Density for Sample Designs with $h_{10} = 0.4$ in. and $V = 100$ mph	158
4.16	Passenger Comfort: Acceleration Spectral Density for Sample Designs with $h_{10} = 0.4$ in. and $V = 300$ mph	159
4.17	Passenger Comfort: Acceleration Spectral Density for Sample Designs with $h_{10} = 0.6$ in. and $V = 100$ mph	160
4.18	Passenger Comfort: Acceleration Spectral Density for Sample Designs with $h_{10} = 0.6$ in. and $V = 300$ mph	161
5.1	Cross Section of Magnet Depicting Flux Paths for Theoretical Model	164
5.2	Circuit Diagrams of Flux Paths a. Direct Representation b. Equivalent Circuit	164
5.3	Permeances at Corners. Numbers denote paths described in Appendix 2. The figure is from [50].	165
5.4	Permeances of Leakage Paths	165
6.1	Effects of Relative Weights on Current Controller Settings	175
6.2	Rms Acceleration, Displacement, Current, and Real Power for Basic Suspension ( $A = 2\pi \times 10^{-7}$ ft., $V = 300$ mph)	180

<u>Figure</u>	<u>Page</u>
6.3	182
Mechanical Analogs of Controlled Magnetic Fields. $k_1$ and $b_1$ are determined by control settings.	
a. Absolute Velocity Feedback b. Relative Velocity Feedback	
7.1	188
Apparent Power for Designs 2 and 4 of Table 3. $A = 2\pi \times 10^{-7}$ ft., $V = 300$ mph	
7.2	191
Effects of Feeding Back $h_{1-p}/(1 + Ts)$ . Magnet Design 2 of Table 3, $v_v = 2.18$ , $l_1 = 30$ ft., $\tilde{\omega}_1 = 0.4$ , $\zeta_1 = 0.707$ , and no Secondary Suspension.	
a. Voltage in control Coil. Solid and Broken Lines are for Indicated Control Strategies b. Root Locus as $\tilde{T}$ Varies	
8.1	196
Static Suspension Force vs. Air Gap for Nonlinear Suspension with Current Control ( $\tilde{\omega}_1 = 0.4$ )	
8.2	197
Current vs. Gap at Zero Velocity for Current Controller with Limiter ( $i + \tilde{i} \geq 0$ )	
8.3	197
Road Input and Acceleration vs. Time for High Input Frequency ( $\tilde{\omega}_1 = 0.4$ , $\zeta_1 = 0.707$ )	
8.4	198
Nonlinear Acceleration Bode Plot	
8.5	199
Nonlinear Voltage Bode Plot	
8.6	201
Average Air Gap vs. Frequency	
8.7	202
Average Current vs. Frequency	
8.8	204
Nonlinear Response to Initial Displacement (at $\tilde{t} = 0$ , $\tilde{h}_1 = -0.5$ , $\tilde{y}_1 = 0$ )	
8.9	205
Nonlinear Response to Initial Displacement (at $\tilde{t} = 0$ , $\tilde{h}_1 = 0.5$ , $\tilde{y}_1 = 0$ )	
8.10	206
Linear Response to Initial Displacement (at $\tilde{t} = 0$ , $\tilde{h}_1 = 0.5$ , $\tilde{y}_1 = 0$ )	
8.11	207
Nonlinear Response to Initial Displacement (at $\tilde{t} = 0$ , $\tilde{h}_1 = -0.95$ , $\tilde{y}_1 = 0$ )	
a. Five Variables b. Expanded Voltage	

<u>Figure</u>		<u>Page</u>
8.12	Inductive Voltages from Drop Tests	210
11.1	Current vs. Frequency: Comparison of Heave and Heave-Pitch Models	245
11.2	Current and Displacement of Heave-Pitch Model ( $\tilde{I} = 4$ , $\tilde{I}^* = -2$ , $\tilde{T} = 5.8$ , $A = 2\pi \times 10^{-7}$ ft., $V = 300$ mph, $L_v = 100$ ft.)	250
12.1	Permeances for Scale Law for Lateral Forces	255
12.2	Lateral Force Measurements (Line is fit to experimental points)	259
12.3	Lateral Motion with Passive Secondary Suspension a. Schematic b. Linear Graph	262
12.4a	Passenger Comfort: Acceleration Spectral Density from Road Input to Lateral Mode	271
12.4b	Passenger Comfort: Acceleration Spectral Density from Wind Input to Lateral Mode	272
12.5	Rms Lateral Acceleration of Unsprung Mass	273
12.6	Rms Lateral Acceleration of Sprung Mass	273
12.7	Rms Lateral Clearance of Secondary Suspension	274
12.8	Rms Lateral Magnet-Rail Clearance	275
12.9	Lateral Magnet-Rail Clearance with Steady Wind	275
A.3.1	Circuit to Convert Voltage Control to Current Control	292
A.4.1	Averaging of Wind Force along Vehicle	298
A.4.2	Finite Length Filtering	298
A.5.1	Circuit Diagram of Magnet Control	300

LIST OF SYMBOLS

A	Road roughness. Complex amplitude of magnetic field
$A_{dis}$	Cross sectional area of coils
$A_{coil}$	Magnet area for heat dissipation
$A_h$	Autofeedback coefficient of relative displacement
$A_L$	Area of vehicle's side
$A_y$	Autofeedback coefficient of absolute velocity
B	Complex amplitude of magnetic field
$\vec{B}$	Magnetic flux density with Cartesian components $B_x, B_y, B_z$
$b_1$	Damping ratio implemented by magnetic field
$b_2$	Damping ratio of secondary suspension
C	Complex amplitude of magnetic field
$c_d$	Wind drag coefficient
$C_h$	Crossfeedback coefficient of relative displacement
$C_y$	Crossfeedback coefficient of absolute velocity
D	Complex amplitude of magnetic field
e	Safety factor in static magnet design
E	Expected value operator, Complex amplitude of magnetic field
f	Frequency. Coil's packing factor, Component of force matrix in heave-pitch analysis (with subscript)
$f_1$	Natural frequency of primary suspension
$f_2$	Natural frequency of secondary suspension
F	Magnet force (with and without subscripts). Complex amplitude of magnetic field.
$F_L$	Finite length filtering of wind

$F_{\text{mag}}$	Finite length filtering of road input
$F_w$	Wind force
$g$	Gravitational constant
$G$	Arbitrary transfer function
$g_1$	Lateral clearance between magnet and rail
$g_2$	Lateral clearance of secondary suspension
$\vec{H}$	Magnetic field intensity
$h_1$	Vertical clearance between magnet and rail
$h_2$	Vertical clearance of secondary suspension
$i$	Current in control coil
$\vec{i}, \vec{j}, \vec{k}$	Unit vectors parallel to x,y,z, axes
$I$	Vehicle's moment of inertia about pitch axis
$\tilde{I}, \tilde{I}^*$	$1 \pm mL_v^2/4I$
$\vec{J}$	Current density
$k$	Magnet to air heat transfer coefficient
$k_L$	Lateral stiffness of magnetic suspension
$k_w$	Factor in wind filter
$k_v$	Coefficient in simplified leakage expressions
$k_1$	Spring constant implemented by magnetic field
$k_2$	Spring constant of secondary suspension
$K_1, K_2$	Coefficients of linearized magnet force
$l_{\text{coil}}$	Mean length of one turn of control coil
$l_p$	Width of magnet's pole face
$l_1$	Magnet length
$l_2$	Width of rail's pole face
$L$	Scale of wind turbulence

$L_v$	Length of vehicle
$L_y$	Coefficient of $h_1$ in linearized inductance
$L_1$	Self inductance of control coil
$m$	Total vehicle mass ( $m_1 + m_2$ )
$m_1$	Mass of magnet (unsprung mass)
$m_2$	Mass of sprung mass
$\tilde{M}, \tilde{M}^*$	$1/4 + I/mL_v^2$
$N$	Turns in control coil
$N_s$	Turns in control coil
$P$	Permeance (with subscript)
P.I.	Performance Index
$P_A$	Apparent power
$P_L$	Lift Pressure
$P_R$	Real power
$P_3$	Power in region 3
$q$	ohmic heating in control coil
$r$	Resistivity
$r_c$	Resistivity of control coil
$R_c$	Resistance of feedback resistor
$R_L$	Resistance of load resistor
$R_s$	Resistance of sensing resistor
RRF	Road roughness factor
$R_1$	Resistance of control coil
$s$	Laplace transform of $d/dt$
$t$	Time

$t_p$	Thickness of permeance path
$t_{\text{rail}}$	Thickness of rail
$T$	Vehicle transit time. Filter time constant
$\Delta T$	Temperature rise in control coil
$v$	Voltage in control coil
$v_{\text{ind}}$	Inductive voltage in control coil
$V$	Vehicle's forward velocity
$V_R$	Wind velocity perpendicular to vehicle motion
$V_T$	Total wind velocity relative to vehicle
$w_1$	Magnet's window width
$w_2$	Clearance between coil and pole face
$w_3$	Length of magnet pole core
$x, y, z$	Cartesian coordinates
$y_0$	Vertical position of road w.r.t. absolute reference
$y_1$	Vertical position of magnet w.r.t. absolute reference
$y_2$	Vertical position of sprung mass w.r.t. absolute reference
$z_1$	Lateral position of magnet w.r.t. absolute reference
$z_2$	Lateral position of sprung mass w.r.t. absolute reference

Greek

$\alpha$	Inverse of complex skin depth
$\beta$	Dimensionless oscillating lateral wind force. Weighting factor of P.I.
$\gamma$	Ratio sprung to unsprung mass
$\delta$	Skin depth

$\Delta$	Denotes incremental variable
$\zeta_1$	Damping ratio implemented by magnetic field
$\zeta_2$	Damping ratio of secondary suspension
$\theta$	Phase angle between flux and control current. Pitch angle
$\lambda$	Wavelength of wind and road irregularities
$\lambda_M$	Magnet width wavelength
$\mu$	Permeability (with subscript)
$\mu_0$	Permeability of free space
$\nu$	Characteristic wind frequency. Flux coefficients (with subscripts)
$\pi_1, \pi_2$	Dimensionless parameters for lateral force
$\rho$	Density, Weighting factor of P.I.
$\sigma$	Conductivity
$\phi$	Flux with subscript
$\phi(s)$ $\phi(\omega)$	Spectral density of variable indicated by subscript
$\omega$	Angular frequency
$\omega_1$	Angular natural frequency of primary suspension
$\omega_2$	Angular natural frequency of secondary suspension

#### Overlines

$\vec{\phantom{x}}$	Vector
$\sim$	Dimensionless quantity

#### Subscripts

For heave pitch model

F	Front
R	Rear

For flux and permeance

- a Air gap
- F Fringing
- L Leakage
- T Total
- u Useful
- v Voltage

General

- av Average
- o Nominal
- p Measured at magnet's midpoint
- x,y,z Cartesian coordinates
- 1,2,3 Regions for eddy current analysis

## PART I. INTRODUCTION AND PRINCIPAL RESULTS

### 1. INTRODUCTION

#### 1.1 Background

To improve present urban and intercity transportation, several unconventional forms of ground transportation have been proposed. Vehicles which possess improved and innovative suspensions and/or propulsion systems have been proposed and include:

- (1) Advanced wheeled vehicles
- (2) Tracked levitated vehicle systems
  - (a) Air cushion
    - (i) externally pressurized
    - (ii) ram air cushion
  - (b) Magnetic
    - (i) electromagnetic
    - (ii) electrodynamic

Overall development of these transportation systems requires consideration of suspensions, propulsion, power pick-up, and guideway construction. This thesis concentrates on one aspect of the task - suspension development.

A suspension must track the guideway and isolate passengers from guideway irregularities and aerodynamic loading. Typical suspensions consist of a primary suspension which contacts the road and a secondary suspension which connects the vehicle body to the primary suspension.

Present railroads use steel wheels as their primary suspension. Since the wheel-rail stiffness is very large, small bumps cause the wheels to bounce at speeds of 150-200 mph. The wheel bounce reduces ride

quality, increases noise levels, and limits the vehicle's speed because adequate traction cannot be maintained. Currently efforts are seeking to eliminate the bounce by improved bogey design and by active suspensions. Since the wheels are virtually in point contact with the rail, the stresses on the rail are high (40,000 psi, [67]<sup>\*</sup>) so that high speed lines like Japan's Tokaido Railroad require continuous, costly maintenance.

Air cushion and magnetic suspensions possess several advantages. Since the load on the guideway is distributed over a large area, the stresses on the guideway are low (1 psi air cushion, 50 psi magnetic) so that maintenance may be reduced and structural requirements relaxed. Because of the large area under the suspension, the influence of small bumps is averaged so that high speed bounce is eliminated although occasional contact may still occur. The absence of vehicle-guideway contact reduces suspension noise. At high speed the frictional loss is low for levitated vehicles but power is consumed for levitation. The noncontacting suspensions are most compatible with noncontacting propulsion devices.

This thesis studies electromagnetic suspensions. The two types of magnetic suspensions which have received primary attention in earlier investigations are:

- (1) large clearance (several inches) repulsive, electrodynamic systems; and
- (2) small clearance (less than one inch) tractive electromagnets.

In electrodynamic systems, a current-carrying coil is built into the vehicle. As the vehicle moves, the flux produced by the current flowing in the on-board coil induces currents either in passive coils

---

\* Numbers in brackets refer to references.

located in the guideway [13-16, 23] or in conducting nonmagnetic sheets (typically aluminum) which form the guideway's surface [3, 4, 6, 7, 17, 18, 19, 28]. The induced currents produce a magnetic flux which opposes that of the coils located on the vehicle and produces lift which is a function of vehicle velocity. By using superconducting cryogenic coils on the vehicle, very high currents and, therefore, fields can be produced with negligible resistance losses. As a result, the vehicle can be lifted several inches above the guideway. Because of these large clearances, electrodynamic systems feature low sensitivity to guideway roughness.

Electrodynamic systems are inherently statically stable and require no feedback control for static stability; however their damping is very low and special provisions must be included to damp vehicle motions (for example, active control). At low speeds (less than 20 mph.), the induced currents are too small to lift the vehicle and typically wheels will be necessary for low speed operation. After the vehicle has lifted and forward speed has increased to the 200-300 mph. range (typically), lift remains high and drag drops to 1/10 to 1/50 of the lift. It has been proposed [19] that the intense magnetic field used for levitation can also be used for propulsion.

A tractive electromagnetic suspension is sketched in Figure 1.1. A magnetic circuit consisting of an iron core in the vehicle and a ferromagnetic rail fixed to the track is excited by a current-carrying coil and the on-board core is attracted to the rail. Lift is provided essentially independently of vehicle velocity. When excited by a simple current or voltage source, the suspension is statically unstable, and

appropriate displacement sensors and control circuits are required to achieve statically stable and dynamically acceptable suspension characteristics.

Actual configurations will resemble Figure 1.1. The brackets which support the rail are designed so that the magnet is a specified distance from the ground. The distance is selected to restrain the vehicle from falling to gaps which are so large that the vehicle leaves the track. The general configuration will have four magnets, one at each corner of the vehicle. Additional magnets may be used for lateral control or, as shown in Chapter 12, it may be possible to obtain lateral guidance with only the lifting magnets.

Advantages of electromagnetic suspensions include compatibility with linear induction motors, the absence of superconductors, levitation at zero speed, and low drag from zero to 300 mph (at 300 mph., estimated lift to drag ratios are approximately 200 for electromagnetic suspensions and 25 for electrodynamic). It has been proposed that the fields used for lift can also be used for propulsion. Disadvantages include on-board weight which may be 10-20% of the total vehicle weight and the active control required to achieve stability.

For Motor Company [18, 28, 35, 70] and Stanford Research Institute [17, 31] have studied electrodynamic suspensions with continuous aluminum guideways. These analyses have focused upon power requirements, magnet cooling, and ride quality. Stanford has built a model with superconducting coils which lifts several hundred pounds. M.I.T.'s National Magnet Lab [19] has proposed an electrodynamic system with continuous aluminum guideway and propulsion coils laid in the guideway. The aluminum provides lift as in the Ford and S.R.I. configurations while the propulsion

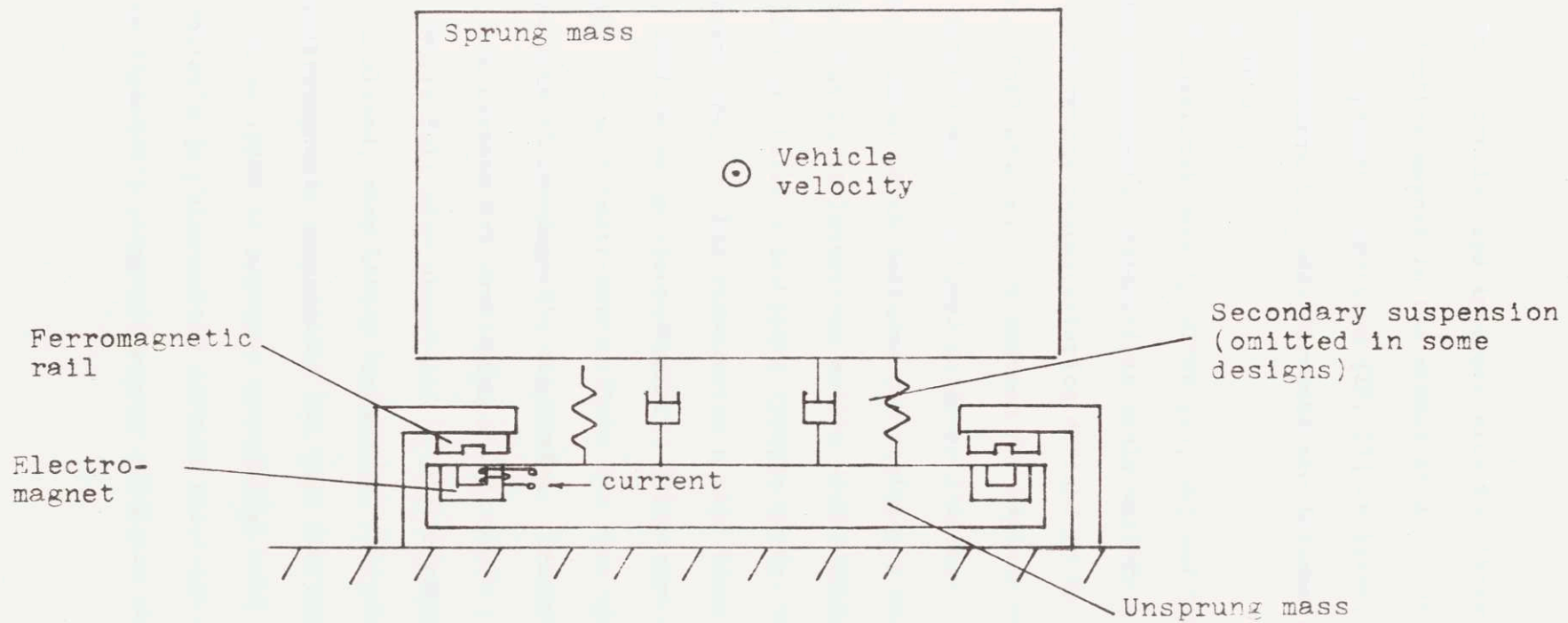


Fig. 1.1. Schematic of Electromagnetic Suspension

coils are controlled and interact with the large lift field of the superconducting magnet in the manner of a synchronous motor.

A Japanese consortium [20, 23] is investigating electrodynamic suspensions where the eddy currents are induced in passive coils located in the guideway.

Theoretical work by MITRE [29, 36] and TRW [26] have indicated that electromagnetic suspensions could satisfy ride comfort and many other performance characteristics desired in an advanced transportation system. Both studies have assumed the magnets were short (point contact) while MITRE's model included guideway dynamics. Ford [28, 35, 70] has studied a model which includes the resistance and voltage of the control coil and has built laboratory models with voltage control. Rohr Corporation [22] has built a low speed (people mover) vehicle. Krauss-Maffel of Germany [24, 25] has constructed a test track and has operated a 10 ton vehicle using electromagnetic suspension at speeds greater than 100 mph. Messerschmitt-Bolkow-Blohm has also operated a large scale test vehicle with electromagnetic suspension. Because of the success of these tests, the Germans are developing a full-scale prototype.

While full size prototypes of electromagnetic suspensions are being developed, very little fundamental analysis or design information for electromagnetic suspensions has been published.

Other types of magnetic suspensions have also been conceived such as Bachelet's [1] alternating current repulsive magnets and Polgreen's and Westinghouse's permanent magnet repulsive schemes [2, 9, 11, and 12].

## 1.2 Thesis Objectives

The primary goal of this thesis is to provide analytical models for electromagnetic suspensions operating in the heave mode so that performance capabilities and limitations may be established and compared with other suspensions.

To accomplish this goal the following specific objectives are considered:

- (1) Identification of the primary physical factors which must be considered in magnet design.
- (2) Formulation of an accurate model of the electromagnetic suspension to enable investigation of system performance.
- (3) Experimental evaluation of the model for zero forward speed.
- (4) Development of general design guidelines and specific design cases.

The principal contribution of this work is an experimentally verified model for the heave (vertical) dynamics of a single electromagnetic suspension. The models investigate eddy currents induced by vertical motion, leakage fluxes, finite magnet length, and optimal magnet control, significant effects which have been neglected in other studies of electromagnetic suspensions [26, 28, 29, 35, 36, 70]. The effects of eddy currents induced by the vehicle's forward motion are included in a preliminary manner. A system having only a primary suspension consisting of the magnet is studied to demonstrate the modeling of the magnet. The model is then extended to systems with secondary suspension. Preliminary analyses of lateral guidance and heave-pitch models are conducted. With guideway irregularities and wind load inputs modeled as stochastic

processes, design curves of system performance (magnet weight, acceleration levels, power, and others) are generated. These curves are then used to establish preliminary guidelines for full scale systems.

### 1.3 Organization of Thesis

Part I introduces the thesis and presents its principal results. Chapter 2 summarizes the development of the basic analytical models. Chapter 3 presents the experimental verification of the model for heave motion. Design algorithms and design data are presented in Chapter 4. The design cases indicate that rails with roughness comparable to highways and aircraft runways at 100 and 300 mph, respectively, can be tolerated while meeting ride comfort criteria. These designs feature air gaps of 0.4 to 0.6 inches, simple secondary suspensions, and magnets whose length is of the order of 10 to 30 feet and whose collective weight is 10-15% of the total vehicle weight.

Part II develops the relations which describe the vertical motion. Chapter 5 presents static relations which demonstrate the importance of leakage flux in limiting maximum magnet lift and in control voltage. In Chapter 6, a magnet current control law which feeds back magnet-rail clearance and absolute magnet velocity is discussed. The effects of finite magnet length and the importance of feeding back the average clearance above the magnet are discussed in Chapter 7. Chapter 8 presents nonlinear simulations which show that the results of the linearized analyses are valid for representative designs as considered in Chapter 4. In Chapter 9, the model is extended to include a secondary suspension which consists of a spring in parallel with a damper. Chapter 10 presents a simple model which predicts the effects of eddy currents associated

with vertical oscillations. This analysis indicates that practical magnet and rail designs may be achieved in which the effects of eddy currents induced by vertical motion do not significantly affect the magnet's performance.

Part III includes preliminary studies of heave-pitch models and lateral guidance. Models with both heave and pitch degrees of freedom demonstrate the deterioration in ride quality which is caused by the coupling of the suspensions at the vehicle's front and rear by the vehicle's rotational inertia. In electromagnetic suspensions, feedback of variables measured at one end of the vehicle into the current control system at the other end of the vehicle cancels the rotational coupling and improves ride quality. The analysis of the lateral guidance indicates that it may be possible to guide the vehicle with the fringing fields of the magnets used for lift so that additional guidance magnets may not be required.

The conclusions and recommendations derived from this thesis are summarized in Part IV.

## 2. SUMMARY OF ANALYTICAL MODELS

### 2.1 Introduction

In order to design electromagnetic suspensions, an analytical model which adequately represents the dominant static and dynamic behavior is required. This chapter describes such a model for a single magnet operating in the heave mode. The models investigate the following important factors:

- (1) Magnet force-current-gap static relationships and static leakage fluxes.
- (2) Dynamic performance in heave operation. Optimal control laws, finite magnet lengths, leakage fluxes, and effects of eddy currents are considered.

In addition, preliminary investigations of lateral guidance and models with heave and pitch degrees of freedom are discussed.

### 2.2 Static Effects

For a typical magnet rail system as diagrammed in Figure 2.1 (the shape of the magnet and rail is discussed later), a lift force can be determined for a static situation. As the vehicle moves forward or vertically, the changing magnetic fields induce in the rail eddy current which may reduce the lift calculated from the static situation at high vehicle speeds or high oscillation frequencies. As a first model, this section considers static effects with no motion. The effects of eddy currents are discussed in Chapters 2.3.5 and 10.

The magnet's lift capability, the voltages required by the control coil, and the eddy current effects require determination of the magnetic flux paths in the magnet rail system. The determination of flux paths

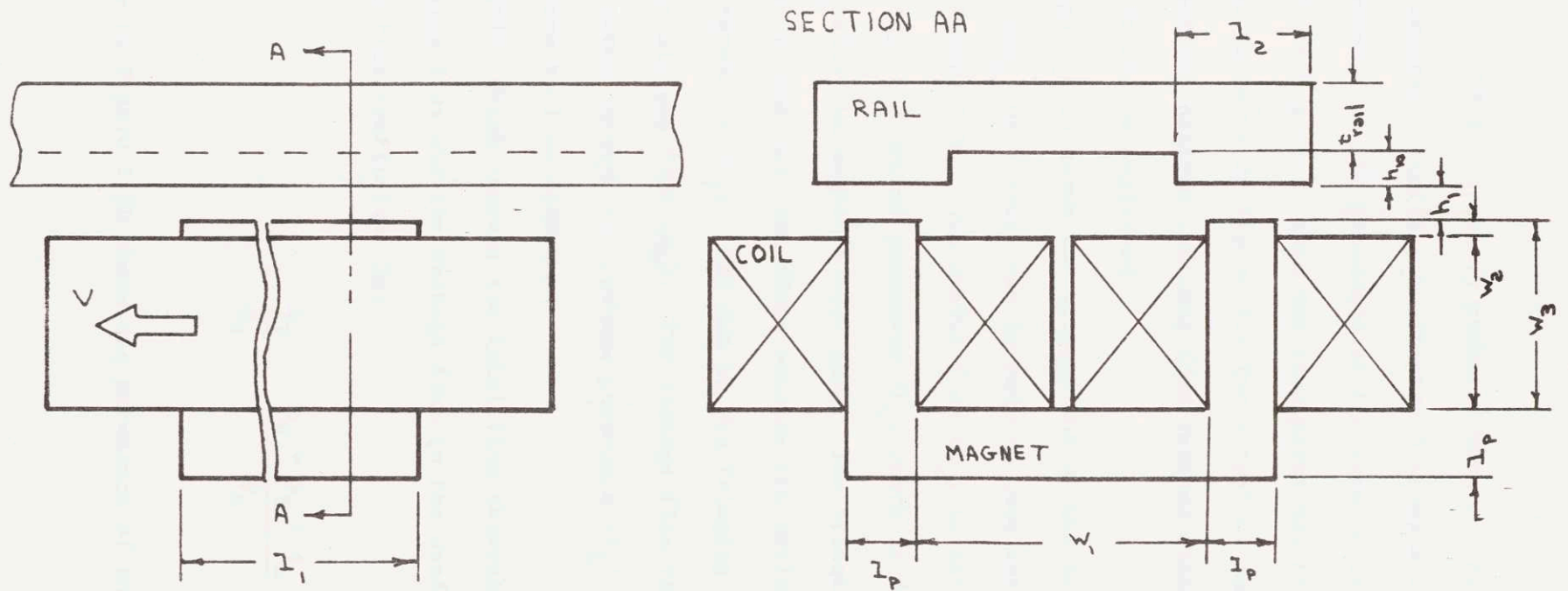


Fig. 2.1. Symbols for Magnet Design

is a complicated field theory problem; however, lumped techniques which are experimentally verified in Chapter 3 provide useful design models. It is assumed that the permeance of the iron parts is high compared to that of the air gaps so that the flux paths may be grouped in lumped permeances as shown in Figure 2.2 for a typical magnet cross section. Since practical designs are long (for reasons discussed in Chapter 2.3.5), end effects can be neglected.

Figure 2.3a shows the arrangement of the permeances in a circuit diagram. The flux circuit can be reduced into the equivalent circuit shown in Figure 2.3b. The useful flux ( $\phi_u$ ) is defined as the flux which flows through the useful permeance ( $P_u$ ) which is determined by the volume directly below the magnet's pole face. The fringing flux ( $\phi_F$ ) goes from the magnet to the rail but flows outside the useful area through the fringing permeance ( $P_F$ ). The sum of the fringing and useful flux is often called the air gap flux ( $\phi_g$ ). The leakage flux ( $\phi_L$ ) flows directly between the pole cores through the leakage permeance ( $P_L$ ) and does not cross the air gap from rail to magnet.

Ratios which compare the total flux through the magnet's yoke ( $\phi_T$ ), the fringing flux and the leakage flux to the useful flux may be defined. The total flux coefficient is:

$$v_T = \frac{\phi_T}{\phi_u} = \frac{\phi_u + \phi_F + \phi_L}{\phi_u} \quad (2.1)$$

Referring to Figure 2.3b where the permeance of the iron is neglected

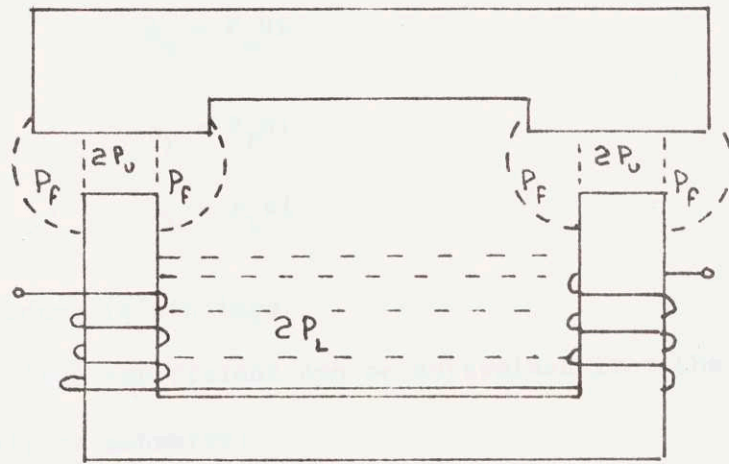


Fig. 2.2. Cross Section of Magnet Depicting Flux Paths

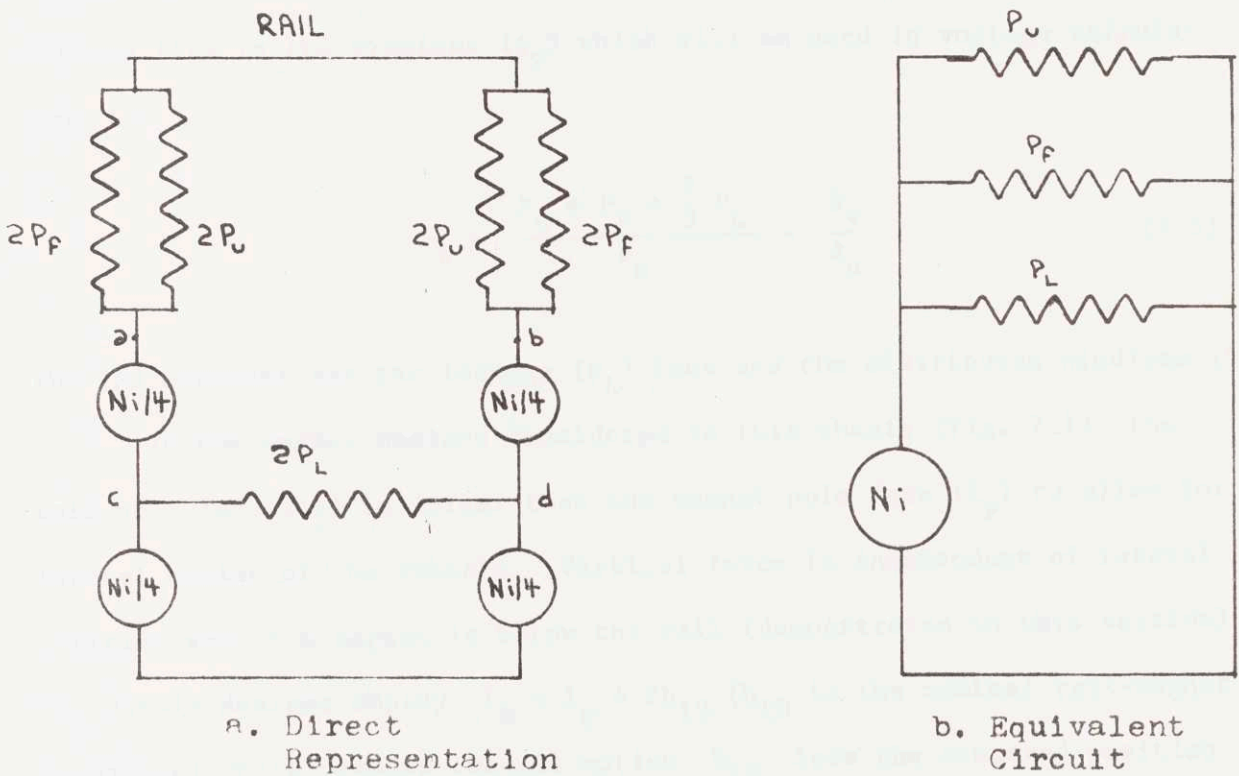


Fig. 2.3. Circuit Diagrams of Flux Paths

$$\phi_u = P_u Ni$$

$$\phi_F = P_F Ni$$

$$\phi_L = P_L Ni$$

where  $Ni$  = amp turns in windings.

Thus, the total flux coefficient can be determined from the permeances which depend only on geometry:

$$v_T = \frac{P_u + P_F + P_L}{P_u} = \frac{P_T}{P_u} \quad (2.2)$$

Similar expressions are derived for other flux coefficients. The average flux in the windings ( $\phi_v$ ) which will be used in voltage calculation is:

$$v_v = \frac{P_u + P_F + \frac{2}{3} P_L}{P_u} = \frac{\phi_v}{\phi_u} \quad (2.3)$$

The  $2/3$  accounts for the leakage ( $\phi_L$ ) loss and the distributed windings [50].

In the magnet designs considered in this thesis (Fig. 2.1), the rail pole face ( $l_2$ ) is larger than the magnet pole face ( $l_p$ ) to allow for lateral motion of the vehicle. Vertical force is independent of lateral position when the magnet is below the rail (demonstrated in this section). The sample designs employ  $l_2 = l_p + 2h_{10}$  ( $h_{10}$  is the nominal rail-magnet clearance) which permits lateral motion  $h_{10}$  from the centered position and allows for lateral forces to be exerted by the lifting magnet. The rail's U shape is based on lateral guidance considerations.

When the magnet's pole face is below the rail's pole face, the useful permeance is (Chapter 5):

$$P_u = \frac{\mu_o l_1 l_p}{2h_1} \quad (2.4)$$

where  $\mu_o$  = permeability of free space =  $4\pi \times 10^{-7}$  nt<sup>2</sup>/amp

$l_1 l_p$  = area of magnet pole face,

$h_1$  = air gap .

For the magnet's pole face below the rail's, the flux coefficient is:

$$v_T = 1 + K_v h_1 \quad (2.5)$$

where  $K_v$  is virtually a constant in the region of design interest (Chapter 3) and is defined in Chapter 5. Similar expressions may be derived for the other flux coefficients.

The vertical force is derived from [50]:

$$F = -\frac{1}{2} (Ni)^2 \frac{\partial P_T}{\partial h_1} \quad (2.6)$$

With substitution of (2.2) and (2.5):

$$F = \frac{\mu_o (Ni)^2 l_1 l_p}{4h_1^2} \quad (2.7)$$

Since  $v_T$  and  $P_u$  are independent of lateral position when the magnet's pole face is below the rail's, the vertical force does not depend on lateral position if the magnet's pole face is below that of the rail, i.e., when saturation is avoided, the lift force depends only on the useful flux with no contribution from the fringing and leakage fluxes. The

maximum force which the magnet can exert is limited by saturation of the magnet yoke; thus, the maximum force is proportional to  $1/v_T^2$ . For typical designs (Table 3),  $v_T$  is approximately 2 (if leakage is ignored,  $v_T = 1$ ).

Since  $v_T$  increases with increasing air gap ( $h_1$ ) (the useful flux decreases and leakage flux increases while fringing flux decreases slightly) and since the total flux through the core is limited by saturation, a limiting gap exists at which the magnet will no longer lift the vehicle regardless of the current. This limiting air gap determines a region of static stability independent of any control laws and safety links are required.

Equations (2.1) to (2.7) provide the basic equations for static lift and flux which are used in this thesis.

### 2.3 Model for Heave Dynamics

In developing the model used for determining the heave performance, the following effects (which are detailed in Part II) are investigated:

- (1) linearized suspension model,
- (2) control laws based on performance indices,
- (3) finite magnet length,
- (4) eddy currents.

Quantitative estimates of the effects of eddy currents induced by the changing magnetic field associated with vertical oscillations are made. The effects of eddy currents induced by the vehicle's forward motion are discussed qualitatively.

- (5) passive secondary suspension.

The heave model is studied because it is simple compared to other vehicle representations but still yields much useful information about the vehicle's performance characteristics.

### 2.3.1 Simple Linearized Model

A simple model for a magnetic suspension which operates in the heave mode appears in Figure 2.4. In this model, the length of the magnet is assumed short compared to the dominant wavelength of the irregularities in the guideway or track; i.e., the air gap between magnet and rail is uniform. The input to the model is the road's irregularity amplitude which is modeled as a stationary stochastic process whose spectral density (which extends from  $-j\infty$  to  $+j\infty$ ) [18, 28, 29, 38, 44] is:

$$\phi_{y_0 y_0}(s) = \frac{AV}{s^2} \quad (2.8)$$

where  $s$  = Laplacian operator

$A$  = road roughness parameter

$V$  = forward velocity of vehicle .

Note that in the frequency domain  $j\omega = s$  where  $\omega$  is the angular frequency which can be related to  $\lambda$  the wavelength of the road's irregularities by

$$\omega = \frac{2\pi V}{\lambda} \quad (2.9)$$

The vehicle model is based upon a single magnet limited to heave motion. In the equation of motion, the magnetic force (2.7) equals the gravitational force plus the mass acceleration:

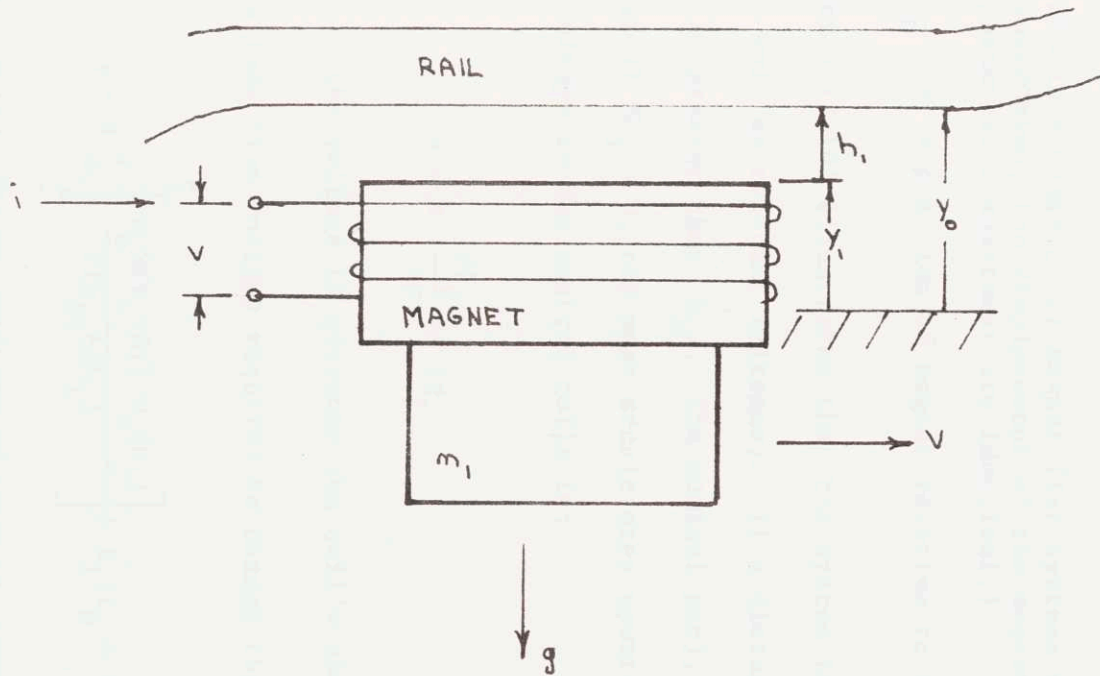


Fig. 2.4. Simple Heave Model of Magnetic Suspension

$$m\ddot{y}_1 + mg = F_o + \Delta F = \frac{\mu_o N^2 (i_o + \Delta i)^2 l_1 l_p}{4(h_{i0} + \Delta h_1)^2} \quad (2.10)$$

At equilibrium:

$$F_o = mg = \frac{\mu_o (Ni_o)^2 l_1 l_p}{4h_{i0}^2}$$

where  $m$  = mass of vehicle

$y_1$  = absolute position of magnet (for systems without a secondary suspension, the displacement of the magnet and that of the passenger compartment are identical.)

$h_1 = y_0 - y_1$  = position of magnet relative to rail.

Equation (2.10) illustrates that the system is unstable for constant currents (as well as constant voltages). If a disturbance occurs so that  $\Delta h_1 > 0$  ( $h_1$  is greater than  $h_{i0}$ , the nominal gap), the mass falls to the ground, while if  $\Delta h_1 < 0$ , the mass accelerates upward to contact the rail.

The voltage in the control coils is:

$$v = N \frac{d\phi_v}{dt} + iR_1$$

where  $iR_1$  is the voltage to overcome the coil's ohmic resistance and

$N \frac{d\phi_v}{dt}$  is the inductive voltage required to change the magnetic fields.

With (2.3)

$$v = N \frac{d}{dt} \left[ \frac{\mu_o N (i_o + \Delta i) v_v (h_1)}{2(h_{i0} + \Delta h_1)} \right] + R_1 (i_o + \Delta i) \quad (2.11)$$

To determine a first estimate of control requirements, a linear model is considered. Equations (2.10) and (2.11) may be linearized about the operating point ( $\Delta h_1 = 0$  and  $\Delta i = 0$ ):

$$\Delta F = m\ddot{y}_1 = K_1 \Delta i - K_2 \Delta h_1 \quad (2.12)$$

$$\Delta v = v_{ind} + R_1 \Delta i = L_1 \frac{d(\Delta i)}{dt} - L_y \frac{d(\Delta h_1)}{dt} + R_1 \Delta i \quad (2.13)$$

where

$$K_1 = \frac{\mu_o N^2 i_o l_1 l_p}{2h_{10}^2}$$

$$K_2 = \frac{\mu_o (Ni_o)^2 l_1 l_p}{2h_{10}^3}$$

$$L_1 = \frac{\mu_o N^2 v}{2h_{10}} \quad v_v = v_v (h_1 = h_{10})$$

$$L_y = \frac{\mu_o N^2 i_o}{2h_{10}^2}$$

### 2.3.2 Control Laws Based on Performance Index

A performance index (P.I.) is constructed to reflect the characteristics desired of an electromagnetic suspension. Although comfort depends on the entire acceleration spectrum (detailed in Chapter 4.2), a P.I. which includes only the rms acceleration provides an approach which yields valuable results. To limit the probability of contact between the rail and the magnet, the incremental gap  $\Delta h_1$  must be limited to a fraction of the nominal gap  $h_{10}$  (Chapter 4.2). The incremental current  $\Delta i$  must be limited because negative currents ( $i_o + \Delta i < 0$ ) seriously deteriorate the system's control characteristics and because thermal and current source restrictions limit the maximum current.

These considerations are reflected in the performance index:

$$P.I. = E[\ddot{y}_1^2] + \rho E[\Delta h_1^2] + \beta E[\Delta i^2] \quad (2.14)$$

where  $E$  is the expected value operator. The factors  $\rho$  and  $\beta$  determine the relative weights of the terms in the performance index. Changing the relative weights changes the importance of the terms in P.I. and are reflected in suspensions which favor the quantities having the largest weighting factor.

Because the equation of motion (2.9) is formulated for current control the optimal controller for the electromagnetic suspension is derived in terms of current and is then extended to voltage. The current control law which minimizes the P.I. for the stochastic road input (2.8) is found by matrix ricatti techniques [54, 56] to be:

$$\Delta i = \frac{1}{K_1} [(K_2 + m_1 \omega_1^2) \Delta h_1 - 2\zeta_1 \omega_1 m_1 \dot{y}_1] \quad (2.15)$$

where  $\omega_1$  is the suspension's natural frequency and  $\zeta_1$  is the damping ratio. As shown in Chapter 6,  $\omega_1$  and  $\zeta_1$  are functions of the relative weights  $\rho$  and  $\beta$ .

The current control law (2.15) which gives the optimal suspension feeds back the relative displacement between the magnet and the rail and the absolute velocity of the magnet. Feeding back the relative displacement makes the system (2.12) stable while the velocity feedback adds damping.

The suspension which minimizes P.I. is:

$$\frac{y_1(s)}{y_0(s)} = \frac{\omega_1^2}{s^2 + 2\zeta_1 \omega_1 s + \omega_1^2} \quad (2.16)$$

This suspension is optimum only for the road spectrum assumed in (2.8). Other spectra will result in different optimum suspensions; however, as long as the magnet does not saturate (Chapter 2.2), the control indicated by (2.15) stabilizes the unstable system of (2.12) regardless of the road input. The control given by (2.15) is also physically realizable (Chapter 3) and has finite static stiffness.

Although the optimal control has been formulated for current control, voltage control can also be used. Since current is related to voltage through (2.13), the optimal suspension (2.16) can be obtained through the voltage control:

$$\begin{aligned}
 v = & \left( \frac{L_1}{K_1} [K_2 + m_1 \omega_1^2] - L_y \right) \dot{h}_1 - \frac{L_1}{K_1} 2\zeta_1 \omega_1 m_1 \ddot{y}_1 \\
 & + \frac{R_1}{K_1} [K_2 + m_1 \omega_1^2] \Delta h_1 - \frac{R_1}{K_1} 2\zeta_1 \omega_1 m_1 \dot{y}_1
 \end{aligned}
 \tag{2.17}$$

To attain the optimal suspension (2.16) with a voltage control requires measurement of the relative displacement and velocity between the magnet and the rail and the magnet's absolute velocity and acceleration. From consideration of the optimal suspension, current control is preferred to voltage control because:

- (1) To obtain optimal performance, current control requires measurement of only two variables compared to four for voltage control; and
- (2) Voltage control introduces into the control loop leakage fluxes (inductances) and resistances that change with gap and with temperature and which cannot easily be compensated for.

The above difficulties arise because voltage is less directly

related to force than is current as shown by (2.12) and (2.13).

In industrial situations, voltage controllers are used more commonly than current controllers; however, the conversion of voltage controllers to current controllers by a feedback loop is discussed in Appendix 3.

Two modes of magnet operation are possible:

- (1) The vehicle can be supported by the magnets alone with no secondary suspension. As discussed in Chapter 4.3 (particularly Table 13) the gains of the control (2.15) of the basic suspension can be set so that the suspension has a low natural frequency; thus, ride quality can be achieved. For example, at 300 mph on welded steel rails, natural frequency of 1.6 hz. and damping ratio of .7 results in acceptable performance.
- (2) A secondary suspension can be used with the magnetic suspension. The control can be set so that the primary magnetic suspension has a high natural frequency which reduces the required clearance and current (Tables 5 and 7) and a soft secondary suspension is used to provide ride comfort. The secondary suspension permits loosening of track tolerances but increases system complexity.

When the magnet's finite length is considered in the next section, the importance of feeding back the average displacement between the magnet and rail, rather than the displacement measured at a point, is demonstrated.

Nonlinear simulations described in Chapter 8 indicate that the linearized analysis will yield accurate preliminary spectral densities and rms values for the magnet system in its normal operating range as discussed in Chapter 4. However, for large displacements from the nominal position where the magnet becomes saturated or when the current tries to become negative ( $\Delta i < -i_0$ ) nonlinear simulations must be used.

### 2.3.3 Finite Magnet Length

In real systems, the wavelength of important road irregularities

are often comparable to the magnet's length so that the point contact model is not valid. It is important to consider the magnet's finite length because of:

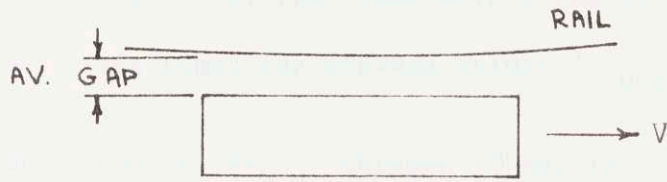
- (1) its influence on control system requirements, particularly sensor requirements.
- (2) its influence on suspension performance.

The magnet's filtering of the guideway irregularities is illustrated in Figure 2.5. For guideway irregularities whose wave length is long compared to the magnet's length, the average air gap and the gap at each point above the magnet are nearly identical (Fig. 2.5a). For guideway wavelengths which are short compared to the magnet's length, the average clearance and the clearance at individual points varies significantly (Fig. 2.5b). Essentially, the magnet's length filters the road input. The importance of this filtering is seen in the linearized force (2.12) which depends on the air gap averaged over the area of the pole face:

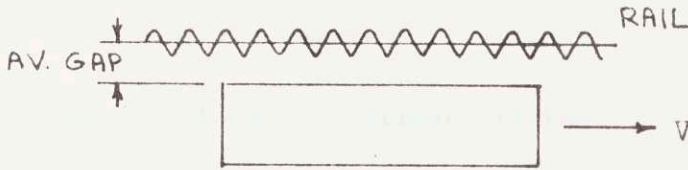
$$\Delta F = K_1 \Delta i - K_2 \Delta h_{1-av} \quad (2.18)$$

Since perturbations are small compared to the nominal, it is assumed that the linearization constants  $K_1$  and  $K_2$  are determined with  $h_{10}$  the nominal air gap for smooth rails. In the point contact model, the air gap was assumed uniform so that the average clearance and that measured at a point were identical.

The filter effects for the linearized model is evaluated by considering the roadway to consist of sinusoids as in Fig. 2.6. This approach will allow the clearance measured at the midpoint of the magnet to be transformed into a clearance averaged over the entire magnet length.



a. Long Wavelength Irregularities



b. Short Wavelength Irregularities

Fig. 2.5. Filtering of Guideway Irregularities by Magnet's Length

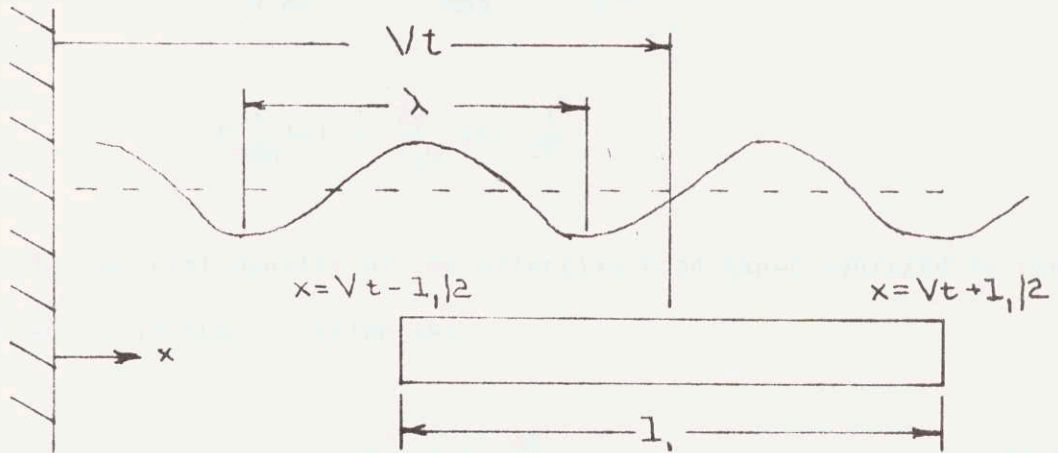


Fig. 2.6. Averaging a Sine Wave over One Pole Face

The change in elevation of the track across the vehicle width is ignored.

At any given time, the average height ( $\Delta y_{0-av}$ ) is related to the height at the midpoint  $\Delta y_{0-p}$  through (Chap. 7):

$$\Delta y_{0-av}(\lambda) = \frac{\lambda}{l_1 \pi} \sin \frac{l_1 \pi}{\lambda} \Delta y_{0-p}(x)$$

where  $l_1$  = length of the magnet

$\lambda$  = wavelength of rail irregularities.

When  $\lambda$  is much greater than  $l_1$ , the average and the point value of gap are identical, but when  $l_1 \gg \lambda$ , the average height is zero. The finite length averaging is displayed in Figure 2.7 and is transformed to the frequency domain by (2.7):

$$\Delta y_{0-av}(j\omega) = F_{mag}(\omega) \Delta y_p(j\omega) \quad (2.19)$$

where

$$F_{mag}(\omega) = \frac{2v}{l_1 \omega} \sin \frac{l_1 \omega}{2v} .$$

The spectral density of the effective road input averaged by the finite magnet length filtering is:

$$\phi_{y_{0-av}} = F_{mag}^2(\omega) \frac{\Delta V}{\omega^2} \quad (2.20)$$

For heave motion, the magnet displacement  $y_1$  has an average equal to the point measurement: i.e.,  $y_{1-av} = y_{1-p} = y_1$ . The average clearance between the magnet and the rail is:

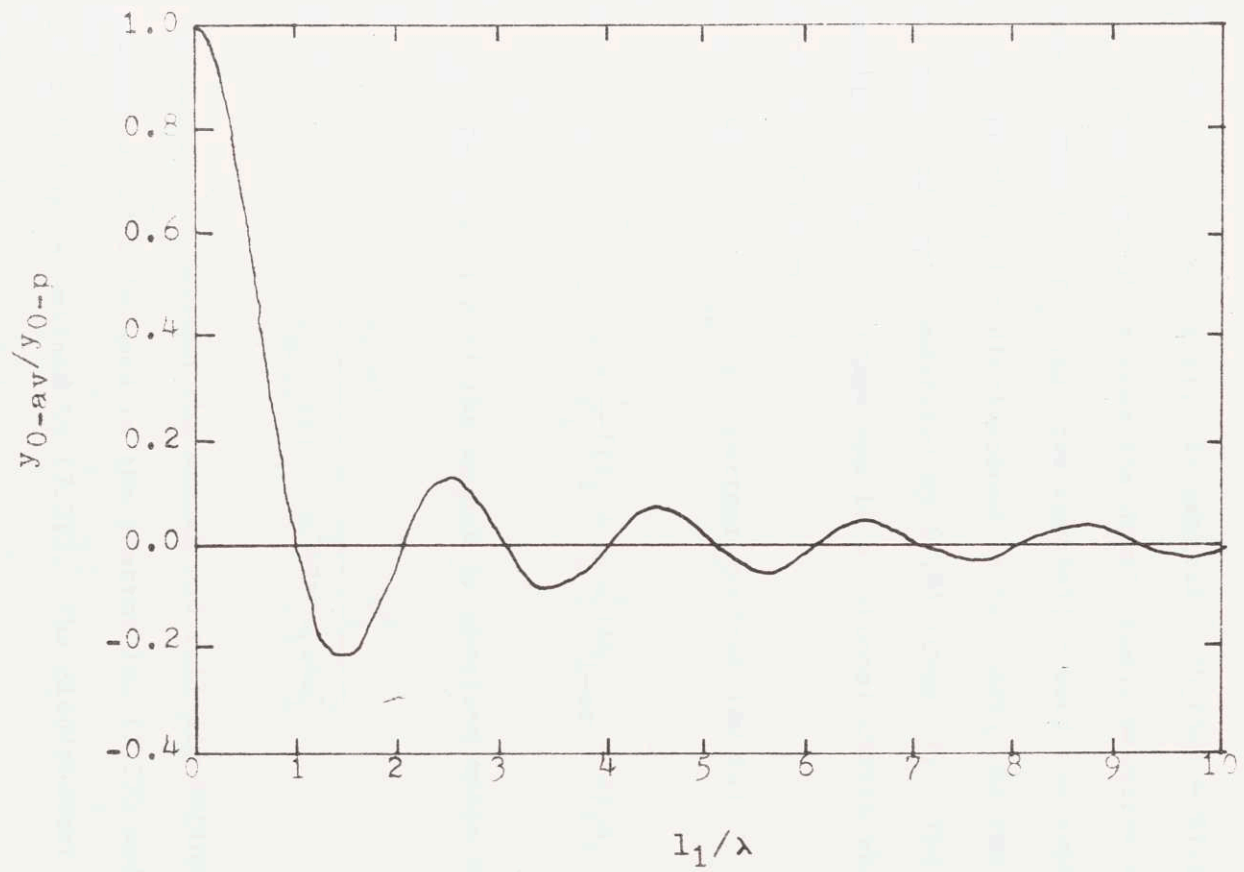


Fig. 2.7. Finite Magnet Length Filtering

$$h_{1-av} = y_{0-av} - y_1 \quad (2.21)$$

The total force (2.18) is related to the average gap; however, in the current control law (2.15), the displacement measured ( $\Delta h_c$ ) can be selected by the designer. In general:  $\Delta h_c(j\omega) = G(\omega) \Delta h(j\omega)$ . When  $G = 1$ , the control  $r$  uses the displacement measured at the magnet's midpoint. When  $G = F_{mag}(\omega)$ , the controller uses the average displacement.

If the point displacement is fed back, the rms voltages are infinite for the road input described by (2.8) (Chap. 7). The use of  $G = F_{mag}$  results in finite voltage and is a rational choice when compared to other forms of  $G$  (Chap. 7).

With  $G = F_{mag}$ , the current control law is:

$$\Delta i = \frac{1}{K_1} [(K_2 + m_1 \omega_1^2) \Delta h_{1-av} - 2y_1 \omega_1 \dot{y}_1] \quad (2.22)$$

The position of the magnet in absolute space is:

$$\frac{y_1(s)}{y_{0-av}(s)} = \frac{\omega_1^2}{s^2 + 2\zeta_1 \omega_1 s + \omega_1^2} \quad (2.23)$$

Two clearances between the magnet and rail are defined. The average clearance which is used in the control law (2.22) and the voltage relations (2.13) is defined by (2.21). The displacement measured at the midpoint of the magnet is:

$$h_{1-p} = y_{0-p} - y_1 \quad (2.24)$$

The point displacement is used to determine vehicle rail contact in Section 4.2.

The influence of finite length filtering on system design is discussed in the design examples of Section 4.3.

#### 2.3.4 Passive Secondary Suspension

The basic model of the magnet is extended to include a secondary suspension as depicted in Figure 2.8. Although a system with just the magnetic suspension can meet ride specifications at 300 mph. on a welded steel rail (Chapter 4.3), practical designs will probably possess a secondary suspension because of improved ride quality and/or loosening of track tolerances. The secondary suspension is modeled as an unsprung mass ( $m_1$ ) and sprung mass ( $m_2$ ) connected by a spring ( $k_2$ ) and damper ( $b_2$ ) in parallel.

The addition of the secondary suspension to the basic magnetic suspension does not change the equations for the voltage in the control coil (2.13). The secondary suspension exerts forces on the magnet which change (2.12) to:

$$m_1 \ddot{y}_1 = K_1 \Delta i - K_2 \Delta h_{1-av} + b_2 \dot{h}_2 + k_2 \Delta h_2 \quad (2.25)$$

where  $h_2$  is the relative displacement between the magnet and passenger compartment.

The acceleration of the sprung mass is:

$$m_2 \ddot{y}_2 + b_2 \dot{h}_2 + k_2 h_2 = 0 \quad (2.26)$$

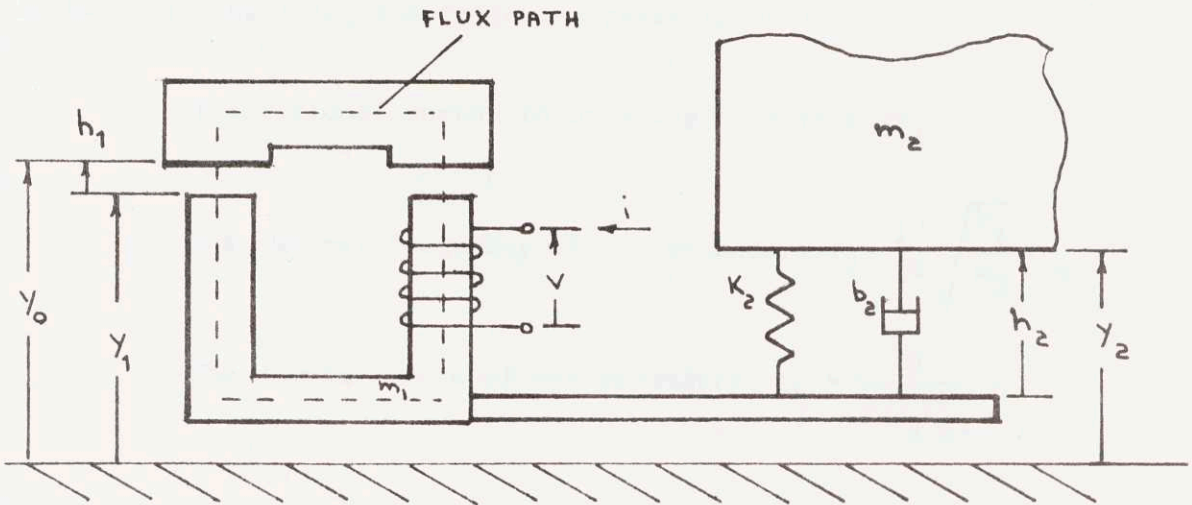


Fig. 2.8. Lumped Model of Electromagnet with Secondary Suspension

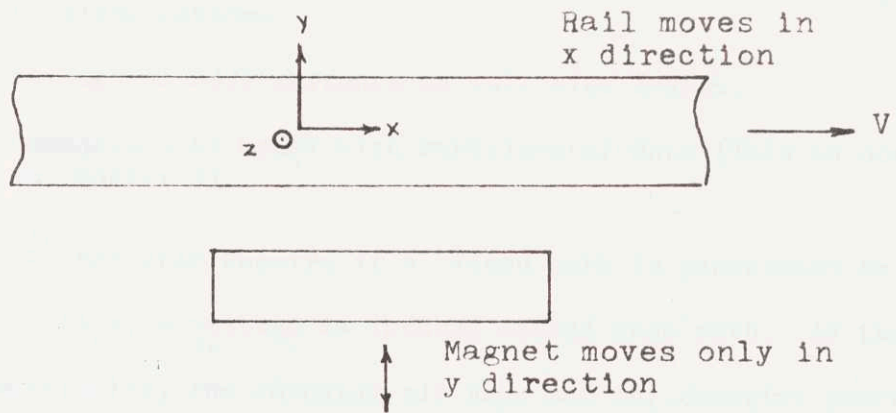


Fig. 2.9. Coordinates for Discussion of Eddy Currents

In later discussions, the following terms appear:

The ratio of sprung to unsprung mass  $\gamma = m_2/m_1$

The natural frequency of the secondary  $f_2 = \frac{1}{2\pi} \sqrt{\frac{k_2}{m_2}}$

The damping ratio of the secondary  $\zeta_2 = \frac{b_2}{2\sqrt{m_2 k_2}}$  .

### 2.3.5 Eddy Currents Induced by Vehicle Motion

In this section, an idealized model is developed so that estimates of the eddy current effects induced by vertical motion can be made. The discussion of eddy currents is arranged as follows:

- (1) Qualitative description of eddy current effects induced by vertical and forward motion.
- (2) Justification for separating the problems for forward and vertical motion.
- (3) Development of model to study eddy currents induced by vertical motion.
- (4) Effects of eddy currents on full size design.
- (5) Comparison of model with experimental data (This is done in Chapter 3).

From electromagnetic theory, if a closed path is penetrated by a changing magnetic flux, a voltage is induced around that path. As the vehicle moves vertically, the changing air gaps and the changing current caused by the controller alter the magnetic fields in the rail over the entire length of the magnet. The changing magnetic fields induce eddy currents which produce a magnetic field that opposes the original field established by the control coil. The net effect of these eddy currents is that the magnetic field from the control coil flows in a thin sheet

near the surface of the material. The thickness of this sheet is called the skin depth or penetration depth. From Table 14 of Chapter 10, the skin depth for 1.75% silicon steel (relative permeability of 3500 and conductivity of  $.25 \times 10^7 [\text{ohm-m}]^{-1}$ ) at 1 hz. is 0.5 cm. At higher frequencies the eddy currents reduce the flux that enters the rail and introduce a phase lag between the flux in the rail and the control current.

Since the flux that enters the rail determines the forces exerted by the magnet, eddy currents reduce the oscillating lift force (the steady component remains constant) and introduce an undesirable phase shift between the exerted force and the control current. Because the magnetic force with eddy currents differs from the force (calculated with no eddy currents), which result in the optimal suspension (2.16), the suspension's heave performance deteriorates (mathematically, the performance index (2.14) increases); hence, it is desirable to design the system so that eddy current effects are small.

As the vehicle moves forward, the rail section in front of the vehicle contains no flux; however, when the vehicle has moved over the rail a magnetic field is generated in the rail and eddy currents are induced in the rail about the magnet's leading and trailing edge. These eddy currents cause a loss of lift and dissipate power (magnetic drag) which must be overcome by the vehicle's propulsion unit.

Maxwell's equations for quasistatic magnetic fields (displacement currents induced by electric fields are negligible) which include material motion are [51, 58]:

$$\frac{1}{\mu\sigma} \nabla^2 \vec{B} = \frac{\partial \vec{B}}{\partial t} - \nabla \times (\vec{V} \times \vec{B}) \quad (2.27)$$

where  $\vec{B}$  is a magnetic field which is fixed in space (arrow denotes vector)

$\vec{V}$  = velocity of material

$\mu, \sigma$  = permeability and conductivity of the medium.

Solution of the complete eddy current problem demands that (2.27) be solved for the situation depicted in Figure 2.9. For this discussion consider a frame of reference where the rail moves with velocity  $V$  in the  $x$  direction and the magnet only moves in the  $y$  direction as in Figure 2.9.

If the magnetic fields are static ( $\partial\vec{B}/\partial t = 0$ ) and if there is no forward motion ( $\vec{V} = 0$ ), (2.27) becomes:

$$\nabla^2 \vec{B} = 0 .$$

This is the situation with no eddy currents which governs the static analysis of Section 2.2.

Throughout this discussion, primary interest is in the magnetic fields in the rail. Since the vehicle magnets are only a small part of the capital investment, it will be relatively cheap to laminate these so that eddy currents are not induced in the magnet; therefore, the discussion focuses on the eddy currents induced in the rail.

As the magnet oscillates in the  $y$  direction, the magnet's control changes the magnetic fields in the rail so that the original static fields are changed by the  $\partial\vec{B}/\partial t$  term. The forward motion of the vehicle induces eddy currents in the rail which change the original static fields through the  $\nabla \times (\vec{V} \times \vec{B})$  term.

With rail motion in the x direction,  $\vec{V} = V\vec{i}$  and

$$\nabla_{\mathbf{x}}(\vec{V}_{\mathbf{x}}\vec{B}) = -V(\vec{i} \frac{\partial B}{\partial x} + \vec{j} \frac{\partial B}{\partial x} + \vec{k} \frac{\partial B}{\partial x}) = -V \frac{\partial \vec{B}}{\partial x}$$

The field produced by the control coil is uniform along the magnet's length ( $\partial/\partial x = 0$ ) and drops to zero near the ends of the magnet ( $\partial/\partial x \neq 0$ ). Since the field produced by the control windings only has  $\partial/\partial x \neq 0$  near the ends of the magnet, the  $\nabla_{\mathbf{x}}(\vec{V}_{\mathbf{x}}\vec{B})$  term and the associated eddy currents are important only near the ends of the magnet. Therefore, minimization of the effects of eddy currents induced by forward motion requires that the region where  $\partial/\partial x \neq 0$  be small compared to the region where  $\partial/\partial x = 0$ . By making the magnets long (which implies thin since lift depends on area) and continuous (few ends), the region of end effects can be made small compared to the region which is not affected by the eddy currents induced by forward motion. A detailed solution of the eddy currents induced by forward motion is not attempted in this thesis; however, [24] and [70] suggest that magnet lengths of the order of thirty feet are required to reduce loss of lift and magnet drag to acceptable limits at 300 mph (estimated drag is roughly 200 kw.).

Forward motion effects depend directly on V and for low speeds may not be important. With forward motion effects confined to regions in the rail near the magnet's ends, the magnetic fields in the rail over much of the magnet's length are described by:

$$\frac{1}{\mu\sigma} \nabla^2 \vec{B} = \frac{\partial \vec{B}}{\partial t} \quad (2.28)$$

This equation is studied in detail where the  $\frac{\partial \vec{B}}{\partial t}$  represents the changing magnetic field induced by the vertical motion. In order to estimate the eddy current effects induced by the vertical motion, the model discussed below is used to investigate the basic phenomena associated with eddy currents and flux penetration in the rail. The model is depicted in Figures 2.10 and 2.11. The following assumptions are made:

- (1) Since the magnet is long compared to its width

$$\frac{\partial}{\partial x} = 0$$

- (2) The magnet and rail can be considered to be infinite half spaces as shown in Figure 2.10. The magnet's width ( $\lambda_M/2$ ) is considered by representing the windings as a current ( $\vec{K}_S$ ) sheet at  $y = 0$ .

$$\vec{K}_S = \vec{i} K_S \sin \omega t \sin k_z z$$
$$k = \frac{2}{\lambda_M} \tag{2.29}$$

where the wavelength of the windings ( $\lambda_M$ ) is derived by considering the magnet-rail configuration as a periodic structure as shown in Figure 2.11; thus,

$$\frac{\lambda_M}{2} = w_1 + 2l_p$$

where  $w_1$  = distance between pole cores

$l_p$  = width of magnet pole face.

In (2.20),  $\sin(\omega t)$  represents the change in current with time and  $\sin(kz)$  represents the periodic structure of the magnet.

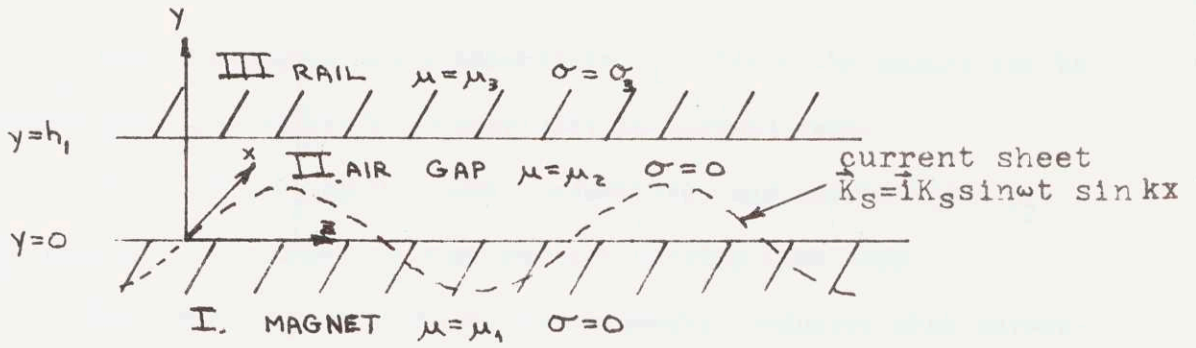


Fig. 2.10. Configuration for Analysis of Eddy Currents in Rail

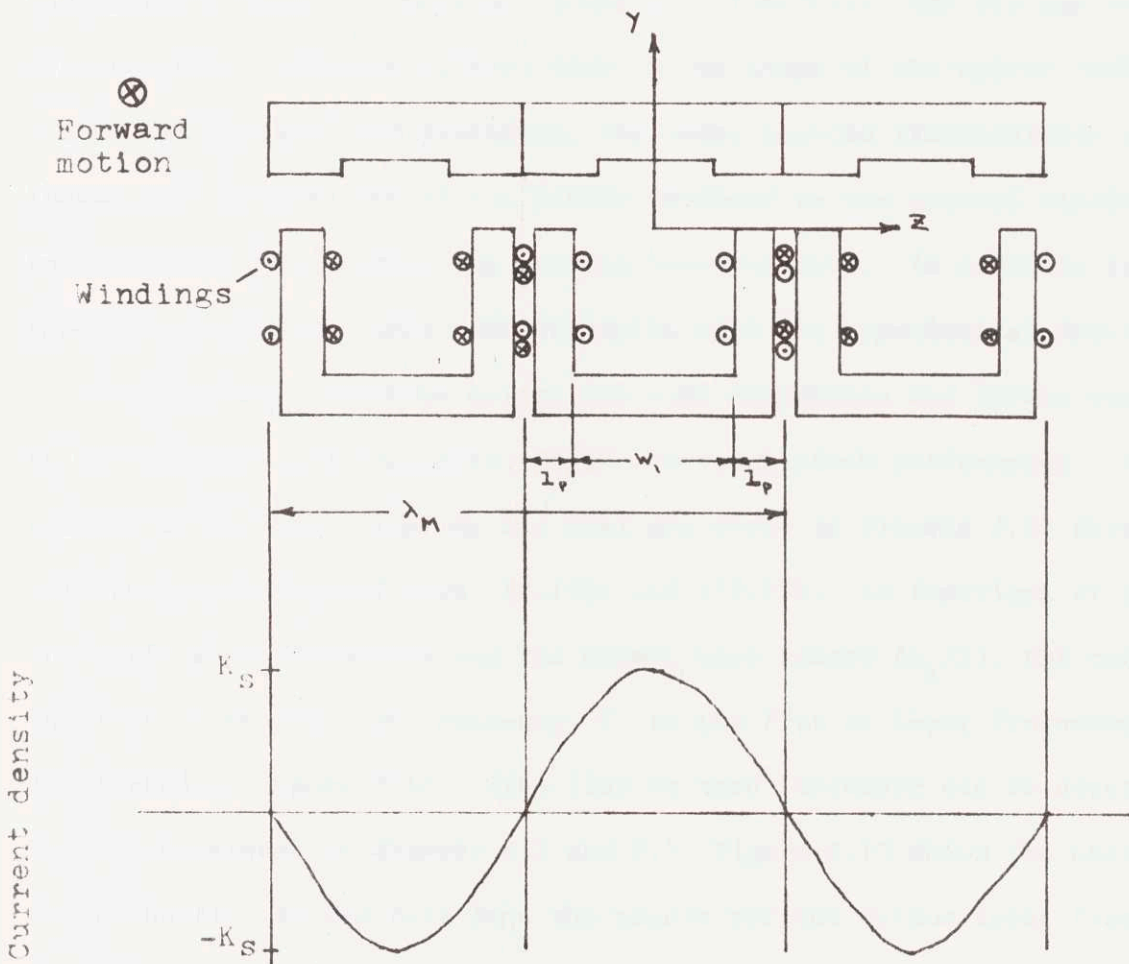


Fig. 2.11. Magnet's Representation as Periodic Structure

(3) The magnet has permeability  $\mu_1$ . Since the magnet can be fully laminated, the magnet's conductivity is assumed zero.

(4) The air gap has zero conductivity and permeability  $\mu_2$ . The air gap ( $h_1$ ) is assumed uniform and not varying with time.

(5) The rail is a thick ferromagnetic conductor with permeability  $\mu_3$  and conductivity  $\sigma$ . Since the solution will depend on a skin depth which is small compared to the rail thickness for practical systems, the thickness of the rail does not enter the analysis.

This model allows consideration of material properties, permeability and conductivity, and important geometric properties, the air gap and the magnet width. Although factors such as the shape of the magnet (pole width, core length) are neglected, the model enables visualization of the fundamental interaction of the fields produced by the control windings and the field produced by the induced eddy currents. In addition the theoretical results agree satisfactorily with the experimental observations.

Since the flux that enters the rail determines the forces exerted by the magnets, eddy currents affect the suspension's performance. The changes in the flux entering the rail are shown in Figures 2.12 through 2.15 which are derived from (10.19b) and (10.27). As functions of the current's input frequency and the magnet wave length ( $\lambda_M/2$ ), the ratio of the flux in the rail at frequency  $f$  to the flux at input frequency zero is plotted in Figure 2.12. (The flux at zero frequency can be determined by the techniques of Chapter 2.2 and 5.) Figure 2.13 shows the phase by which the flux in the rail lags the magnet current versus input frequency and magnet width. In Figure 2.14, the flux ratio is plotted versus input frequency and gap height  $h_1$ . Figure 2.15 plots the phase lag versus input frequency and air gap.

Figures 2.12 and 2.15 show that as input frequency is increased the magnitude of the flux into the rail decreases and the phase lag increases. For example, with air gap of .6 inches and magnet width of 10 inches, the phase lag and flux ratio are 0.94 and 4 degrees at 10 hz. and 0.54 and 23 degrees at 100 hz.

The effects of the eddy currents (flux drop, phase shift) increase as the magnet width increases and as the air gap decreases. For example, at 100 hz and 0.6 inch air gap, the flux ratio and phase lag are 0.82 and 10 degrees for 10 inch magnet width and .50 and 30 degrees for 20 inch magnet width.

Practical magnets can be designed in which the eddy currents induced by vertical motion do not affect the suspension performance. As a guideline consider the following case. With magnet width of 10 inches and air gap of 0.6 inches, the flux ratio at 10 hz. is 0.94 (i.e., 94% of the flux's changing component is entering the rail while the nominal flux component is unaffected) and the phase lag is 4 degrees. These values of flux ratio and phase lag will not significantly change the system's performance from that predicted by the models of Chapters 2.3.1 to 2.3.4 so that the optimal suspension given by (2.16) is attainable.

Since long magnets are required to reduce the effects of eddy currents induced by forward motion and since lift is proportional to pole face area, magnets whose width is less than 10 inches can be designed for typical vehicle load intensities (weight/vehicle length) of 1000 lb./ft. as shown in Table 4. Because of the finite length filtering by the long (10 to 30 ft.) magnets, the suspension is insensitive to road inputs greater than 10 hz. for speeds less than 300 mph. (Chapter 4.3). Thus,

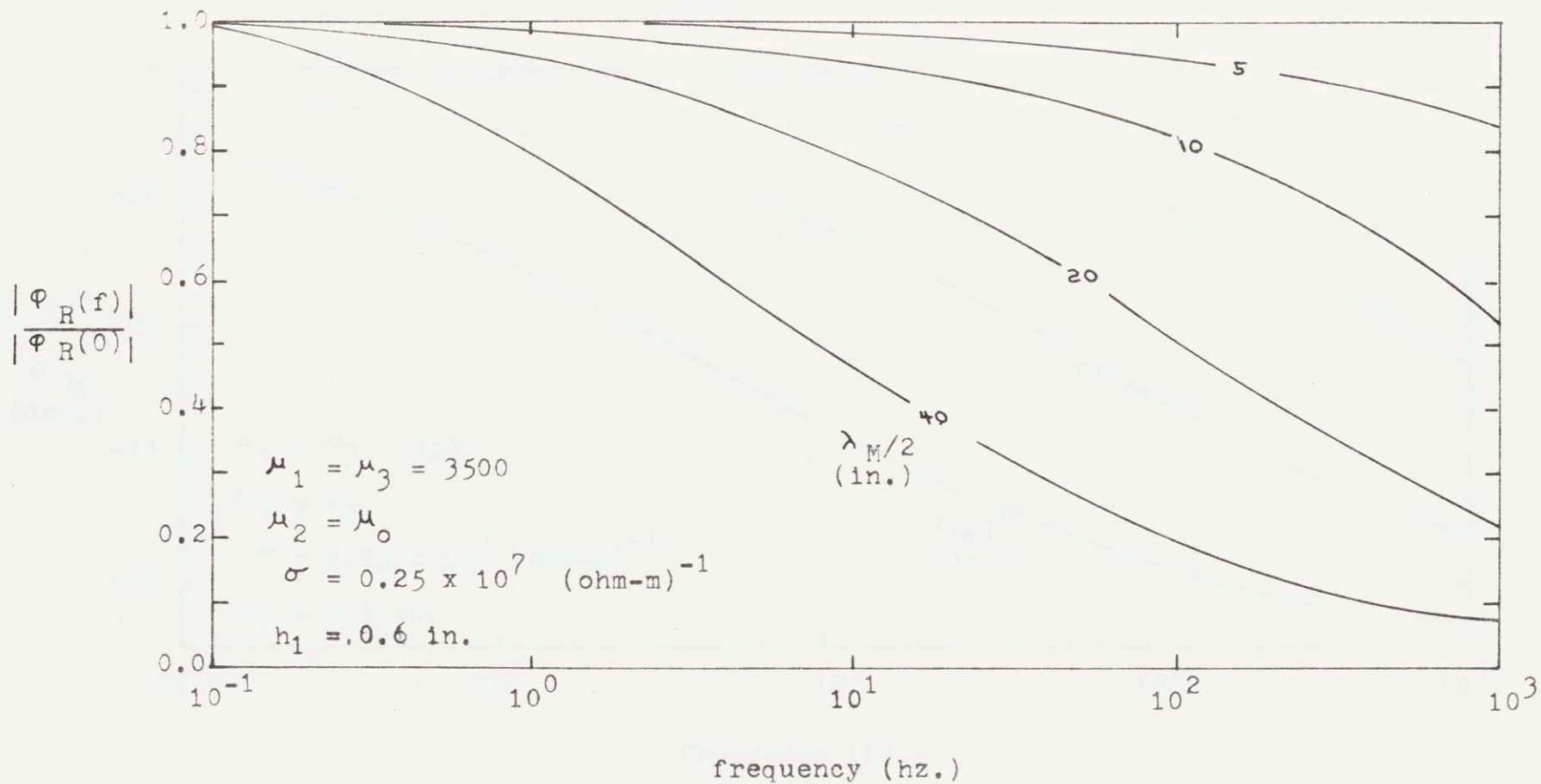


Fig. 2.12. Flux Density Ratio vs. Current Frequency and Magnet Wave Length

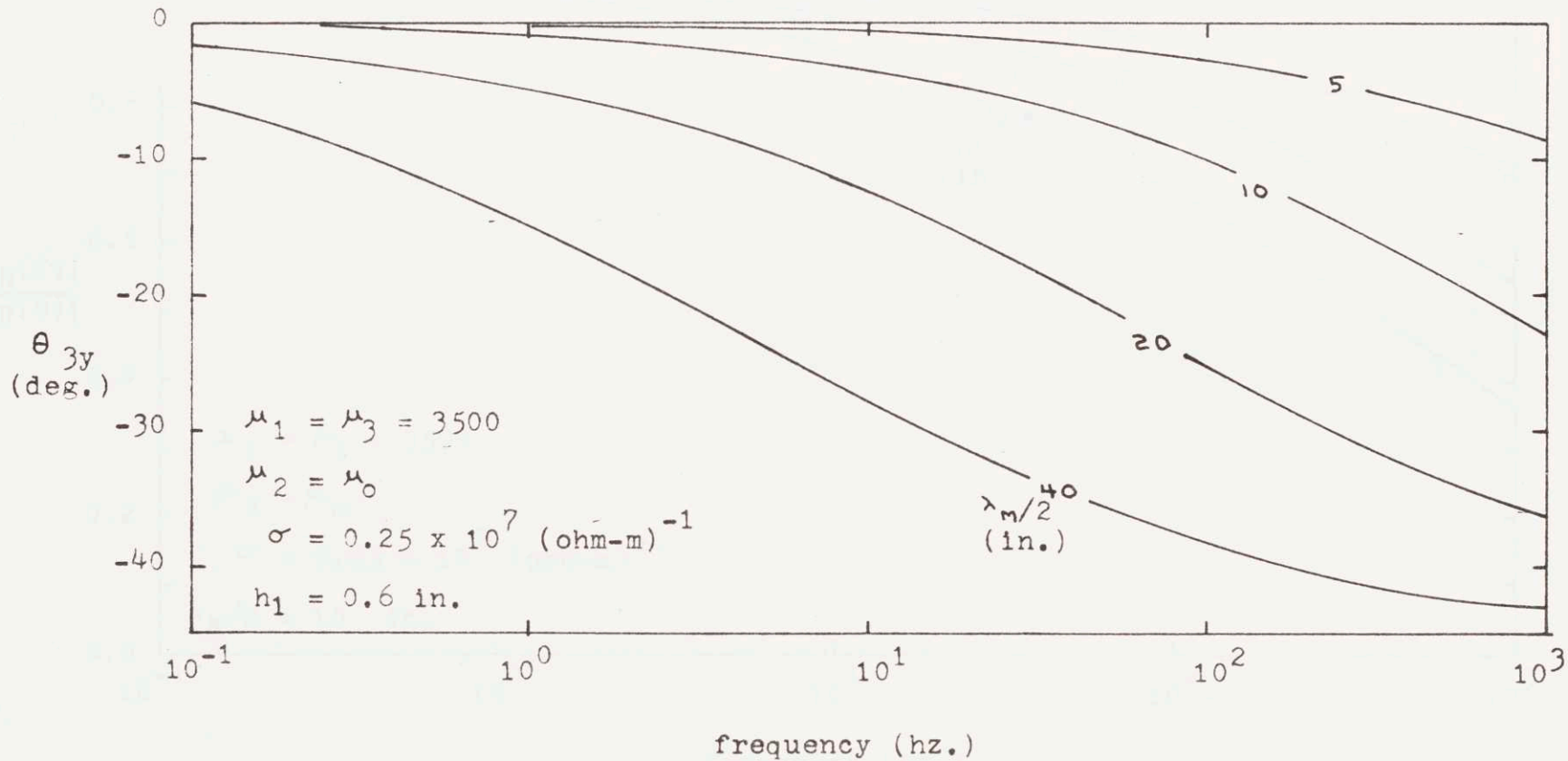


Fig. 2.13. Phase between Current and Flux in Rail vs. Current Frequency and Magnet Wavelength

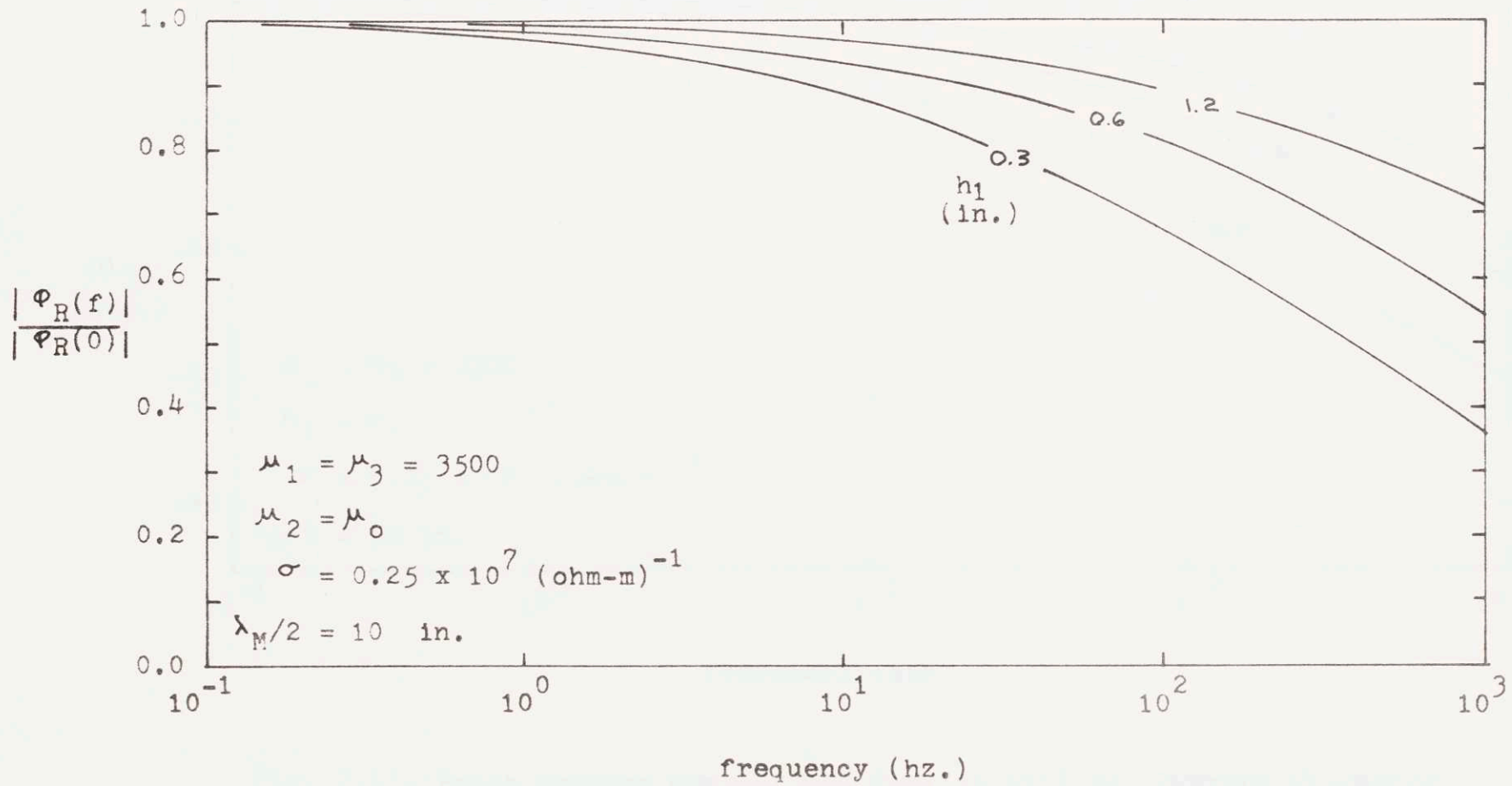


Fig. 2.14. Flux Density Ratio vs. Current Frequency and Air Gap

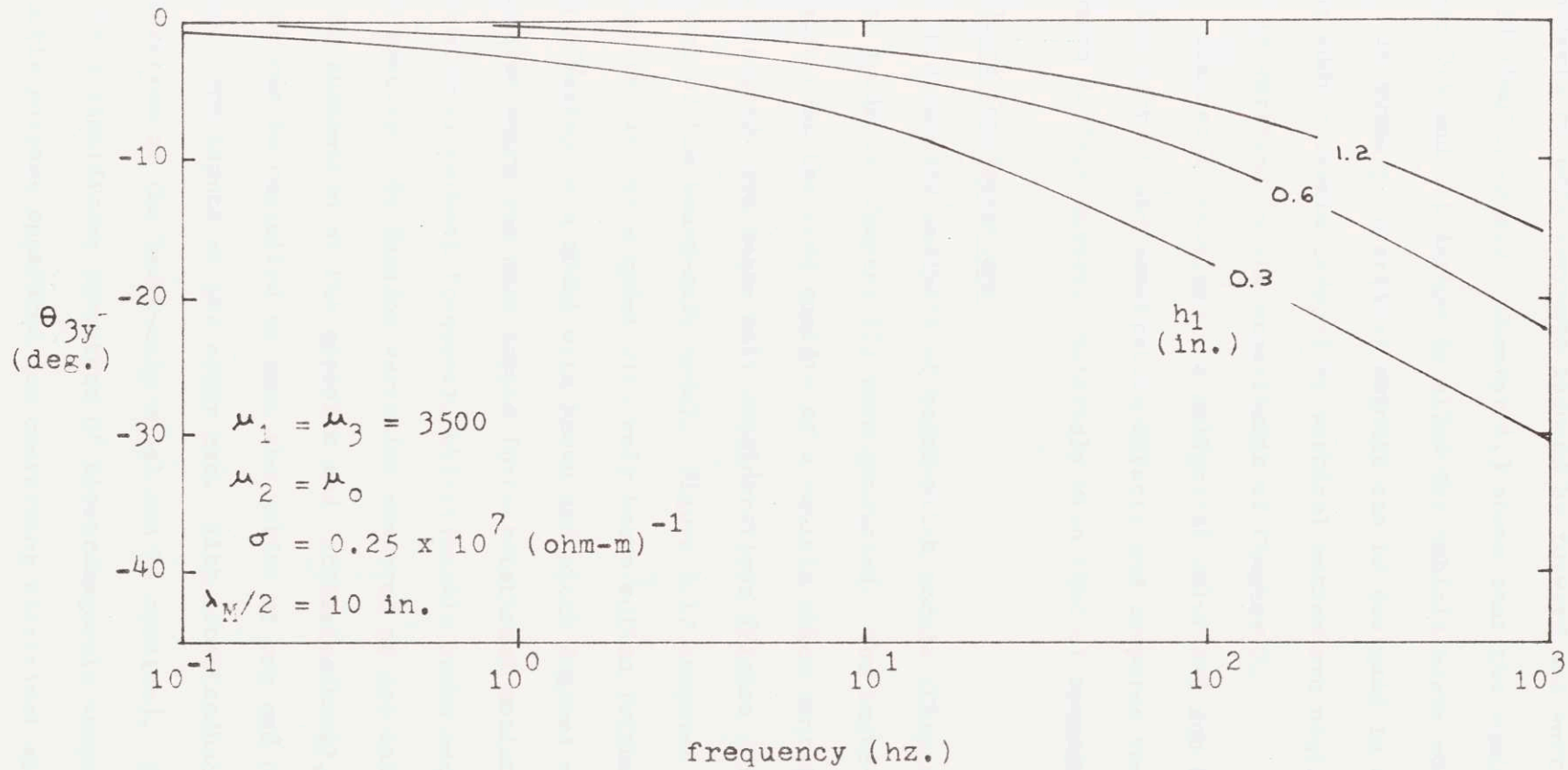


Fig. 2.15. Phase between Current and Flux in Rail vs. Current Frequency and Air Gap

the effects of eddy currents induced by forward and vertical motion are reduced simultaneously. Chapter 4.3 shows that the nominal air gap is between 0.4 and 0.6 inches to allow for vehicle heave motion.

In summary, practical magnets can be designed in which the effects of the eddy currents induced by vertical motion are negligible, a fact which is verified by the experiments of Chapter 3.

Chapter 10 develops the analytical solutions and describes further the eddy current and penetration effects and compares the penetration phenomena in ferromagnetic materials with that of nonmagnetic materials.

#### 2.4 Other Considerations

Preliminary analyses of heave-pitch models (Chapter 11) and lateral guidance (Chapter 12) were conducted. The heave-pitch analysis indicates that the ride quality of a vehicle which contains two suspensions designed from heave only considerations (Figure 2.16) is poorer than that of the heave-only model. Figure 2.17 compares the acceleration spectral density of a model with only heave motion (without finite magnet length effects) to a model with heave and pitch degrees of freedom. At frequencies where the road inputs force rotational motion at multiples of the rotational natural frequency, objectionable peaks occur in the acceleration spectra. By feeding variables measured at one end of the vehicle into the suspension at the opposite end (crossfeedback), the rotational coupling can be cancelled so that the motion at one end of the vehicle is isolated from inputs at the other end. With crossfeedback, the acceleration spectrum of the heave-only model can be attained. Crossfeedback could be a significant advantage of electromagnetic suspensions which inherently possess apparatus for converting electrical signals into suspension forces.

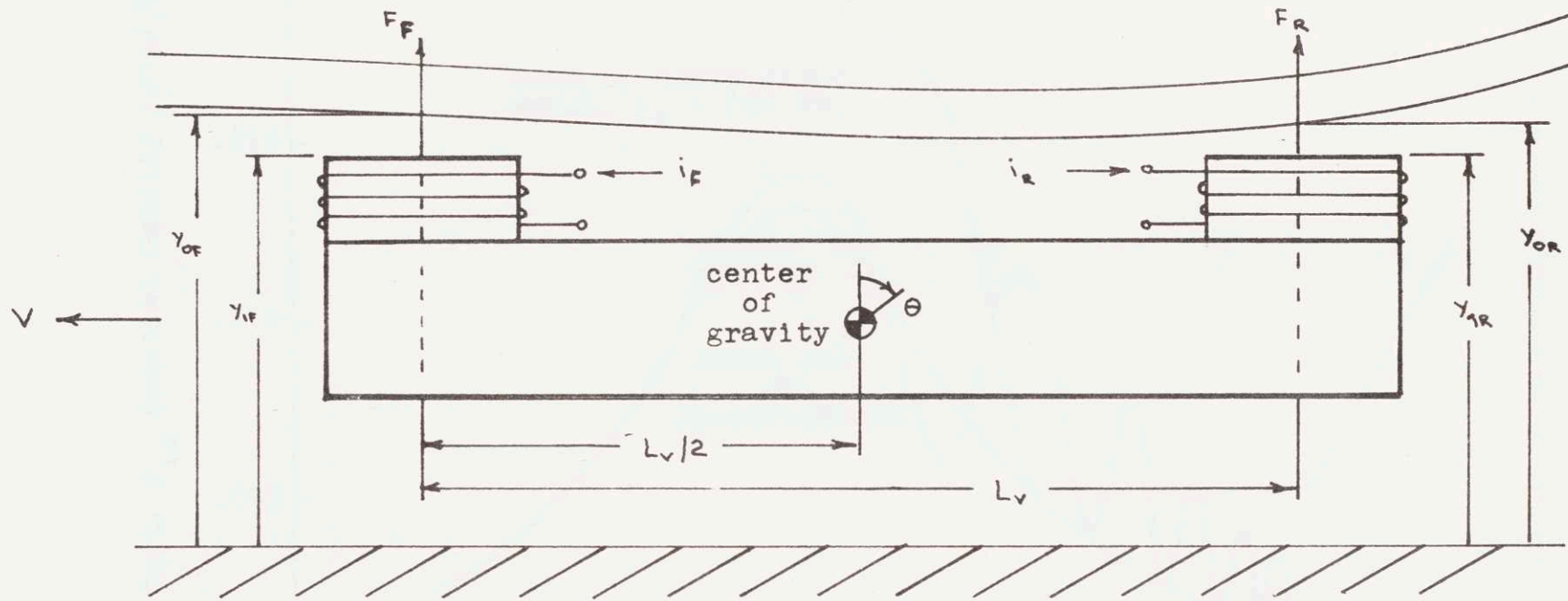


Fig. 2.16. The Heave-Pitch Model without Secondary Suspension

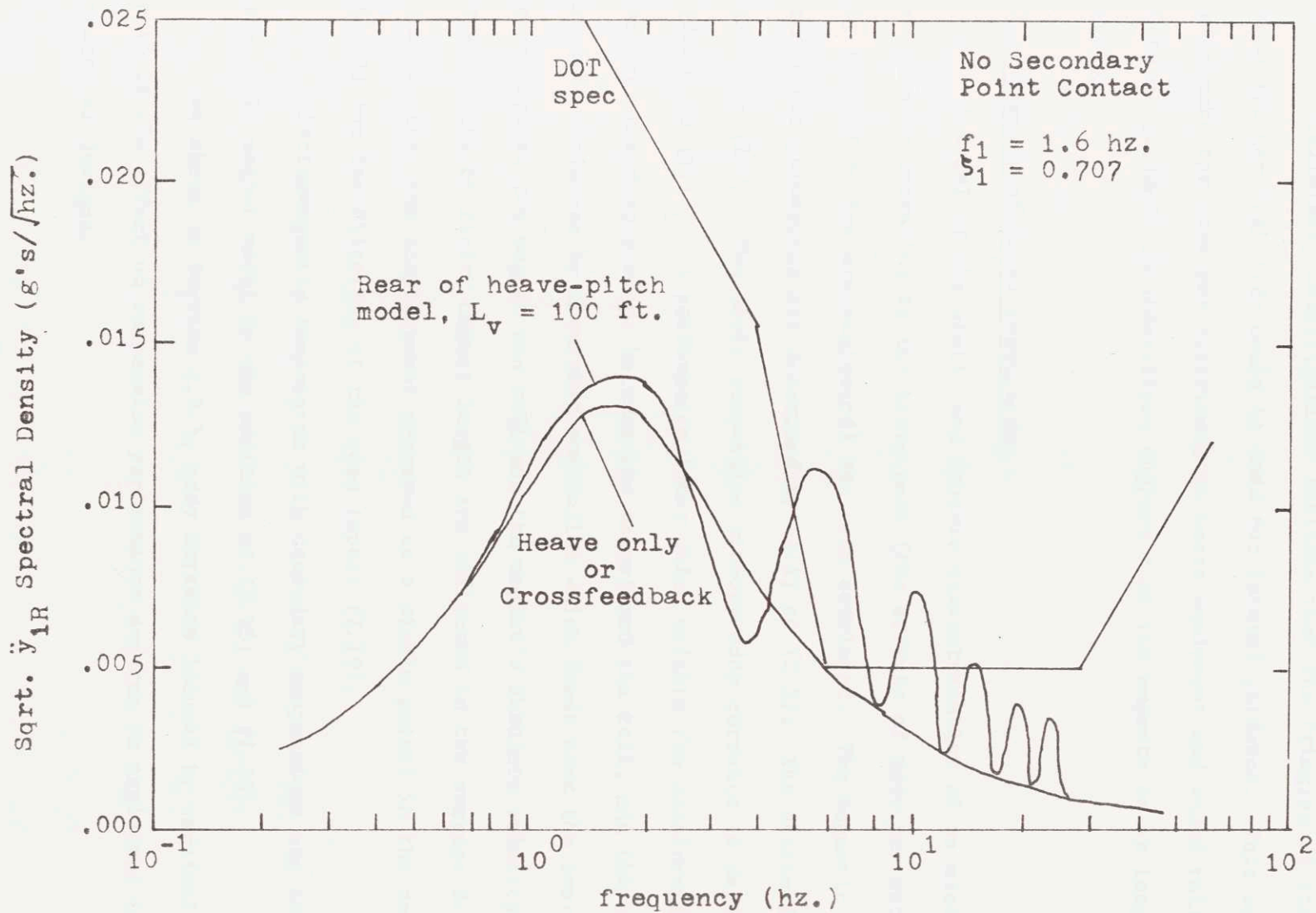


Fig. 2.17. Acceleration Spectrum in Heave-Pitch Model

Preliminary investigations indicate that the fringing of the magnets used for vertical lift could be used for lateral guidance. This would eliminate the need for additional on-board equipment and added rails. Lateral guidance considerations suggest that the magnets be as long as possible.

## 2.5 Summary of Model Formulation

A model of the static and dynamic characteristics of an electromagnetic suspension operating in the heave mode (the effects of eddy currents induced by forward motion are neglected) has been developed. The magnetic flux paths and their permeances are described by (2.1) to (2.5). The static force is given by (2.7). The basic suspension without eddy currents is defined by (2.10) to (2.13). A performance index which weights the acceleration of the magnet, the displacement between the magnet and the rail, and the control current is minimized by a current controller which feeds back the average clearance between the magnet and rail and the magnet's absolute velocity (2.22). The effects of finite magnet length are reflected in the average displacement (rather than the displacement measured as a single point) in the control law (2.22) and the filtering of the road inputs (2.19).

Electromagnetic suspension with secondary suspensions are derived from the basic magnet model by the addition of (2.25) and (2.26).

As shown in Section 2.3.5, eddy currents induced by vertical motion have little effect on suspension performance and can be neglected in most practical designs.

### 3. EXPERIMENTAL PROGRAM

#### 3.1 Introduction

An experimental model of a magnetic suspension operating in the heave mode has been designed and built. The primary objectives of the experimental tests is to evaluate the theoretical model developed in Part II and summarized in Chapter 2. The following tests were conducted:

- (1) Static and dynamic (eddy current effects) measurements of magnetic flux.
- (2) Static measurement of magnet forces.
- (3) Frequency responses of vehicle motion to road inputs.

Preliminary measurements of lateral forces are described in Chapter 12.

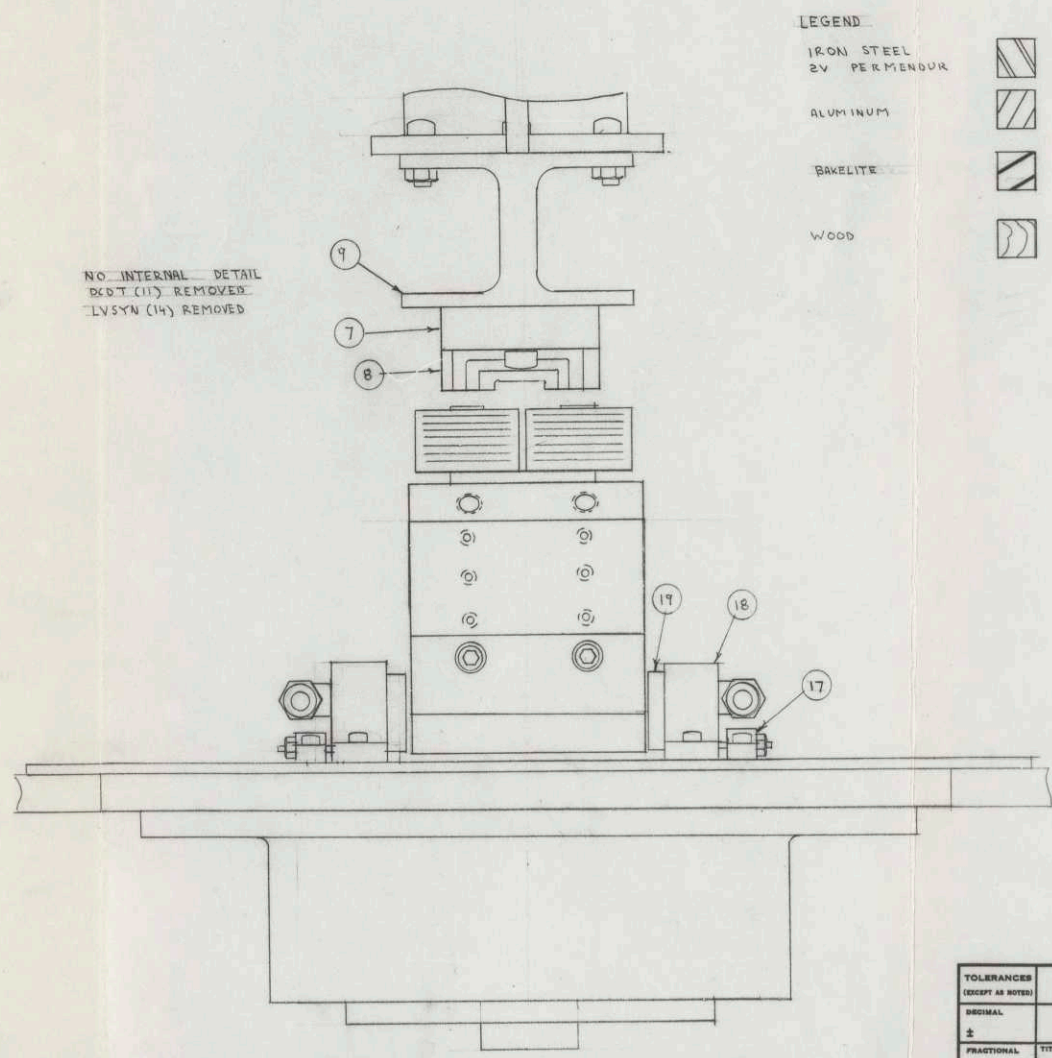
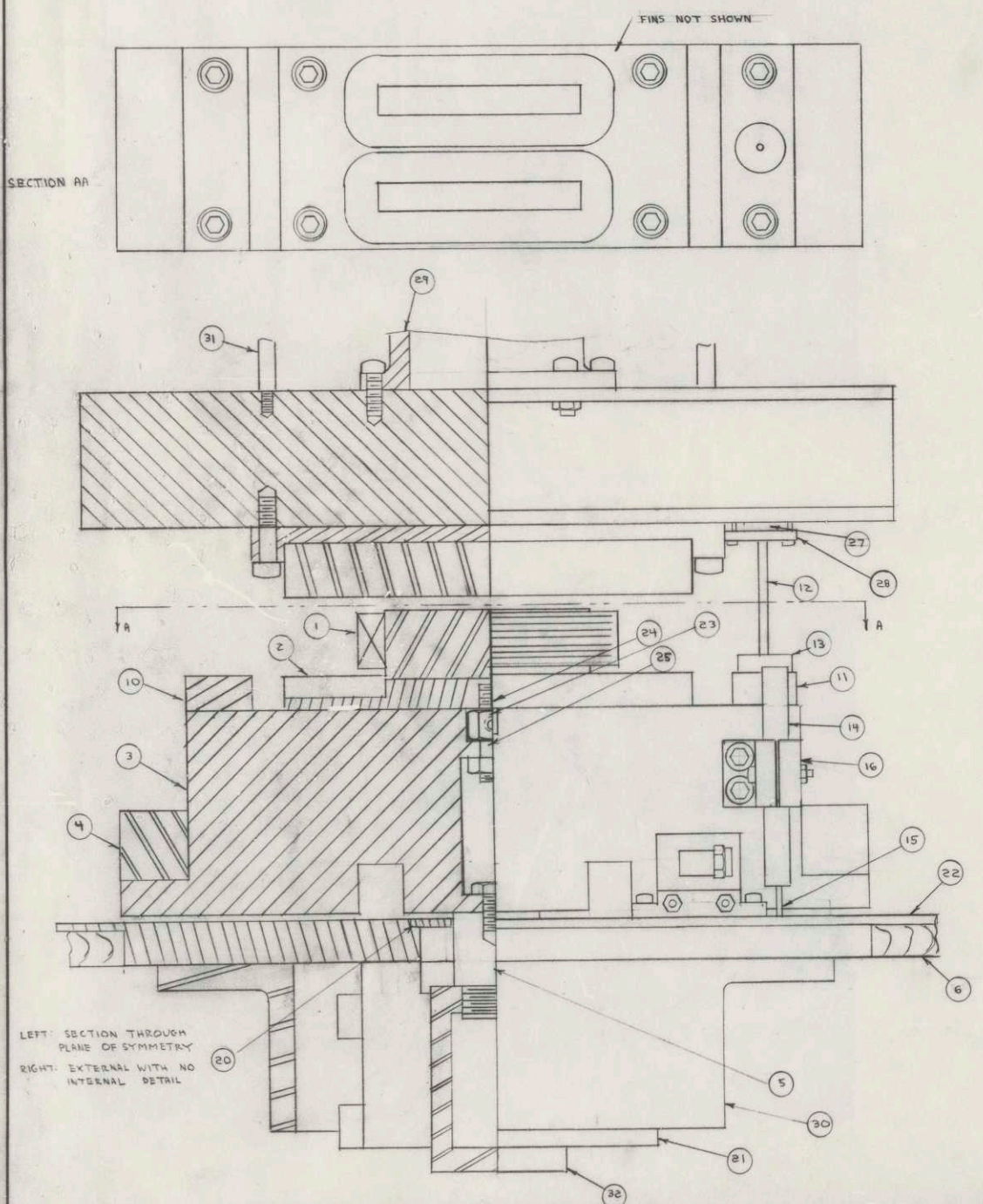
In this chapter, the experimental test apparatus, the experiment's design and scaling, and the experimental procedures and results are described.

#### 3.2 Description of Test Facility

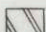
The complete magnetic suspension test is shown in Figures 3.1 through 3.6. Part numbers mentioned in the text correspond to those of the assembly drawing (Fig. 3.1). The principal parts are:

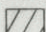
- (1) The magnet and windings (Part 1, Fig. 3.3) are epoxied to an aluminum support plate (Part 2, Fig. 3.6) which is ribbed to enhance its heat dissipation characteristics. The support plate is mounted on the 'vehicle' (Part 3) which rides in air bearings (Parts 19 and 21).


DATE	BY	REVISION RECORD	AUTH.	DR.	OK.

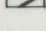


LEGEND

IRON STEEL 

2V PERMENDUR 

ALUMINUM 

BAKELITE 

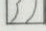
WOOD 

Fig. 31 ASSEMBLY DRAWING OF TEST FACILITY

TOLERANCES (EXCEPT AS NOTED)		SCALE	DRAWN BY
DECIMAL		FULL	<i>[Signature]</i>
FRACTIONAL			APPROVED BY
ANGULAR			
TITLE		DATE	DRAWING NUMBER
MAGNETIC SUSPENSION EXT.		11/29/72	

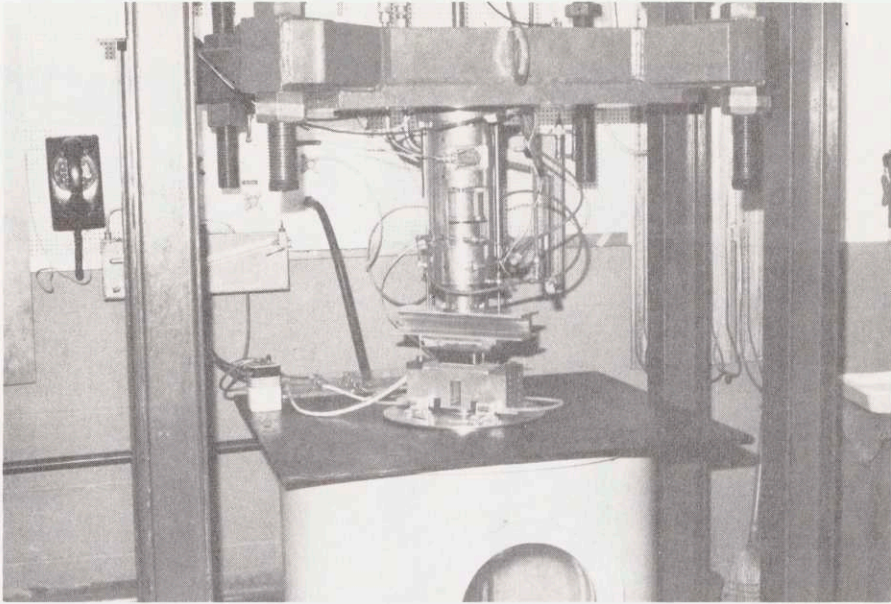


Fig. 3.2 MAGNETIC SUSPENSION EXPERIMENT

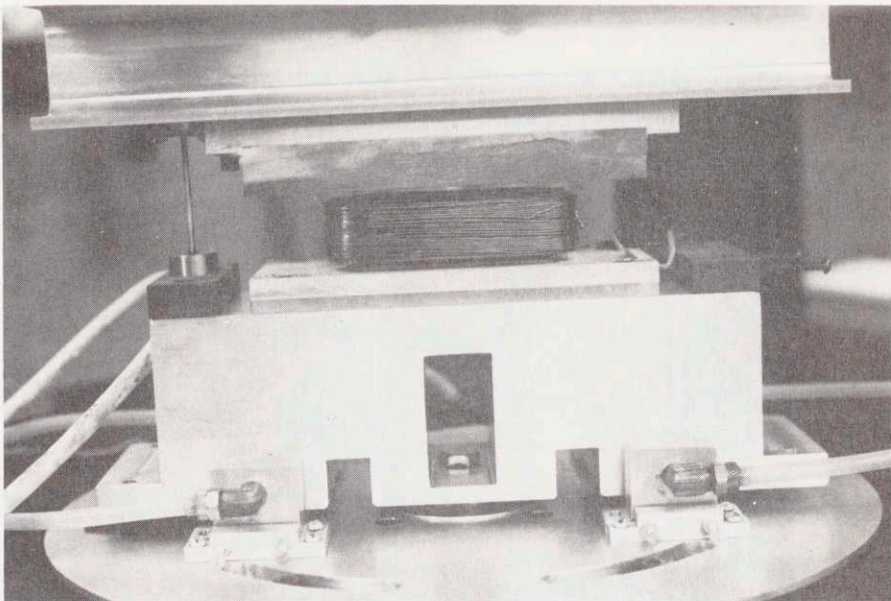


Fig. 3.3 MAGNET, RAIL, VEHICLE ASSEMBLY

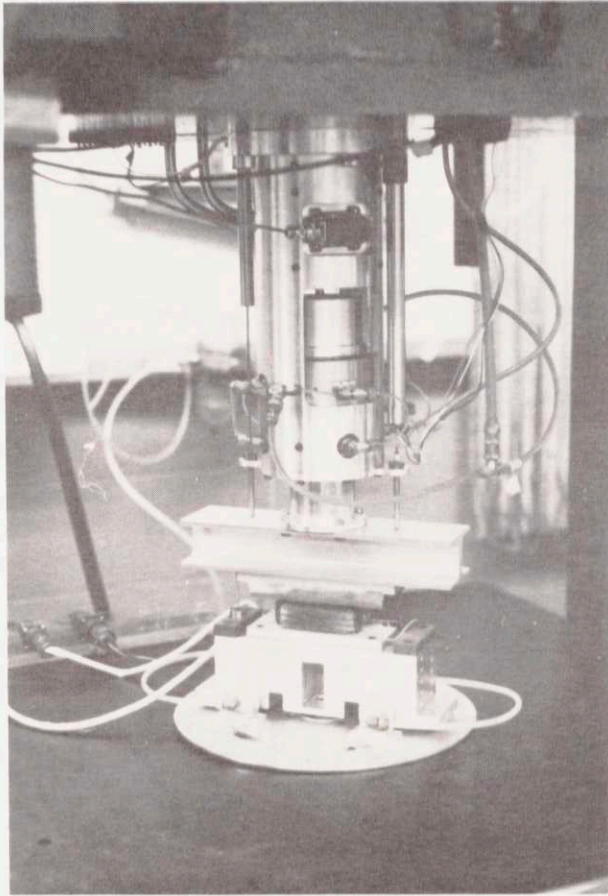


Fig. 3.4 MAGNET AND SHAKER

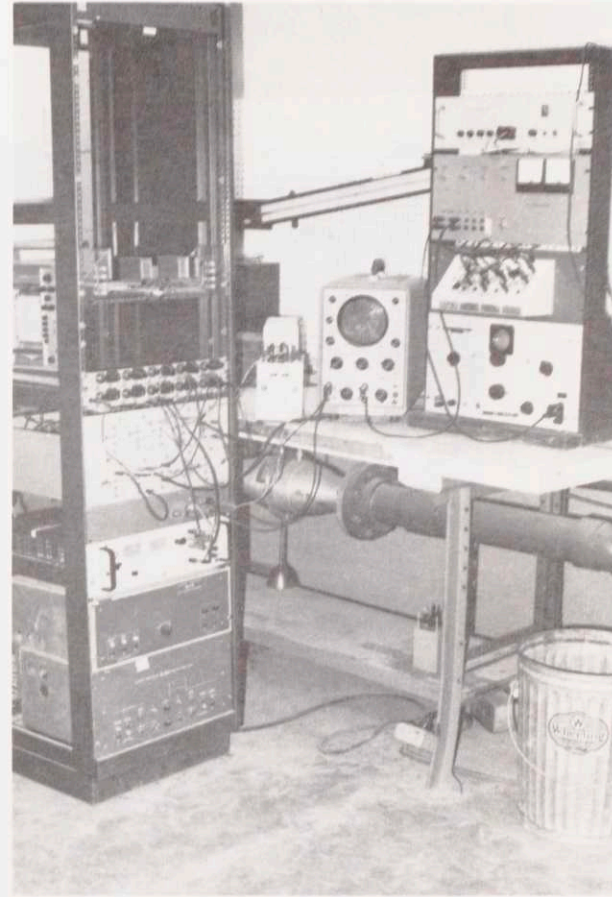


Fig. 3.5 CONTROL PANEL

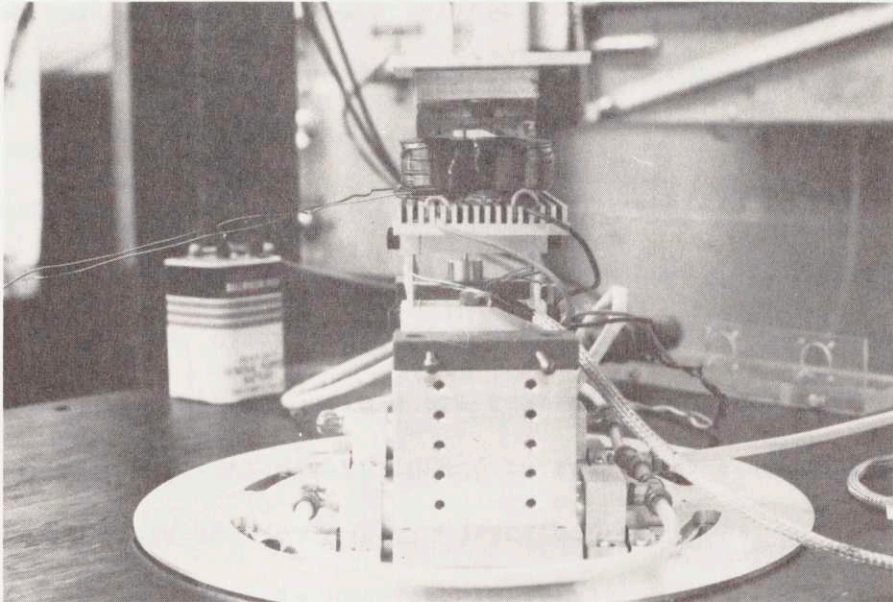


Fig. 3.6 END VIEW WITH LATERAL FORCE TRANSDUCER.

Wires that protrude on left side of magnet  
are connected to search coil.

(2) The ferromagnetic rail is attached to the electrohydraulic shaker which simulates road irregularities.

(3) The magnet's control senses the displacement between the magnet and the rail and the absolute velocity to regulate the coil's current so that stability and the desired ride characteristics are achieved.

Air bearings (Parts 19 and 21) restrain the vehicle to heave motion while reducing friction to minimal levels. The vehicle is connected by the link (Part 5) to the cylindrical journal which slides in the air bearing (Part 21) so that lateral motions are restrained but the vehicle is free to move in the vertical direction and to rotate about a vertical axis. The air bearings and journal are described in [66]. To restrain the rotational motion, four air bearings (Parts 18 and 19) were added.

Since the primary interest of these experiments was to develop a model of the magnetic field interactions, transducers which physically connected the vehicle to the rail and the reference ground were used to measure the control variables although implementation in actual systems demands non-contacting transducers.

The relative displacement was measured by a Hewlett Packard 7 DCDT 100 (Part 13). The output voltage is proportional to the position of the core which is connected to the I-beam by the connecting rod (Part 12). Normally, a passive first order filter with break frequency at 170 hz. is built into the transducer. The transducer was ordered without the filter and the output was filtered by a second order filter with damping ratio  $\approx .2$  and natural frequency  $\approx 800$  hz. in the control circuitry.

The absolute velocity was measured by a Hewlett Packard LVSYN 3LVA5 (Part 14). The output voltage of the device depends on the load to which it is coupled; therefore, the velocity transducer is isolated from any pots by an operational amplifier with 50 kohm input resistor (Appendix 5). The sensitivity of the LVSYN was 125 mv/in/sec (factory calibration) and is dynamically flat to at least 300 hz.

The control circuitry which is discussed in Appendix 5 was patched on an operational amplifier manifold. The magnet's power supply is a Kepco Bipolar Operational Power Supply which supplies 5 amps and 72 volts in any of four quadrants.

The circuitry uses the signals generated by the displacement and velocity transducers to control the current so that the control law (3.3) is effected. The dimensional current is:

$$\Delta i = i_o + \frac{i_o}{h_{10}} \left( 1 + \frac{\omega_1^2 h_{10}^2}{2g} \right) \Delta h_1 - \frac{\zeta_1 \omega_1 i_o \dot{y}_1}{g}$$

The circuitry which is described in Appendix 5 also filters the output of the displacement transducer and limits the control current to positive values as outlined in Chapter 8.

The ferromagnetic rail (Part 8) is epoxied into an aluminum holder which contains two slots that enable the rail to be screwed to the I-beam and still allow alignment between the magnet and rail. The I-beam is attached to the electrohydraulic shaker (Fig. 3.4) which drives the rail.

The shaker is fed by a 3000 psi pump which charges two accumulators. To eliminate pump noise, the tests were run with the accumulators' dis-

charge after the pump had been stopped. The pump and control valves are described in [65].

The shaker's circuitry and the electrically operated valve enables the ram displacement to follow an electrical input signal within the system's dynamic characteristics. For the tests, sinusoids could be generated from 4-60 Hz. at amplitudes ( $\frac{1}{2}$  peak to peak) from 0.02 inches to 0.05 inches.

### 3.3 Scaling of the Experimental Model

The experimental model's design is based upon the scaling of a full size prototype suspension. The following factors influenced the design of the model:

(1) To insure applicability to full-scale designs, laws of similitude must be obeyed; that is:

(a) The model must be geometrically similar to full size prototypes.

(b) The model must be dynamically similar to the full scale designs and the dimensionless parameters of the equations of motion must lie in the region of design interest.

(2) The average air gap ( $h_{10}$ ) between the magnet and the rail was selected so that motion can be detected by eye to permit demonstration of magnetic suspensions. This limits the minimum nominal air gap to 0.1 inches.

(3) The weight of the model was limited to 15 lbs to accommodate the available shaker.

The basic equations used to scale from the full size designs (for example, Table 4) to the experimental apparatus are summarized below. Dimensionless parameters are summarized in Table 2.

The dimensionless static force (6.5) is:

$$\tilde{F} = \left( \frac{1 + \tilde{i}}{1 + h_1} \right)^2 \quad (3.1)$$

The linearized dynamic equations are summarized. The dimensionless acceleration of the basic magnet (6.6) is:

$$\ddot{\tilde{y}}_1 = 2\tilde{h}_1 + 2\tilde{i} \quad (3.2)$$

The current control (6.10) is:

$$\tilde{i} = \left( 1 + \frac{\tilde{\omega}_1^2}{2} \right) \tilde{h}_1 - \zeta_1 \tilde{\omega}_1 \dot{\tilde{y}}_1 \quad (3.3)$$

The voltage in the control coil is an auxiliary variable:

$$\tilde{v} = \tilde{s} \tilde{L}_1 \tilde{i} - \tilde{s} \tilde{h}_1 + \tilde{i} R_1 \quad (3.4)$$

Since the magnet is parallel to the rail in the experiments, the average gap and that measured at a point are identical; i.e.,  $\tilde{h}_1 = \tilde{h}_{1-p} = \tilde{h}_{1-av}$ .

The total flux coefficient ( $\phi_T$ ) is the ratio of the flux in the magnet's yoke ( $\phi_T$ ) to the flux that contributes to the magnet's vertical

lift ( $\phi_u$ ) and is determined from:

$$v_T = \frac{\phi_T}{\phi_u} = 1 + \tilde{K}_V(1 + \tilde{h}_1) \quad (3.5)$$

The air gap fringing coefficient ( $v_a$ ), the voltage coefficient ( $v_v$ ) and the leakage coefficient ( $v_L$ ) are defined by relations similar to (3.5) as discussed in Chapter 5 and Appendix 2.

The effects of eddy currents on flux penetration in the rail and magnet, respectively, are from (10.27) and (10.28):

$$\frac{\phi_R(\omega)}{\phi_R(0)} = \frac{B_{3y}(\omega)}{B_{3y}(0)} \quad (3.6)$$

$$\frac{\phi_T(\omega)}{\phi_T(0)} = \frac{B_{1y}(\omega)}{B_{1y}(0)} \quad (3.7)$$

where the flux densities  $B_{3y}$  and  $B_{1y}$  are defined by (10.13b) and (10.15b). Equations (3.6) and (3.7) are scaled by the magnetic Reynolds number  $R_M$  defined in Table 1 and in Chapter 10.

The model was designed to approximately scale Design 4 of Table 4. The widest of the sample designs was selected to allow eddy current effects to appear at the lowest frequency which the samples allowed. The model and the full size are compared in Table 2.

TABLE 1

DIMENSIONLESS TERMS

Dynamic Variables

$$\tilde{h}_1 = \frac{\Delta h_1}{h_{10}} = \text{magnet-rail clearance}$$

$$\tilde{y}_1 = \frac{\Delta y_1}{h_{10}} = \text{absolute position of magnet}$$

$$\tilde{i} = \Delta i / i_0 = \text{control current}$$

$$\tilde{v} = \frac{Ni_0}{2my\sqrt{gh_{10}}} = \text{control voltage}$$

$$\tilde{f} = f/mg = \text{force}$$

Time

$$\tilde{t} = t\sqrt{g/h_{10}}$$

$$\tilde{\omega} = \omega\sqrt{h_{10}/g}$$

COEFFICIENTS OF EQUATIONS

$$\begin{aligned} \tilde{K}_v = & \frac{h_{10}}{l_p} \left\{ 1.92 \left( 1 + \frac{l_p}{l_1} \right) + 3.23 \frac{h_{10}}{l_1} + [w_3 - h_{10}] \left[ \frac{1}{w_1} \right. \right. \\ & \left. \left. + \frac{2}{l_1} \left( \frac{\mu_0}{\pi} \ln \left( 1 + \frac{2l_p}{w_1} \right) + .26 \right) \right] \right\} \end{aligned}$$

where

$l_p$  = width of magnet's pole face

$l_2$  = width of rail's pole face

$l_1$  = length of magnet

$w_3$  = length of pole core

$w_1$  = distance between pole cores

$\tilde{L}_1 = v_v =$  self inductance of control coil

$$\tilde{R}_1 = \frac{R_1 2h_{10}}{\mu_o l_1 l_p N^2} \sqrt{h_{10}/g} = \text{resistance of control coil}$$

MAGNETIC REYNOLDS NUMBER

$$R_M = \frac{\mu_3 \sigma_3 \omega}{k^2}$$

where

$\mu_3$  = permeability of rail

$\sigma_3$  = conductivity of rail

$$k = \text{wave number of magnet} = \frac{\pi}{2l_p + w}$$

The magnet's cross section is scaled by approximately 1/6. Where the air gap is 0.6 in. and the pole width 2.12 in. for the full scale, the model has a 0.1 inch air gap and pole width of 0.42 in. The distance between the pole cores ( $w_1$ ) and the length of the cores ( $w_3$ ) were set at 1.00 and 0.85 inches, respectively, to allow space for the coils in proportion similar to the full-scale designs.

Scaling the magnet's length ( $l_1$ ) by 1/6 results in a model length of 1.7 ft (10 ft/6) a figure too large for the available shaker. The magnet length was set at 3 inches which gives a magnet length to pole width ratio ( $l_1/l_p$ ) of seven. Since magnet length does not appear in the scaling of long magnets, the validity of the results is affected little; however, the finite length is considered in the calculations of the flux coefficients.

The flux coefficient (3.5) and the static forces (3.1) are dynamically scaled for geometrically scaled models. Dynamic frequency is set by the controller and the road input so that dynamic similarity can be maintained in (3.2) through (3.4).

The dimensionless inductance ( $\tilde{L}_1$ ) is scaled dynamically for a geometrically scaled model (if the reluctance of the iron parts is negligible). Since the coil's dimensionless resistance ( $\tilde{R}_1$ ) appears only in the auxiliary equation (3.4), effort was not made to scale  $\tilde{R}_1$  dynamically.

The effects of eddy currents (3.6) and (3.7) are scaled by the magnetic Reynolds number ( $R_M$ ) which depends on geometry, the material

properties of the rail, and the frequency of the magnetic field. It was impossible to scale simultaneously frequency

$$\tilde{\omega} = \omega \sqrt{h_{10}/g} \propto \omega h_{10}^{1/2}$$

and Reynolds number

$$R_M = \frac{\mu_3 \sigma_3}{k^2} \propto \sigma_3 \omega h_{10}^2$$

where the air gap is used as a characteristic dimension. The difficulty in scaling Reynolds number and frequency was overcome by measuring the motion effects and the eddy current effects in separate tests. In addition, inferences about eddy effects could be drawn from the motion tests.

With 1/6 scaling, model frequency ( $f_M$ ) is related to full size frequency ( $f_F$ ) through:

$$f_M = \sqrt{6} f_F \quad (3.8)$$

Assuming the permeability of the model rail and the full scale rail are identical and with the model's conductivity  $\frac{1}{4}$  that of the full size:

$$f_M = 9 f_F \quad (3.9)$$

TABLE 2  
SCALING OF MODEL

MAGNET	TEST MODEL	DES. 4 OF TABLE 4	DES. 2 OF TABLE 4
$h_{10}$ (in)	0.1	0.6	0.6
$l_p$ (in)	0.42	2.12	1.38
$w_1$ (in)	1.00	5.2	3.8
$w_3$ (in)	0.85	6.0	5.3
$t_y$ (in)	0.18	2.12	1.38
$l_1$ (ft)	0.25	30	10
RAIL	ARMCO IRON	1.75% Si STEEL	1.75% Si STEEL
$\sigma$ [ohm-m] <sup>-1</sup>	1.6 .93 × 10 <sup>7</sup>	1.6 .26 × 10 <sup>7</sup>	1.6 .26 × 10 <sup>7</sup>
	SIMILAR B-H CURVES		
$l_2$ (in)	.620	2.58	3.32

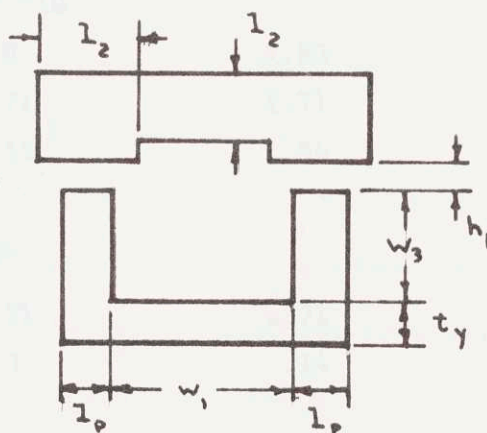


Fig. 3.7 MAGNET PARAMETERS

	TEST MODEL	DES. 4 of TABLE 4	DES. 2 OF TABLE 4
Veh. wt. per Mag. (lb)	13.3	22,000	22,000
COIL	COPPER	ALUMINUM	ALUMINUM
$N i_0$ (amps)	$1.24 \times 10^3$ (1.9 amps, 650 turns)	$2.09 \times 10^4$	$1.49 \times 10^4$
$R_1 i_0^2$ (kw)	.21 ( $R_1 = 5.7 + 1$ ohm)	8.5	19
$\sigma$ (ohm-m) <sup>-1</sup>	$5.8 \times 10^7$ (20°)	$2.5 \times 10^7$ (160°C)	$2.5 \times 10^7$ (160°C)

NORMALIZING PARAMETERS

$\sqrt{g/h_{10}}$ (hz)	62.3	25.5	25.5
$\frac{2mg\sqrt{gh_{10}}}{i_0}$ (volts <sup>-1</sup> )	10.0	$75/i_0$	$75/i_0$

FLUX COEFFICIENTS AT  $h_{10}$

$v_T$	1.8	1.83	2.38
$v_v$	1.71	1.71	2.18
$v_\partial$	1.55	1.54	1.83

NON DIMEN. PARAMETERS

$\tilde{L}_1$	1.71	1.71	2.18
$\tilde{R}_1$	1.3	.14	.26

For example, if eddy current effects appear at 90 hz. in the model, the effects will appear at 10 hz. in the full size system.

Two rails, both with rail pole width equal to rail thickness equal to 0.62 in., were constructed from armco iron with resistivity of 10.7 ohm-cm (1/4 that of the 1.75% silicon steel recommended for the full size design) and with B-H curve similar to silicon steel. One rail was solid while the other was constructed from four U-shaped laminations each 0.155 in. thick.

For realistic scaling, 2V permendur, the material recommended for full size designs, was used in the model. To eliminate eddy currents in the magnet, the core was constructed of flat, 0.014 in. thick, U-shaped laminations. In order that the model and the full size magnet operate at the same position on the B-H curve, the thickness of the magnet's yoke was reduced to 0.18 in. (rather than  $0.42 \text{ in.} = \frac{l}{p}$ ).

Both rails and the magnet core were milled and heat treated to obtain optimum magnetic properties. The 2V permendur was baked at 1450°F in dissociated ammonia, cooled at 150°F/hr, and removed from the furnace. The armco iron was heated to 1700°F in a dry hydrogen atmosphere (dew point 0°F) held at 1700°F for 2 hours, and furnace cooled.

The coils are 650 turns ( $325 \times 2$  cores) of 21 gauge copper wire which carry a nominal current of 1.9 amps to support the 13.3 pounds of the vehicle at 1/10 inch air gap. Where the dimensionless resistance ( $\tilde{R}_1$ ) of the full scale's coil is in the .2 to .3 region (calculated for Table 4),  $\tilde{R}_1$  of the model is 1.3. Since the only voltage an auxiliary variable depends on  $\tilde{R}_1$  the validity of the experiment is affected little.

### 3.4 Experimental Procedure

The experimental procedures are described for the following tests whose results appear in Section 3.5:

- (1) measurements of magnetic flux;
- (2) static force measurements; and
- (3) dynamic frequency response.

Flux measurements were conducted by driving an alternating current

$$i = I_o \sin(2\pi f t)$$

through the magnet's control coil while the vehicle and rail were stationary. Flux in the rail ( $\phi_R$ ) and the magnet's yoke ( $\phi_T$ ) were measured by search coils positioned as indicated in Figure 3.8.

The amplitude of the flux was determined from the search coil's voltage which was read on an oscilloscope. From electromagnetic inductance:

$$v_s = N_s \frac{d\phi}{dt}$$

where  $v_s$  is the voltage measured at the leads of the search coil and  $N_s$  is the number of turns in the search coil. Since the search coil is connected to a high impedance oscilloscope and phasemeter, virtually no current flows in the search coil. The amplitude of the voltage is related to the amplitude of the magnetic flux by:

$$\phi_o = v_o / (N_s)$$

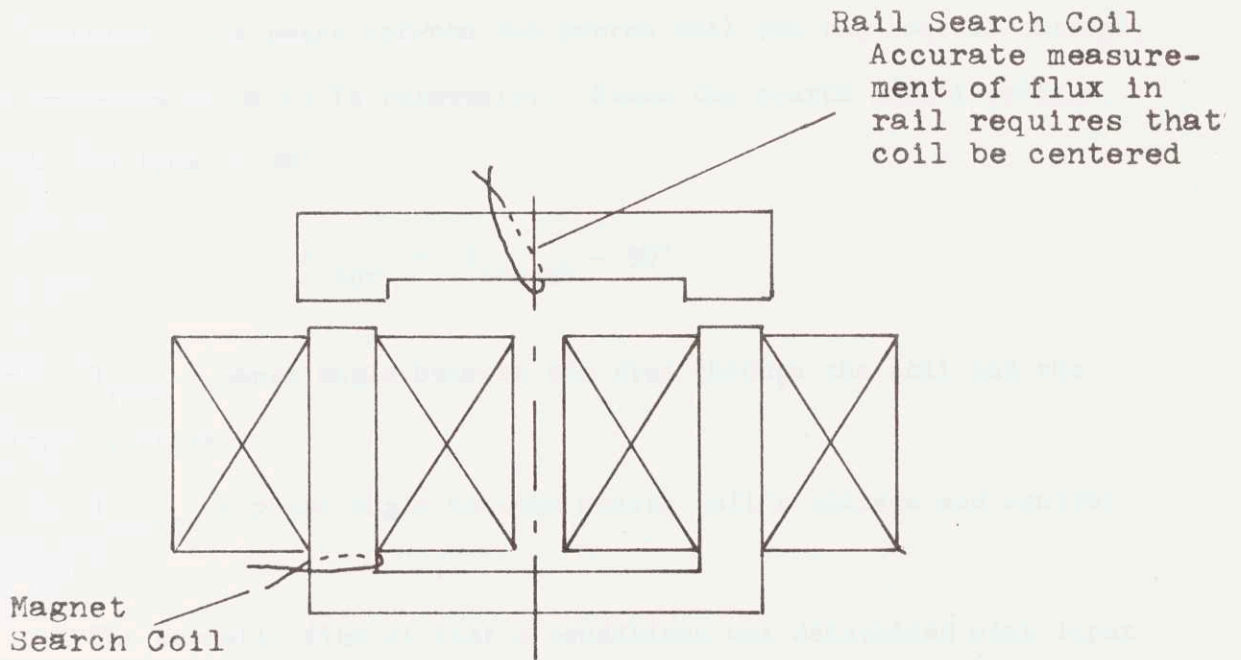


Fig. 3.8. Positions of Search Coils for Flux Measurement

where the subscript  $\theta$  indicates the amplitude of a sinusoid. Since the coils are wrapped tightly only flux in the ferromagnetic material is measured. The phase between the search coil and the control current was measured on an Ad Yu phasemeter. Since the search coil's voltage leads the flux by  $90^\circ$ ,

$$\theta_{\text{flux}} = \theta_{\text{search}} - 90^\circ$$

where  $\theta_{\text{flux}}$  = phase angle between the flux through the coil and the control voltage

$\theta_{\text{search}}$  = phase angle between search coil's voltage and control current.

The magnetic flux at static conditions was determined with input current amplitudes of 1 to 3 amps and frequencies of 10-30 hz. The input frequencies were chosen because smaller frequencies induced a weak output signal while higher frequencies introduced eddy current effects which are described in the measurements of flux versus input frequency; i.e., for the displacements measured flux gain does not roll off until 50 hz.

For all flux measurements the magnet was centered below the rail. Preliminary measurements show that the flux is insensitive to the magnet's position as long as the magnet's pole face is below that of the rail.

Because measurements were taken at different currents and because of its common usage [50], it is convenient to plot fluxes as dimensionless ratios. In the experiments, the total flux coefficient

$$v_T = \frac{\phi_T}{\phi_u} \quad (3.10)$$

and the leakage coefficient

$$v_L = \frac{\phi_T - \phi_R}{\phi_u} \quad (3.11)$$

are used where  $\phi_T$  is the flux in the magnet's yoke and  $\phi_R$  is the flux in the rail. To facilitate manipulations, the useful flux is defined by (2.4):

$$\phi_u = \frac{\mu_o N i l_1 l_p}{2h_1} \quad (3.12)$$

If a different  $\phi_u$  is defined,  $v$  will change accordingly, but the final results will be the same.

For measurements at high frequency where eddy current effects occur, it is convenient to consider the ratio of the flux at a frequency  $f$  to the flux at zero frequency.

For the measurements of static force versus current and air gap, the currents were read from meters on the power supply and from an oscilloscope which monitored the voltage across the sensing resistor. Displacements were measured from the displacement signal of the control circuit or by using a spacer to physically measure the larger gaps.

The force was measured by two techniques. A reliable measurement was obtained by running the magnet with the closed loop control and no input from the rail. The magnet would then sit quietly at a position. Since there was no motion, the magnetic field exerted a force equal to the vehicle's weight. The second method used a force transducer which

consists a two cantilevers with strain gages on both sides so that a full bridge was realized. The transducer was placed in one of the two grooves seen in Fig. 3.2 and was calibrated by the weight of the vehicle. As the magnet force increased, the force on the transducer decreased. The transducer was excited and balanced by a Sanborn 321 recorder. Because of the soft bonding material used (Duco cement), the transducer exhibited hysteresis effects which were accounted for in the measurements. During the force measurements the air bearing was operating so that friction forces were eliminated.

The dynamic tests were conducted by sinusoidally oscillating the shaker to provide a vertical rail displacement ( $y_0$ ). The motion of the rail was monitored by a displacement transducer in the shaker's control circuitry. The displacement, current, and voltage of the magnet were measured from the appropriate points in the magnet's controller. For acceleration measurements, an accelerometer (PAL 5218) was mounted to the block of part 10 .

### 3.5 Experimental Results

The experimental results for static flux, static force, dynamic frequency, and dynamic flux penetration response are described below. The experimental results are compared to the theory summarized in (3.1) to (3.7) for the parameters of Table 2. For all figures in this section, the points were measured experimentally while the solid curves are theoretical.

In Figure 3.9, experimental values of total flux coefficient and leakage coefficient are compared with the theoretical curves derived from

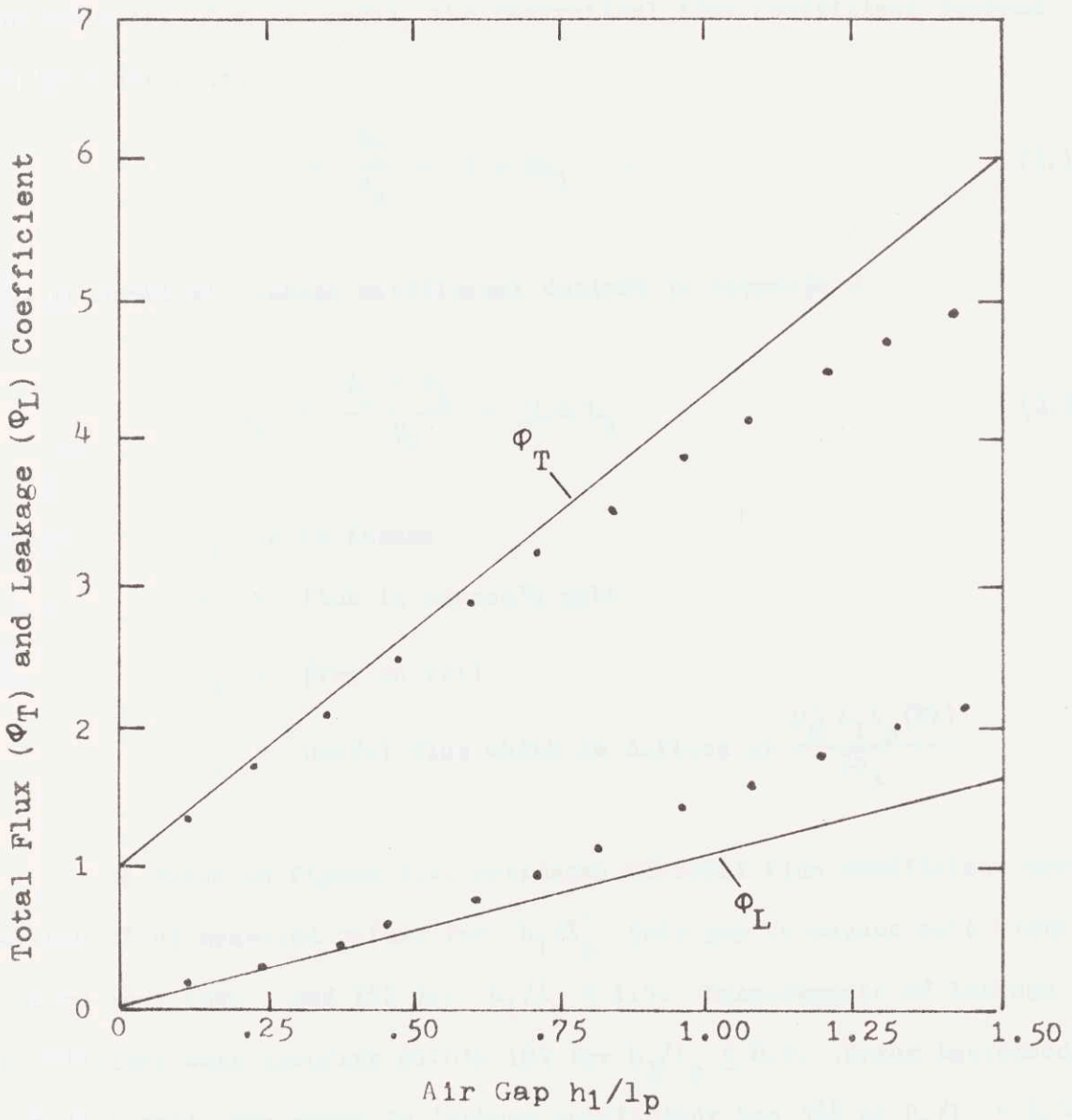


Fig. 3.9. Total Flux and Leakage Coefficient vs. Air Gap

the lumped flux path model of Chapter 5 and Appendix 2. The theoretical coefficients are predicted from only the rail-magnet geometry (tabulated in Table 2). For the model, the theoretical flux coefficient derived in Appendix 2 is:

$$v_T = \frac{\phi_T}{\phi_U} = 1 + 8h_1 \quad (3.13)$$

The theoretical leakage coefficient derived in Appendix 2:

$$v_L = \frac{\phi_T - \phi_R}{\phi_U} = 2.6 h_1 \quad (3.14)$$

where

$h_1$  is in inches

$\phi_T$  = flux in magnet's yoke

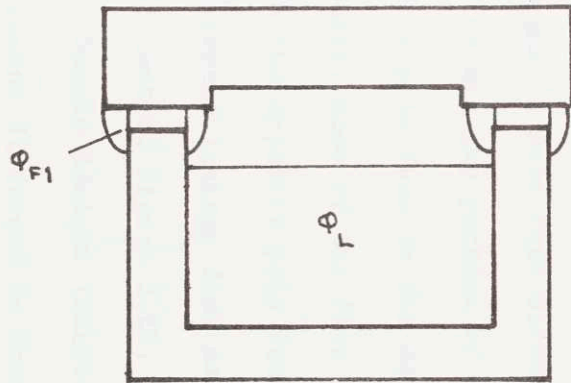
$\phi_R$  = flux in rail

$\phi_U$  = useful flux which is defined as  $\frac{\mu_o l_1 l_p (NI)}{2h_1}$

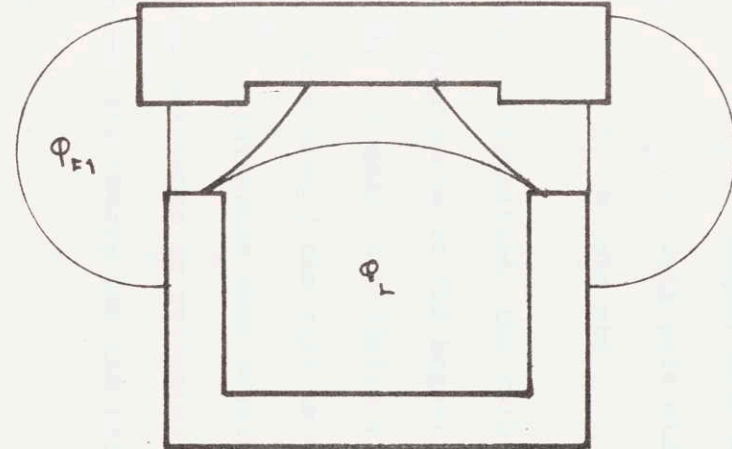
As shown in Figure 3.9, estimates of total flux coefficient were within 5% of measured values for  $h_1/l_p$  (air gap to magnet pole width ratio) less than 1 and 15% for  $h_1/l_p \leq 1.5$ . Measurements of leakage coefficient were accurate within 10% for  $h_1/l_p \leq 0.6$ . Error increased steadily until the error in leakage coefficient was 35% at  $h_1/l_p = 1.5$ .

Because of the model used, qualitative discussions which appear in [50] and [53] indicate that the form of these results is expected. The design equations (3.10) and (3.11) were derived for

$$l_2 = l_p + 2h_1$$



a. Small Gap (used in theoretical model)



b. Large Gap

Fig. 3.10. Flux Paths as Air Gap Changes

where  $l_p$  = magnet pole width  
 $l_2$  = rail pole width  
 $h_1$  = air gap

For this configuration, the rail appears as an infinite plane to the magnet and the flux paths at the magnet face may be diagrammed as in Figure 3.10a. At larger air gaps, the finite width of the rail causes the fringing flux  $\phi_{F1}$  to curve around the rail as shown in Figure 10.3b. The longer path has a lower permeance than predicted by the infinite plane model. The decreased permeance is reflected in differences between the measured points and the theory for the total flux coefficient at larger air gaps ( $h_1/l_p < 1$ ).

The model of Chapter 5 also assumes that all the flux leaving the magnet's pole face crosses the air gap and enters the rail as sketched in Figure 3.10a. As discussed in [50], this is true for window width ( $w_1$ ) greater than approximately  $4h_1$ . When  $4h_1 > w_1$ , the flux path from the magnet's pole face directly to the opposite pole face becomes shorter than the air gap portion of some of the flux paths which go from the magnet's pole face to the rail to the opposite pole face. As the air gap increases, some of the flux leaving the pole face goes not to the rail but to the opposite pole face as sketched in Figure 3.10b. This increases the expected leakage flux as demonstrated in the data for leakage flux coefficient of Figure 3.10.

Sample designs (Chapter 4.3) were compiled with  $l_2 = l_p + 2h_{10}$  for reasons discussed in Chapter 2.2. Practical designs require  $w_1 > 4h_1$

(to allow sufficient space for coils) so that the lumped flux model is valid for preliminary design purposes since, in the region of design interest ( $h_1/l_p < 0.5$ ), the fluxes are predicted within 5% (Figure 3.9) For design with  $l_2 \geq l_p + 2h_{10}$  or  $w_1 < 4h_1$ , different flux paths must be determined as outlined in [50].

In the next test, the static force was measured as a function of the magnet's current and gap and compared to the theoretical force. From (3.2) the dimensional theoretical force is:

$$F = \frac{\mu_0 l_1 l_p (NI)^2}{4h_1^2}$$

Measurements of static force (Fig. 3.11) were accurate within 10% for air gaps ( $h_1$ ) that ranged from 1/4 to 1 1/2 times the pole width of the magnet ( $l_p$ ).

The force is derived from the total flux ( $\psi_T P_u$ ) by (5.8) and (5.9):

$$F = \frac{1}{2} (NI)^2 \frac{\partial}{\partial h_1} \left[ \frac{\psi_T l_1 l_p}{h_1} \right]$$

Thus, the measurements of static force and leakage are compatible with each other and with the theoretical models of (3.1) and (3.5).

The dynamic frequency response data is presented in Figures 3.12 to 3.19 as dimensionless gains of acceleration, relative displacement, current, and voltage for the rail input versus the dimensionless input frequency:

$$\tilde{f} = f \sqrt{h_{10}/g}$$

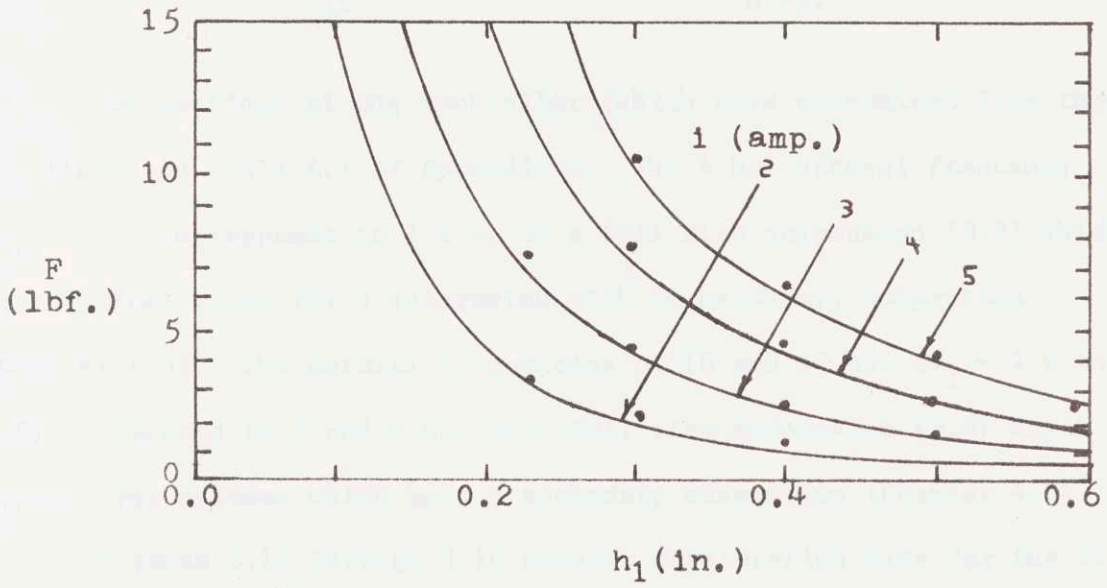
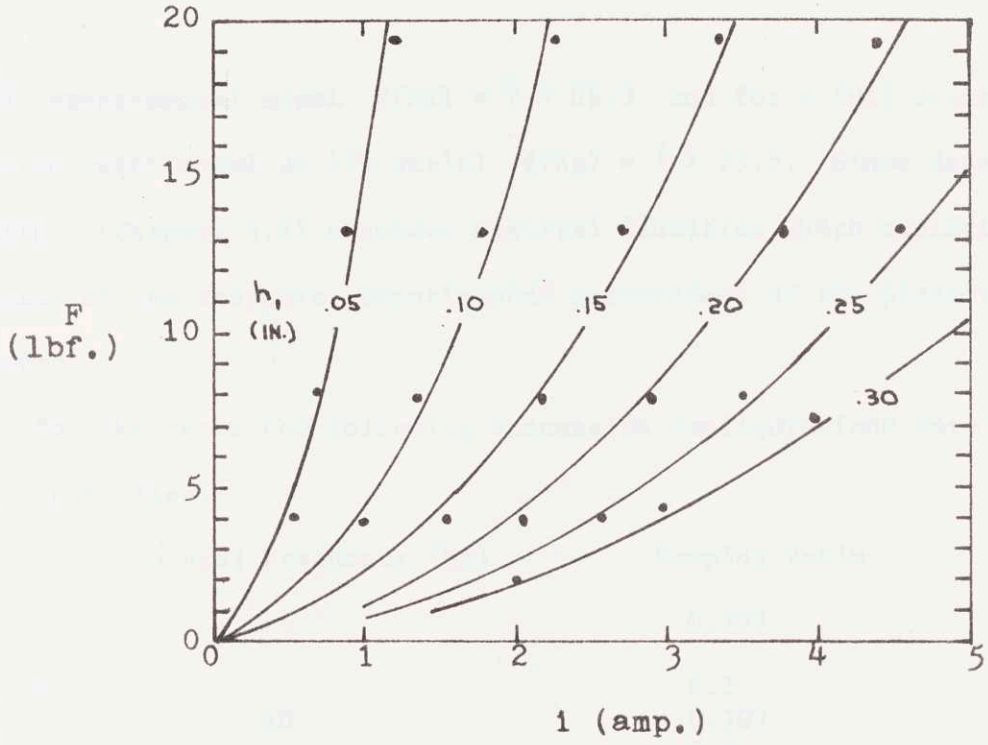


Fig. 3.11. Static Force Tests

For the experimental model  $f(\text{hz}) = \tilde{f} \times 62.3$  and for a full scale prototype (with model at 1/6 scale)  $f(\text{hz}) = \tilde{f} \times 25.5$ . Since design algorithms (Chapter 4.2) consider spectral densities which neglect the phase of the response, experimental measurement of the phase was neglected.

For the tests the following suspension configurations were set on the controller:

Natural Frequency (hz)	Damping Ratio
4	0.707
	0.2
10	0.707
	2.0
15	0.707

The settings of the controller (which were determined from theory) are listed in Table A.1 of Appendix 5. The 4 hz. natural frequency ( $\tilde{\omega}_1 = 0.4$ ) corresponds to 1.6 hz on a full size suspension (3.8) which is a typical value for a suspension with no secondary suspension (Chapter 4.3). The natural frequencies of 10 and 15 hz. ( $\tilde{\omega}_1 = 1.0$  and 1.5) correspond to 4 and 6 hz. on a full size suspension (3.8) which is typical for systems which have a secondary suspension (Chapter 4.3).

Figures 3.12 through 3.16 present acceleration data for the five control settings mentioned above. Figures 3.17 through 3.19 present the relative displacement, control current, and control voltage respectively for a suspension with natural frequency of 10 hz. ( $\tilde{\omega}_1 = 1$ ) and damping ratio of 0.707. The solid rail was used for all measurements except in

Figure 3.13 where the data for the solid rail is compared to that of the laminated rail described in Section 3.3.

In all cases, the points are experimental and the lines are based on the theory of (3.2) through (3.4). The basic linearized equation of motion (3.2) in dimensional form is:

$$m \ddot{y}_1 = K_1 \Delta i - K_2 \Delta h_1$$

The natural frequency and the damping ratio are analytically determined from the current control (3.3) which is dimensionally:

$$\Delta i = \frac{1}{K_1} [(K_2 + m \omega_1^2) \Delta h_1 - 2\zeta_1 \omega_1 m \dot{y}_1]$$

Finally, the voltage (3.4) necessary to implement the current control is:

$$\Delta v = L_1 \frac{d(\Delta i)}{dt} - L_y \frac{d(\Delta h_1)}{dt} + R_1 \Delta i$$

where

$$K_1 = \frac{\mu_o N_o^2 i_o l_1 l_p}{2h_{10}^2}$$

$$K_2 = \frac{\mu_o (N i_o)^2 l_1 l_p}{2h_{10}^3}$$

$$L_1 = \frac{\mu_o N^2 v_v}{2h_{10}} \quad , \quad v_v = v_v(h_1 = h_{10})$$

$$L_y = \frac{\mu_o N^2 i_o}{2h_{10}^2}$$

At the nominal position, the air gap was 0.1 inches which required a nominal current of 1.9 amps to support the vehicle's 13.3 lb. The vertical motion was independent of the lateral position as long as the magnet was below the rail.

Measured points for acceleration, displacement, and current are within 10% of the estimated values. The voltage which depends directly on flux coefficients is predicted with less accuracy (several points fall in the 10-15% accuracy range) than are the other variables such as displacement, current, and acceleration which do not depend as heavily on the additional parameters. The differences in predictability reinforces the contention of Chapters 2.3 and 6 that current control is superior to voltage control.

Figure 3.13 shows that the damping ratio is slightly lower (less than 5%) in the solid rail than in the laminated rail (4 laminations). Since measurements of flux penetration versus frequency in the solid rail reveal only small eddy current effects in the 10 to 100 hz. range, the closeness of the responses with the two rails is expected. In addition, the dynamic behavior is accurately predicted up to 60 hz. (shaker maximum) by the static model which neglects eddy current effects. Scaling 60 hz. by the magnetic Reynolds number which is demonstrated by (3.9) indicates

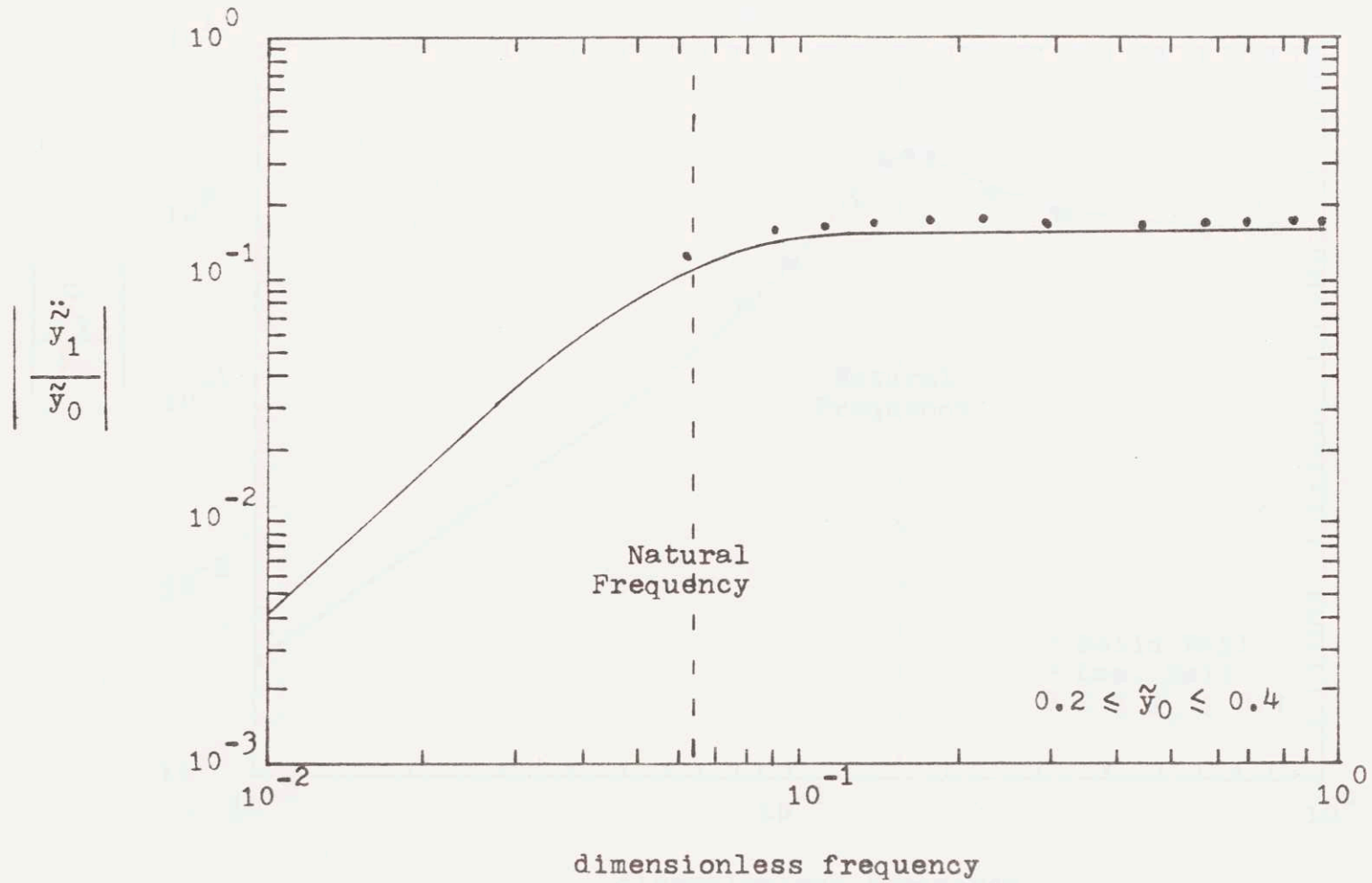


Fig. 3.12. Acceleration Gain vs. Frequency  
 $\tilde{\omega}_1 = 0.4, \zeta_1 = 0.707$

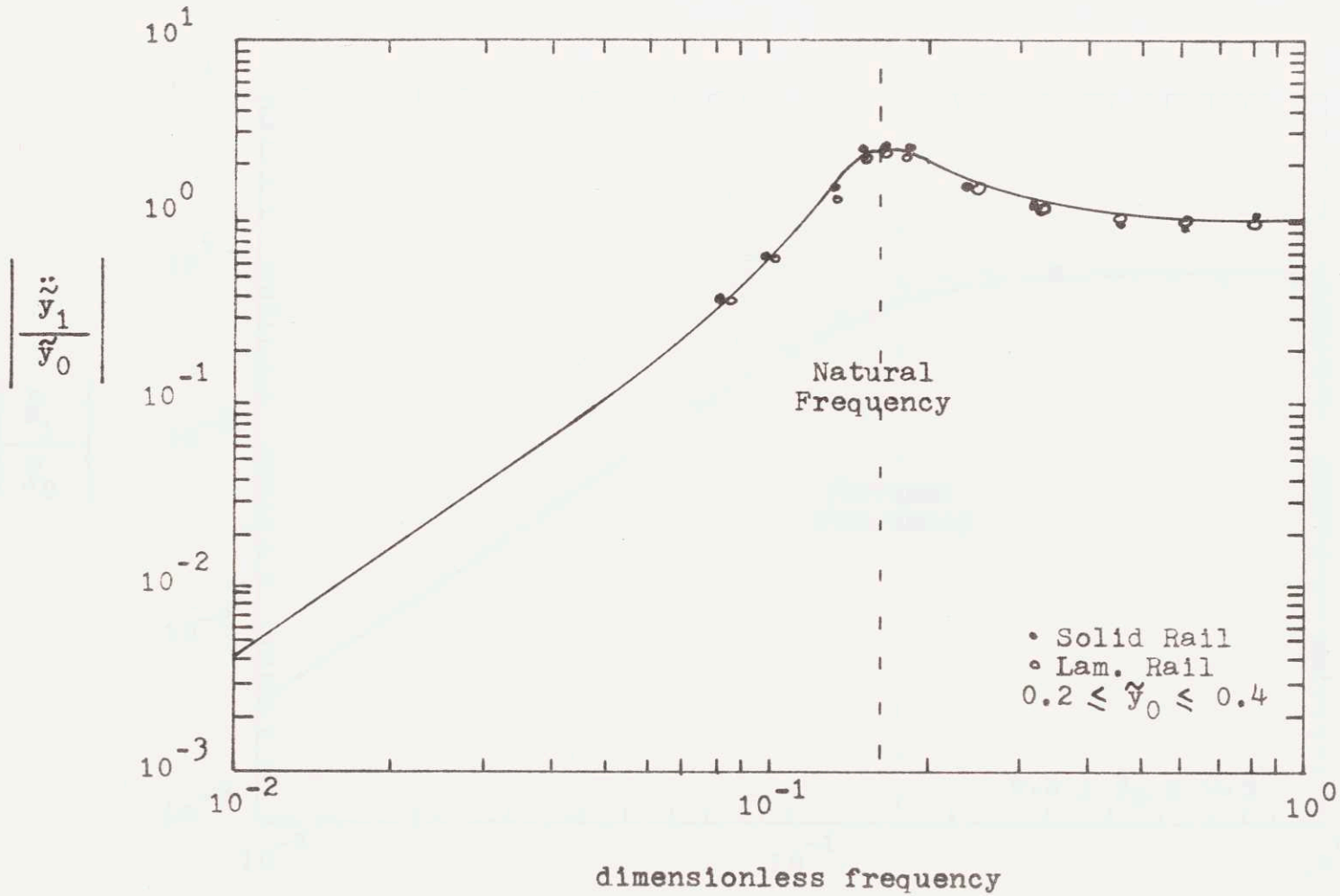


Fig. 3.13. Acceleration Gain vs. Frequency for Laminated and Solid Rail.  $\zeta_1 = 1.0, \zeta_1 = 0.2$

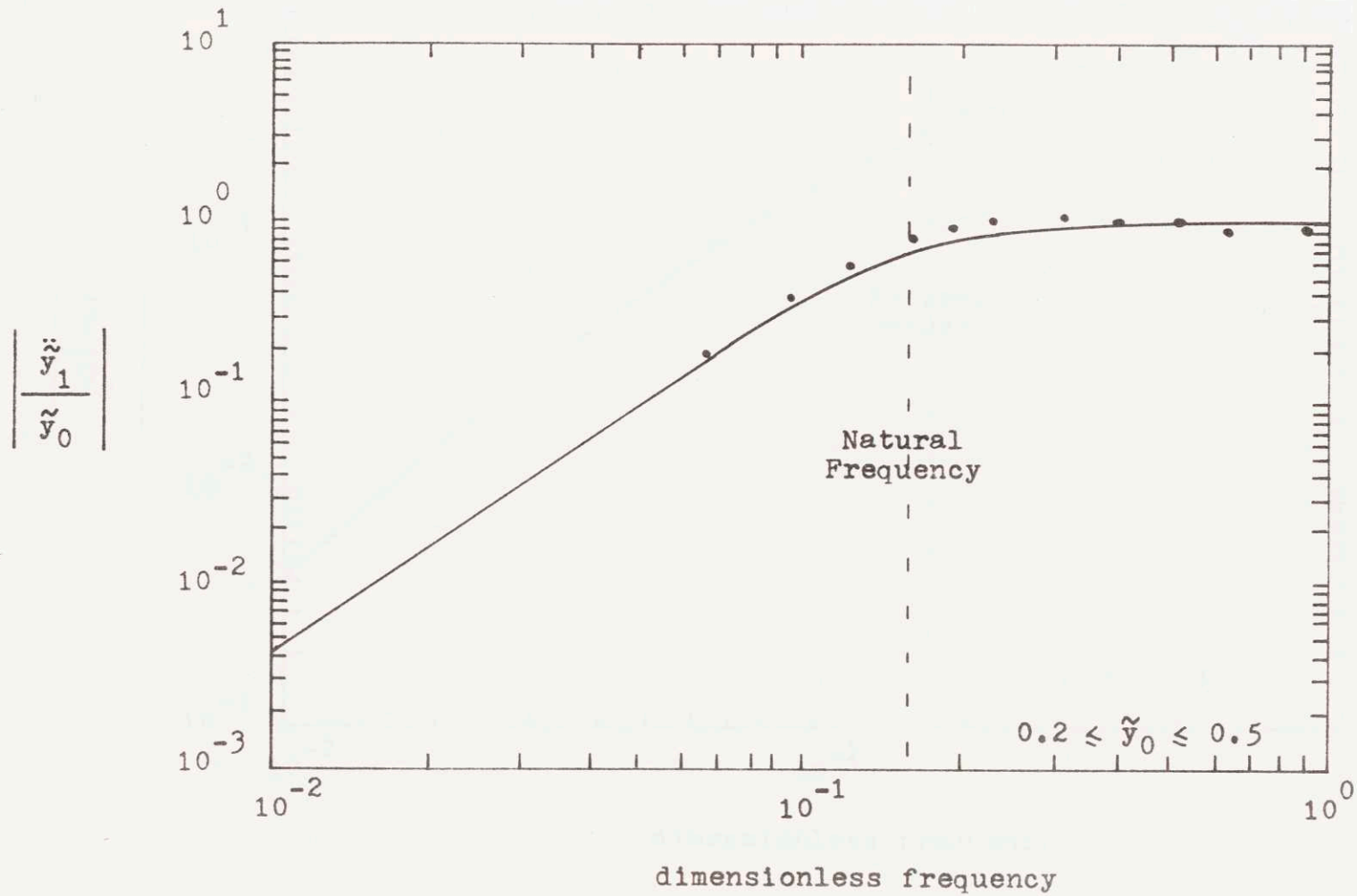


Fig. 3.14. Acceleration Gain vs. Frequency  
 $\tilde{\omega}_1 = 1.0, \zeta_1 = 0.707$

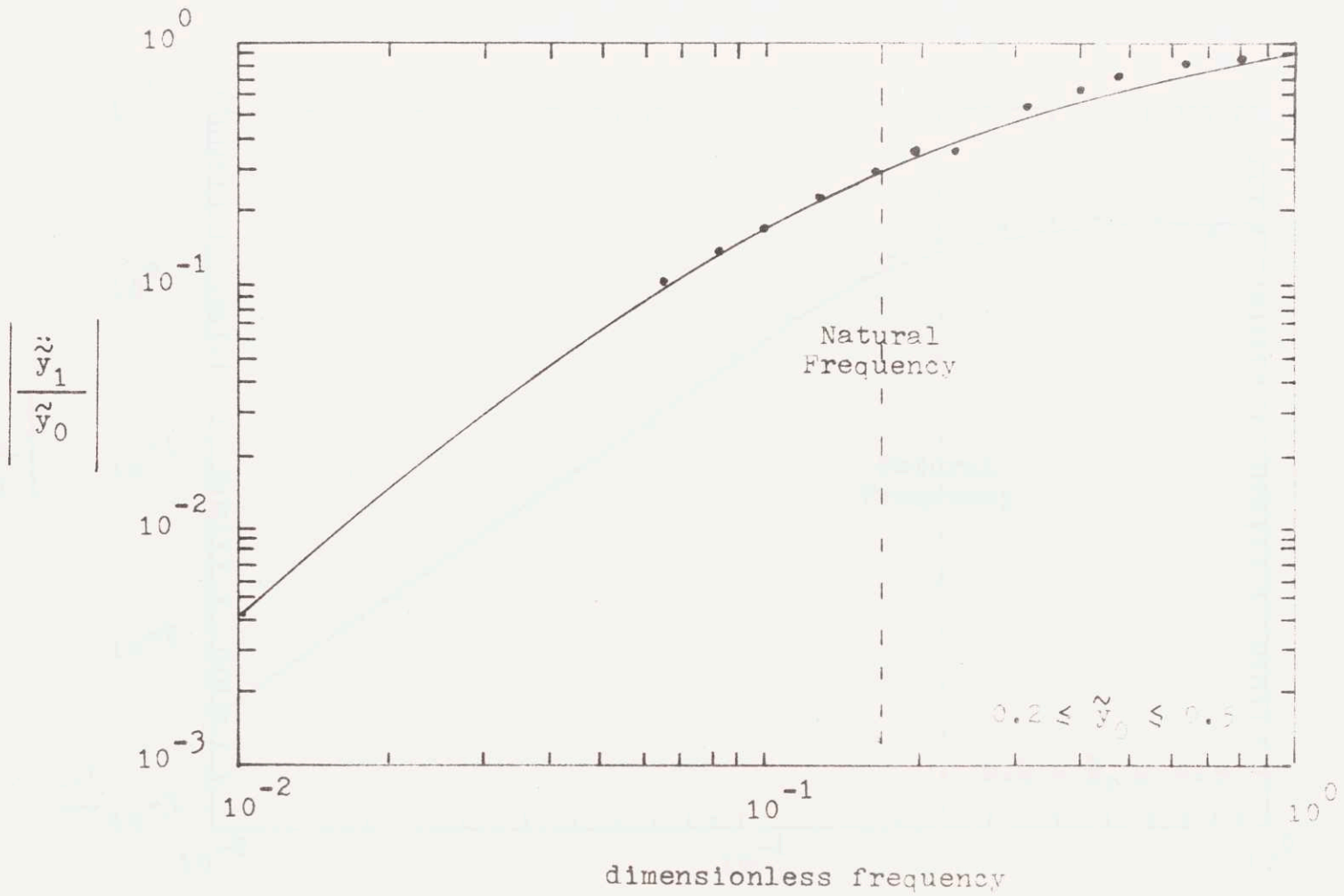


Fig. 3.15. Acceleration Gain vs. Frequency  
 $\zeta_1 = 1.0, \zeta_1 = 2.0$

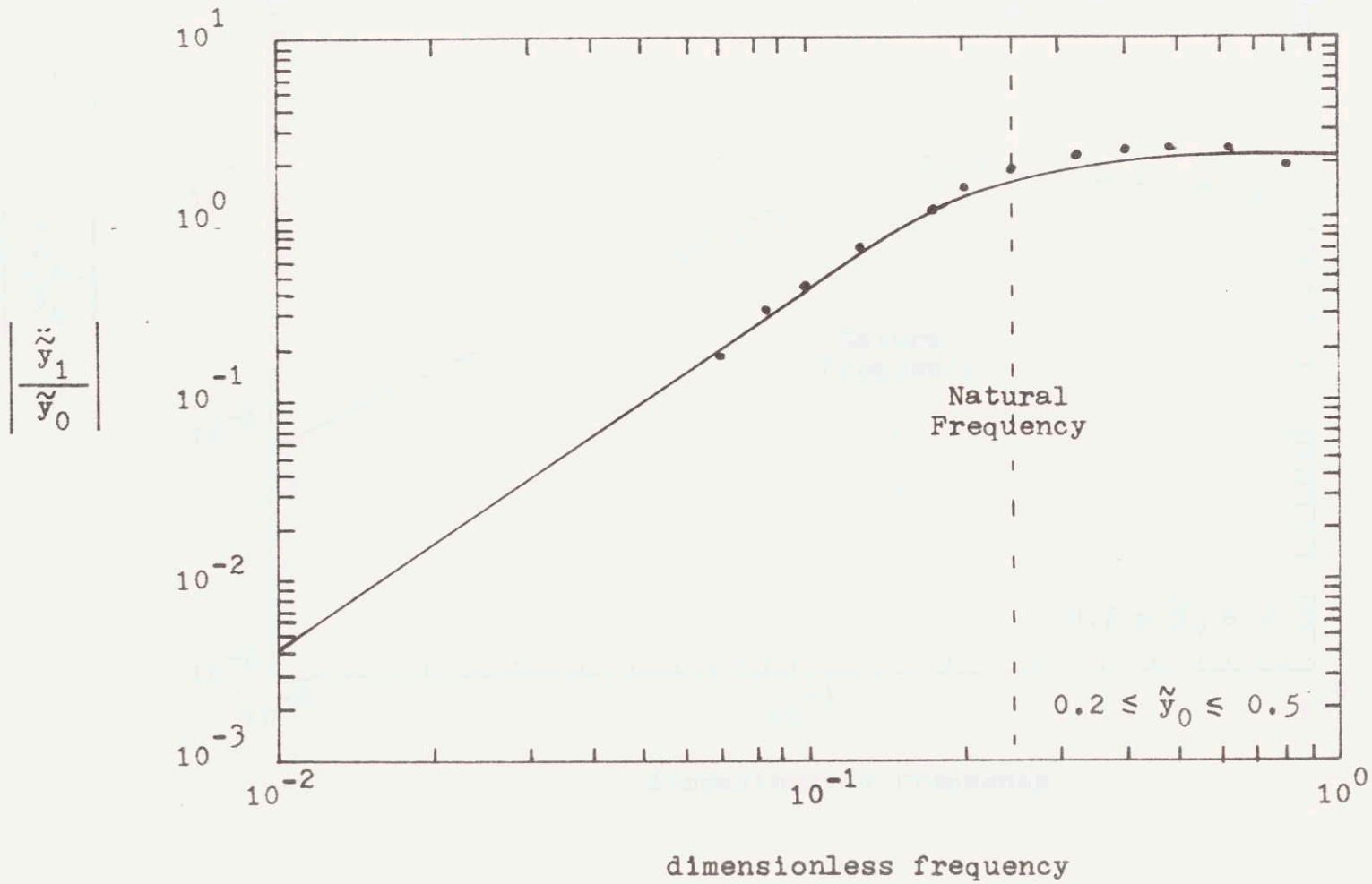


Fig. 3.16. Acceleration Gain vs. Frequency  
 $\zeta_1 = 1.5, \quad \xi_1 = 0.707$

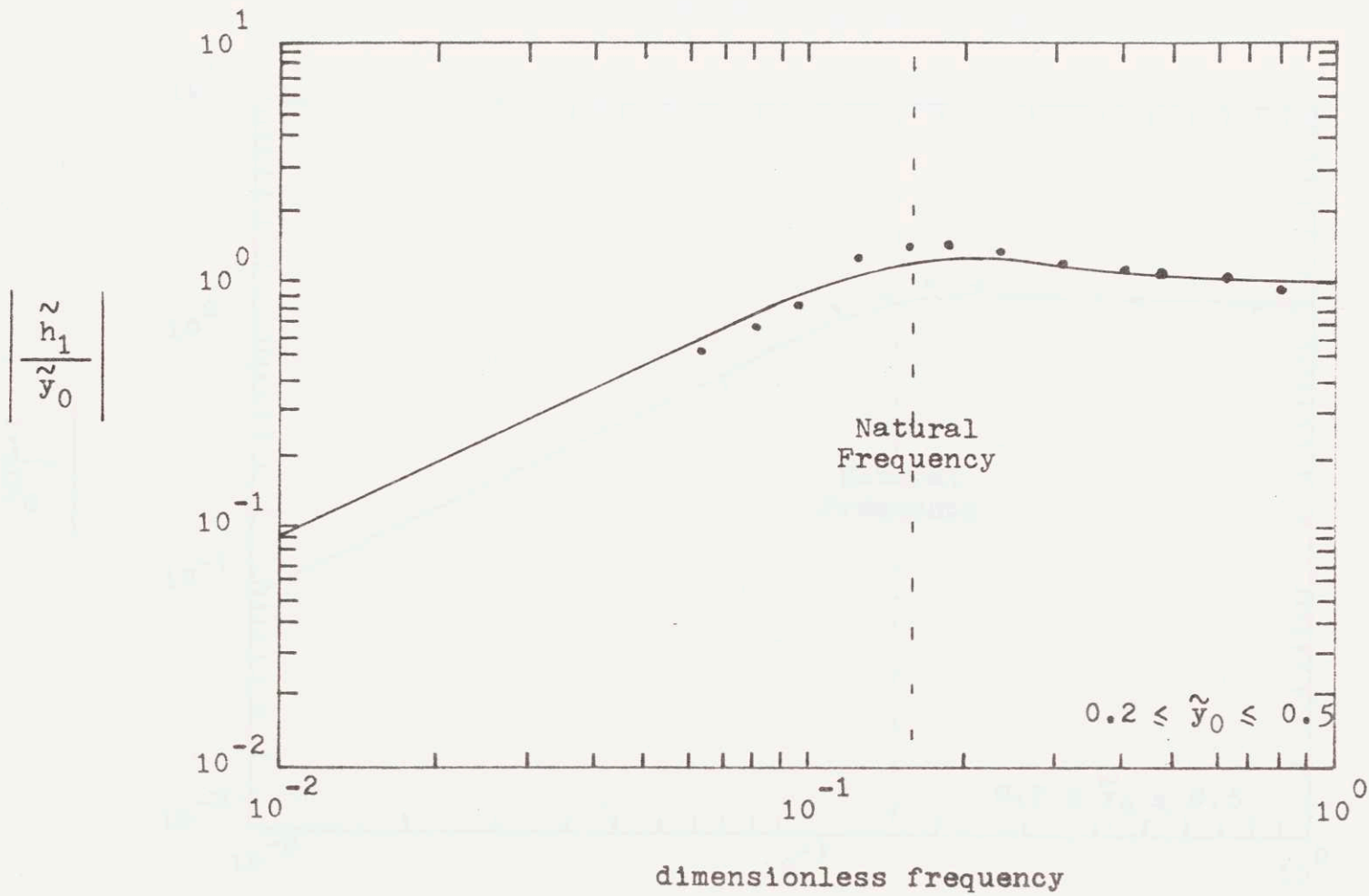


Fig. 3.17. Displacement Gain vs. Frequency  
 $\omega_1 = 1.0, \zeta_1 = 0.707$

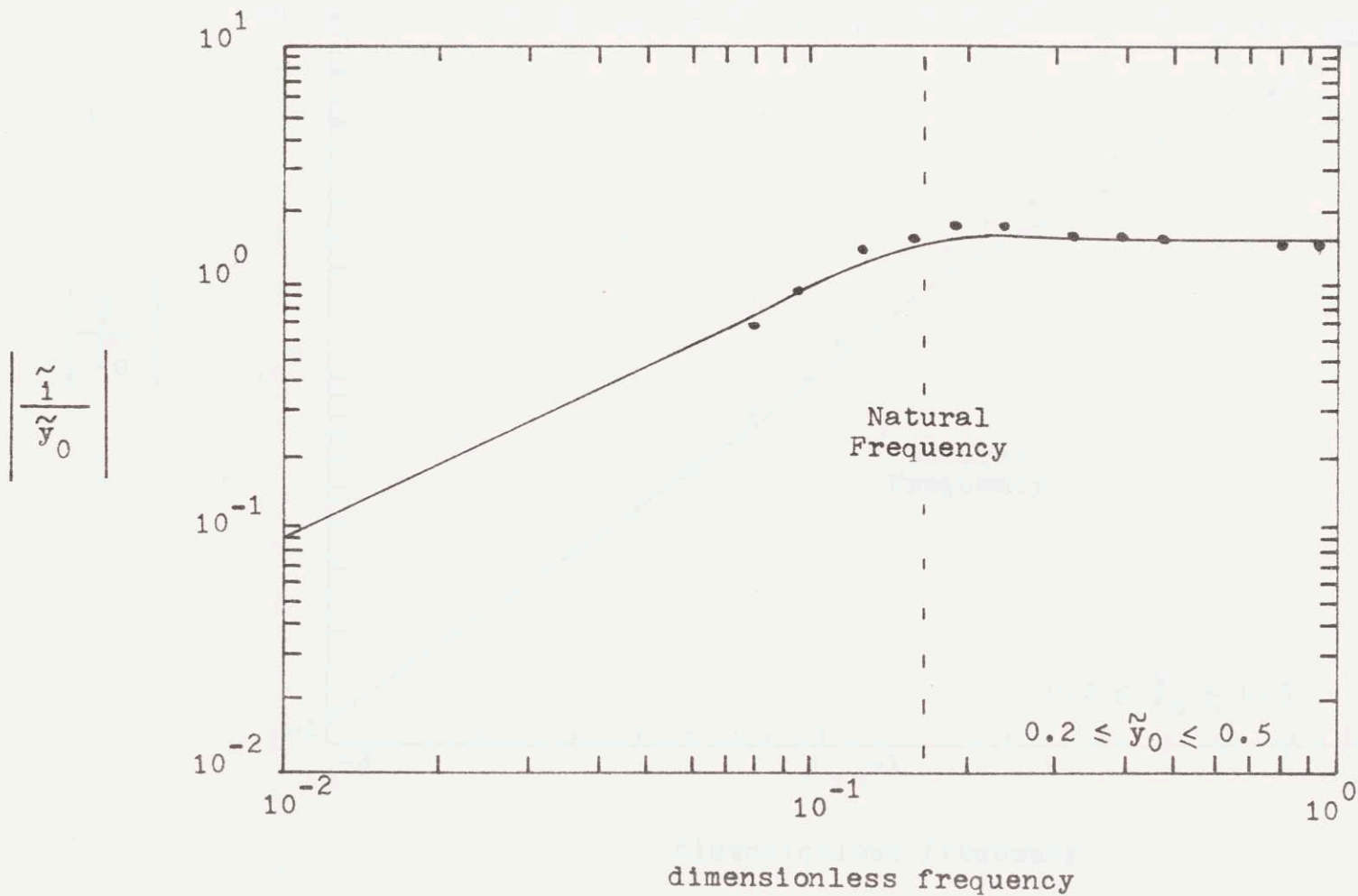


Fig. 3.18. Current Gain vs. Frequency  
 $\omega_1 = 1.0, \zeta_1 = 0.707$

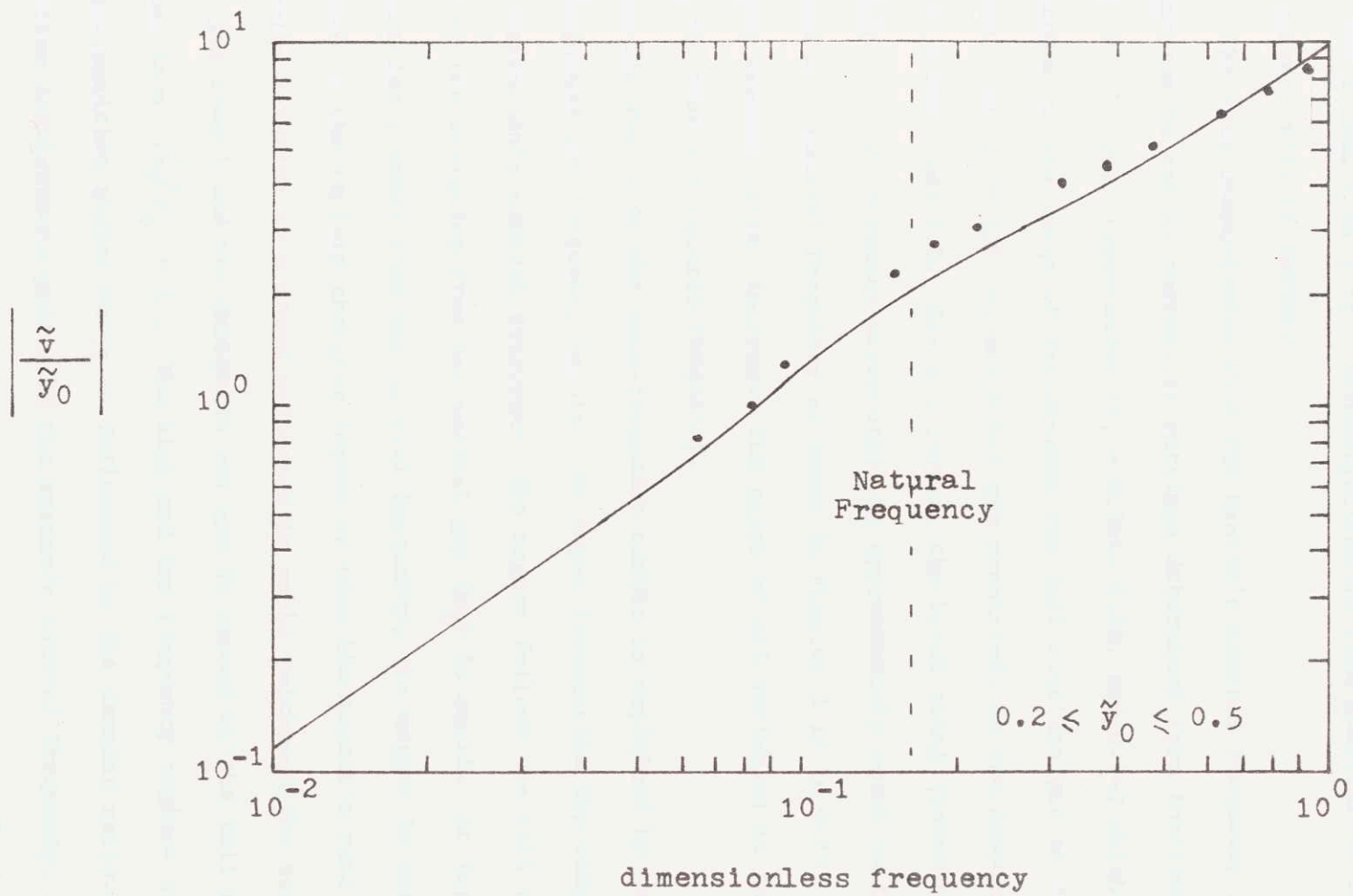


Fig. 3.19. Voltage Gain vs. Frequency  
 $\xi_1 = 1.0, \zeta_1 = 0.707$

that full scale suspensions are not affected by eddy currents for frequencies less than 7 hz. Investigations of flux penetration consider eddy current effects further.

The data demonstrates that the system's natural frequency and damping can be set by controller settings determined from theoretical analysis. Natural frequencies ( $\tilde{f}_1 = 0.064, 0.16, \text{ and } 0.24$ ) which correspond to the range of frequencies for full size designs as discussed in Chap. 4.3 ( $f_1 = 1.6, 4, \text{ and } 6$  hz) are predicted, as are damping ratios of 0.2, 0.707, and 2.0. For all curves, the break point (intersection of high and low frequency asymptotes) is approximately equal to the suspension's natural frequency as shown in Figures 3.12 to 3.19. Lowering the damping ratio increases the gains of all variables in the region near the system's natural frequency.

The shapes of the gain-frequency curves is explained by considering high and low frequency inputs. At input frequencies low compared to the suspension's natural frequency, the magnet follows the rail closely so that the deviation from the nominal gap ( $\tilde{h}_1$ ) is small. At input frequencies greater than the natural frequency, the magnet is unable to respond to the rapidly changing inputs so that the magnet's position and velocity relative to a fixed reference is small (although the acceleration is significant) and the change in air gap is caused by the rail motion alone; thus,  $|\tilde{h}_1/\tilde{y}_0| = 1$ . The high and low frequency regimes are linked by a transition region which is influenced by the damping ratio. The relative displacement gain near the system's natural frequency, like the gains for the other variables, increases as the damping ratio decreases (Figs. 3.13 to 3.15).

Because of the rail's slow motion at low input frequencies and because the magnet responds as though it were locked to the rail, the gains for velocity and acceleration of the magnet are small for input frequencies lower than the suspension's natural frequency. At high frequencies, the absolute position and velocity of the magnet change little but the air gap is changing as described in the previous paragraph. The changing air gap is fed into the current controller (3.3). As the current changes, the force on the magnet and, hence, acceleration changes rapidly so that the acceleration has a constant gain asymptote at frequencies greater than the suspension's natural frequency as shown in Figure 3.12 through 3.16.

Since relative displacements and absolute velocity and acceleration are low, little force and hence, current, is needed at low input frequencies. At high input frequencies the current has a constant asymptote since velocity is insignificant compared to relative displacement in the current control law (3.3).

The voltage is ohmic and, therefore, proportional to the current at input frequencies lower than the suspension's natural frequency as shown in (3.4) and Figure 3.19. The voltage at high frequencies is needed primarily to overcome the inductance of the control coil. Since the inductive voltage is proportional to the derivative of current minus displacement (3.4) and since current and displacements have high frequency asymptotes which are constant the voltage asymptote at high input frequency is proportional to the input frequency.

The experimental scale model's agreement with the theoretical model provides a good confidence level in the use of the basic model for preliminary design purposes; however, differences exist between the theory and experiment. Factors which limit the accuracy of the analysis include:

(1) Experimental errors. The principal error source is the reading of the oscilloscope. Resolution of the scope is approximately 1 part in 30 because of the finite number of divisions on the scope. Since the gains are ratios of two different readings, accuracy to 1 part in 20 (assuming reading errors are uncorrelated) or 5% can be expected. These error values should not affect the conclusions of this chapter.

(2) Model limitations. Although measurements of the total flux were accurate to 5% at the nominal air gap (0.1 in), several voltage readings for the dynamic system are only accurate to 15% (Figure 3.19). At high frequency, the absolute velocity of the magnet is small compared to the relative displacement  $h$  so that  $di/dt$  is proportional to  $dh/dt$  by (3.3). The voltage at high frequency (3.4) is proportional to  $v_T(1 + \tilde{\omega}_1^2) - 1$ . With  $v_T = 1.7$  and  $\tilde{\omega}_1 = 1.0$ , an error of 5% causes a 9% error in voltage. With other errors such as experimental, the 15% error in voltage can be reached.

At high road input frequencies whose amplitude has zero mean, the non-linear suspension force characteristics of (3.1) requires that the nominal gap increase so that the time average acceleration is zero. The average current must increase to support the vehicle at the larger air gap. Additional dynamic tests were conducted to verify these non-linear

results. Figure 3.20 depicts the average displacement and Figure 3.21, the average current for  $\tilde{\omega}_1 = 1$  and  $\zeta = 0.707$  and input amplitude  $\tilde{y}_0 = 0.5$ . The theoretical lines are based on the non-linear analysis of Chapter 8. The scatter of data points is attributed to difficulty in reading the oscilloscope for the low amplitudes involved.

Measurements of flux penetration as frequency increases with the magnet and rail stationary appear in Figures 3.22 through 3.25. Figure 3.22 displays the ratio of the flux in the rail at frequency  $f$  [ $\phi_R(f)$ ] to the flux for zero input frequency [ $\phi_R(0)$ ]. In Figure 3.23, the phase lag ( $\theta_{3y}$ ) between the flux in the rail and the control current is plotted. Figure 3.24 shows the ratio of the fluxes in the magnet's yoke [ $\phi_T(f)/\phi_T(0)$ ] while Figure 3.25 presents the phase lag ( $\theta_{1y}$ ) between the flux in the magnet's yoke and the control current.

Each figure contains theoretical curves based on (3.6) and (3.7) and experimental data for air gaps of 0.05 and 0.10 inches. The conductivity of the rail is  $0.93 \times 10^7$  (ohm-m)<sup>-1</sup> and the magnet width ( $\lambda_M/2$ ) is 1.8 inches. For the theoretical curves, the permeability of magnet and rail were assumed to be 3500.

At low frequencies (less than 20 hz.), both the theoretical model and experimental data show for all cases that the flux at frequency  $f$  is equal to the static flux and that the phase lag between the flux and input current are less than one degree.

As frequency increases, the experimental and theoretical flux ratios roll off and both phase lags increase. Although both theoretical

$$\left| \frac{h_{1-av}^2}{y_0^2} \right|$$

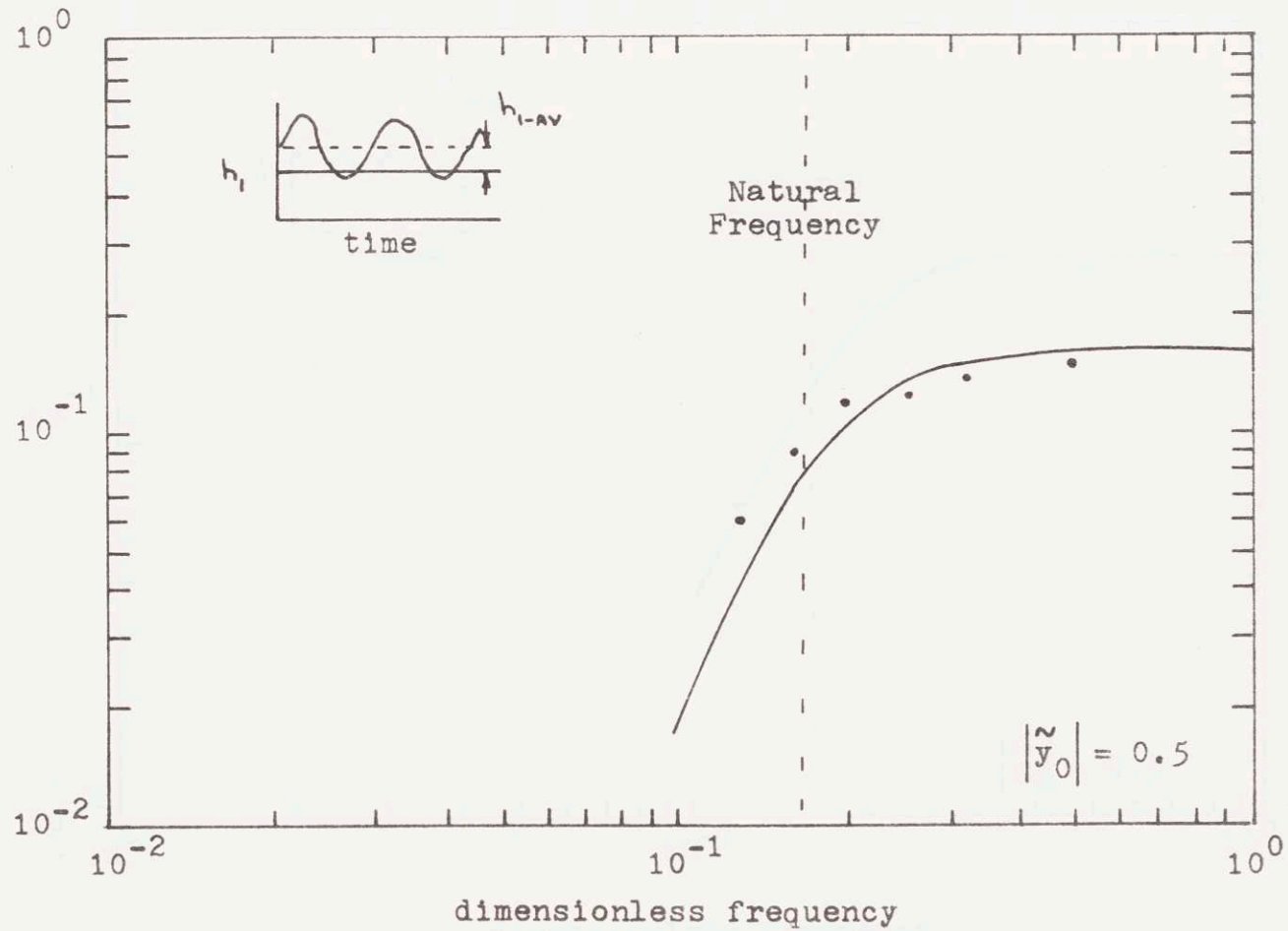


Fig. 3.20. Average Air Gap vs. Frequency  
 $\xi_1 = 1.0, \zeta_1 = 0.707$

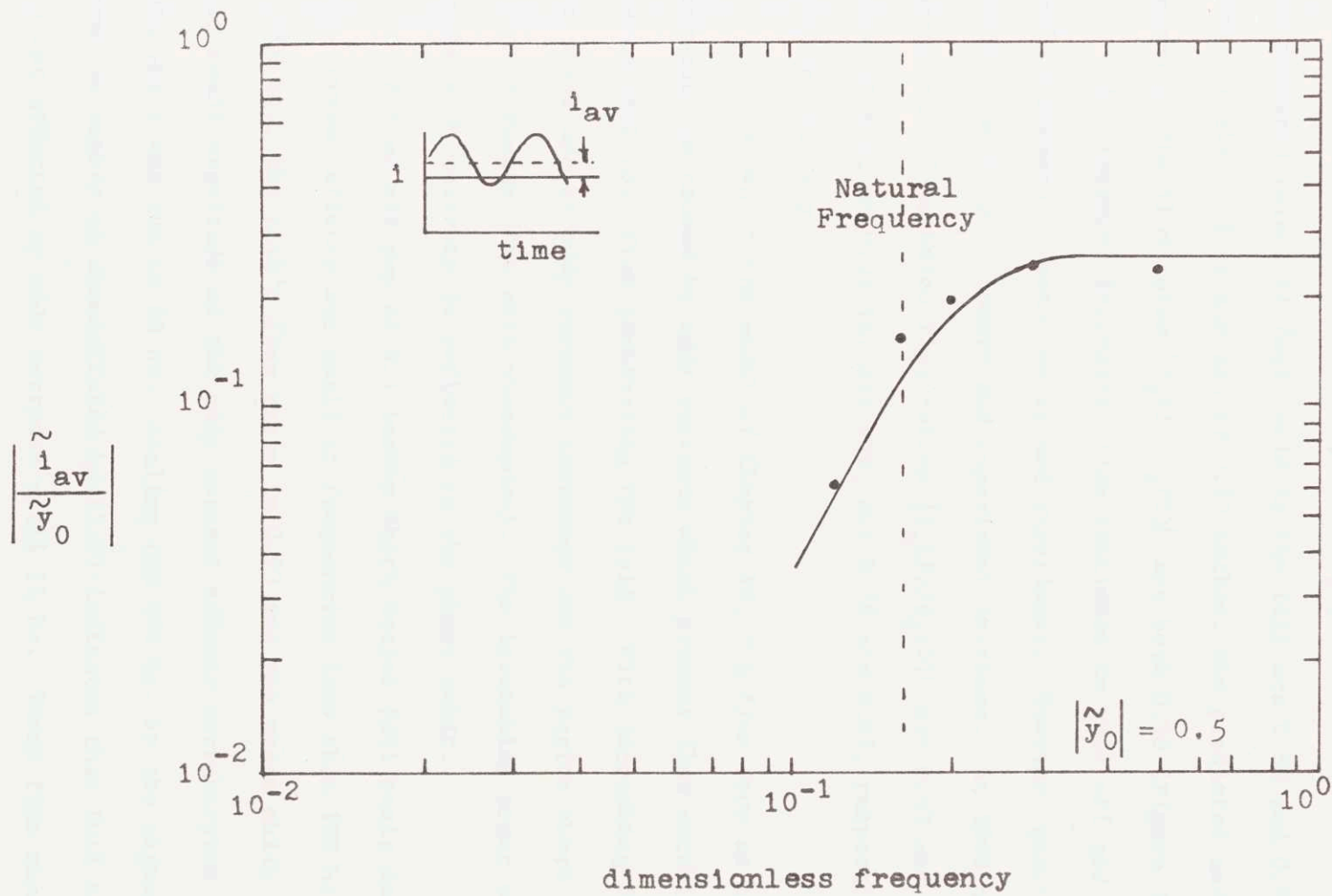


Fig. 3.21. Average Current vs. Frequency  
 $\xi_1 = 1.0, \zeta_1 = 0.707.$

and experimental curves have similar shape, quantitative differences appear. For example at 100 hz., at air gaps of 0.05 inches the predicted and measured values of flux ratio in the rail are 0.86 and 0.91, respectively, and at air gap of 0.10 inches, the predicted and measured values of the flux ratio  $|\phi_R(f)/\phi_R(0)|$  are both 0.93 (Figure 3.22).

As frequency increases, flux continues to roll off and phase shift increases in both theory and experiment. However, quantitative differences between theory and experiment increase. At 1000 hz., the predicted and measured flux ratios  $|\phi_R(f)/\phi_R(0)|$  are 0.63 and 0.61, respectively, at 0.05 in. air gap, and 0.78 and 0.67, respectively, at 0.10 in. air gap.

As shown by the model of Chapter 10, the flux drop at higher frequency is caused by eddy currents which prevent flux established by the control coil from penetrating the rail. With increasing frequency, the magnitude of eddy currents increases and the region where the eddies occur decreases (the skin phenomenon). The increasing power consumed by the eddy currents is reflected in the phase shift.

For an air gap of 0.1 inches which scales full scale designs, eddy current effects are small at frequencies less than 100 hz; for example, at 100 hz., the rail's flux ratio is 0.93 and the phase shift is 7°. This small magnitude of the eddy current effects corroborates the dynamic data which was run to 60 hz. Scaling the 100 hz. by the magnetic Reynolds number as demonstrated by (3.9) indicates that full scale systems are not affected by eddy currents until 11 hz. These flux measurements and the dynamic response to road inputs support the contention of Chapter

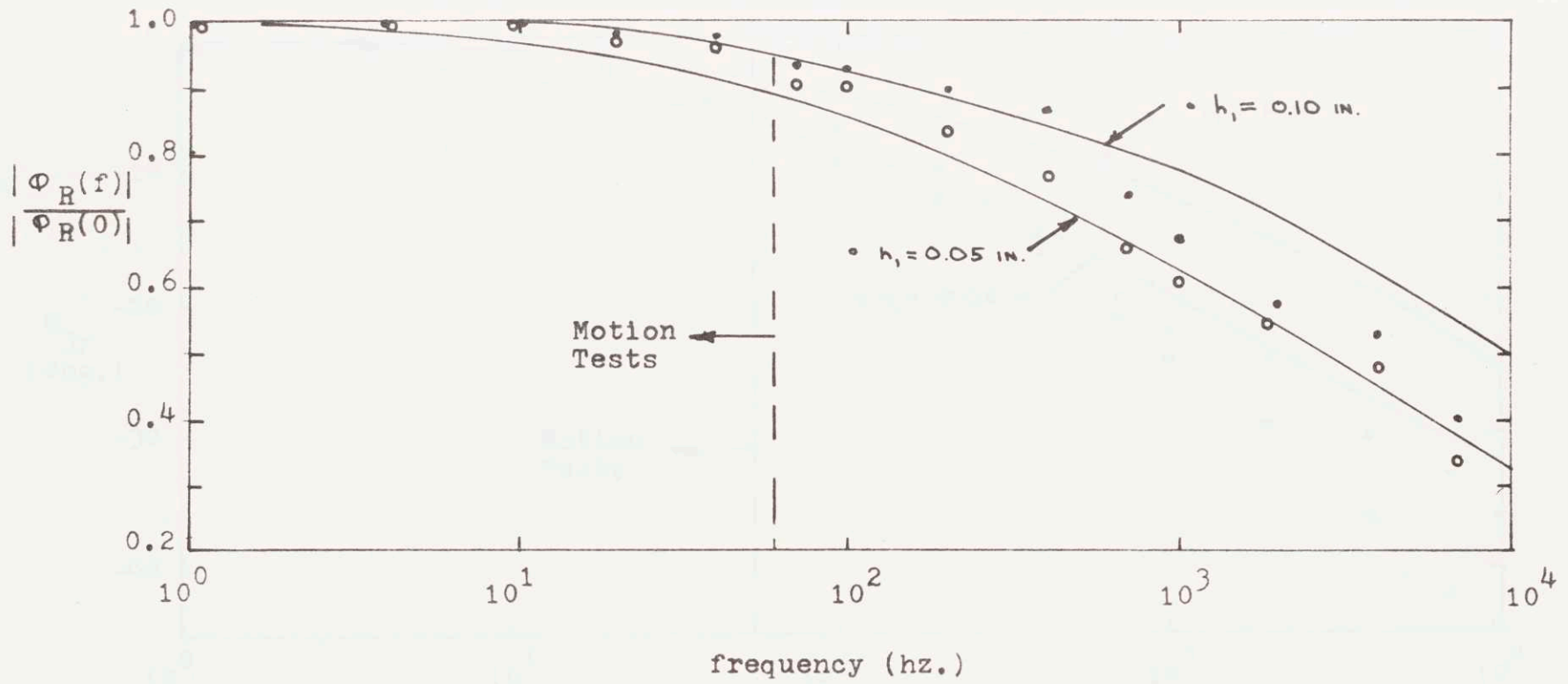


Fig. 3.22. Flux in Rail vs. Frequency

Fig. 3.21. Phase Angle vs. Frequency  
 Fig. 3.22. Flux in Rail vs. Frequency

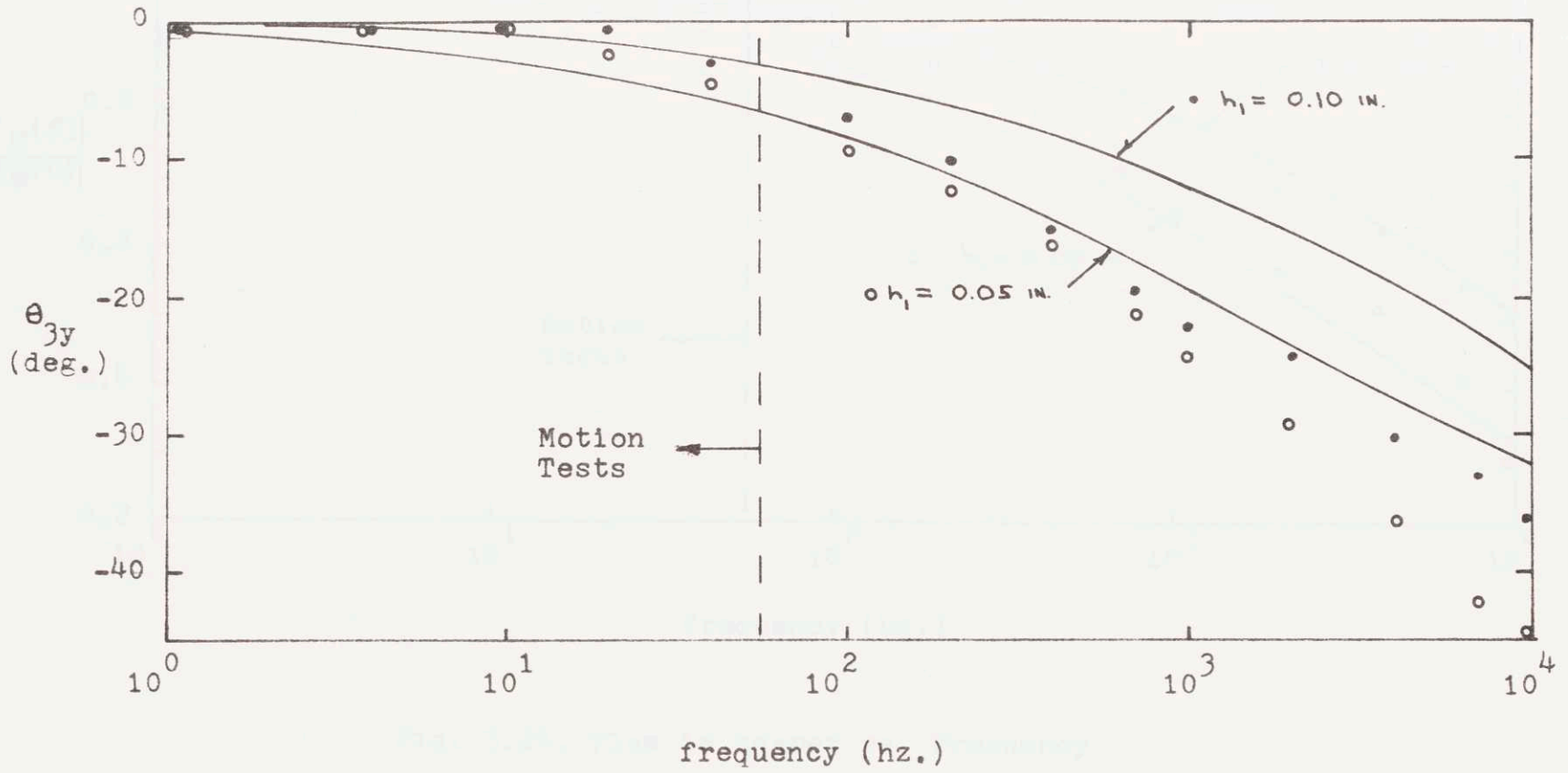


Fig. 3.23. Phase Angle between Flux in Rail and Current vs. Frequency

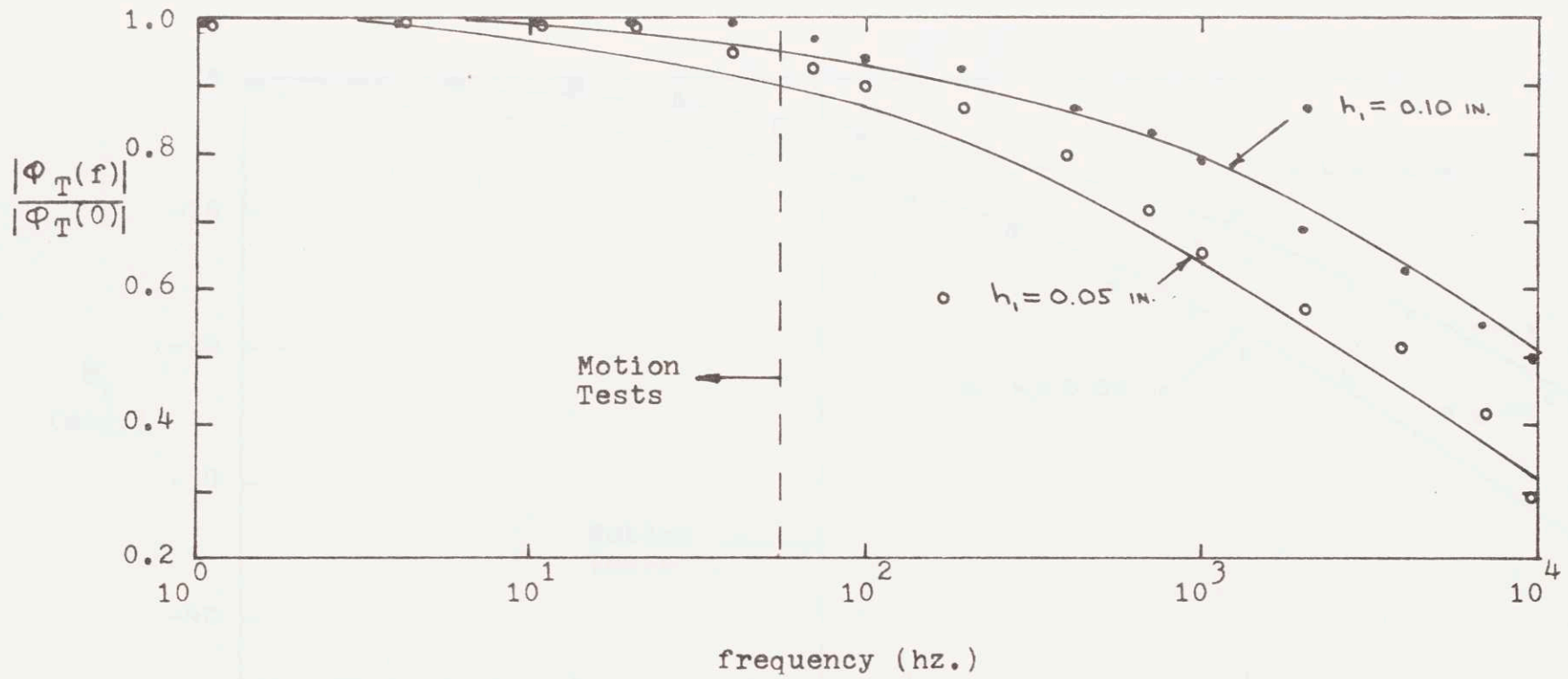


Fig. 3.24. Flux in Magnet vs. Frequency

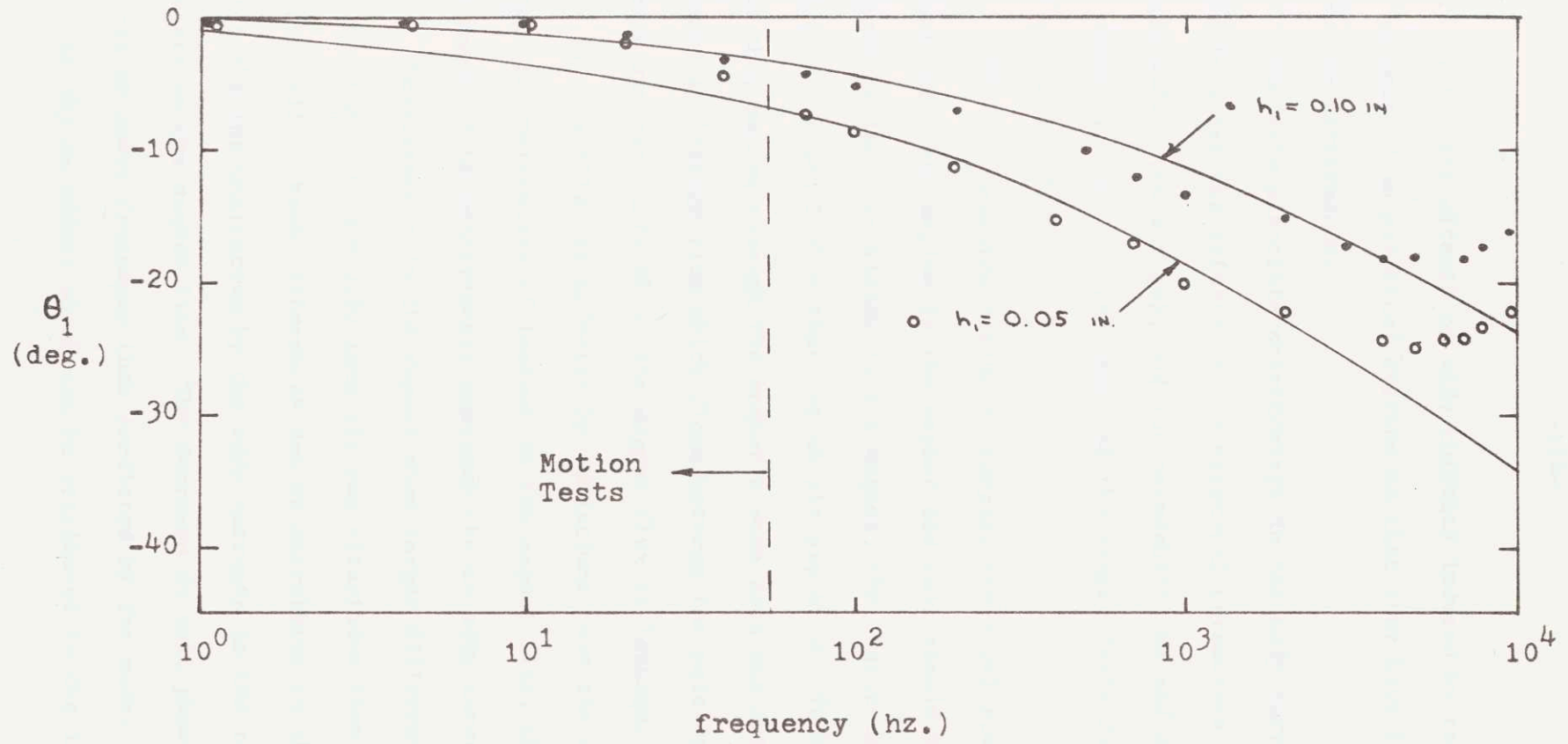


Fig. 3.25. Phase Angle between Flux in Magnet and Current vs. Frequency

2.3.5; i.e., the effects of eddy currents induced by the heave motion may be reduced in practical systems so that they have little influence on system performance.

The data pinpoints shortcomings in the eddy current model. The model includes the effects of the principal parameters such as the magnet width, the air gap, and the permeabilities and conductivities of the material; however, the shape of the magnet (pole face, window width) are not included.

For the measured frequency ranges, the model predicts that the fluxes and phase angles in the magnet and rail should be nearly identical. Because of the deep window in the magnet, the static considerations of Chapters 2.2 and 5 show that, at an air gap of 0.1 inches, 15% of the flux that passes through the magnet's yoke does not enter the rail but appears as leakage flux which flows between the pole cores. At 0.05 inches air gap, only 8% of the magnet flux is leakage. Since leakage flux is only slightly affected by conditions near the air gap, the larger the percentage of leakage in the magnet flux, the more closely should the magnet flux measurements approach the no eddy current situation.

Measurements in the magnet show larger differences (factor of 2) between the 0.05 and 0.10 inch air gap situations than do measurements in the rail. These differences can be attributed to the leakage flux which remains unaffected by the eddy currents in the rail but which appears in the magnet flux. The decrease in rail phase lag (Fig. 3.23) occurs at lower frequency than predicted by the model (Table 15 of Chapter 10) an effect which can be attributed to the leakage flux.

The model for eddy currents and flux penetration can be used to give approximate estimates of the frequencies at which eddy effects become important. Because the model neglects the details of the rail-magnet geometry, the model is not suited for calculations of high accuracy.

In summary, the test results indicate that the theoretical models for leakage coefficients, static forces, and heave motion (Eqs. 3.1 through 3.5) are suitable for preliminary design purposes since the experimental and theoretical results agree and since the model was scaled to represent full scale systems. The model for eddy currents can estimate approximately the frequency at which eddy current effects become important and can be improved by models which reflect geometry more accurately.

## 4. SUSPENSION DESIGN

### 4.1 Introduction

The use of the heave model for preliminary static and dynamic magnet design is illustrated. Design constraints and objectives for magnets and suspensions are developed to establish guidelines for:

- (1) Magnet configuration and ohmic power.
- (2) Rail requirements (material and road roughness).
- (3) Dynamic suspension performance.

### 4.2 Design of Magnets

#### 4.2.1 Static Considerations

The first step in suspension design is selection of the magnet rail geometry. The following design examples assume the configuration depicted in Figure 2.1 and discussed in Chapter 2.2. After the geometrical configuration is selected, materials and dimensions must be chosen. The factors which must be considered in these choices are:

- (1) the on-board weight of the magnets and coils;
- (2) the weight of the magnetic material in the rail  
and the rail dimensions;
- (3) the heating of the coils; and
- (4) dynamic performance and drag which are affected by  
parameters that depend on the rail-magnet geometry.

As discussed in Section 2.3.5, the effects of eddy currents induced by forward motion are restrained to acceptable limits by magnets whose length is of the order of thirty feet for 300 mph. Lower speeds require shorter magnets. Thus, magnet lengths of 10, 20, and 30 feet, are used in the following sample designs of Chapter 4.3 and should be realistic for actual vehicles. The sample designs are selected so that the eddy currents induced by the heave motion do not affect the suspension dynamics.

First the maximum required lift force is considered. Since a vehicle can only move one nominal gap up before it contacts the rail, it is assumed that the magnet can only move one nominal gap downward, a restraint which can be enforced by the mechanical stops mentioned in Chapter 1.2. Therefore, the magnets are designed so that they can lift the vehicle when the gap is  $2h_{10}$  (with an allowance for error or control force if desired). For long, thin magnets, (2.2) provides a good estimate of total flux independent of the magnet's length. Thus, the nominal useful flux density ( $B_{uo}$ ) necessary to lift the weight of the vehicle is:

$$B_{uo} = \frac{B_{SATC}}{v_T \Big|_{h_1=2h_{10}}} e \quad (4.1)$$

where

$B_{SATC}$  = the flux density at which the core saturates

$e$  = a safety factor

$v_T$  = total flux coefficient which depends on magnet geometry (Chapter 5)

The total flux consists of useful flux which provides lift and leakage and fringing fluxes which contribute no lift and increase relative to the useful flux as the gap increases. Leakage and fringing greatly reduce  $B_{uo}$  and, hence, magnet lift since  $v_T$  is usually about 2. Since the yoke and pole face area are the same, no area correction appears in (4.1).

Equation (4.1) determines the region of stability of the system. For  $e=1$ , if the gap should become larger than  $2h_{10}$ , the magnet cannot lift the vehicle toward the rail because of flux saturation in the magnet. At a large enough air gap, the saturation minus the leakage and fringing fluxes leaves insufficient flux to support the vehicle's weight so that the vehicle must drop unless restraints are present.

For a given  $B_{uo}$ , the total magnet lift surface area required is:

$$n l_1 l_p = \frac{2mg \mu_o}{B_{uo}^2} \quad (4.2)$$

where

$n$  = number of magnets

$mg$  = total vehicle weight

Four lift magnets ( $n=4$ ) and magnet lengths of 10, 20, and 30 feet are considered in the sample designs of Chapter 4.3.

The magnet's amp turns are determined from  $B_{uo}$  as:

$$Ni_o = \frac{2h_{10} B_{uo}}{\mu_o} \quad (4.3)$$

The weight of one of the four magnetic cores on a vehicle is:

$$W_{\text{core}} = \rho_{\text{core}} l_1 (w_1 l_p + 2 l_p [2l_p + w_3]) \quad (4.4)$$

where  $\rho_{\text{core}}$  is the density of the core material. The weight of the coils in one magnet is:

$$W_{\text{coil}} = \rho_{\text{coil}} l_{\text{core}} A_{\text{coil}} \quad (4.5)$$

where

$\rho_{\text{coil}}$  = density of the coil and the weight of the insulation is neglected.

For dynamic purposes and to minimize the weight of the magnetic iron in the structure, it is desirable to make the rail thickness ( $t_{\text{rail}}$ ) as small as possible; therefore,  $t_{\text{rail}}$  is designed so that the rail saturates at the same time that the magnet saturates. From continuity of flux across the air gap:

$$t_{\text{rail}} = \left[ \frac{v_{\partial}}{v_T} \right]_{h_1 = 2h_{10}} \frac{B_{\text{SATC}}}{B_{\text{SATR}}} l_p \quad (4.6)$$

where

$B_{\text{SATR}}$  = saturation flux density of rail

The width of the magnet ( $\lambda_M/2$ ) which is used in the calculation of the eddy currents induced by the vertical motion is:

$$\lambda_M/2 = 2 l_p + w_1 \quad (4.7)$$

To estimate the heating, the simple model of Figure 4.1 is used. With proper design, the coil and the core are in good thermal contact and there is no temperature gradient in the coil-core structure. The static thermal balance at the nominal position is then:

$$q = i_o^2 R_1 = k A_{dis} \Delta T \quad (4.8)$$

where

$R_1$  = resistance of the coil

$i_o$  = nominal current in one magnet

$k$  = heat dissipation coefficient across the air-solid interface

$A_{dis}$  = area in contact with air

$\Delta T$  = temperature difference between magnet which is modeled as isothermal and ambient air

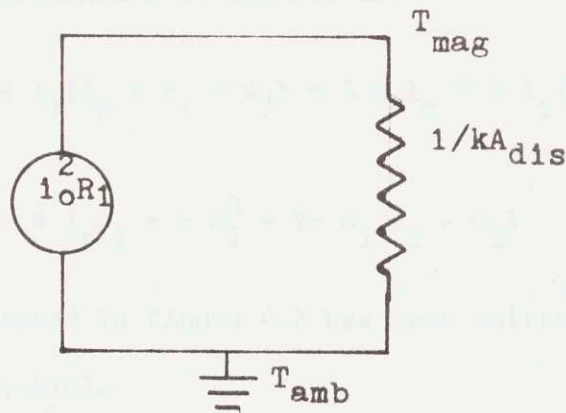


Figure 4.1 Electric circuit analog for magnet heating by ohmic losses in coil.

The resistance of the coil, in terms of the notation in Figure 2.1, is:

$$R_1 = \frac{r_c l_{\text{coil}} N^2}{A_{\text{coil}}} \quad (4.9)$$

where

$$l_{\text{coil}} = \text{mean length of one turn} = 2(l_1 + l_p + \frac{\pi w_1}{4})$$

$$A_{\text{coil}} = \text{area available for windings} = f w_1 (w_3 - w_2)$$

where the packing factor  $f$  accounts for the fact that wires cannot completely fill the volume allotted because of insulation and shape.

$r_c$  = the resistivity of the coil, which is a function of temperature. In the design examples, the resistance at the design temperature is used. Note that for fixed geometry, the heating  $q$  is proportional to  $(Ni_o)^2$

The area for heat dissipation to the air is:

$$A_{\text{dis}} = 4 l_1 (l_p + w_1 + w_3) + 4 w_3 l_p + 2 l_p (2 l_p + w_1) + 4 l_p w_1 + \pi w_1^2 + 2\pi w_1 (w_3 - w_2) \quad (4.10)$$

where the area indicated in Figure 4.2 has been omitted since the magnets must attach to the vehicle.

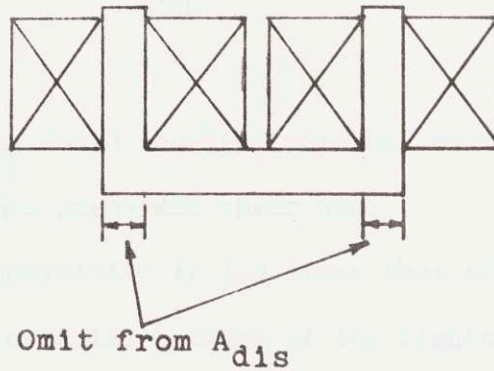


Figure 4.2 Calculation of  $A_{dis}$ . Areas shown do not contact air since magnet must be fastended to vehicle.

The relations (4.1 through 4.10) form the basis for the sample magnet designs (Table 4) and parametric curves of this section. The selection of materials and other parameters which are fixed for the sample designs are discussed below and summarized in Table 3.

The vehicle is assumed to weigh 88,000 lbf. (a figure often used for passenger vehicles) and to be 100 ft. long, 10 ft. wide and 10 ft. high.

2V permendur was selected for the magnet material because of its high saturation flux density (2.3 tesla compared to 1.6 for conventional magnet materials) which allows a reduction in on-board suspension weight compared to conventional materials.

Silicon steel was selected for the rails because of its relatively high resistivity (an important parameter in the dynamic analysis) and its low cost. Because of their high resistivities (several orders of magnitude greater than metals), ceramic ferrites were considered for a rail material. Although their structural brittleness might have been overcome by proper design, their low saturation flux densities (approx-

mately 0.5 tesla) which would require increased on-board weight and their costly manufacture precluded their use.

Although its resistivity is 1.5 times that of copper, aluminum was selected for the coil material because of its lighter density (.10 to .32 lbm/ft) which allows a 1-2 thousand pound reduction in coil and core weight with negligible power loss for the design cases.

The coil's packing factor is assumed to be 0.7 which is reasonable for carefully wound coils.

The distance  $w_2$  is 0.2 inches to allow clearance for a protective cover.

The maximum temperature rise is limited to 140°C which is within the range of insulations available today. If higher temperature rises are allowed (for example, higher temperature insulation is used), the area needed for heat dissipation can be made smaller so that the on-board weight will decrease; however, the ohmic power will increase, because the coil window shrinks as the magnet becomes smaller.

The heat transfer coefficient ( $k = 0.009 \text{ watts}/^\circ\text{C-in}^2$ ) was obtained from [50] for air that is not moving relative to the magnets. With forced convection (from vehicle motion or fans), the heat transfer coefficient can be increased by as much as an order of magnitude. The area needed for heat dissipation can then be made smaller so that the on-board weight will decrease but the ohmic power will increase.

To develop a static design, the nominal gap ( $h_{10}$ ), the width of the pole face ( $l_p$ ), and the width of the coil window ( $w_1$ ) are selected first. The height of the coil window is then iterated until the tempera-

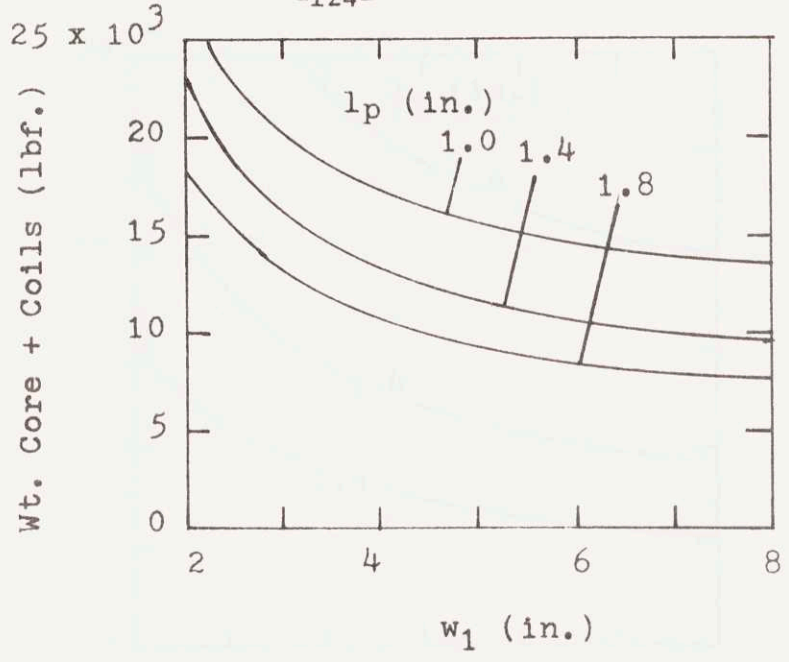


Fig. 4.3. Weight of Magnets and Coils vs.  $l_p$  and  $w_1$

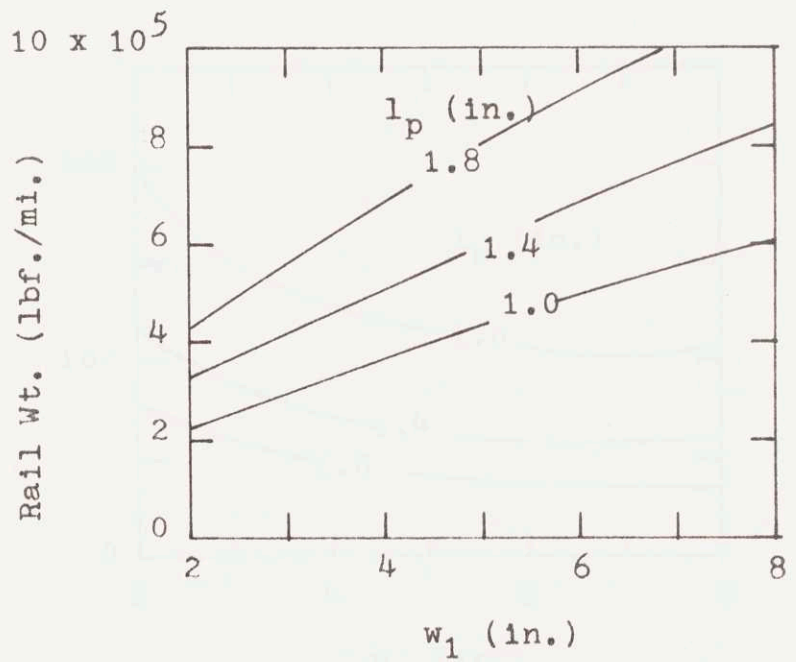


Fig. 4.4. Rail Weight vs.  $l_p$  and  $w_1$

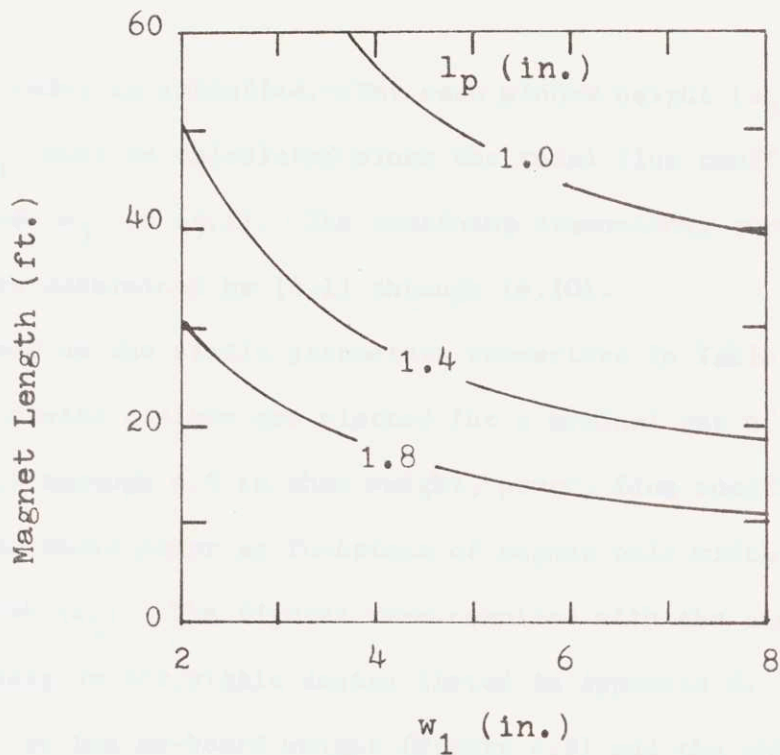


Fig. 4.5. Magnet Length vs.  $l_p$  and  $w_1$

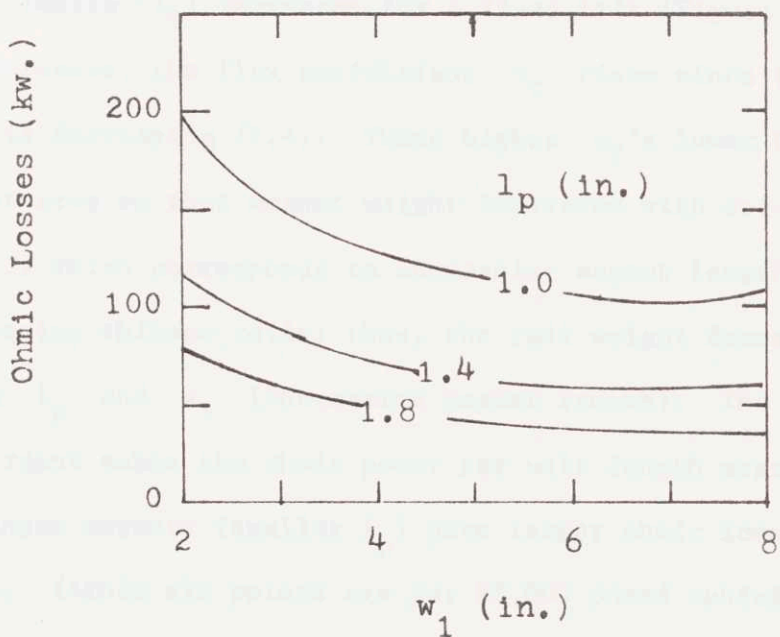


Fig. 4.6. Ohmic Losses in Coil vs.  $l_p$  and  $w_1$

ture constraint is satisfied. For each window height ( $w_3$ ), a new magnet length ( $l_1$ ) must be calculated since the total flux coefficient is a function of  $w_3$  in (4.1). The remaining dimensions, currents, and weights are determined by (4.1) through (4.10).

Based on the static parameters summarized in Table 3, parametric curves of static designs are plotted for a nominal gap of 0.6 in. in Figures 4.3 through 4.6 to show weight, power, flux coefficients, magnet length, and ohmic power as functions of magnet pole width ( $l_p$ ) and window width ( $w_1$ ). The figures were compiled with the aid of the computer program for static design listed in Appendix 6. The figures show that, as the on-board weight (Figure 4.3) and the ohmic power decrease (Figure 4.6), the weight of the magnetic material in the rail increases (Figure 4.4).

Since lift depends on pole area, as the pole width  $l_p$  decreases, the magnet length ( $l_1$ ) increases for a fixed lift (Figure 4.6); however, as  $l_p$  decreases, the flux coefficient  $v_T$  rises since the useful permeance is decreasing (2.4). These higher  $v_T$ 's lower the lift per unit magnet area so that magnet weight increases with decreasing  $l_p$  (Figure 4.3) which corresponds to increasing magnet length. Thinner magnets require thinner rails; thus, the rail weight decreases with decreasing  $l_p$  and  $w_1$  (increasing magnet length). The temperature rise constraint makes the ohmic power per unit length nearly constant so that longer magnets (smaller  $l_p$ ) have larger ohmic losses as shown in Figure 4.6. (Since all points are for 88,000 pound vehicle, the ohmic power is proportional to the power per pound.)

Magnet designs with smaller air gaps reduce the current needed for lift and the associated heating problems which allow the on-board weight and ohmic heating to decrease. Decreasing the air gap decreases the flux coefficient so that higher magnetic fields can be used and magnet weight is reduced further.

#### 4.2.2 Dynamic Considerations

The magnet-rail design determines the nominal air gap which defines limits on heave motion and influences eddy current effects. As discussed in Chapter 4.2.1, the effects of eddy currents induced by forward motion are reflected in the long magnets (10, 20, and 30 ft.) which are used in the sample designs. The effects of eddy currents induced by vertical motion may be eliminated by proper magnet design.

With rail design selected, the heave performance is evaluated from the spectral densities and the root mean square of the output variables. The input to the spectral density of an output variable is [55, 60]

$$\phi_{00}(s) = G(s) G(-s) \phi_{II}(s) \quad (4.11)$$

where  $\phi_{00}$ ,  $\phi_{II}$  are the spectral densities of the output and input variables, respectively.

$G(s)$  relates the input to the output. The root mean square is determined from:

$$[\text{RMS } 0]^2 = \frac{1}{j} \int_{-j\infty}^{+j\infty} \phi_{00}(s) ds \quad (4.12)$$

For example for the point contact suspension whose transfer function is (2.16) and for the road input (2.8) the acceleration spectral density is:

$$\phi_{\ddot{y}_1 \ddot{y}_1}(s) = + \omega_1^4 AV \frac{s}{s^2 + 2\zeta_1 \omega_1 s + \omega_1^2} \frac{-s}{s^2 - 2\zeta_1 \omega_1 s + \omega_1^2}$$

and the root mean square acceleration is ([55] tabulates formulae when  $G(s)$  is the ratio of polynomials):

$$[\text{RMS } \ddot{y}_1]^2 = \frac{\pi AV \omega_1^3}{2\zeta_1}$$

Note that for all the rms values considered in this thesis,  $\text{rms} \propto A^{1/2}$  while  $\text{rms} \propto V^{1/2}$  only for point contact models because of the finite magnet length filter.

The heave performance is determined from the model described in Chapters 2.2 and 2.3 and summarized by the transfer functions (9.1) through (9.5).

In the dynamic design the following constraints must be considered:

(1) Passenger comfort standards based on spectral density and root mean square of acceleration are used. The U.S. Department of Transportation has defined comfort by acceleration spectral density (Figure 4.16 is an example). For a vehicle's ride to be acceptable, the spectral density averaged over a one cycle bandwidth centered at integer frequencies must lie below the specification. For preliminary comparisons in this thesis, the rms acceleration is used while the spectral density is used for more detailed work.

(2) Relative displacement must be limited so that magnet-rail contact is held to acceptable limits; therefore, in this thesis the constraint

$$\text{RMS } \Delta h_{1-p}/h_{10} \leq \frac{1}{3}$$

is used. Since the road input is Gaussian [44,46], the probability of contact is 0.25%. This design goal is arbitrary since the effects of vehicle rail contact are unknown.

(3) Since downward acceleration is limited by gravity, the acceleration for the unsprung mass which is determined by linearized analysis must be limited. In this thesis, the constraint

$$\text{RMS } \ddot{y}_1 < g/3$$

is used. Since the road input is Gaussian [44,46], the probability of the unsprung mass acceleration's exceeding  $1g$  is 0.25%

(4) The control current  $\Delta i$  must be limited. Since the magnet's force is proportional to the current squared, currents less than zero seriously alter the system's dynamic characteristics. To prevent negative currents which effectively causes positive feedback, a limiter is built into the controller so that currents are always non-negative. In the linearized analysis, when  $i_o + \Delta i < 0$ , the system expects the force to decrease as  $\Delta i$  becomes more negative. The controller will not permit this decrease in force so that the system's performance as predicted by the linearized model will differ greatly from that of a non-linear

system. Therefore, the following constraint is used in this thesis:

$$\text{RMS } \Delta i / i_o < \frac{1}{3}$$

Thus, the probability of  $i_o + \Delta i$  being negative is 0.25%.

(5) The relative displacement between the sprung and unsprung masses must be limited to practical magnitudes consistent with the vehicle geometry. The following constraint is used in this thesis:

$$\text{RMS } \Delta h_2 < 0.6 \text{ in.}$$

#### 4.2.3 Summary of Design Procedures

Sample designs have been developed to satisfy the static and dynamic design constraints discussed in Chapters 4.2.1 and 4.2.2 which are summarized in Table 3. The examples were developed as follows:

- (1) Select a nominal air gap ( $h_{10}$ ).
- (2) Search for a static design by the procedure described in Chapter 4.2.1.

Magnet designs are selected with consideration of magnet dimensions, on-board vehicle weight, ohmic heating, and rail dimensions and weight as discussed in Chapter 4.2.1. This thesis employs the rail magnet configuration depicted in Figure 2.1 where the width of the rail's pole face ( $l_2$ ) is equal to the magnet pole width ( $l_p$ ) plus twice the nominal air gap ( $h_{10}$ ) as discussed in Chapter 2.2.

The air gap between the magnet and rail, the magnet's length, and the ratio ( $\gamma$ ) of magnet weight to the weight of the unsprung mass are used in the dynamic suspension design.

(3) Select a forward velocity ( $V$ ).

(4) Choose a suspension configuration and control law for reasons discussed in Chapter 2.3. This work uses the current control law (2.22) and either the basic magnetic suspension or the basic suspension with the passive secondary suspension.

(5) Determine the suspension parameters so that the road roughness ( $A$ ) is maximized subject to the design constraints of Section 4.2. If the basic magnetic suspension is the selected configuration, only the natural frequency ( $f_1$ ) and damping ratio ( $\zeta_1$ ) of the control law must be selected. If the passive secondary is chosen, the natural frequency ( $f_2$ ) and the damping ratio ( $\zeta_2$ ) of the secondary suspension must be determined also. The techniques used for determining the parameters are discussed in Section 4.2.2. Guidelines and selections of parameters are illustrated in Section 4.3.

(6) If the design is unacceptable, return to the appropriate step and iterate.

#### 4.3 Design Examples

To illustrate the use of the models and the design procedures, preliminary designs are selected first to demonstrate the influence of static and dynamic design parameters and then final designs are selected to show the capabilities of magnetic suspensions.

Sample magnet designs based on the static constraints and parameters of Table 3 are compiled in Table 4. Magnet lengths of 10, 20, and 30 feet are selected to represent the range of possible magnet lengths demanded

Table 3

PARAMETERS AND CONSTRAINTS ON SYSTEM DESIGN

STATIC CONSIDERATIONS

Total Vehicle Weight	88,000 lb.
Magnet: 2V Permendur	$\rho = .28 \text{ lbm/in}^3$
	$B_{\text{SAT}} = 2.3 \text{ T}$
Coils: Aluminum	$\rho = .10 \text{ lbm/in}^3$
	$r(140^\circ\text{C}) = 1.6 \text{ } \mu\text{-ohm-in}$
Rail: 1.75% Si Steel	$\rho = .27 \text{ lbm/in}^3$
	$(20^\circ\text{C}) = 16 \text{ } \mu\text{-ohm-in}$
	$B_{\text{SAT}} = 1.6 \text{ T}$
$\Delta T_{\text{max}}$ Coil and Core	$140^\circ\text{C}$
$k(140^\circ\text{C}, \text{ stationary coil})$	$0.009 \text{ watts}/(^\circ\text{C-in}^2)$
$e(\text{ safety factor})$	1.0
$w_2$ (pole face-coil clearance)	0.2 in

DYNAMIC CONSIDERATIONS

Unsprung Mass Acceleration	$\text{rms } \ddot{y}_1 < g/3$
Passenger Acceleration	DOT specs
Displacements:	
Air Gap	$\text{rms } \Delta h_1 < \frac{h_{10}}{3}$
Secondary Suspension	$\text{rms } \Delta h_2 < 0.6 \text{ in}$
Control Current	$\text{rms } \Delta i < i_o/3$

Table 4

		SAMPLE DESIGNS (BASED ON TABLE 3)			
DESIGN		1	2	3	4
MAGNET:	$h_{10}$ (in)	0.4	0.6	0.6	0.6
	$l_1$ (ft)	30	30	20	10
	$l_p$ (in)	1.0	1.38	1.54	2.12
	$w_1$ (in)	4.0	3.8	5.0	5.2
	$w_3$ (in)	3.8	5.3	5.1	6.0
	$\lambda_M/2$ (in)	6.0	6.6	8.1	9.5
	Wt. Core + Coil (lbf)	8,800	13,600	10,800	8,300
	Ohmic Power (kw)	63	77	55	34
Rail	$l_2$ (in)	2.2	2.58	2.74	3.32
	$l_3$ (in)	5.7	6.0	7.6	8.7
	$t_{\text{rail}}$ (in)	1.1	1.4	1.8	2.4
	Weight (lbf/mi)	$0.31 \times 10^6$	$0.42 \times 10^6$	$0.66 \times 10^6$	$1.0 \times 10^6$
FLUX LEAKAGE	$v_T$	2.11	2.38	2.10	1.83
COEFFICIENT	$v_\partial$	1.77	1.83	1.75	1.54

by consideration of eddy currents induced by forward motion. Air gaps of 0.4 and 0.6 inches are selected for the examples. The magnet lengths, requiring as much as thirty feet, could present problems in negotiating curves; however, magnets with flexible joints might eliminate this dilemma.

The magnet designs of Table 4 have been designed so that the effects of eddy currents induced by vertical motion are small. Section 2.3.5 shows that for magnet widths less than 10 inches, eddy currents induced by vertical motion scarcely affect the penetration of flux into the rail and the heave dynamics. For example, with design 4, which has a magnet width of 10 inches and air gap of 0.6 inches, the ratio of flux entering the rail at frequency of 10 hz. compared to the flux at static conditions is 0.94 and the phase lag between the flux and the control current is only 4 degrees as shown in Section 2.3.5.

As noted in Table 4, with increasing magnet length, the magnet's weight and the ohmic heating increase. At 0.6 inches, the total magnet weight and ohmic heating for the 88,000 lb vehicle is 8,300 lb. and 34 kw., respectively, for 10 foot magnets and 13,600 lb. and 77 kw., respectively, for 30 foot magnets. The reasons for this are discussed in Section 4.2.1.

Designs 1 and 2 demonstrate that decreasing the air gap reduces the current needed for lift and the associated heating problems which allow the on-board weight and ohmic heating to decrease. For 30 foot magnets, the on-board weight and ohmic power at 0.6 inch air gap is 13,600 lb and 77 kw. compared with 8,300 lb. and 66 kw. at 0.4 inch air gap. The ohmic heating is small compared to the wind drag (approximately 3000 kw. at 300 mph from Appendix 1).

Lengthening and thinning the magnets and reducing the air gap saves track weight. For 10 foot magnets at 0.6 inch air gap (design 4), the track weight is  $1 \times 10^6$  lbm/mile. For 30 foot magnets at 0.6 inch air gap (design 2), the track weight is reduced to  $0.42 \times 10^6$  lbm/mile. By reducing the air gap to 0.4 inch, the track weight for a 30 foot design (design 1) is  $0.31 \times 10^6$  lbm/mile.

From the discussion of magnet length and air gap important trade-offs are evident. As the magnet is lengthened, on-board weight increases while road material decreases; thus, the initial guideway cost is weighed against additional revenues. Decreasing the air gap, reduces the on-board weight, but requires closer track tolerance (as discussed in the design examples which follow); thus, maintenance and initial costs must be weighed against possible additional revenue.

Having selected the static design parameters, the designer must choose the suspension's dynamic characteristics and the control law (step 4 of the design procedure, Section 4.2.3). The design examples use the current control law (2.22) and compare two basic configurations -- the electromagnetic suspension alone and the electromagnetic suspension with a passive secondary suspension (Section 2.3).

The final designs are selected to maximize road roughness while maintaining ride quality at the DOT standard. The designs also could have been accomplished by assuming a road roughness and then seeking to optimize ride quality. When the suspension is improved, the vehicle can traverse rougher roads (larger A) with satisfactory ride quality or the vehicle can follow roads of the same roughness with improved ride comfort.

Before presenting final designs, the effects of parametric variations in the natural frequency and damping ratio of the primary and secondary suspensions are presented.

Tables 5 and 6 and their associated acceleration spectra (Figures 4.7 and 4.8) demonstrate the performance of the basic primary suspension without secondary suspension for selected natural frequency ( $f_1$ ) and damping ratio ( $\zeta_1$ ) which are determined by the control settings. Since the system does not have a secondary suspension, the acceleration of the magnet ( $\ddot{y}_1$ ) corresponds to the acceleration of the passenger compartment ( $\ddot{y}_2$ ). The sample designs were developed with the computer program described in Appendix 6.

The natural frequencies for the system, approximately 1.6 hz, are selected to achieve ride comfort without secondary suspension. Table 5 shows that, as the natural frequency increases, acceleration increases while the clearance decreases. The damping ratio has an optimum setting near 0.7 for which the acceleration spectral density, the rms clearance, and the rms current satisfy the dynamic constraints.

In Tables 7 through 10, the suspension characteristics of a magnetic suspension with primary mass and passive secondary suspension are varied. With the system with secondary suspension, unsprung mass natural frequencies higher than those of the basic suspension without secondary suspension are used to improve the magnet's tracking of the guideway. Ride comfort is achieved by the soft secondary suspension. Increasing the primary suspension's natural frequency decreases the clearance ( $\Delta h_1$ ) but increases the acceleration of the unsprung mass and that of the sprung mass, particularly at higher frequencies (Table 7 and Figure 4.9).

Table 5

EFFECTS OF  $f_1$  IN BASIC SUSPENSION

STATIC DESIGN 2,  $h_{10} = .6$   $l_1 = 30$  ft,  $\gamma = 0$

$A = 2\pi \times 10^{-7}$ ,  $V = 300$  mph

$\zeta = 0.71$ ,  $\ddot{y}_1$  S.D. in Fig. 4.7

$f_1$	RMS $\ddot{y}_1$ (G's)	RMS $\Delta h_{1-p}/h_{10}$	RMS $\Delta i/i_o$	RMS ( $v_{ind}^2 4i_o$ ) (kw)
1.0	.011	.33	.34	50
1.6	.021	.27	.26	52
2.2	.032	.23	.22	56

Table 6

EFFECTS OF  $\zeta_1$  IN BASIC SUSPENSION

STATIC DESIGN 2,  $h_{10} = .6$  in,  $l_1 = 30$  ft,  $\gamma = 0$

$A = 2\pi \times 10^{-7}$  ft,  $V = 300$  mph

$f_1 = 1.6$  hz,  $\ddot{y}_1$  S.D. in Fig. 4.8

$\zeta_1$	RMS $\ddot{y}_1$ (G's)	RMS $\Delta h_{1-p}/h_{10}$	RMS $\Delta i/i_o$	RMS ( $v_{ind}^2 4i_o$ ) (kw)
.4	.030	.26	.26	57
.71	.021	.27	.26	52
1.2	.015	.30	.30	49

Lowering the damping of the primary (Table 8 and Figure 4.10) which is effected by the control, raises the acceleration of the unsprung mass and that of the sprung mass at frequencies near the natural frequency of the unsprung mass. Current and clearance are affected little. As in the system without secondary suspension, the primary suspension has an optimum damping ratio (which is set by the current controller) of 0.707.

Table 9 shows that softening the secondary suspension decreases the acceleration and improves ride quality greatly. (Figure 4.11 shows that decreasing  $f_2$  from 1.0 to 0.5 hz. decreases the rms spectral density by a factor of 2) while the air gap displacement and current also decrease and the acceleration of the primary and the displacement of the secondary suspension increase. As the secondary is softened, the coupling between the primary and secondary decreases so the primary suspension acts as though it were stiffer (i.e., higher  $f_1$ ). Although soft secondary suspensions are advantageous, to date practical considerations (such as external loading and the steady state forces required to support the vehicle's mass) have limited passive secondaries to natural frequencies greater than 1 hz., the value used in the sample designs.

Table 10 shows that raising the damping of the secondary suspension decreases the secondary's acceleration spectra at the secondary natural frequency and increases the spectra at higher frequencies (Table 10 and Figure 4.12). Thus,  $\zeta_2 = 0.25$  is an optimum for spring dashpot secondaries with respect to minimum acceleration. The optimum damping ratio ( $\zeta_2 = 0.25$ ) for the spring dashpot in parallel differs from that ( $\zeta_1 = 0.707$ ) of the

Table 7

EFFECT OF UNSPRUNG MASS NATURAL FREQUENCY ( $f_1$ )

## WITH SECONDARY SUSPENSION

STATIC DESIGN 2,  $h_{10} = .6$  in,  $l_1 = 30$  ft,  $\gamma = 5^*$

$A = 2\pi \times 10^{-7}$  ft,  $V = 300$  mph

$\zeta_1 = .71$ ,  $f_2 = 1$  hz,  $\zeta_2 = .25$ ,  $\ddot{y}_2$  S.D. in Fig. 4.9

$f_1$ (hz)	RMS $\ddot{y}_1$ (G's)	RMS $\ddot{y}_2$ (G's)	RMS $\Delta h_{1-p}/h_{10}$	RMS $\Delta i/i_o$	RMS $\Delta h_2$ (in) <sup>2</sup>	RMS ( $v_{ind} 4i_o$ ) (kw)
2.5	.024	.014	.29	.28	.12	51
5.0	.061	.021	.17	.16	.17	46
7.5	.093	.024	.13	.11	.18	45

\* In this thesis, the unsprung mass is primarily magnet. Including propulsion units in unsprung mass would decrease  $\gamma$ .

Table 8

EFFECTS OF PRIMARY DAMPING RATIO ( $\zeta_1$ ) WITH  
SECONDARY SUSPENSION

STATIC DESIGN 2,  $h_{10} = 0.6$  in,  $l_1 = 30$  ft,  $\gamma = 5$

$A = 2\pi \times 10^{-7}$  ft,  $V = 300$  mph

$f_1 = 5$  hz,  $f_2 = 1$  hz,  $\zeta_2 = .25$ ,  $\ddot{y}_2$  S.D. in Fig. 4.10

$\zeta_1$	RMS $\ddot{y}_1$ (G's)	RMS $\ddot{y}_2$ (G's)	RMS $\Delta h_{1p}/h_{10}$	RMS $\Delta i/i_o$	RMS $\Delta h_2$ (in)	RMS ( $v_{ind} 4i_o$ ) (kw)
.4	.081	.023	.15	.14	.18	48
.71	.061	.021	.17	.16	.17	46
1.2	.043	.018	.19	.18	.16	44

Table 9

EFFECTS OF THE SECONDARY SUSPENSION NATURAL FREQUENCY ( $f_2$ )

STATIC DESIGN 2,  $h_{10} = 0.6$  in,  $l_1 = 30$  ft,  $\gamma = 5$

$A = 2\pi \times 10^{-7}$  ft,  $V = 300$  mph

$f_1 = 5$  hz,  $\zeta_1 = .71$ ,  $\zeta_2 = .25$ ,  $\ddot{y}_2$  S.D. in Fig. 4.11

$f_2$ (hz)	RMS $\ddot{y}_1$ (G's)	RMS $\ddot{y}_2$ (G's)	RMS $\Delta h_{1p}/h_{10}$	RMS $\Delta i/i_o$	RMS $\Delta h_2$ (in)	RMS $v_{ind} 4i_o$ (kw)
.5	.070	.010	.15	.14	.30	46
1.0	.061	.021	.17	.16	.17	46
2.0	.046	.040	.21	.21	.09	49

Table 10

EFFECTS OF SECONDARY SUSPENSION DAMPING RATIO ( $\zeta_2$ )

STATIC DESIGN 2,  $h_{10} = 0.6$  in.,  $l_1 = 30$  ft,  $\gamma = 5$

$A = 2\pi \times 10^{-7}$  ft,  $V = 300$  mph

$f_1 = 5$  hz,  $\zeta_1 = .71$ ,  $f_2 = 1$  hz.,  $\ddot{y}_2$  S.D. in Fig. 4.12

$y_2$	RMS $\ddot{y}_1$ (G's)	RMS $\ddot{y}_2$ (G's)	RMS $\Delta h_{1p}/h_{10}$	RMS $\Delta l/i_o$	RMS $\Delta h_2$ (in)	RMS $v_{ind}^4 i_o$ (kw)
.1	.069	.024	.17	.15	.22	46
.25	.061	.021	.17	.16	.17	46
.4	.055	.021	.17	.16	.14	47
.7	.048	.024	.18	.17	.10	48

basic suspension without secondary suspension where the effective spring was connected to the guideway but the effective damper was connected to inertial reference (Chapter 6 elaborates).

Table 11 and Figure 4.13 demonstrate the magnet's filtering of guideway irregularities as speed changes. When  $l_1 = 0$ , no filtering by the magnet length occurs and the output spectra are proportional to AV; therefore, to demonstrate the filtering, AV is constant in the samples. The magnet's filtering depends on the ratio of irregularity wave length to magnet length. As speed decreases, the irregularities of a given wave length represent lower input frequencies; thus, the acceleration spectrum is reduced at higher frequencies. Rms variables such as the acceleration and displacement of the secondary which depend heavily on the secondary's low natural frequency change little while the current and primary acceleration which are affected by high input frequencies are filtered greatly. At high frequencies, the absolute position ( $y_1$ ) is small so that the clearance ( $\Delta h_1$ ) is a function of the road and has little dependence on the filtering.

Table 12 and Figure 4.14 show that ride quality is improved at the critical 6 hz. as longer magnets are used. The improvement is caused by the increased filtering of the magnet's finite length.

Final design with and without secondary suspensions are summarized in Table 13 for air gaps of 0.4 and 0.6 inches and magnet length of 30 feet (Designs 1 and 2 of Table 4) and speeds of 100 and 300 mph. To allow comparison of designs, the dynamic parameters were selected to maximize the road roughness factor (RRF) which is defined as:

Table 11

## EFFECTS OF VELOCITY ON FINITE LENGTH FILTERING

STATIC DESIGN 2,  $h_{10} = 0.6$  in,  $l_1 = 30$  ft,  $\gamma = 5$

$f_1 = 5$  hz,  $\zeta_1 = .71$ ,  $f_2 = 1$  hz.,  $\zeta_2 = .25$ ,  $\ddot{y}_2$  S.D. in Fig. 4.13

V(mph)	A(ft $\times 10^{-7}$ )	RMS $\ddot{y}_1$ (G's)	RMS $\ddot{y}_2$ (G's)	RMS $\Delta h_{1p}/h_{10}$	RMS $\Delta i/i_o$	RMS $\Delta h_2$ (in)	RMS( $v_{ind} 4i_o$ ) (kw)
100	$6\pi$	.024	.018	.17	.12	.16	19
200	$4\pi$	.045	.020	.17	.15	.17	33
300	$2\pi$	.061	.021	.17	.16	.17	46

Table 12

## EFFECTS OF MAGNET LENGTH

$$h_{10} = 0.6 \text{ in}$$

$$A = 6\pi \times 10^{-7} \text{ ft}, \quad V = 100 \text{ mph}$$

$$f_1 = 5 \text{ hz}, \quad \zeta_1 = 0.71, \quad f_2 = .25, \quad \zeta_2 = .25$$

$\ddot{y}_2$  S.D. in Fig. 4.14

STATIC DESIGN	$l_1$ (ft)	$\gamma$	RMS $\ddot{y}_1$ (G's)	RMS $\ddot{y}_2$ (G's)	RMS $\Delta h_1/h_{10}$	RMS $\Delta i/i_o$	RMS $\Delta h_2$ (in)	RMS $(v_{ind} 4i_o)$ (kw)
2	30	5	.024	.018	.17	.12	.16	19
3	20	8	.031	.019	.19	.16	.16	24
4	10	9	.051	.020	.20	.17	.17	30

$$\text{RRF} = \frac{A_{\text{max}}}{A_{\text{welded steel}}}$$

where  $A_{\text{max}}$  is the maximum road roughness which allows the dynamic constraints (Table 3) on accelerations, displacement, and currents to be satisfied and:

$$A_{\text{welded steel}} = 6.3 \times 10^{-7} \text{ ft}$$

The factors which prevent further increase in RRF are listed in limiting factors; for example, sample 1 has an RRF of 4.2 which cannot be increased because of the rms clearance and the acceleration spectral density at 2 hz where the DOT standard is used as the standard.

Operating speeds effect selection of suspension characteristics. At lower speeds the acceleration spectrum near 6 hz. ceases to be of concern. Thus, in systems with secondary,  $\zeta_2$  can be increased to lower the acceleration spectrum at the natural frequency of the secondary. This decrease in acceleration allows the natural frequency of the primary to increase so that the clearance is also decreased. The improvement in RRF is then greater than the simple  $AV = \text{constant}$  which point contact models predict (Chapter 4.3). Similar effects occur in systems without secondary suspension.

When the nominal air gap ( $h_{10}$ ) is decreased, the primary's natural frequency ( $f_1$ ) should be increased to decrease  $\Delta h_1$  to satisfy the displacement constraint. This raises the acceleration so that larger air gaps usually imply higher RRF; however, the RRF of sample 6 ( $h_{10} = 0.6$  in. and  $V = 100$  mph.) is limited by the acceleration spectrum

Table 13

DESIGNS FOR V = 100, 300 mph  $h_{10} = .4, .6$  in

SAMPLE	STATIC DES.	$h_{10}$ (in)	$l_1$ (ft)	$\gamma$	$A(ft \times 10^{-7})$	V (mph)	$f_1$ (hz)	$\zeta_1$	$f_2$ (hz)	$\zeta_2$	rms $\ddot{y}_1$ (G's)	rms $\ddot{y}_2$ (G's)	$\ddot{y}$ S.D. Fig. #	rms $\Delta h_{10}/h_{10}$	rms $\Delta i/i_0$	rms $\Delta h_2$ (in)	rms $v_{ind}^4 i_0$ (kw)	RRF	LIMITING FACTORS FOR RRF
1	1	.4	30	0	$6\pi$	100	2.8	.707	-	-	-	.023	4.14	.28	.22	-	19	4.2	$\Delta h_p$ $\ddot{y}_2$ (2 hz)
2	1			9			12	.707	1	.4	1038	.018		.18	.083	.13	11	11.5	$\Delta h_p$ $\ddot{y}_2$ (1 hz)
3	1			0	$2\pi$	300	1.6	.707			-	.028	4.16	.36	.35	-	43		UNACCEPTABLE
4	1			9			7	.707	1	.25	.075	.021		.22	.20	.18	35	1.9	$\Delta h_p$ $\ddot{y}_2$ (6 hz)
5	2	.6		0	$6\pi$	100	2.0	0.707	-	-	-	.018	4.17	.23	.19	-	26	6	$\Delta h_p$ $\ddot{y}_1$ (2 hz)
6	2			5			9.0	0.707	1	.4	.036	.019		.13	.066	.13	16	11.5	$\ddot{y}_2$ (1 hz)
7	2			50	$2\pi$	300	1.6	.707	-	-	-	.021	4.18	.27	.26	-	52	1.0	$\Delta h_p, \Delta i$ $\ddot{y}_2$ (6 hz)
8	2			5			6.9	.707	1	.25	.061	.021		.17	.16	.17	46	2.4	$\Delta h_p$ $\ddot{y}_2$ (6 hz)

at 1 hz. Stiffening the primary suspension affects the acceleration little so that the gaps can be decreased to 0.4 in. without decreasing the RRF (sample 2), with the result that on-board weight may be reduced (Table 4).

Considerations of performance in the heave mode indicate that the long (30 ft.), thin magnets of designs 1 and 2 are preferred to shorter magnets because of their filtering of guideway irregularities. The effects of eddy currents induced by forward motion and lateral guidance considerations (Chapter 12) also indicate the benefits of long magnets. As indicated in Table 13, the long magnets (10-15% of vehicle weight by Table 4) are feasible with air gaps of 0.4 and 0.6 inches and allow road roughnesses (the input spectrum is defined from  $-j\infty$  to  $+j\infty$ ) of  $1.5 \times 10^{-6}$  ft. at 300 mph. and of  $7 \times 10^{-6}$  ft. at 100 mph. with the simple passive secondary.

Secondary suspensions, lower speeds, and larger air gaps permit rougher roads (as quantitatively shown in Table 13) and/or improved ride quality. Although acceptable designs are possible with just the basic electromagnetic suspension at 300 mph (with welded steel rails  $A = 6.3 \times 10^{-7}$  ft.), the increase in permissible road roughness (factor of 2 - 3) or improvement in ride quality make systems with secondary suspensions more attractive. Decreasing speed from 300 to 100 mph allows road roughness to increase by a factor of 5.

The selection of dynamic parameters such as suspension natural frequencies and damping ratio depend on the precise form of the performance constraints (Section 4.2); however, the general conclusions of this section are unaffected.

The design examples have shown that if the constraint on rms displacement between magnet and rail are loosened by using a larger air gap, softer suspensions which improve ride quality or allow rougher roads can be used.

Changing the comfort standard affects system configuration greatly. If the comfort requirements were relaxed (i.e., D.O.T. specifications were moved upward), stiffer suspensions could be used to improve tracking so that rougher roads or smaller air gaps could be used.

At high speeds (300 mph) the restraint on control current is important. Since the rms current ratio ( $\Delta i/i_0$ ) is proportional to the rms clearance ratio ( $\Delta h_1/h_{10}$ ), tightening the control current restraint requires that the suspension be stiffened; thus, ride quality suffers or smoother roads are required. If the requirements on  $\Delta i/i_0$  are loosened, the requirements on  $\Delta h_1/h_{10}$  dominate and system configuration is unchanged.

The current requirements at low speeds (100 mph) and the restraints at speeds to 300 mph on the displacement of the secondary suspension and the acceleration of the primary do not restrain the sample designs; thus, these restraints can be tightened by a factor of two without affecting system design.

#### 4.4 Summary of Sample Designs

The model for heave motion (with eddy current effects reflected in the long, thin magnets) shows that air gaps of 0.4 to 0.6 inches are feasible. As indicated in Tables 4 and 13, road roughness (A) of  $1.5 \times 10^{-6}$

ft at 300 mph and of  $7 \times 10^{-6}$  ft at 100 mph are possible with simple secondary suspensions and magnets which are 10-15% of the vehicle's total weight.

Road roughness is limited by passenger comfort and rail clearance. Since the acceleration of the primary ( $\ddot{y}_1$ ) and the clearance between magnet and sprung mass ( $\Delta h_2$ ) have considerable leeway, improved suspensions could permit still greater road roughness.

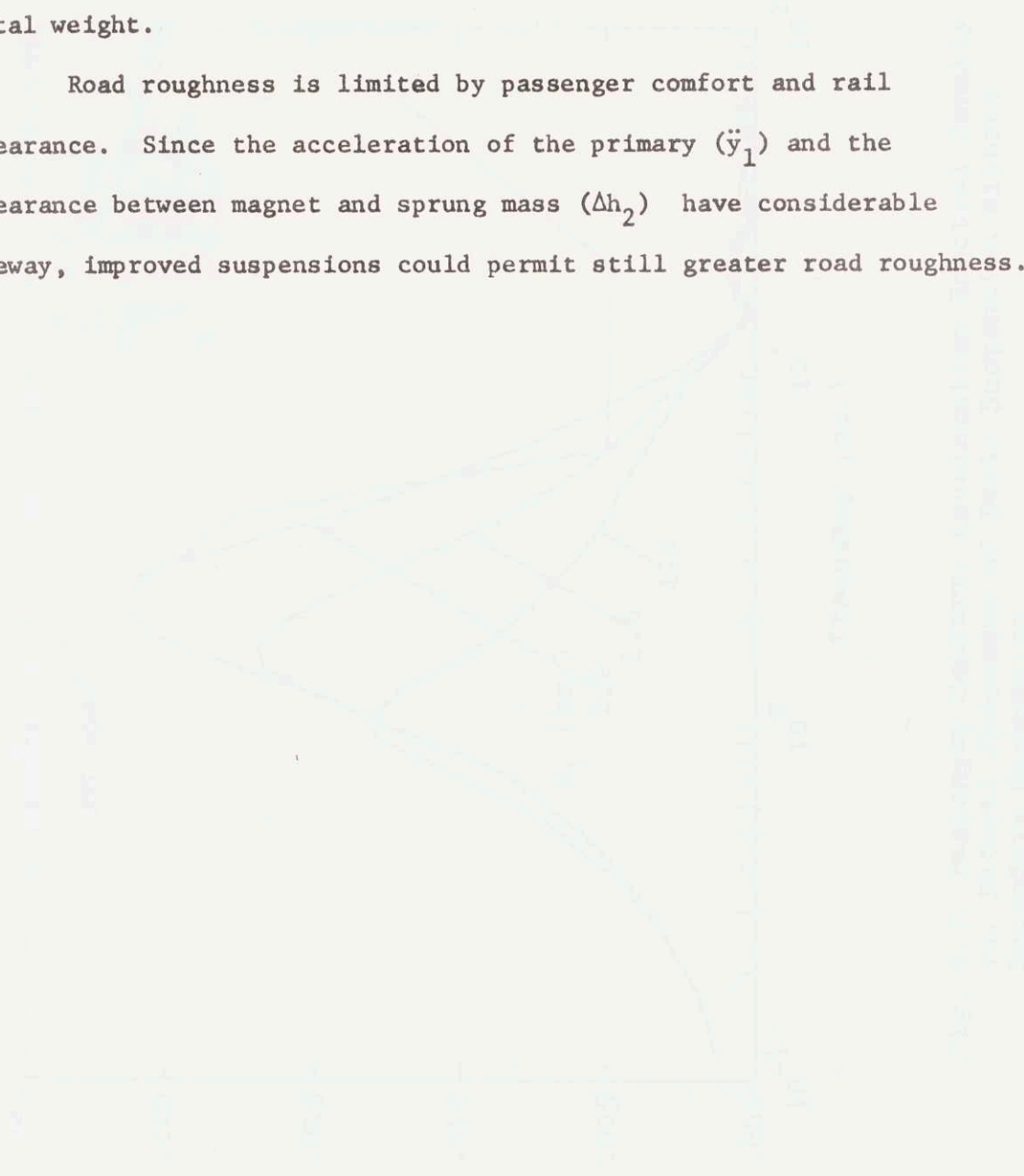


Fig. 1. Secondary Suspension. Acceleration in g's (1000 ft/sec<sup>2</sup>) vs. Frequency (rad/s) of Primary Suspension. Secondary Suspension.

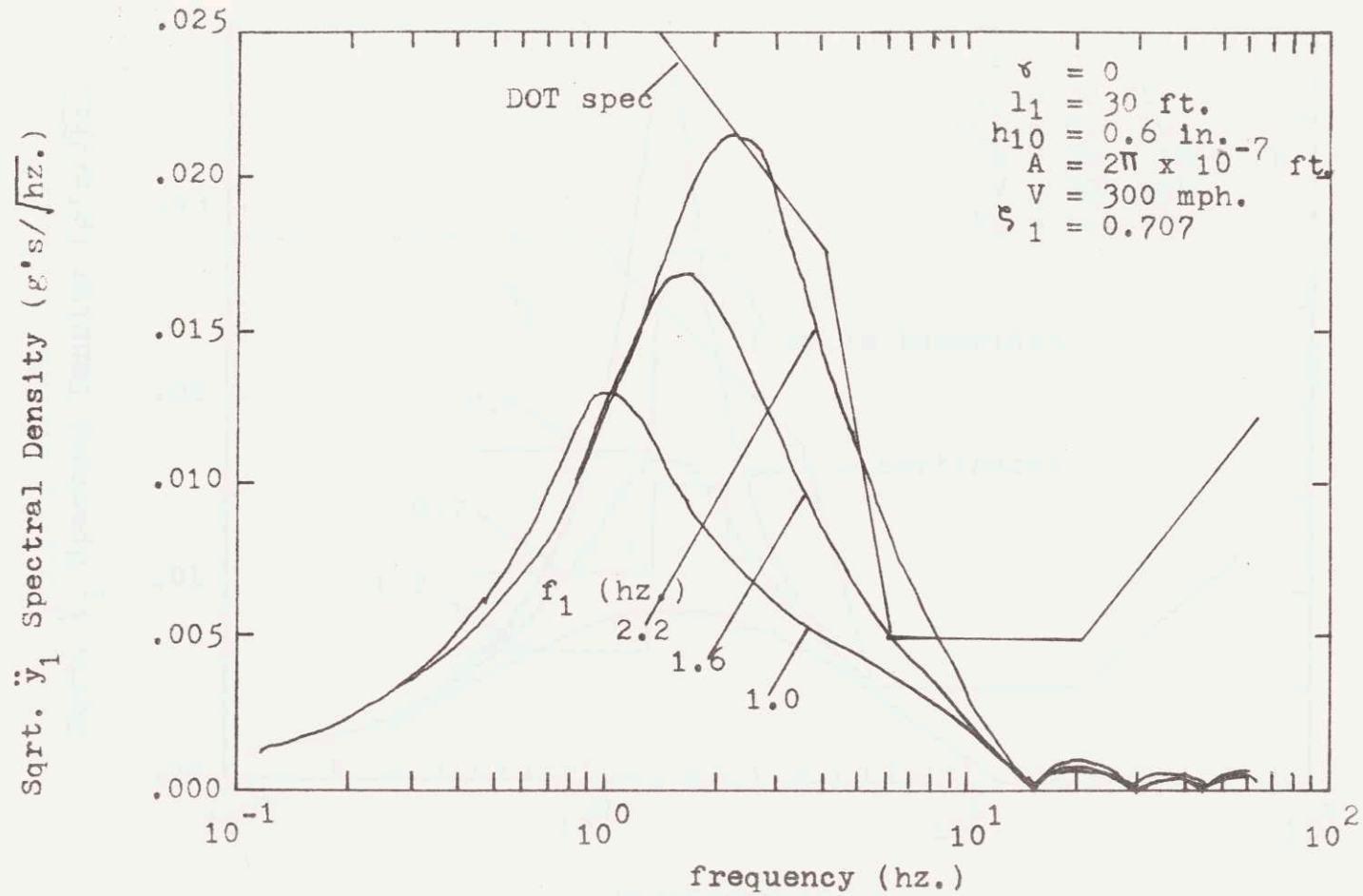


Fig. 4.7. Passenger Comfort: Acceleration Spectral Density vs. Natural Frequency of Basic Suspension without Secondary Suspension

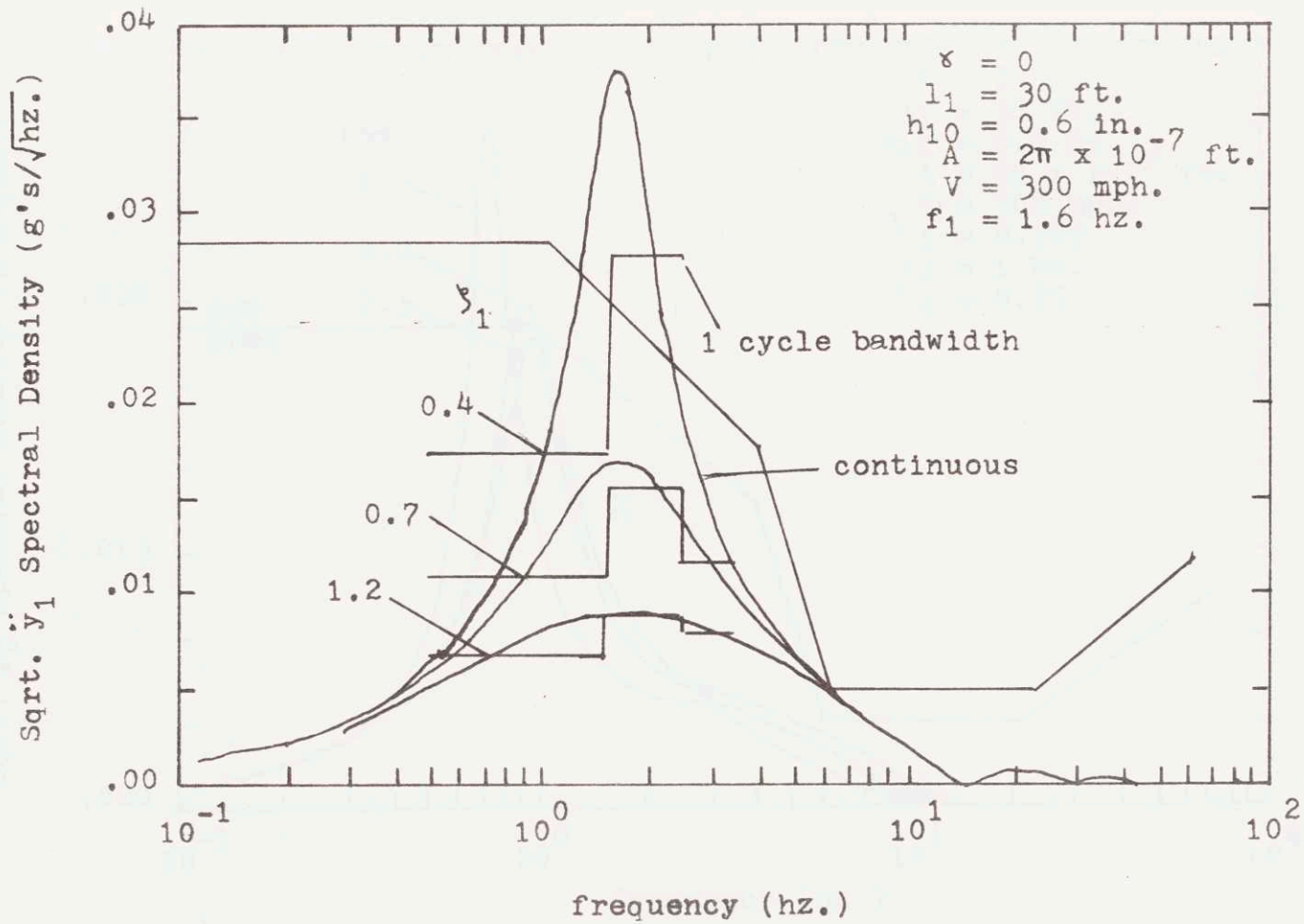


Fig. 4.8. Passenger Comfort: Acceleration Spectral Density vs. Damping Ratio of Basic Suspension without Secondary Suspension

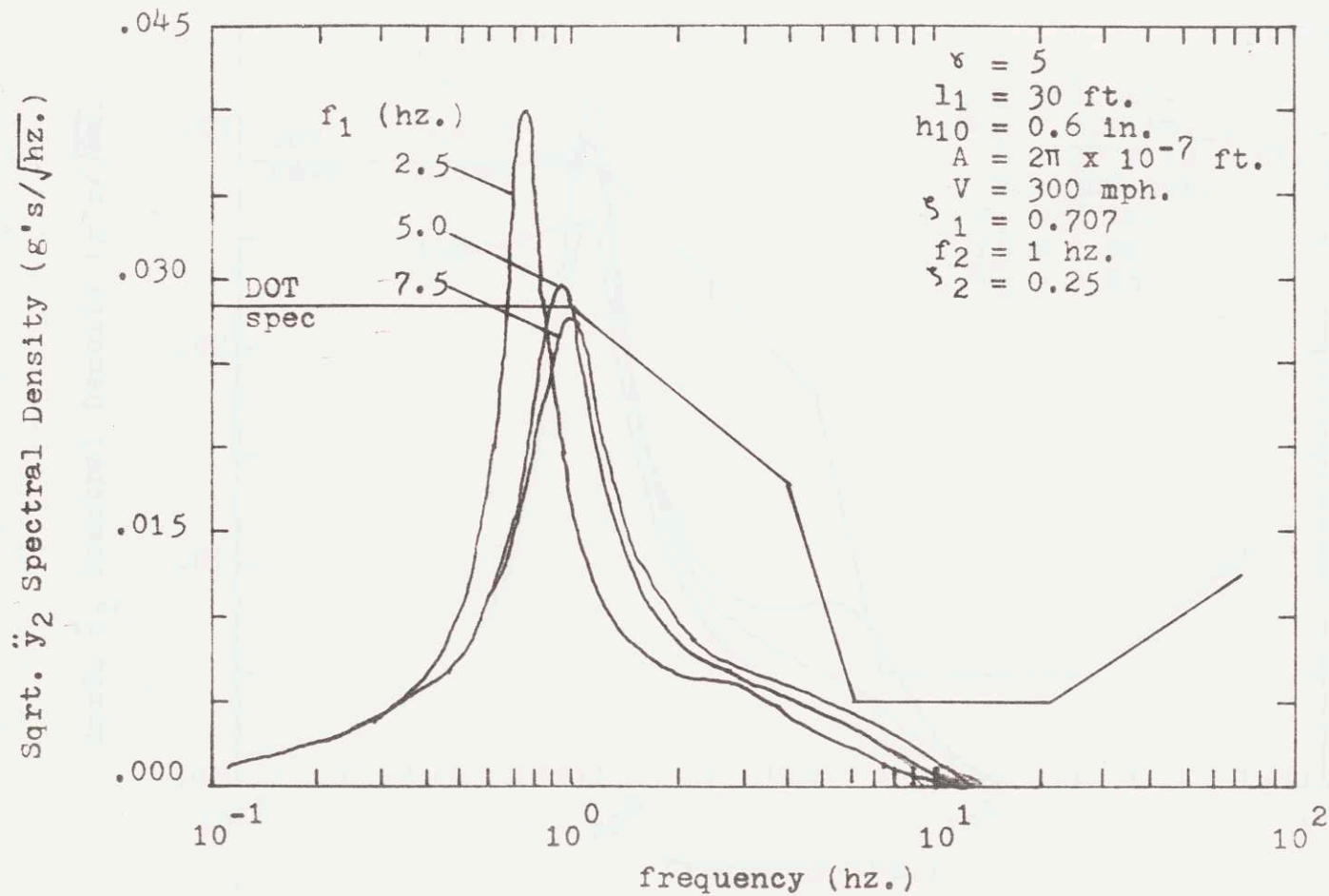


Fig. 4.9. Passenger Comfort: Acceleration Spectral Density vs. Primary Suspension Natural Frequency

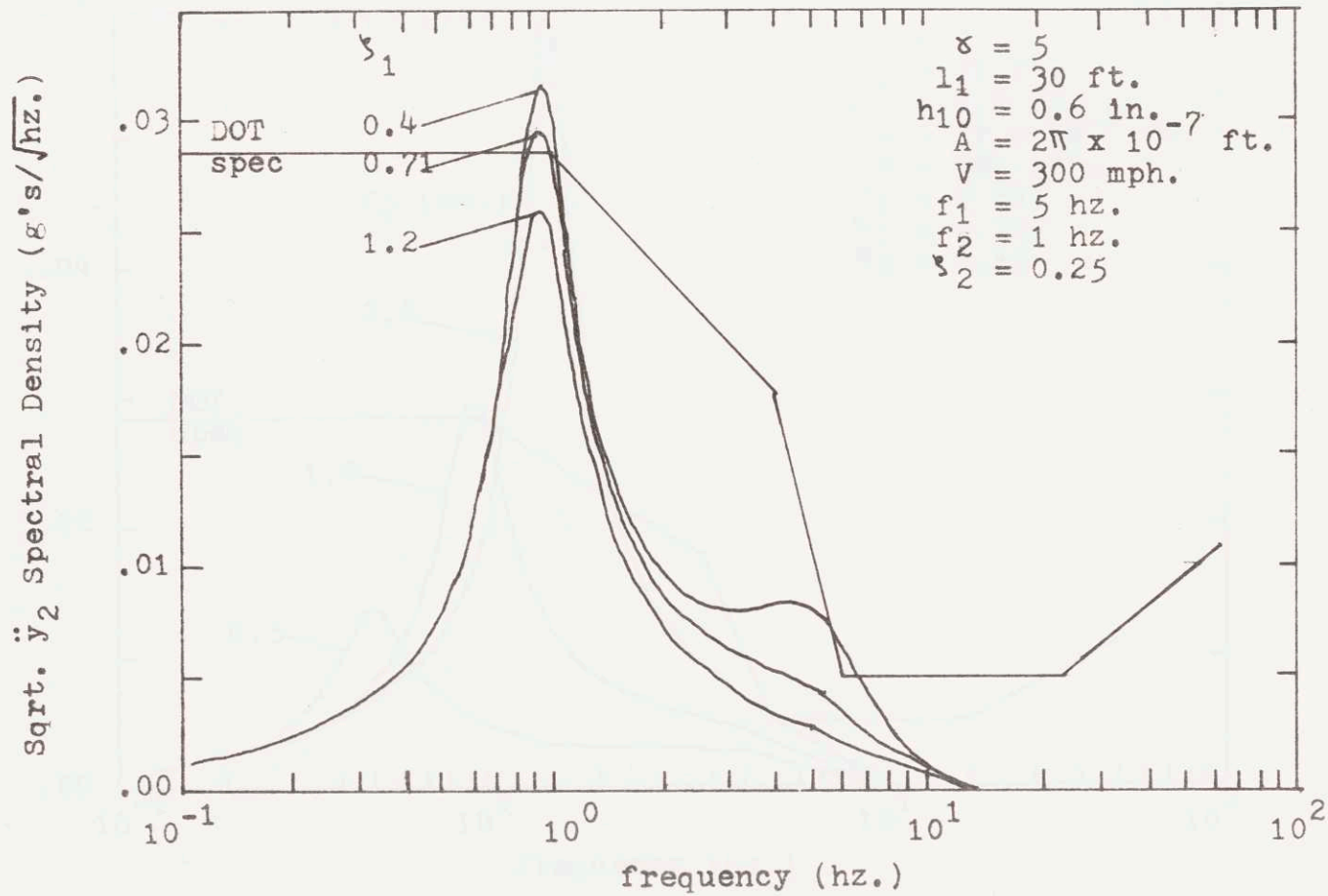


Fig. 4.10. Passenger Comfort; Acceleration Spectral Density vs. Primary Suspension Damping Ratio

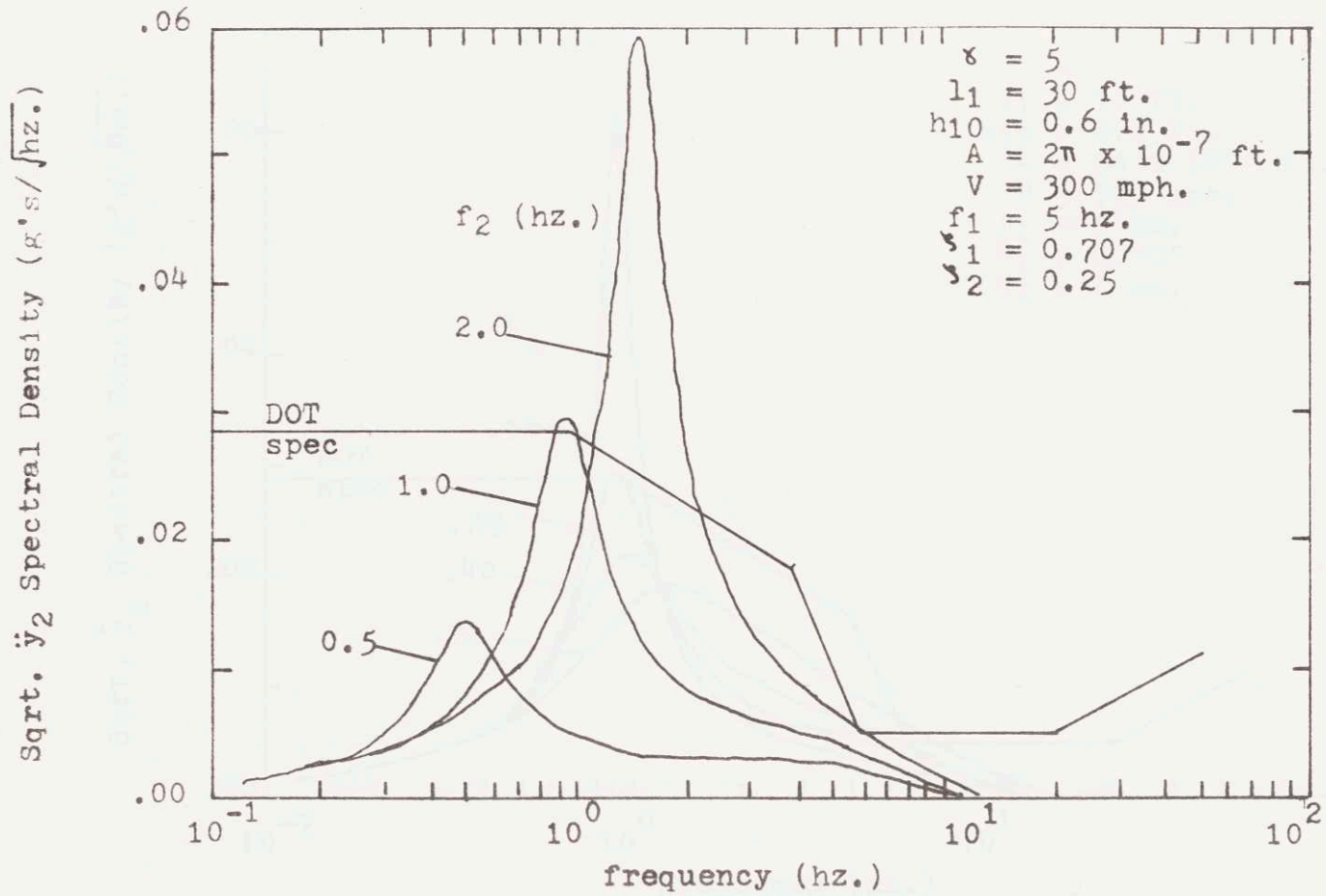


Fig. 4.11. Passenger Comfort: Acceleration Spectral Density vs. Secondary Suspension Natural Frequency

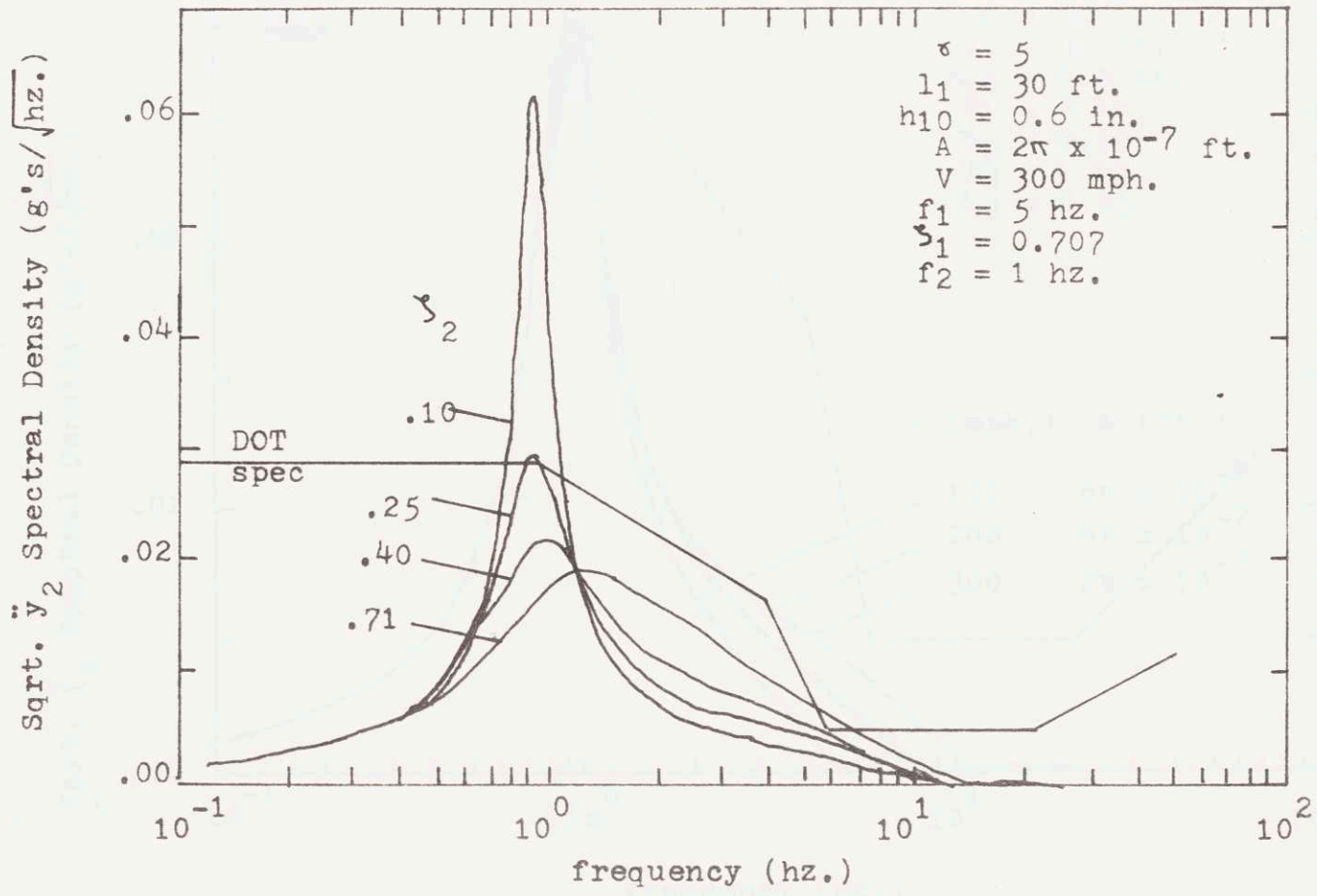


Fig. 4.12. Passenger Comfort: Acceleration Spectral Density vs. Secondary Suspension Damping Ratio

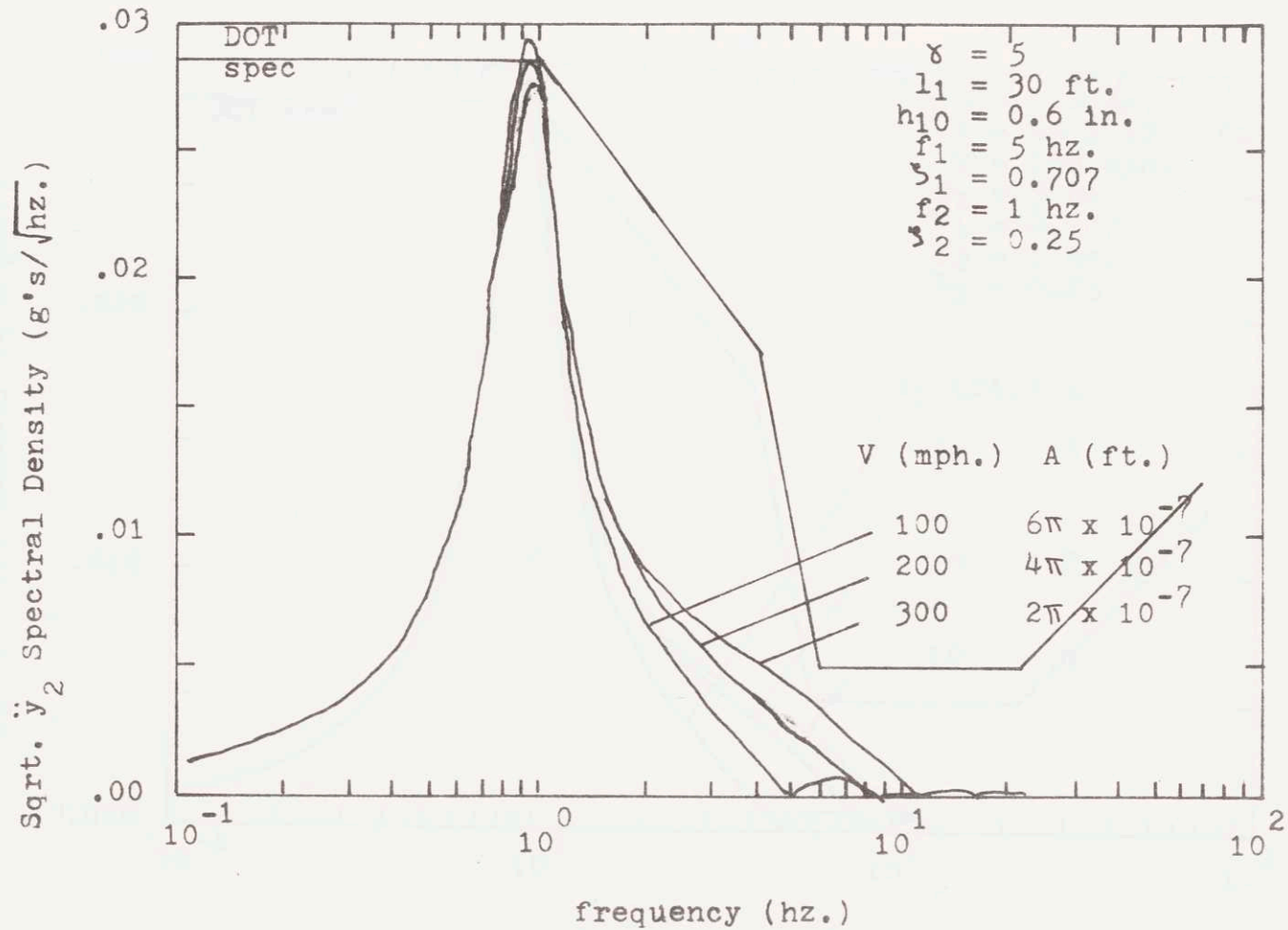


Fig. 4.13. Passenger Comfort: Acceleration Spectral Density vs. Finite Length Filtering at Different Speeds

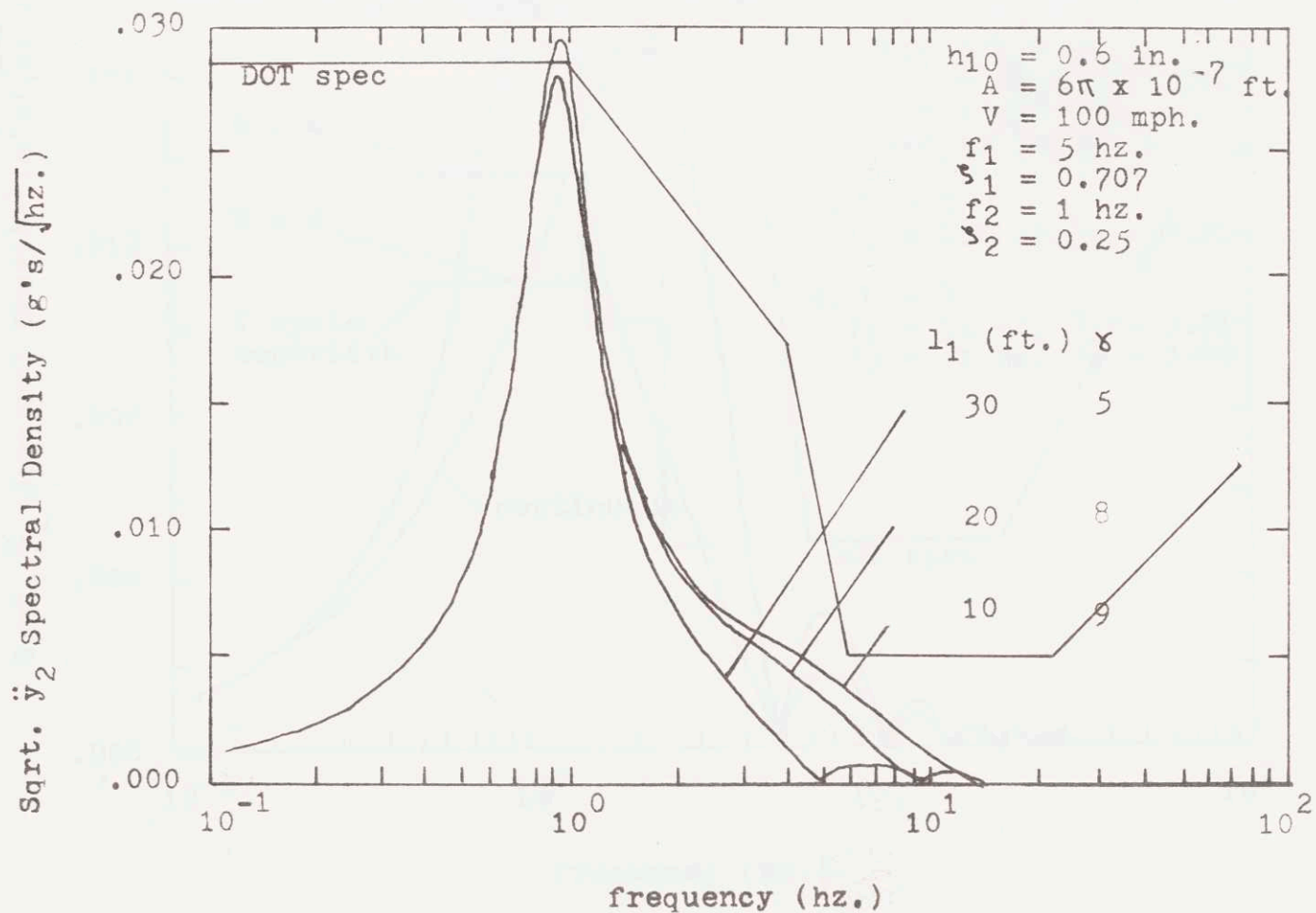


Fig. 4.14. Passenger Comfort: Acceleration Spectral Density vs; Magnet Length

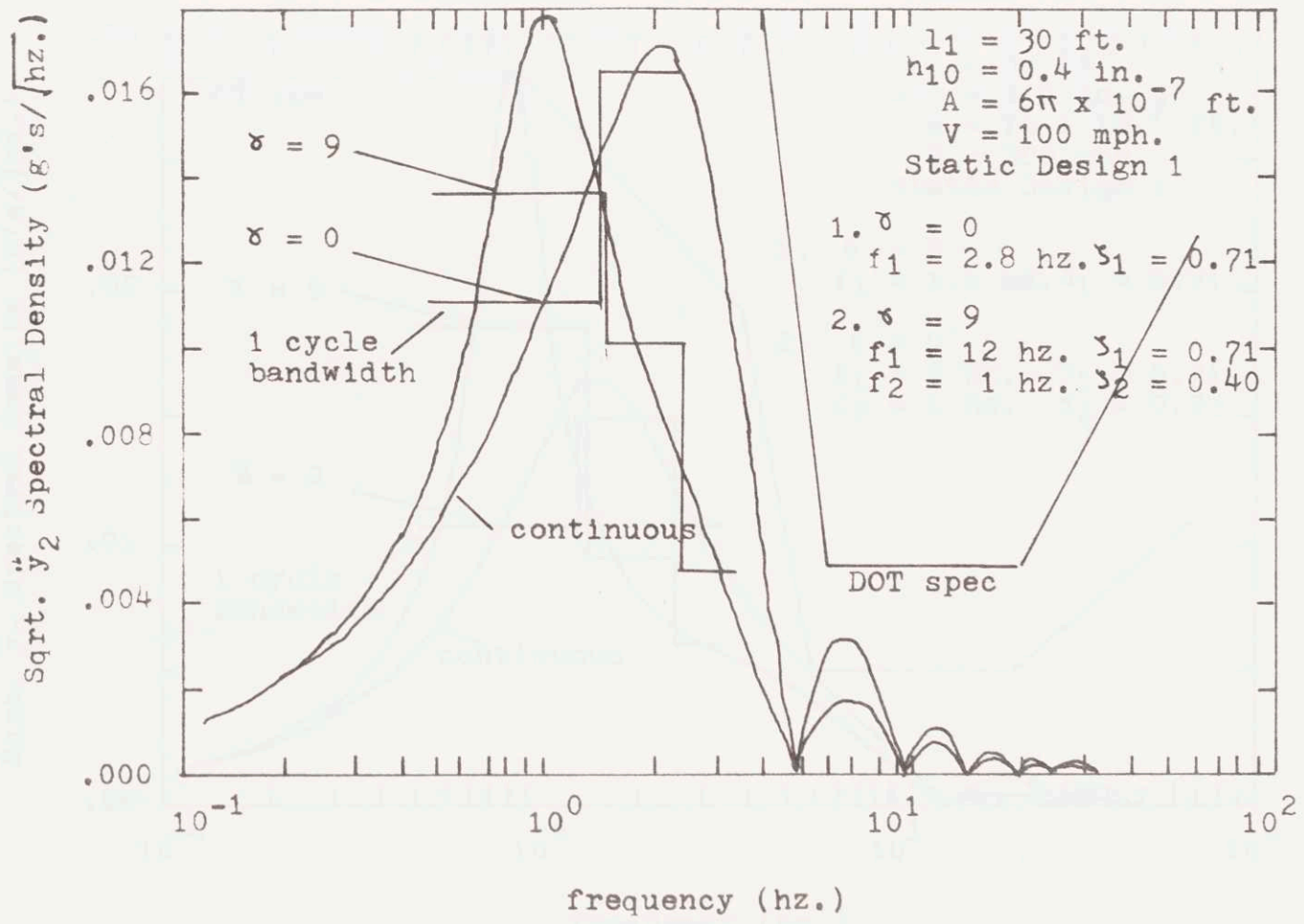


Fig. 4.15. Passenger Comfort; Acceleration Spectral Density for Sample Designs with  $h_{10} = 0.4 \text{ in.}$  and  $V = 100 \text{ mph.}$

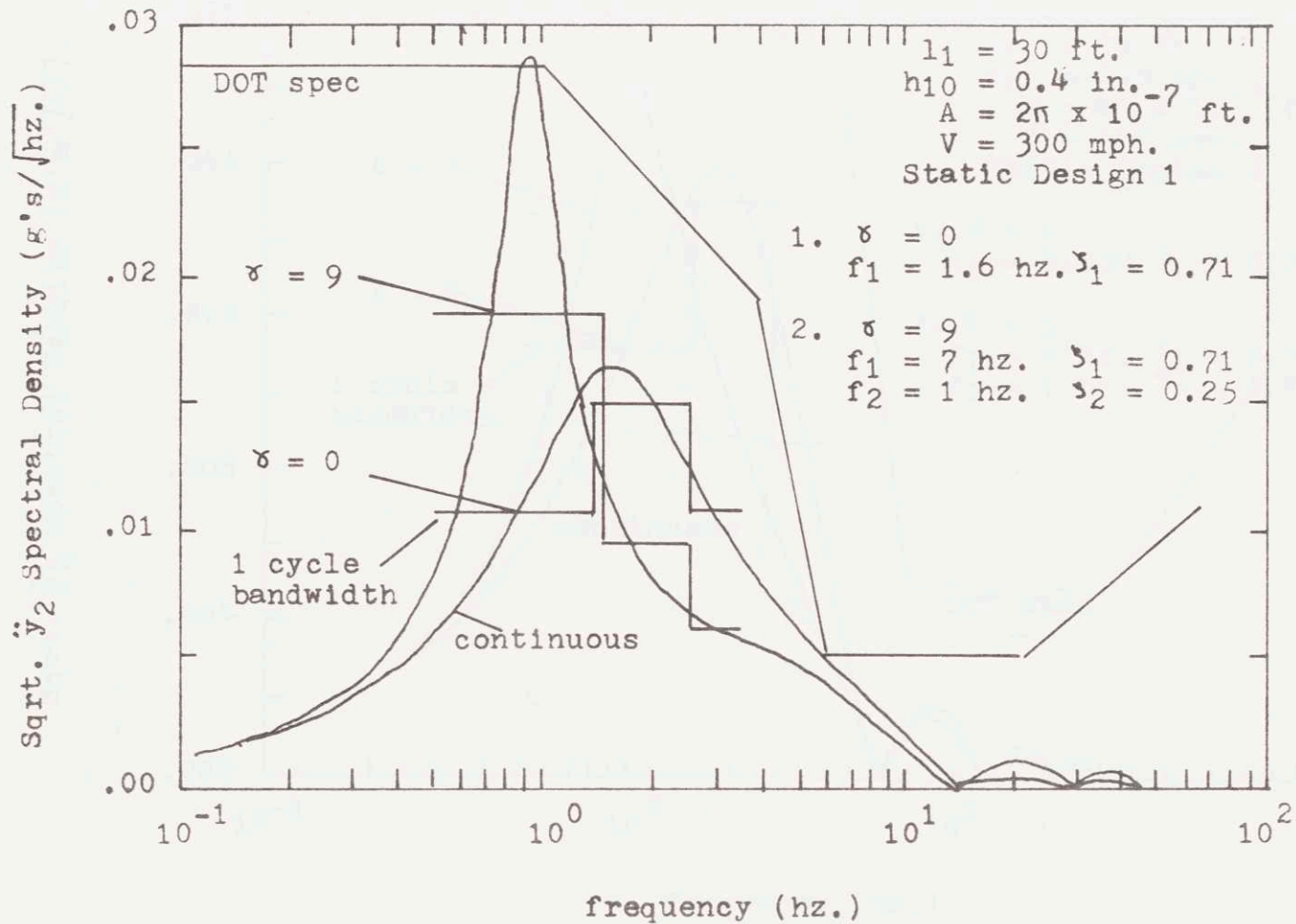


Fig. 4.16. Passenger Comfort: Acceleration Spectral Density for Sample Designs with  $h_{10} = 0.4 \text{ in.}$  and  $V = 300 \text{ mph.}$

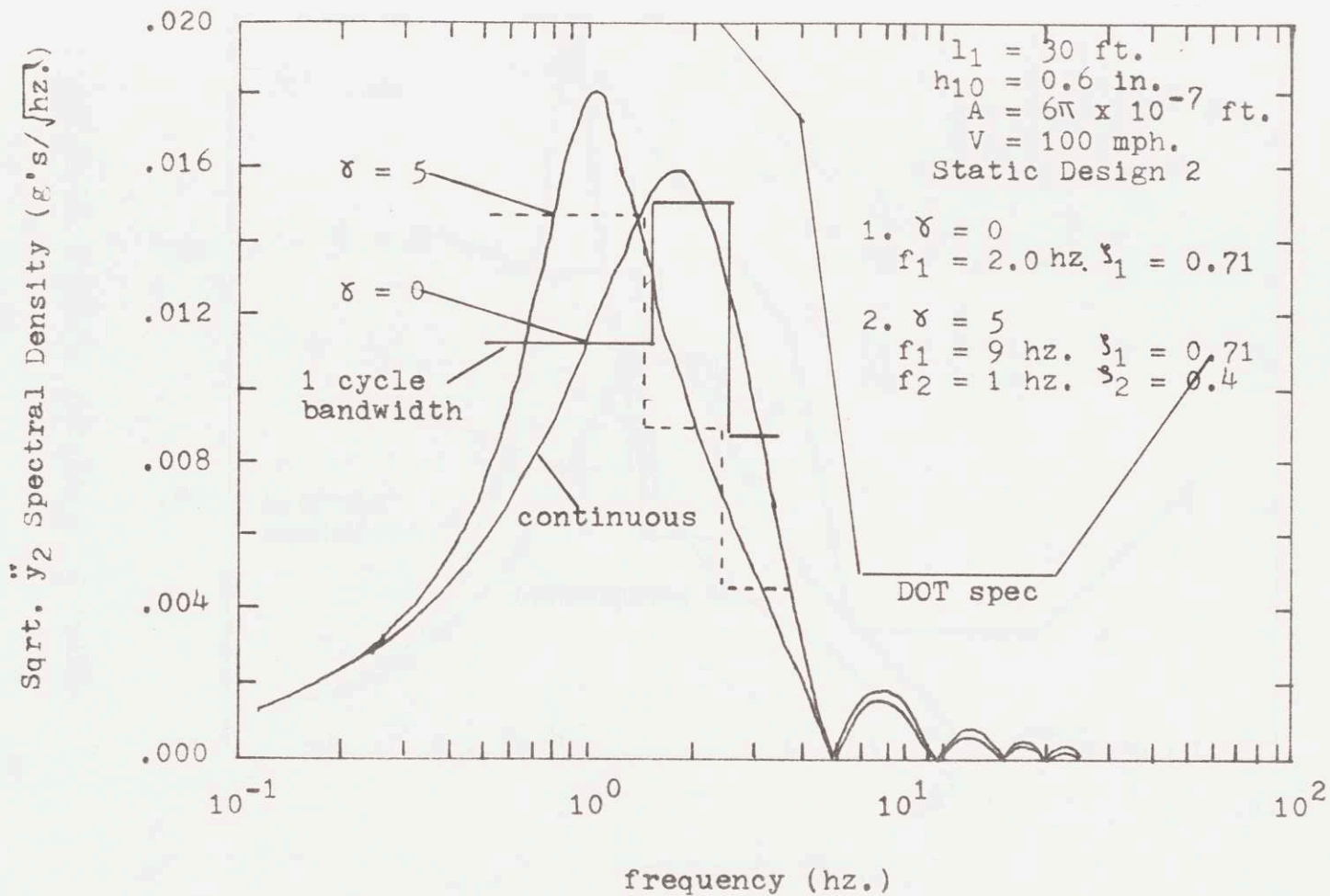


Fig. 4.17. Passenger Comfort: Acceleration Spectral Density for Sample Designs with  $h_{10} = 0.6 \text{ in.}$  and  $V = 100 \text{ mph.}$

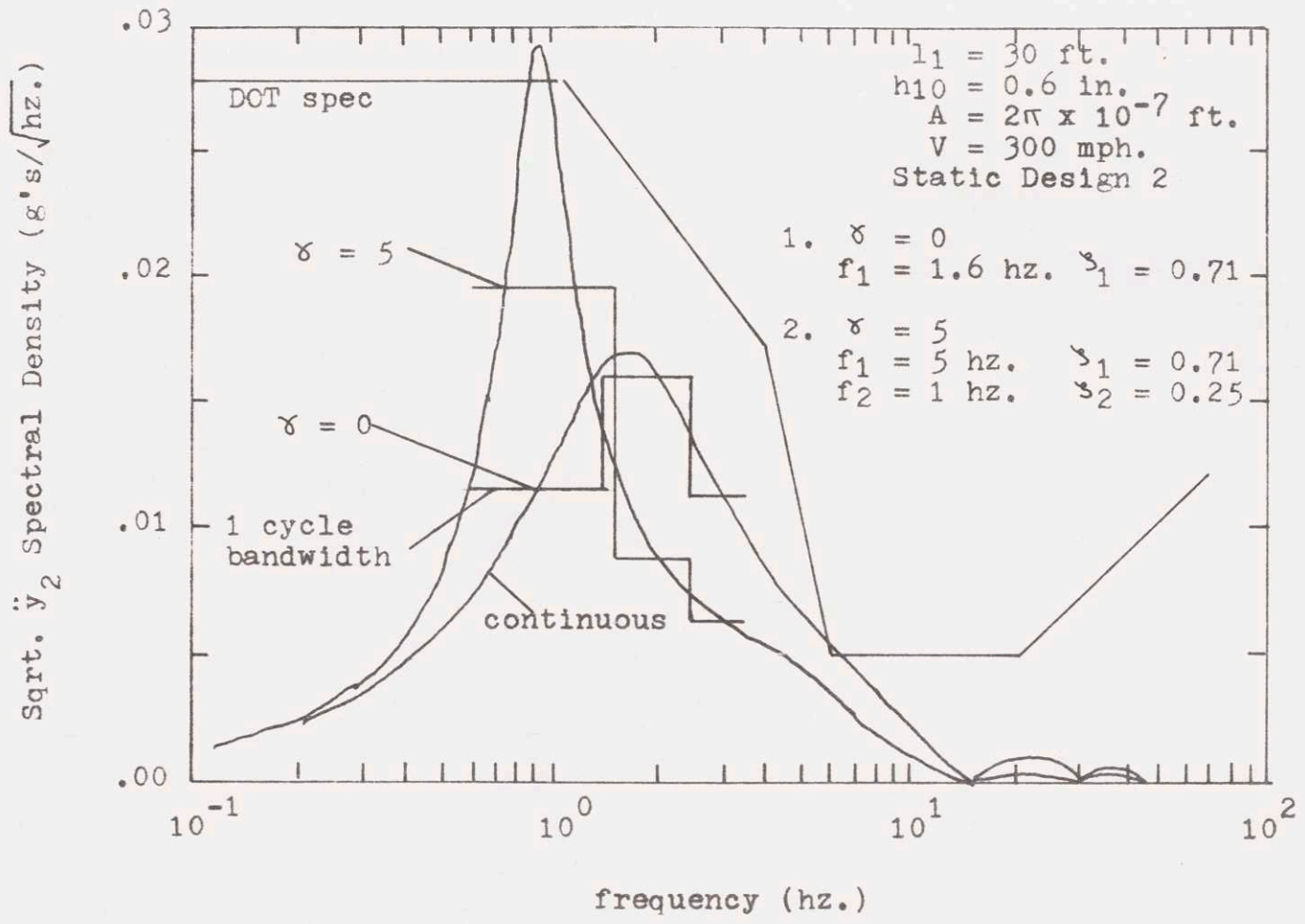


Fig. 4.18. Passenger Comfort; Acceleration Spectral Density for Sample Designs with  $h_{10} = 0.6 \text{ in.}$  and  $V = 300 \text{ mph.}$

## PART II. EQUATIONS FOR HEAVE MOTION

In this part, the model for the heave motion which was outlined in Part I is constructed in detail. The use of the model, the effects of the parameters, and the capabilities of electromagnetic suspensions were described in Part I so that Part II is dedicated to model formulation.

### 5. STATIC RELATIONS FOR MAGNETS

Equations for the flux paths, the forces, and voltages of the electromagnetic suspension are derived.

#### 5.1 Permeances of Magnetic Paths

The flux paths of the magnet must be known in order to determine the magnet forces, the maximum flux in the iron, the voltages in the coils, and the eddy currents. Omission of flux leakage typically leads to errors (factor of five) in determining the maximum lift force and errors in control voltage (factors of 2) (Sections 2.2).

Precise determination of the leakages is a complicated field theory problem. Since this thesis is directed to the development of design equations, lumped techniques which are experimentally verified in Chapter 3 are used to compute the fluxes. Since this is a static problem, eddy currents are not considered.

For situations where the window width ( $w_1$ ) is greater than roughly four times the air gap ( $h_{10}$ ) (Fig. 2.1), the lumped flux model depicted in Figures 5.1 through 5.4 is useful. (For  $w_1 < 4h_1$  some of the flux leaving the end of the magnet's pole would find the path to the opposite pole shorter than the path to the rail and would flow to the opposite pole; thus, the flux paths must be redefined.) Since saturation is

avoided except at extreme operating conditions, the permeance of metallic part is assumed infinite compared to that of the air paths. Section 4.3 shows that normal magnet operation must produce fluxes below the saturation limit (because gaps larger than the nominal require higher flux levels) so that this assumption is valid.

The infinite permeance of the metal implicitly eliminates the effects of hysteresis in the magnetic material on the magnet's forces and, hence, on system dynamics. Although the permeance of the magnet can assume different values at the same flux density depending on the history of the magnetic fields, this is neglected since the magnet's permeance is assumed infinite. The power dissipated by hysteresis is negligible compared to power drained by magnetic drag, ohmic loss, and apparent power used for magnet control.

To determine the fluxes for the vertical motion, the geometry of the rail is simplified from the U shape of Figure 2.1 to the infinite plane depicted in Figures 5.1 and 5.3. This is valid for rail pole width ( $l_2$ ) greater than magnet pole width ( $l_p$ ) plus twice air gap ( $h_{10}$ ). Smaller  $l_2$  (i.e.,  $l_2 < l_p + 2h_{10}$ ) will reduce the fringing permeance [50]. The experimental results (Chapter 3) demonstrate that this model is conservative (less than 10% error), but valid for design purposes. The errors are attributed to the uncertainty of the lumped approximation.

Figure 5.1 illustrates a cross section of the magnet. The useful permeance ( $P_u$ ) is defined as that permeance which is determined by the volume directly below the pole face of the magnet. The fringing flux goes from the magnet to the rail but flows outside of the useful area and flows through the fringing permeance ( $P_f$ ). The sum of the useful

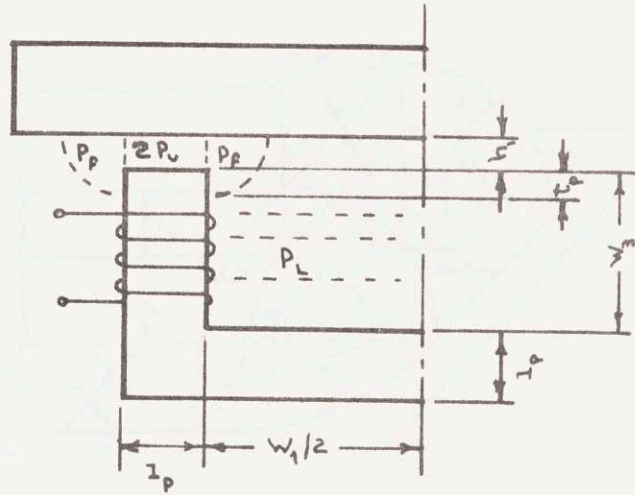
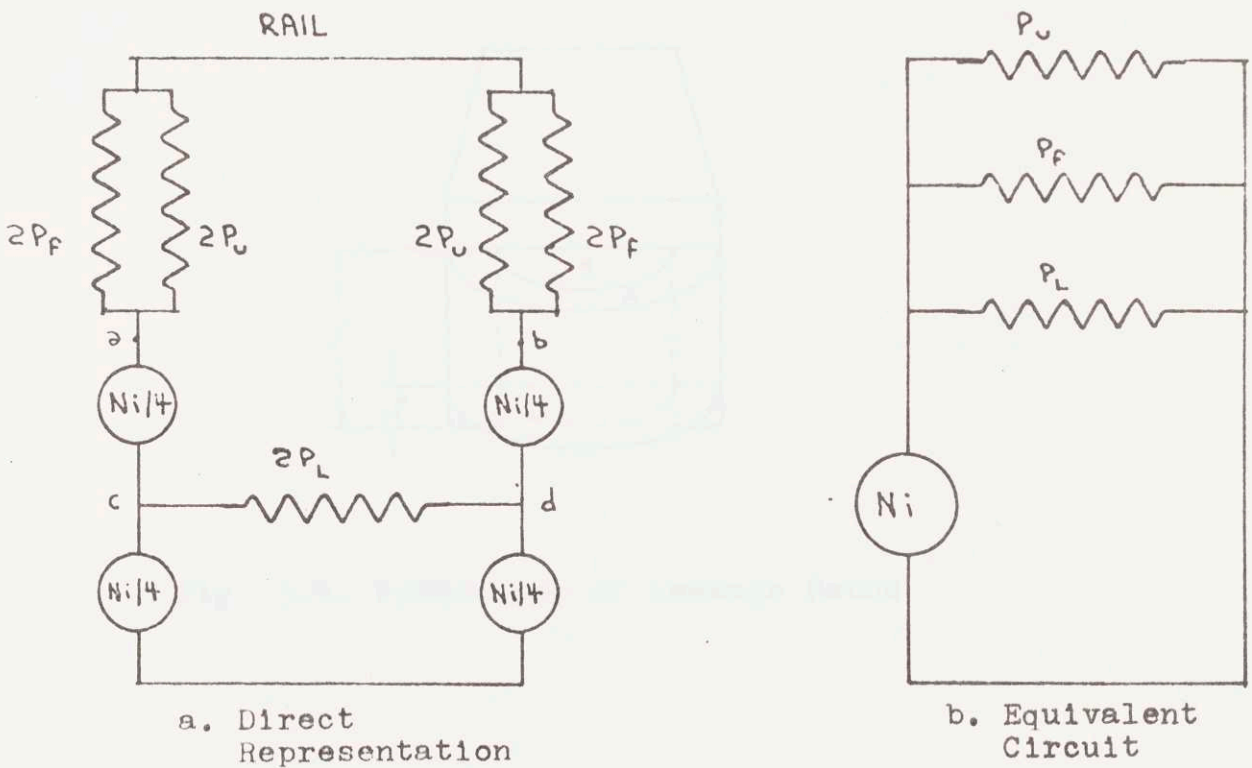


Fig. 5.1. Cross Section of Magnet  
 Depicting Flux Paths for  
 Theoretical Model



a. Direct Representation  
 b. Equivalent Circuit

Fig. 5.2. Circuit Diagrams of Flux Paths

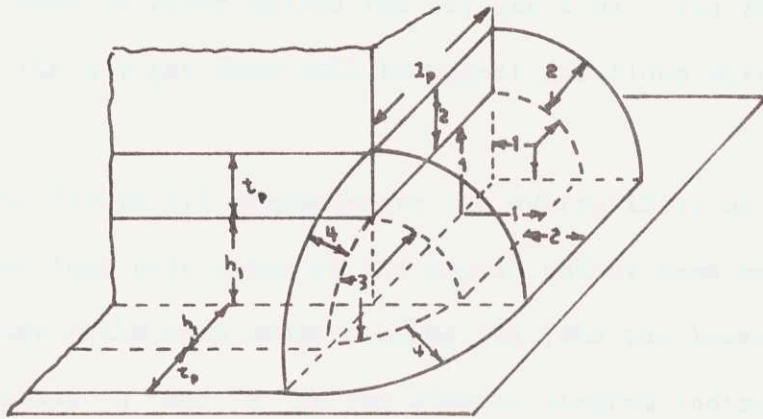


Fig. 5.3. Permeances at Corners. Numbers denote paths described in Appendix 2. The figure is from [50].

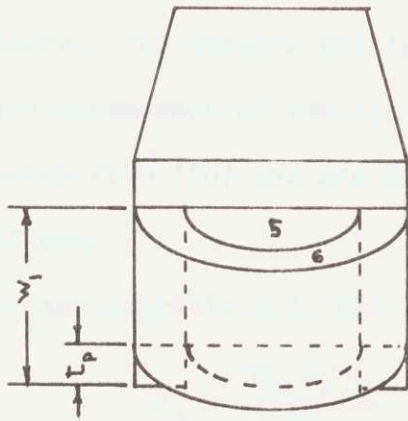


Fig. 5.4. Permeances of Leakage Paths

and fringing fluxes is often called the air gap flux. The leakage flux does not cross the air gap from rail to magnet and flows directly between the pole cores.

Note that Figure 5.2 demonstrates the advisability of winding the coils on the vertical pole cores of the magnet rather than on the horizontal yoke. If the coils were wrapped about the yoke the leakage permeance would connect nodes a and b on the circuit diagram instead of nodes c and d as depicted in Figure 5.2. In addition the configuration shown simplifies the winding of the coils since the coils need not be wound in place.

The model of Figure 5.1 is adequate for long models ( $l_p/l_1 > 20$ ,  $l_1$  = magnet length) where end effects can be neglected. Although full-scale designs can be modeled as long, the experimental prototype used in Chapter 3 is short so the model of Figures 5.3 and 5.4 are used to include end effects. The results for long magnets will be listed here.

The lumped permeances of the circuit diagram (Figure 5.2) are calculated directly from [50] and are summarized in Appendix 2 which includes end effects.

From [50] and Appendix A.2, the useful permeance is:

$$P_u = \frac{\mu_o l_1 l_p}{2h_1} \quad (5.1)$$

where  $\mu_o$  = permeability of a vacuum =  $4\pi \times 10^{-7}$  nt/amp<sup>2</sup>.

Ratios which compare the fringing and leakage fluxes to the useful fluxes are defined (and evaluated numerically for the experimental model) in Appendix A.2. For  $w_3 \gg h_1$  and  $w_1 < 4h_1$  (See Appendix 2 and Chapter 3.4) the leakage flux coefficient is:

$$v_L = \frac{P_L}{P_v} = \frac{w_3 h_1}{w_1 l_p} \quad (5.2)$$

In the region of design interest ( $l_2 \approx l_p + 2h_{10}$ ), the fringing coefficient is:

$$v_F = \frac{P_F}{P_v} = \frac{1.92h_1}{l_p} \quad (5.3)$$

The regions over which (5.1) to (5.3) are valid are discussed in the experimental results (Chapter 3.4). The air gap flux coefficient which is used in the eddy current analysis is:

$$v_{\partial} = 1 + v_F = \frac{P_u + P_f}{P} \quad (5.4)$$

Typical values of  $v_{\partial}$  are in the 1.5 to 2 range.

The total flux coefficient for saturation and force determination is:

$$T = \frac{P_u + P_F + P_L}{P_u} = 1 + \left[ \frac{1.92}{l_p} + \frac{w_3}{w_1 l_p} \right] h_1 \quad (5.5)$$

Typical values for practical designs are approximately 2 (Table 4).

Finally, the total leakage coefficient for determining the self-inductance of the coil:

$$v_v = 1 + v_F + \frac{2v_L}{3} \quad (5.6)$$

The 2/3 accounts for leakage flux ( $\phi_L$ ) through the distributed windings [50].

The total leakage coefficient (5.5) is of the form

$$v_T = 1 + K_v h_1, \quad K_v = \text{constant} \quad (5.7)$$

and is virtually independent of lateral displacement. Experimental results (Chapter 3.4) indicate that (5.7) is true for  $h_1/l_p < 1-1/2$ . With (5.1) the total permeance is

$$P_T = \frac{\mu_o l_1 l_p}{2h_1} v_T(h_1) \quad (5.8)$$

If leakage is negligible,  $v_T = 1$ .

## 5.2 Magnet Force and Voltage

The vertical force is derived from [50] as:

$$F = \frac{1}{2} (Ni)^2 \frac{\partial P_T}{\partial h_1} \quad (5.9)$$

so that vertical force is determined almost exclusively by the flux that passes through the useful permeance with little influence from the leakage.

Combining (5.7) to (5.9) yields:

$$F = \frac{\mu_o (Ni)^2 l_1 l_p}{4h_1^2} \quad (5.10)$$

where the magnet and rail are attracted to one another and where

$Ni$  = ampere turns in coil

$h_1$  = air gap

$l_1$  = length of magnet

$l_p$  = width of magnet pole face .

(5.10) is valid when the air gap above the magnet is uniform. Although the leakage does not appear in the force equation, the leakage determines the maximum force which the magnet can exert and the voltages in the control coils (Chapter 2.2).

The voltage in the control coil consists of an inductive and an ohmic portion

$$v = v_{ind} + v_{ohmic} \quad (5.11)$$

where  $v_{ohm} =$  ohmic voltage  $= R_1 i$

$R_1 =$  resistance of the coil (defined in Section 4.3)

$$v_{ind} = \text{inductive voltage} = \frac{d}{dt} [\mu_T(h_1) \frac{\mu_0 N^2 l_1 l_2}{2h_1}] \quad (5.12)$$

As described in Section 2.2 large errors in voltage (factor of 5) occur for typical designs if the leakage is neglected.

## 6. MAGNET CONTROL FOR SIMPLE SUSPENSION

### 6.1 Introduction

Based on a linearized model of the basic electromagnet, a rational first control for an electromagnetic suspension is selected. In this section, the effects of eddy currents are neglected. Since electromagnetic suspensions are basically unstable, active control is required for stability. The selection of a current control law which feeds back the average magnet-rail clearance and the magnet's absolute velocity is based on optimization techniques, practical considerations, and comparisons with other control strategies. The optimization technique minimizes a performance index that reflects the desired performance of the suspension. Because of its simplicity, the control law is also a reasonable first choice for models which include eddy currents and secondary suspensions as shown in Chapter 2.3.5 and 4.

### 6.2 Simple Linearized Model

A simple model for the basic magnetic suspension operating in the heave mode appears in Figure 2.4. In this model, the length of the magnet is assumed short compared to the irregularities in the road; i.e., the air gap between magnet and rail is constant. The input to the model is the road which is modeled as a stationary stochastic process whose spectral density extends from  $-j\omega_0$  to  $+j\omega_0$  is [18, 28, 29, 38, 44]:

$$\phi_{y_0 y_0}(s) = \frac{-AV}{s^2} \quad (6.1)$$

where  $s$  = Laplacian operator

A = road roughness parameter

V = forward velocity of vehicle .

Note that  $j\omega = s$  where  $\omega$  is the angular frequency which can be related to  $\lambda$  the wavelength of the road's irregularities by:

$$\omega = \frac{2\pi V}{\lambda} \quad (6.2)$$

In nondimensional notation, the road input is:

$$\phi_{\tilde{y}_0 \tilde{y}_0}(\tilde{s}) = - \frac{AV}{\tilde{s}^2} \quad (6.3)$$

where  $\tilde{AV} = \frac{AV}{h_{10}^{3/2} g^{1/2}}$  ,  $s = \tilde{s} \sqrt{\frac{h_{10}}{g}}$

The tilda denotes nondimensionalized quantities.

The vehicle model is based upon a single magnet limited to heave motion. The magnet force (5.10) equals the gravitational force plus the mass acceleration so that the equation of motion is:

$$F_o + \Delta F = m\ddot{y}_1 + mg = \frac{\mu_o N^2 (i_o + \Delta i)^2 \frac{1}{1} \frac{1}{p}}{4 (h_{10} + \Delta h_1)^2} \quad (6.4)$$

where  $m$  = mass of vehicle

$y_1$  = absolute position of vehicle

$h_1 = y_o - y_1$  = position of magnet relative to rail.

Equation (6.4) illustrates that the system is unstable for constant currents (as well as constant voltage). If  $h_1$  is greater than  $h_{10}$ , the nominal gap, the mass falls to the ground, while, if  $\Delta h_1$  is negative

the mass accelerates upward to contact the rail. For simulations, it is convenient to nondimensionalize (6.4) by using the vehicle weight:

$$F_o = mg = \frac{\mu_o (Ni_o)^2 l_1 l_p}{4h_{10}^2}$$

which gives:

$$1 + \Delta\tilde{F} = \ddot{\tilde{y}}_1 + 1 = \frac{(1 + \tilde{I})^2}{(1 + \tilde{h}_1)^2} \quad (6.5)$$

where

$$\tilde{I} = \Delta i / i_o$$

$$\ddot{\tilde{y}}_1 = \ddot{y}_1 / g$$

$$\tilde{h}_1 = \Delta h_1 / h_{10}$$

$$\tilde{t} = t \sqrt{\frac{g}{h_{10}}}$$

$$\tilde{F} = F / mg$$

To determine a first estimate of control requirements, a linear model is considered. Equation (6.5) is linearized about the operating point ( $\tilde{h}_1 = 0$  and  $\tilde{I} = 0$ ) so that the linearized acceleration is:

$$\ddot{\tilde{y}}_1 = -2\tilde{h}_1 + 2\tilde{I} \quad (6.6)$$

The voltage in the control coil is given by (5.11) which is linearized and nondimensionalized to give:

$$\tilde{v} = \tilde{v}_{ind} + \tilde{I} \tilde{R}_1 = v_v \dot{\tilde{I}} - \dot{\tilde{h}}_1 + \tilde{I} \tilde{R}_1 \quad (6.7)$$

where the following dimensionless terms are defined.

$$\tilde{v} = \frac{i_o v}{2mg\sqrt{gh_{10}}}$$

$$\tilde{R}_1 = \frac{\tilde{R}_1 i_o^2}{2mg\sqrt{gh_{10}}}$$

Note that the equation of motion (6.6) has considered the leakage flux effects.

### 6.3 Selection of Control Laws

Since the basic system is unstable, active control of the current or voltage is needed to achieve stability. To achieve stability and suitable ride characteristics, a performance index (P.I.) is constructed to reflect the desired characteristics of an electromagnetic suspension. Although comfort depends on the entire acceleration spectrum (Chapter 4.2) the performance index (P.I.) includes the total rms acceleration an approach which yields valuable results. To limit contact between the rail and the magnet,  $\tilde{h}_1$  must be limited (Chapter 4.2). The current  $\tilde{i}$  must be limited to avoid negative currents ( $i_o + \Delta i < 0$ ) which alter the system's control characteristics (Chapter 4.2). These considerations are reflected in the performance index:

$$P.I. = E[\tilde{y}_1^2] + \rho E[\tilde{h}_1^2] + \beta E[\tilde{i}_1^2] \quad (6.8)$$

where E is the expected value operator. The factors  $\rho$  and  $\beta$  determine the relative weights of the terms in the performance index. Changing the relative weights changes the importance of the terms in P.I. and is reflected in the suspensions which minimize the performance index.

The equation of motion of the uncontrolled magnet (6.6) can be written in terms of the state variables  $\tilde{h}_1$ , and  $\dot{\tilde{y}}_1$  and the input current  $\tilde{i}$  and the guideway disturbance  $\tilde{y}_o$ :

$$\frac{d}{dt} \begin{bmatrix} \tilde{h}_1 \\ \dot{\tilde{y}}_1 \end{bmatrix} = \begin{bmatrix} 0 & -1 \\ 2 & 0 \end{bmatrix} \begin{bmatrix} \tilde{h}_1 \\ \dot{\tilde{y}}_1 \end{bmatrix} + \begin{bmatrix} 0 & 1 \\ 2 & 0 \end{bmatrix} \begin{bmatrix} \tilde{i} \\ \dot{\tilde{y}}_o \end{bmatrix} \quad (6.9)$$

In this representation, the road input described by (6.1) is white noise so that the matrix ricatti techniques [54, 56] can be used to formulate the control law which minimizes the performance index of (6.8). From the matrix ricatti optimization, the current control required to minimize P.I. is:

$$\ddot{y} = \left(1 + \frac{\tilde{\omega}_1^2}{2}\right)\ddot{h}_1 - \zeta_1 \tilde{\omega}_1 \dot{y}_1 \quad (6.10)$$

where  $\tilde{\omega}_1$  = the dimensionless angular natural frequency of the suspension and  $\zeta_1$  = damping ratio.

$\tilde{\omega}_1$  and  $\zeta_1$  are functions of the relative weights  $\beta$  and  $\rho$  as depicted in Figure 6.1.\*

The suspension which minimizes P.I. is found by substituting (6.10) into (6.6):

$$\frac{\tilde{y}_1(\tilde{s})}{\tilde{y}_0(\tilde{s})} = \frac{\tilde{\omega}_1^2}{\tilde{s}^2 + 2\zeta_1 \tilde{\omega}_1 \tilde{s} + \tilde{\omega}_1^2} \quad (6.11)$$

If the road input spectral density is not described by (6.1), the optimization will yield a different form of optimum suspension; however, the control indicated by (6.10) provides a stable electromagnetic suspension. The control (6.10) is also physically realizable and is statically stiff.

Mathematically, the optimal suspension (6.10) can also be obtained using the following current control laws:

\*For  $\beta = 0$ , P.I. becomes that of Hullender (Ref. 38) for an unspecified suspension without secondary. From Fig. 6.1  $\zeta_1 = 0.707$  when  $\beta = 0$ , Hullender's result.

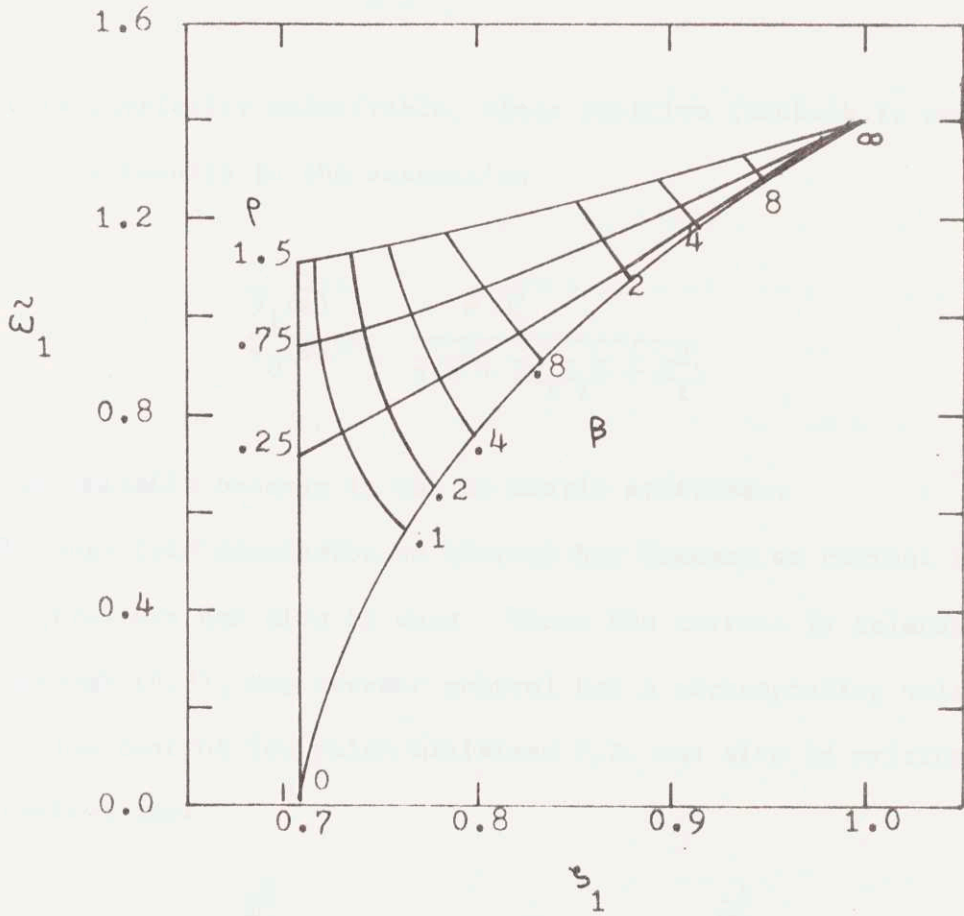


Fig. 6.1. Effects of Relative Weights on Current Controller Settings

$$\ddot{y} = \left(\frac{1}{2} + \frac{1}{\tilde{\omega}_1^2}\right)\ddot{y}_1 + \frac{2\zeta_1}{\tilde{\omega}_1} \dot{y}_1 \quad (6.12a)$$

$$\ddot{y}(\tilde{s}) = \frac{\left(\frac{1}{2\zeta_1\tilde{\omega}_1} + \frac{\tilde{\omega}_1}{4\zeta_1}\right)\tilde{s} + 1}{\frac{\tilde{s}}{2\zeta_1\tilde{\omega}_1} + 1} \ddot{h}_1(\tilde{s}) \quad (6.12b)$$

The first is physically undesirable, since positive feedback is required.

The second law results in the suspension

$$\frac{\ddot{y}_1(\tilde{s})}{\ddot{y}_0(\tilde{s})} = \frac{\tilde{s} \tilde{\omega}_1^2}{\tilde{s}(\tilde{s}^2 + 2\zeta_1\tilde{\omega}_1\tilde{s} + \tilde{\omega}_1^2)} \quad (6.13)$$

which is undesirable because it has no static stiffness.

Although this discussion on control has focused on current control, voltage controllers can also be used. Since the current is related to the voltage through (6.7), any current control has a corresponding voltage control law. The control law which minimizes P.I. can also be written as the voltage control law:

$$\tilde{v} = [v_v(1 + \frac{\tilde{\omega}_1^2}{2}) - 1]\ddot{h}_1 - v_v\zeta_1\tilde{\omega}_1\dot{y}_1 + \tilde{R}_1(1 + \frac{\tilde{\omega}_1^2}{2})\ddot{h}_1 - \tilde{R}_1\zeta_1\tilde{\omega}_1\dot{y}_1 \quad (6.14)$$

To attain the optimal suspension (6.11) with a voltage control requires measurement of the relative displacement and velocity between the magnet and the rail and the magnet's absolute velocity and acceleration. From

considerations of the optimal suspension, current control is preferred to voltage control because:

(1) to obtain optimal performance, current control requires measurement of only two variables compared to four for voltage control; and

(2) voltage control introduces into the control loop leakage fluxes (inductances) and resistances that change with gap and with temperature and which cannot easily be compensated for.

The above difficulties arise because voltage is less directly related to force than is current as shown by (6.6) and (6.7).

In industrial situations, voltage controllers are used more commonly than current controllers; however, the conversion of voltage controllers to current controllers by a feedback loop is discussed in Appendix 3.

Other performance variables such as relative displacement, current, voltage, and real power may be derived for the suspension with the current control of (6.10). The relative displacement ( $\tilde{h}_1 = \tilde{y}_0 - \tilde{y}_1$ ) is:

$$\frac{\tilde{h}_1(s)}{\tilde{y}_0(s)} = \frac{\tilde{s}^2 + 2\zeta_1\tilde{\omega}_1\tilde{s}}{\tilde{s}^2 + 2\zeta_1\tilde{\omega}_1\tilde{s} + \tilde{\omega}_1^2} \quad (6.15)$$

The current is determined by substituting (6.11) and (6.15) into (6.10)

$$\frac{\tilde{I}(\tilde{s})}{\tilde{y}_0(\tilde{s})} = \frac{(1 + \frac{\tilde{\omega}_1^2}{2})\tilde{s}^2 + 2\zeta_1\tilde{\omega}_1\tilde{s}}{\tilde{s}^2 + 2\zeta_1\tilde{\omega}_1\tilde{s} + \tilde{\omega}_1^2} \quad (6.16)$$

To determine the voltage transfer function, substitute (6.15) and (6.16) into (6.7):

$$\frac{v(s)}{y_0(s)} = \frac{\tilde{s}^3 [v_v (1 + \frac{\tilde{\omega}_1^2}{2}) - 1] + \tilde{s}^2 [2\zeta_1 \tilde{\omega}_1 (v_v - 1) + (1 + \frac{\tilde{\omega}_1^2}{2}) \tilde{R}_1] + \tilde{s} 2\zeta_1 \tilde{\omega}_1 \tilde{R}_1}{\tilde{s}^2 + 2\zeta_1 \tilde{\omega}_1 \tilde{s} + \tilde{\omega}_1^2} \quad (6.17)$$

Root mean square value for the expected outputs are calculated from (4.10) and (4.11). The rms acceleration is:

$$\text{RMS } \ddot{y}_1 = \left[ \frac{\pi \tilde{A} \tilde{V} \tilde{\omega}_1^3}{2\zeta_1} \right]^{1/2} \quad (6.18)$$

The rms relative displacement is:

$$\text{RMS } \tilde{h}_1 = \left[ \frac{\pi \tilde{A} \tilde{V}}{\tilde{\omega}_1} \left( \frac{1}{2\zeta_1} + 2\zeta_1 \right) \right]^{1/2} \quad (6.19)$$

The rms current is:

$$\text{RMS } \tilde{i} = \left[ \frac{\pi \tilde{A} \tilde{V}}{2\zeta_1 \tilde{\omega}_1} \left( \left(1 + \frac{\tilde{\omega}_1^2}{2}\right)^2 + 4\zeta_1^2 \right) \right]^{1/2} \quad (6.20)$$

The real power extracted from the mechanical system by the electrical control is implemented through the velocity feedback in the control law.

This real power which must be supplied by the vehicle's propulsion unit is

$$E[\tilde{P}_R] = \frac{E[P_R]}{2mg \sqrt{gh_{10}}} = E[\tilde{i} \tilde{v}_{ind}] = \zeta_1 \tilde{\omega}_1 E[\tilde{y}_1^2] = \frac{\pi \tilde{A} \tilde{V} \tilde{\omega}_1^2}{2} \quad (6.21)$$

Finite rms voltages in the control coil cannot be calculated from the point contact model. At high frequencies, the voltage spectrum approaches a non-zero, constant asymptote (from (6.1) and (6.17)) because the voltage

depends on the derivative of the road input which is white noise. However, finite voltages are calculated from a model which includes the finite length of the magnet (Sec. 7.4).

The root mean squares of (6.18), (6.19), and (6.20) are proportional to the square root of the road roughness ( $A^{1/2}$ ), a relation which will hold for all the rms values determined in this thesis. The output's proportionality to  $V^{1/2}$  (vehicle velocity) is valid only for models where the magnet's length is neglected. Finite magnet length alters the root mean square's dependence on velocity as outlined in Chapters 2.3.3 and 7.

Although the effects of the parameters are detailed in Section 4.3, the rms values of  $\ddot{y}_1$ ,  $\tilde{h}_1$ ,  $\tilde{I}$ , and  $\tilde{P}_R$  are plotted in Figure 6.2 for the simple magnetic suspension. These curves are plotted for  $A = 6.3 \times 10^{-7}$  ft which corresponds to welded steel rails. The air gap is 0.6 inches which is selected to allow a suspension without secondary. Forward speed ( $V$ ) of 300 mph is a design goal for high speed suspensions. The influence of eddy currents and finite magnet length on these curves is discussed in Chapters 2.3.3, 2.3.5, 7 and 10.

Figure 6.2 shows that displacement increases with decreasing natural frequency while acceleration decreases, the fundamental trade-off in suspension design. Displacement has a minimum for damping ratio of 1/2. The current has an absolute minimum at  $\tilde{\omega}_1 = 1.4$  ( $f_1 = 5.6$  hz) which corresponds to  $\beta = \infty$  in Fig. 6.7. The minimum occurs because, at low natural frequencies, displacements are large and require large currents to maintain stability while, at high frequencies, large accelerations require large forces and, therefore, currents. The real power's independence of  $\zeta_1$  is a result of the input spectrum. Since  $2mg\sqrt{gh_{10}} = 300$  kw (for  $mg = 4 \times 10^5$  nt and  $h_{10} = 0.6$  in),

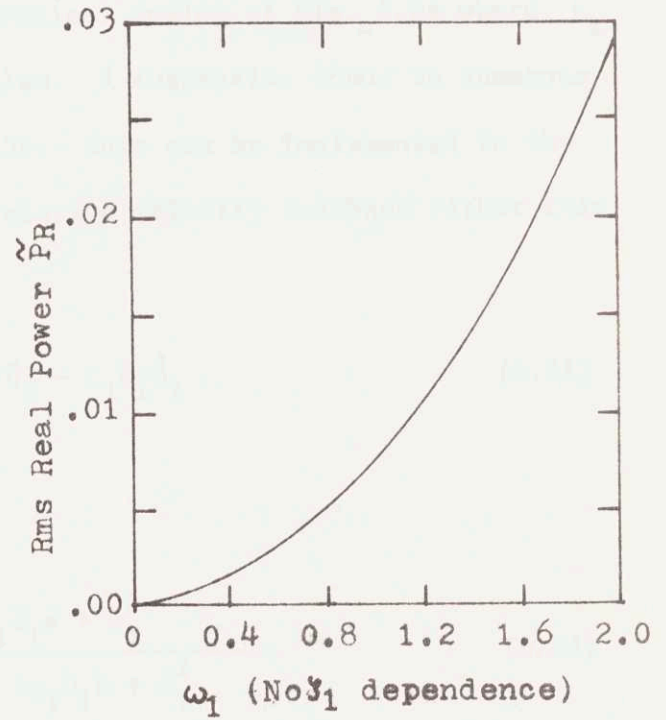
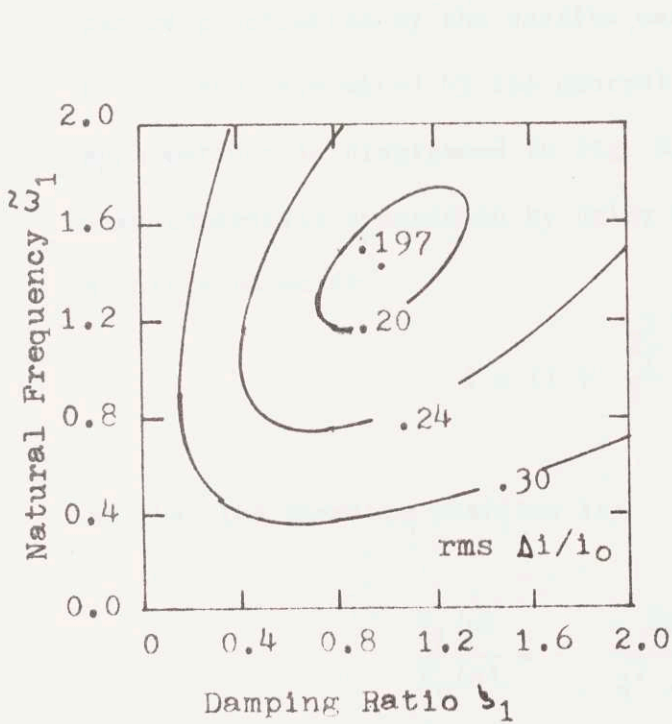
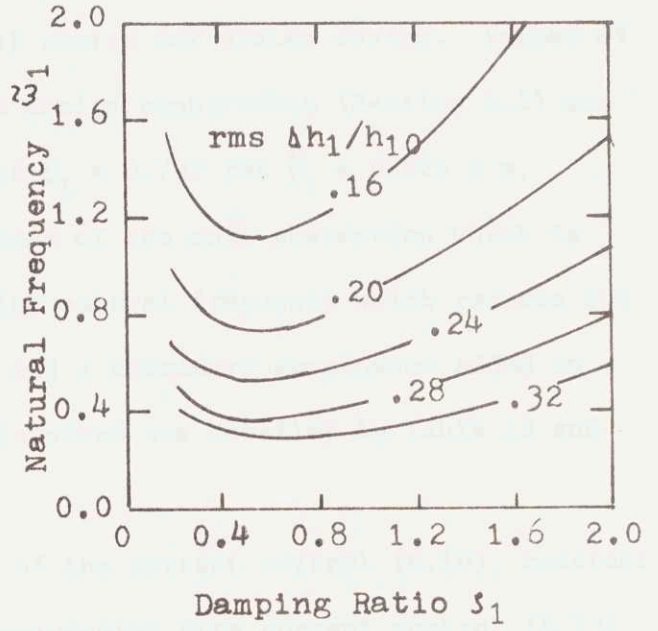
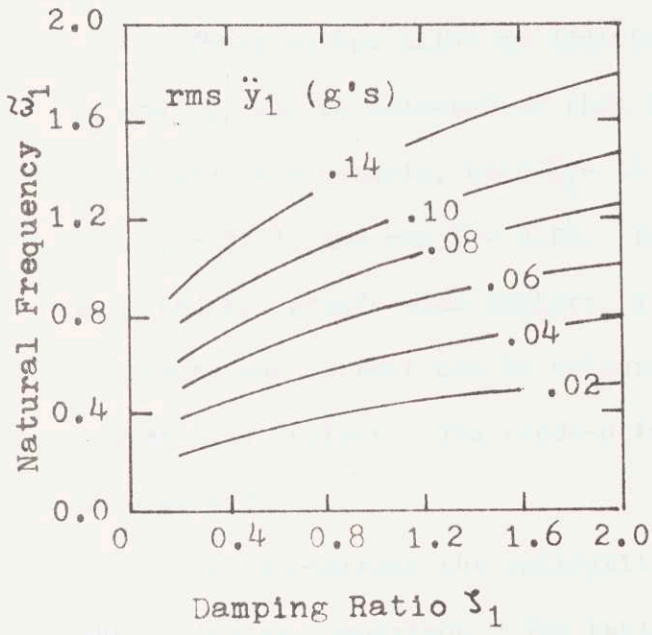


Fig. 6.2. Rms Acceleration, Displacement, Current, and Real Power for Basic Suspension ( $A = 2\pi \times 10^{-7}$  ft.,  $V = 300$  mph.)

the real power which must be supplied is small compared to magnetic drag and ohmic losses and is not considered further.

These curves allow an additional choice for system design. Values of  $\tilde{\omega}_1$  and  $\zeta_1$  can be selected so that the design constraints (Section 4.2) are satisfied; for example, with  $\tilde{\omega}_1 = .4$  and  $\zeta_1 = 0.707$  rms  $\ddot{y}_1 = 0.025$  g's, rms  $\dot{h}_1 = 0.27$ , and rms  $\ddot{y} = 0.28$ . Instead of the soft suspension which is selected to satisfy ride comfort, a high natural frequency which reduces the clearance and current can be selected and a secondary suspension added to assure ride comfort. The trade-offs involved are detailed in Table 13 and Chapter 4.3.

To demonstrate the rationality of the current control (6.10), consider the following comparison. The basic suspension with current control (6.10) can be represented by the passive mechanical analog of Fig. 6.3a where  $k_1$  and  $b_1$  are determined by the control law. A suspension found in numerous applications is diagrammed in Fig. 6.3b. This can be implemented in the electromagnetic suspension by using relative velocity feedback rather than absolute velocity:

$$\ddot{y} = \left(1 + \frac{\tilde{\omega}_1^2}{2}\right) \ddot{h}_1 - \zeta_1 \tilde{\omega}_1 \dot{h}_1 \quad (6.21)$$

so that the absolute position is:

$$\frac{\tilde{y}_1(s)}{\tilde{y}_0(s)} = \frac{2\zeta_1 \tilde{\omega}_1 \tilde{s} + \tilde{\omega}_1^2}{\tilde{s}^2 + 2\zeta_1 \tilde{\omega}_1 \tilde{s} + \tilde{\omega}_1^2} \quad (6.22)$$

With relative velocity feedback, the vehicle is locked to the road at a high rail input frequencies while, with absolute velocity feedback, the vehicle is

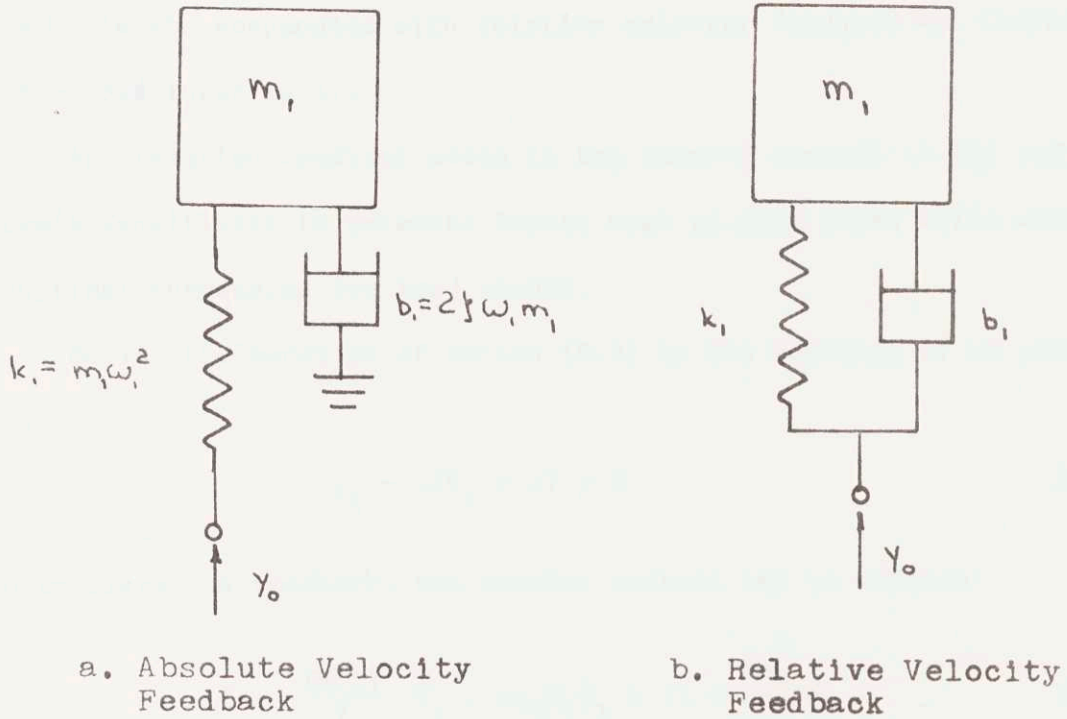


Fig. 6.3. Mechanical Analogs of Controlled Magnetic Fields.  $k_1$  and  $b_1$  are determined by control settings.

fixed to the stationary reference so the ride is more comfortable. Numerically, the suspension with absolute velocity feedback has finite rms accelerations while the suspension with relative velocity feedback has finite rms  $\ddot{y}_1$  for the road input (6.1).

Acceleration feedback added to the current control (6.10) reduces the system's sensitivity to external inputs such as wind gusts while maintaining the optimal suspension for road inputs.

Modify the equation of motion (6.6) by the addition of an external force

$$\ddot{y}_1 = -2\tilde{h}_1 + 2\tilde{I} + \tilde{w} \quad (6.23)$$

With acceleration feedback, the current control may be written:

$$\tilde{I} = -\frac{(\tilde{m}-1)}{2} \ddot{y}_1 - \tilde{m}\zeta_1\tilde{\omega}_1\dot{y}_1 + \left(1 + \frac{\tilde{m}\omega_1^2}{2}\right)\tilde{h}_1 \quad (6.24)$$

where  $\tilde{m} > 1$  and is selected by the controller. Inserting (6.24) into (6.23):

$$\ddot{y}_1 (\tilde{s}^2 + 2\zeta_1\tilde{\omega}_1\tilde{s} + \tilde{\omega}_1^2) = \tilde{\omega}_1^2 \tilde{y}_0 + \frac{\tilde{w}}{\tilde{m}} \quad (6.25)$$

The acceleration feedback has increased the effective mass of the vehicle so that the effects of external inputs are reduced as shown by (6.25). Acceleration feedback is not pursued further in this thesis since the transfer functions that relate output variables to the road inputs are identical when either (6.10) or (6.25) is used.

The importance of feeding back the average displacement between the magnet and rail, rather than the displacement measured at a point is developed in the next section.

## 7. FINITE MAGNET LENGTH

### 7.1 Characteristics of Finite Length Filtering

Guideway irregularities of short wavelength (which correspond to high input frequencies by (6.2) are averaged by the magnet's finite length which essentially filters the input. The properties of the finite length filter and its influence upon system design are discussed.

The importance of this filtering is seen in the linearized force (6.6) where the force depends on the air gap averaged over the area of the pole face; i.e.

$$\Delta \ddot{F} = \ddot{\tilde{y}}_1 = 2\ddot{y} - 2\ddot{h}_{1-av} \quad (7.1)$$

This averaging of the air gap will alter the point contact model, where the air gap was assumed uniform, and where the clearance measured at any point is identical to the average clearance. The voltage is:

$$\tilde{v} = v \dot{y} - \dot{h}_{1-av} + \dot{y} R_1 \quad (7.2)$$

The filter effects for the linearized model are evaluated by considering the roadway to consist of sinusoids as shown in Fig. 2.6. This approach will allow the input measured at the midpoint ( $y_{0-p}$ ) of the magnet to be transformed into a clearance averaged over the entire magnet length ( $y_{0-av}$ ). At any point the road input is (Fig. 2.6):

$$\Delta y_{0-p}(x) = Y_0 \sin \frac{2\pi}{\lambda} (x)$$

This height is averaged over the magnet's length

$$\Delta Y_{0-av} = \frac{Y_0}{l_1} \int_{Vt-l_1/2}^{Vt+l_1/2} \sin \left[ \frac{2\pi}{\lambda} x \right] dx$$

which yields

$$\Delta y_{0-av} = \frac{\lambda}{l_1 \pi} \sin \frac{\pi l_1}{\lambda} [Y_0 \sin \frac{2\pi}{\lambda} Vt] = \frac{\lambda}{l_1 \pi} \sin \frac{\pi l_1}{\lambda} y_{0-p}$$

where  $l_1$  = length of the magnet

(7.3)

$\lambda$  = wavelength of rail irregularities

When  $\lambda$  is much greater than  $l_1$ , the average and the point value of the gap are identical, but when  $l_1 \gg \lambda$ , the average height is zero. The finite length averaging is displayed in Fig. 2.7 and is transformed to the frequency domain by (6.2):

$$y_{0-av}(j\omega) = F_{mag}(\omega) y_{0-p}(j\omega)$$

(7.4)

where

$$F_{mag}(\omega) = \frac{2V}{l_1 \omega} \sin \frac{\omega l_1}{2V}$$

The dimensionless spectral density of the average road input is:

$$\tilde{\phi}_{y_0 y_0}(\tilde{\omega}) = \frac{\Delta V}{\tilde{\omega}^2} (F_{mag}[\tilde{\omega}])^2$$

(7.5)

For heave motion, the magnet displacement  $\tilde{y}_1$  has an average equal to the point measurement; i.e.,  $\tilde{y}_{1-p} = \tilde{y}_{1-av} = \tilde{y}_1$ . The average clearance which appears in the force equation (7.1) is:

$$\tilde{h}_{1-av} = \tilde{y}_{0-av} - \tilde{y}_1$$

(7.6)

The total force is related to the average gap; however, in the current control law (6.10), the displacement used ( $\tilde{h}_c$ ) can be selected. In general:

$$\tilde{h}_c(\tilde{s}) = G(\tilde{s}) \tilde{h}_{1-p}(\tilde{s}) \quad (7.7)$$

Three possibilities for the displacement used in the control law are:

(1) When  $G = 1$ , the controller uses the displacement measured at the magnet's midpoint.

(2) When  $G = F(\omega)$ , the controller employs the average displacement between the rail and the magnet.

(3)  $G(s)$  can be a filter designed into the control system. Further considerations show that the average displacement should be used in the control.

If the average displacement is used:

$$\tilde{y} = \left(1 + \frac{\tilde{\omega}_1^2}{2}\right) h_{1-av} - \zeta_1 \tilde{\omega}_1 \dot{\tilde{y}}_1 \quad (7.8)$$

The absolute displacement, the average relative displacement, the current, and the voltage are given by (6.13), (6.15), (6.16), and (6.17) respectively where the input at a point is replaced by the average input. Two relative displacements are defined. The average relative displacement is given by (7.6). For consideration of rail-magnet clearance, a more realistic indicator is the gap at the midpoint of the magnet:

$$\tilde{h}_{1-p} = \tilde{y}_{0-p} - \tilde{y}_1 \quad (7.9)$$

$$\frac{h_{1-p}(s)}{y_{0-p}(s)} = \frac{\tilde{s}^2 + 2\zeta_1 \tilde{\omega}_1 \tilde{s} + \tilde{\omega}_1^2 [1 - F_{mag}(\omega)]}{DEN} \quad (7.10)$$

$$\text{when DEN} = \tilde{s}^2 + 2\zeta_1 \tilde{\omega}_1 \tilde{s} + \tilde{\omega}_1^2 .$$

When the average gap is used in the control law, the expected voltages are finite as shown in Fig. 7.1 where the apparent power is plotted. The apparent power which does not include ohmic heating is defined as:

$$P_A = \tilde{v}_{\text{ind rms}} \tilde{i}_{\text{(rms)}} = \frac{\tilde{i}_{\text{rms}} \tilde{AV}}{j} \int_{-j\infty}^{+j\infty} F_{\text{mag}}^2(\tilde{\omega}) \left| \frac{[\tilde{v}_v (1 + \frac{\tilde{\omega}_1^2}{2}) - 1] \tilde{s}^2 + 2\zeta_1 \tilde{\omega}_1 (\nu_v - 1) \tilde{s}}{\text{DEN}} \right|^2 ds$$

The power is plotted rather than the voltage because the voltage can be altered by changing the number of turns (hence,  $i_0$ ) while the power is independent of the number of turns. For our sample designs, the apparent power is about 18 kw. which compares with ohmic power of 50 kw.

With the point measurement in the current control, the absolute position is:

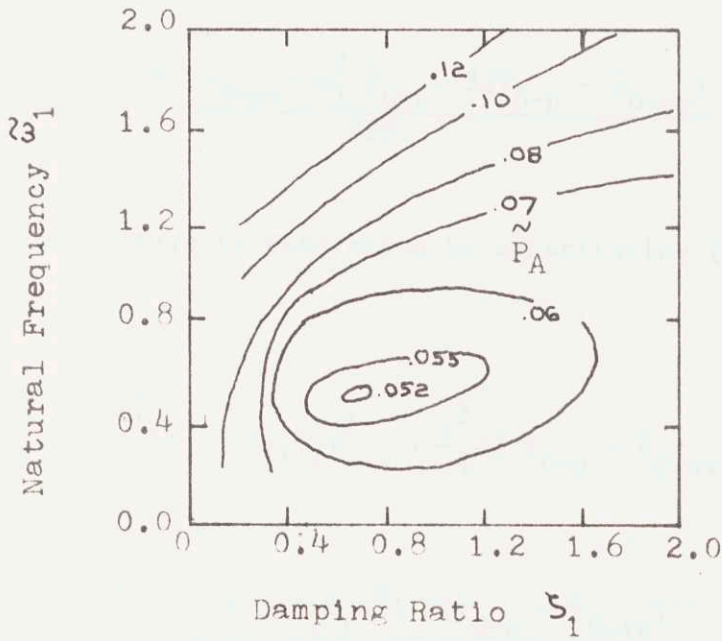
$$\tilde{y}_1(\tilde{s}) = \frac{\tilde{\omega}_1^2 \tilde{y}_{0-p}(\tilde{s})}{\text{DEN}} + \frac{2[\tilde{y}_{0-p}(\tilde{s}) - \tilde{y}_{0-av}(\tilde{s})]}{\text{DEN}} \quad (7.11)$$

The relative position measured at the magnet's midpoint is:

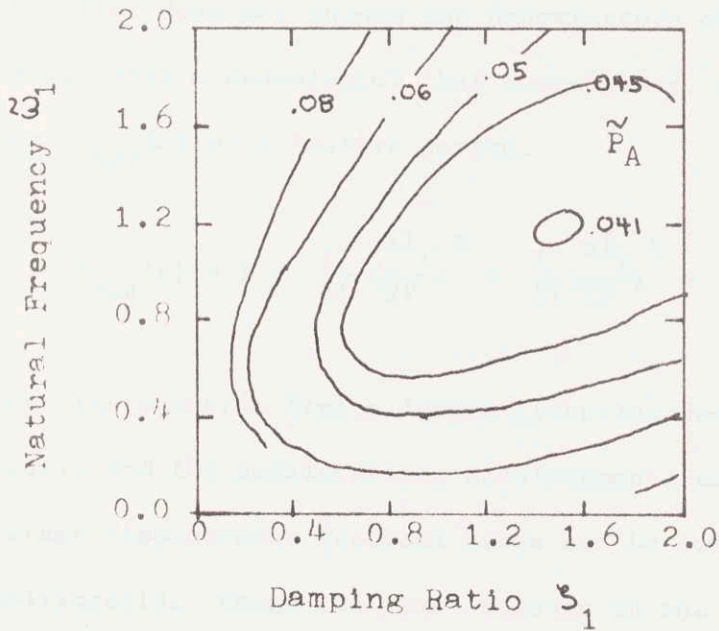
$$\tilde{h}_{1-p}(\tilde{s}) = \frac{\tilde{s}^2 + 2\zeta_1 \tilde{\omega}_1 \tilde{s}}{\text{DEN}} \tilde{y}_{0-p}(\tilde{s}) - \frac{2[\tilde{y}_{0-p}(\tilde{s}) - \tilde{y}_{0-av}(\tilde{s})]}{\text{DEN}} \quad (7.12)$$

The control current is:

$$\tilde{i}(\tilde{s}) = \frac{\{(1 + \frac{\tilde{\omega}_1^2}{2}) \tilde{s}^2 + 2\zeta_1 \tilde{\omega}_1 \tilde{s}\} \tilde{y}_{0-p}}{\text{DEN}} - \frac{(1 + \frac{\tilde{\omega}_1^2}{2} + \zeta_1 \tilde{\omega}_1 \tilde{s}) 2(\tilde{y}_{0-p} - \tilde{y}_{0-av})}{\text{DEN}}$$



a.  $L_1 = 1.73$ ,  $l_1 = 10$  ft.



b.  $L_1 = 2.18$ ,  $l_1 = 30$  ft.

Fig. 7.1. Apparent Power for Designs 2 and 4 of Table 3.  
 $A = 2\pi \times 10^{-7}$  ft.,  $V = 300$  mph.



An alternative to feeding back the average displacement between the magnet and rail measures the displacement at the magnet's midpoint and passes this signal through a filter  $G(s)$  before entering the feedback control so that:

$$\ddot{Y} = \left(1 + \frac{\tilde{\omega}_1^2}{2}\right) G(\tilde{s}) \tilde{h}_{1-p} - \zeta_1 \tilde{\omega}_1 \dot{\tilde{y}}_1 \quad (7.16)$$

Since the envelope of the finite magnet length's filtering is  $1/s$  as shown in (7.4), a filter  $G(\tilde{s})$  would produce results (i.e. finite voltages) similar to the average displacement feedback  $G = F_{\text{mag}}$  if  $G(s)$  decreases in a manner similar to  $F_{\text{mag}}(\tilde{\omega})$ . At low frequencies the clearance in the feedback should not be altered; therefore, a first order lag is suggested:

$$G(\tilde{s}) = \frac{1}{1 + \tilde{T}\tilde{s}} \quad (7.17)$$

where  $\tilde{T}$  is an adjustable parameter whose impact is studied.

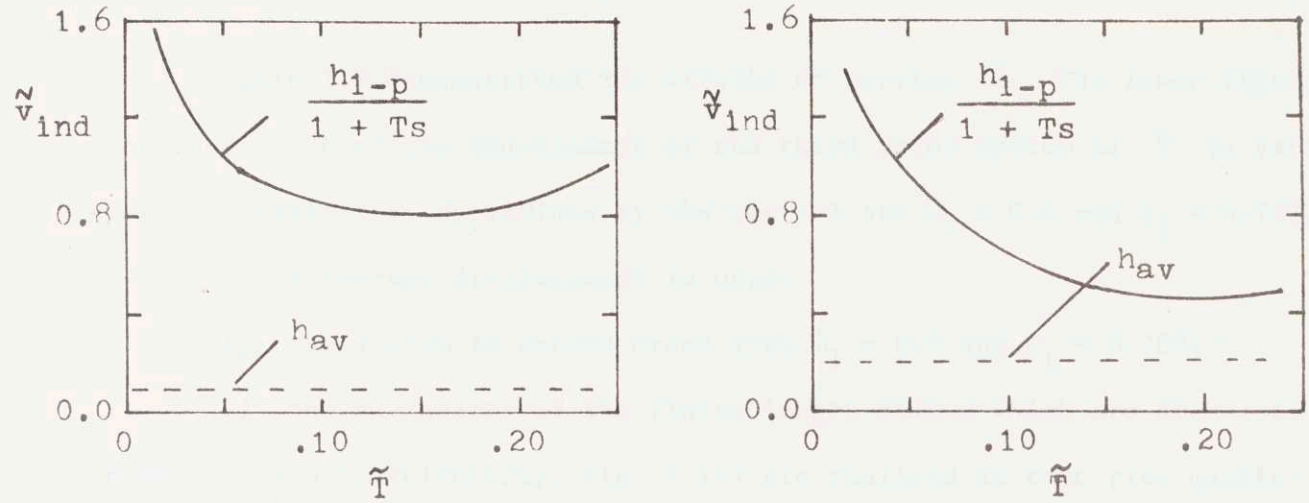
The transfer function of the absolute displacement is then

$$\frac{\tilde{y}_1(\tilde{s})}{\tilde{y}_{0-p}(\tilde{s})} = \frac{2\left(1 + \frac{\tilde{\omega}_1^2}{2}\right) - 2F_{\text{mag}}(\tilde{\omega}) [\tilde{T}\tilde{s} + 1]}{\tilde{T}\tilde{s}^3 + (1 + 2\zeta_1\tilde{\omega}_1\tilde{T})\tilde{s}^2 + (2\zeta_1\tilde{\omega}_1 - 2\tilde{T})\tilde{s} + \tilde{\omega}_1^2} \quad (7.18)$$

The clearance at a point is given by (7.8) and the current is determined by (7.16). The voltage with no ohmic terms is:

$$\tilde{v}_{\text{ind}} = v_v \dot{\tilde{I}} - \dot{\tilde{h}}_{1-\text{av}}$$

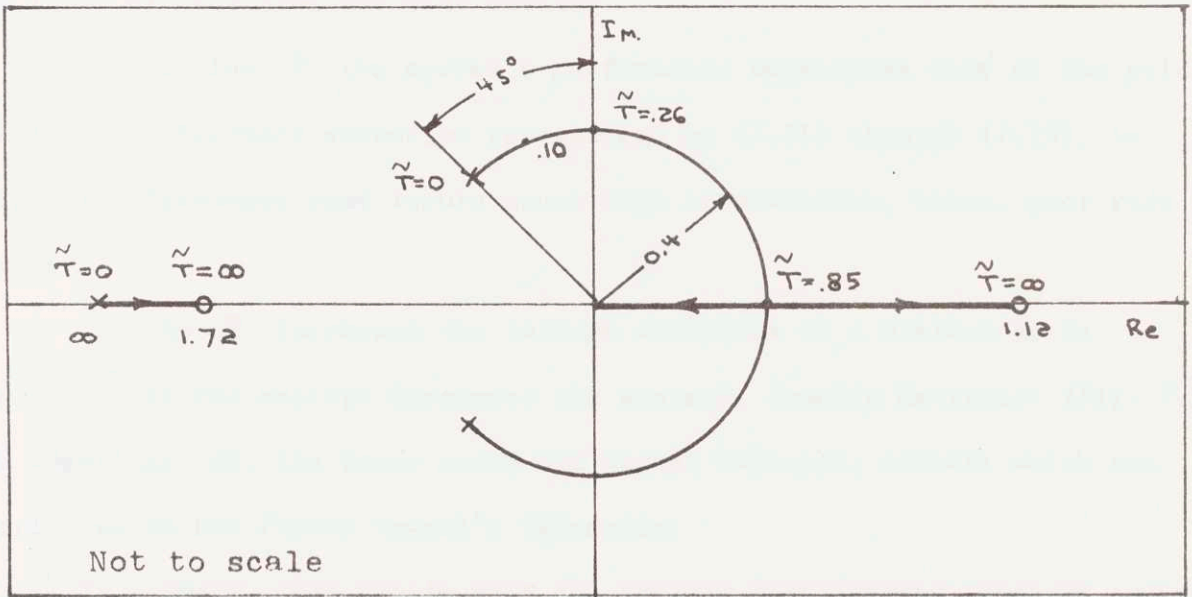
When  $\tilde{T}\tilde{s}$  is small the system's performance is that of the point contact model. At high frequencies, the clearance that is inserted in the controller is reduced by the filter so that the voltages are finite.



$V = 100 \text{ mph}$ ,  
 $A = 6\pi \times 10^{-7} \text{ ft}$ .

$V = 300 \text{ mph}$ ,  
 $A = 2\pi \times 10^{-7} \text{ ft}$ .

a. Voltage in Control Coil. Solid and broken lines are for indicated control strategies.



b. Root Locus as  $\tilde{T}$  Varies

Fig. 7.2. Effects of Feeding Back  $\frac{h_{1-p}}{(1 + Ts)}$ .  
 Magnet Design 2 of Table 3,  $v_v = 2.18$ ,  $l_1 = 30 \text{ ft}$ .,  
 $\zeta_1 = 0.4$ ,  $\xi_1 = 0.707$ , and no secondary suspension.

Figure 7.2 demonstrates the effects of varying  $\tilde{T}$ . The lower figure is a root locus of the denominator of the third order system as  $\tilde{T}$  is varied where the parameters determined by the control are  $\tilde{\omega}_1 = 0.4$  and  $\zeta_1 = 0.707$ .

If the average displacement is used:

- (1) the system is second order with  $\tilde{\omega}_1 = 0.4$  and  $\zeta_1 = 0.707$ ;
- (2) the advantages of the finite length filter which are discussed in Chapter 4.3 (particularly, Fig. 4.14) are realized so that ride quality is improved at higher frequencies; and
- (3) the rms voltage is as shown in Fig. 7.2.

If the point displacement with the filter (7.17) is used:

- (1) The eigenvalues of the system are functions of  $\tilde{T}$  (Fig. 7.2). Increasing  $\tilde{T}$  lowers the damping of the system which (shown in Chapter 4.3 and Table 6) decreases the ride quality.
- (2) For low  $\tilde{T}$  the system's performance approaches that of the point displacement feedback situation represented by (7.11) through (7.15), in which high frequency road inputs cause high acceleration, hence, poor ride quality.

(3) As  $\tilde{T}$  increases the voltage decreases to a minimum as in Fig. 7.2. As the voltage decreases the system's damping decreases (Fig. 7.2). For identical AV, the lower speed has higher voltages, effects which are attributed to the finite length's filtering.

In summary, this thesis uses the average displacement feedback rather than that at a point because:

- (1) The inductive voltages are lower than point measurements with (7.17) (at  $\tilde{T} = 0.05$ , the differences are greater than a factor of five).

(2) The system with average displacement has better ride quality because the system's damping is not reduced by the filter and because the absolute accelerations depend only on the average road input which is much smaller than the point input at higher frequencies.

The effects of magnet length and vehicle speed on system dynamics for an electromagnetic suspension with average displacement feedback (7.7) are discussed in Chapter 4.3.

Several suggestions for measuring the average displacements are possible. The average magnetic fields over a region can be measured by search coils or bismuth spirals and related to the displacement through (4.5). The forces exerted by the magnet could be measured by force transducers and related to the average displacement through (5.10). These techniques are valid when the iron is not in regions near saturation or when eddy current effects can be neglected. More direct techniques measure the displacement at a point which is then averaged by a signal processor. A single sensor could be placed at the leading edge and the following algorithm used:

$$h_{1-av}(t) = \frac{1}{T} \int_{t-T}^t h_{1-p}(\tau) d\tau$$

where  $t$  is the present time and  $T = l_1/V$  is the transit time of the magnet.

8. NON-LINEAR SIMULATIONS

Although our analyses focus on linearized models, non-linear effects are evaluated to identify the region of validity for the linearized results. Analog computer simulations of transient responses to initial displacements and frequency responses of the non-linear force-current-gap relation (6.5) with current control (6.10) are conducted.

Combining the open loop non-linear equations of motion (6.5) and the control law (6.10) gives the non-linear closed loop equations of motion:

$$\ddot{\tilde{y}}_1 + 1 = \left[ \frac{1 + (1 + \frac{\tilde{\omega}_1^2}{2})\tilde{h}_1 - \zeta_1 \tilde{\omega}_1 \dot{\tilde{y}}_1}{1 + \tilde{h}_1} \right]^2 \quad (8.1)$$

where the voltage is:  $\tilde{v} = \tilde{v}_{ind} + \tilde{R}_1 \tilde{i}$

$$\tilde{v} = \frac{v_v}{\tilde{h}_1} \left[ (1 + \frac{\tilde{\omega}_1^2}{2})\tilde{h}_1 - \zeta_1 \tilde{\omega}_1 \ddot{\tilde{y}}_1 \right] - \left[ \frac{\tilde{h}_1}{\tilde{h}_1^2} - \tilde{R}_1 \right] \left[ 1 + (1 + \frac{\tilde{\omega}_1^2}{2})\tilde{h}_1 - \zeta_1 \tilde{\omega}_1 \dot{\tilde{y}}_1 \right] \quad (8.2)$$

where leakage coefficient  $v_v = 1 + k_v y$

nondimensional time  $\tilde{t} = t \sqrt{\frac{g}{h_{10}}}$

In the model, a limiter is placed on the current controller so that the current cannot become negative (i.e.,  $1 + \tilde{i} > 0$ ) and the current is reduced to zero before the magnet contacts the rail ( $\tilde{h}_1 = 1$ ) so that the magnet cannot stick to the rail.

Figure 8.1 shows the static suspension forces which are exerted by the magnet with the current control with limiter. The static

suspension force is defined from (8.1):

$$\tilde{F}_{\text{sus}} = \left| \frac{1 + (1 + \frac{\tilde{\omega}_1^2}{2})\tilde{h}_1}{1 + \tilde{h}_1} \right|^2 - 1 \quad (8.3)$$

As the magnet approaches the rail the suspension's static stiffness increases as indicated in Fig. 8.1. At small clearances the stiffness increases rapidly as the gap changes. The current ( $\tilde{i}$ ) with limiter versus the change from nominal gap ( $\tilde{h}_1$ ) is plotted in Fig. 8.2 for zero magnet velocity.

Typical wave forms for the acceleration versus time for high frequency road inputs are shown in Fig. 8.3. Figure 8.4 shows the dimensionless acceleration gain  $|\tilde{y}_1/\tilde{y}_0|$  versus the frequency of the sinusoidal road input ( $\tilde{y}_0$ ) for several input amplitudes. The **asymmetry** of the peaks at frequencies above the natural frequency is caused by the asymmetric nature of the suspension force about the nominal position ( $\tilde{h}_1 = 0$ ) as shown in Fig. 8.1. Since the average of the positive and negative peaks lies close to the linear model result, the calculations based on the spectral density of the linearized system will be accurate.

Figure 8.5 portrays a sample of the dimensionless voltage where the asymmetry of the acceleration plots appears again. As for the acceleration, voltage calculations based on spectral density are adequate for design use.

In a linear system, an input with zero mean produces an output with zero mean; however, for the non-linear magnetic suspension, a zero mean guideway input ( $\tilde{y}_0$ ) produces a mean value of displacement, current, and voltage, but not acceleration. At frequencies greater than the suspension's natural frequency, the average gap as shown in Fig. 8.6 is

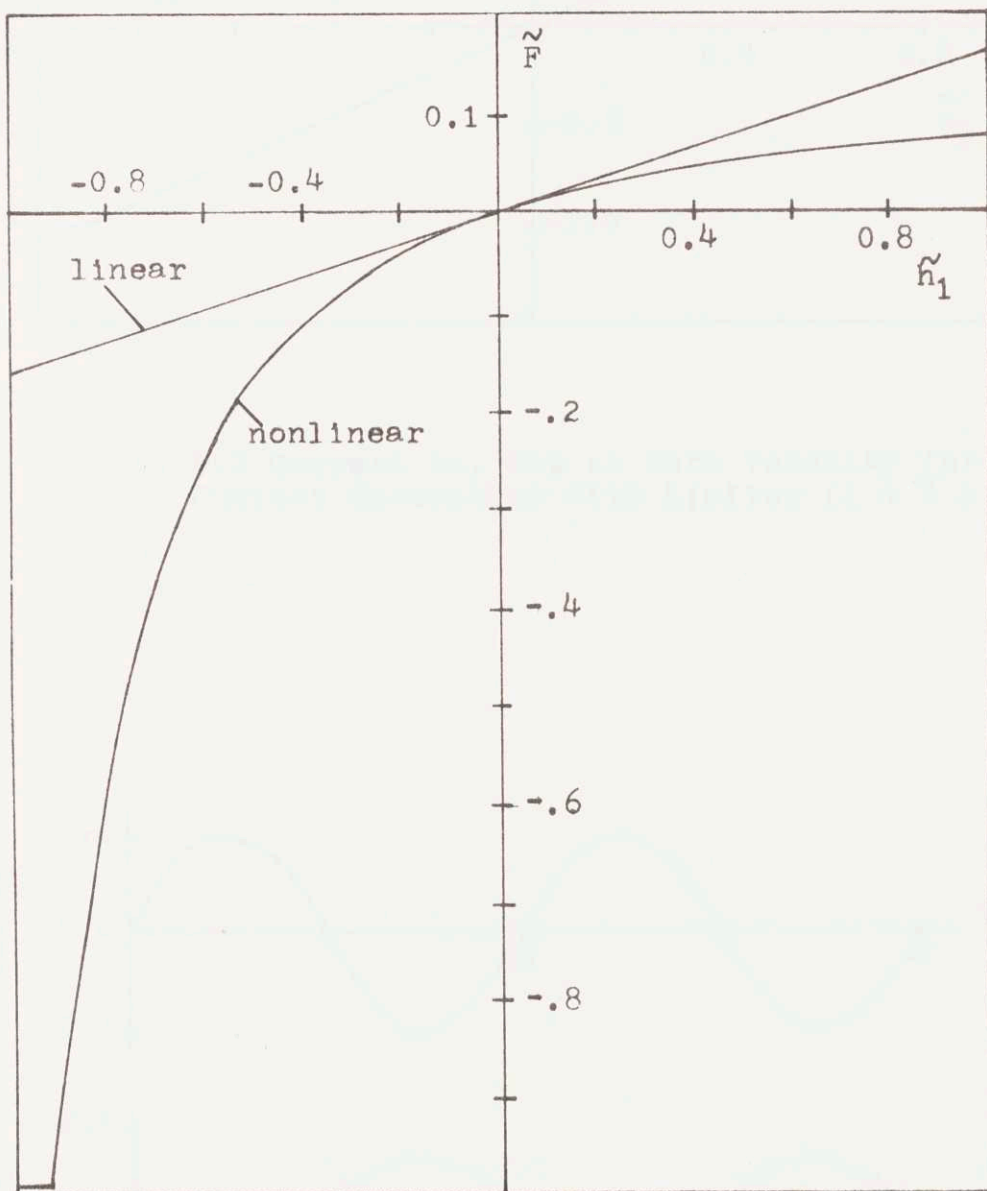


Fig. 8.1. Static Suspension Force vs. Air Gap for Nonlinear Suspension with Current Control ( $\tilde{\omega}_1 = 0.4$ )

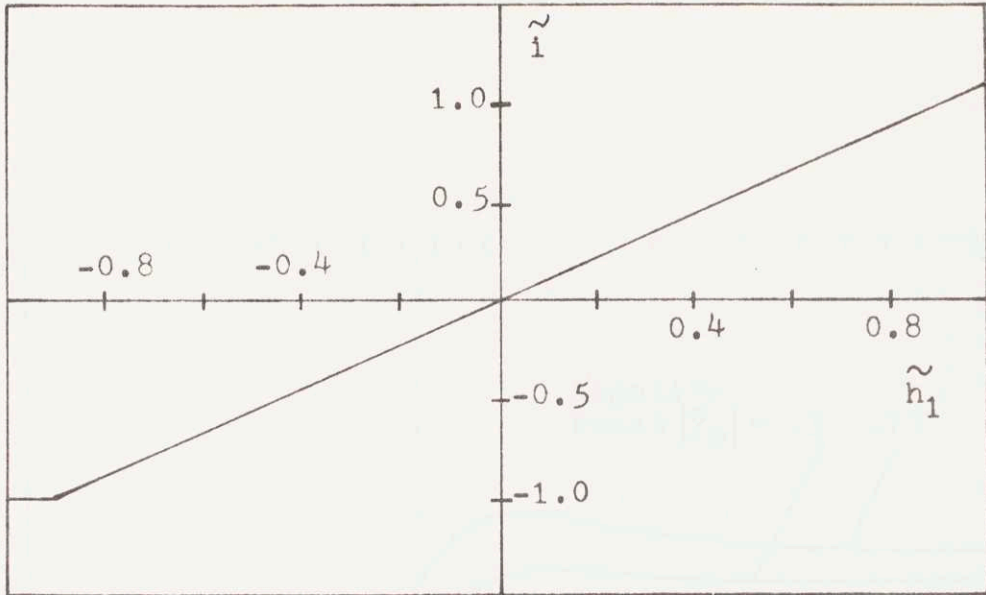


Fig. 8.2 Current vs. Gap at Zero Velocity for Current Controller with Limiter ( $1 + \tilde{i} \geq 0$ )

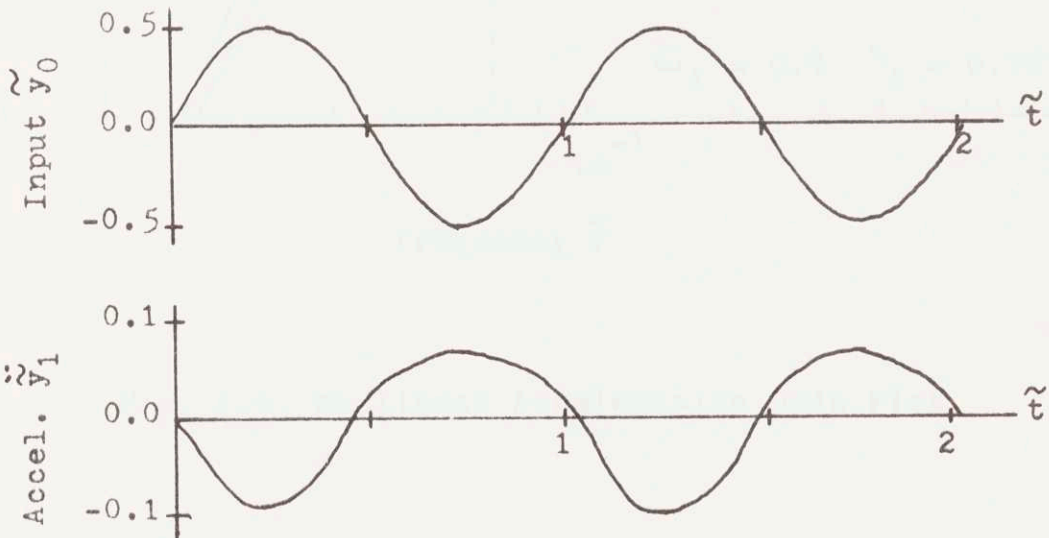


Fig. 8.3. Road Input and Acceleration vs. Time for High Input Frequency ( $\tilde{\omega}_1 = 0.4, \tilde{\zeta}_1 = 0.707$ )

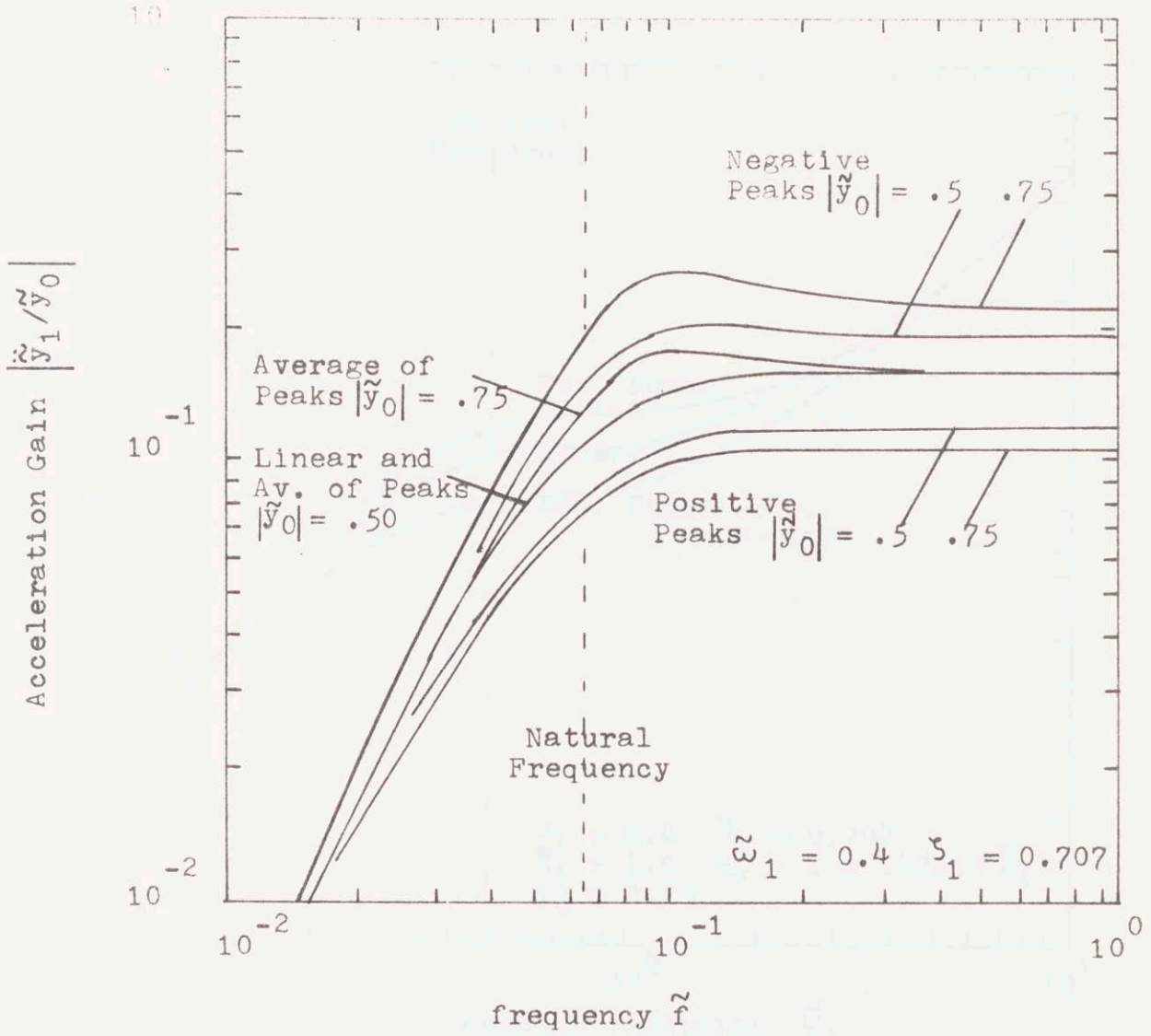


Fig. 8.4. Nonlinear Acceleration Bode Plot

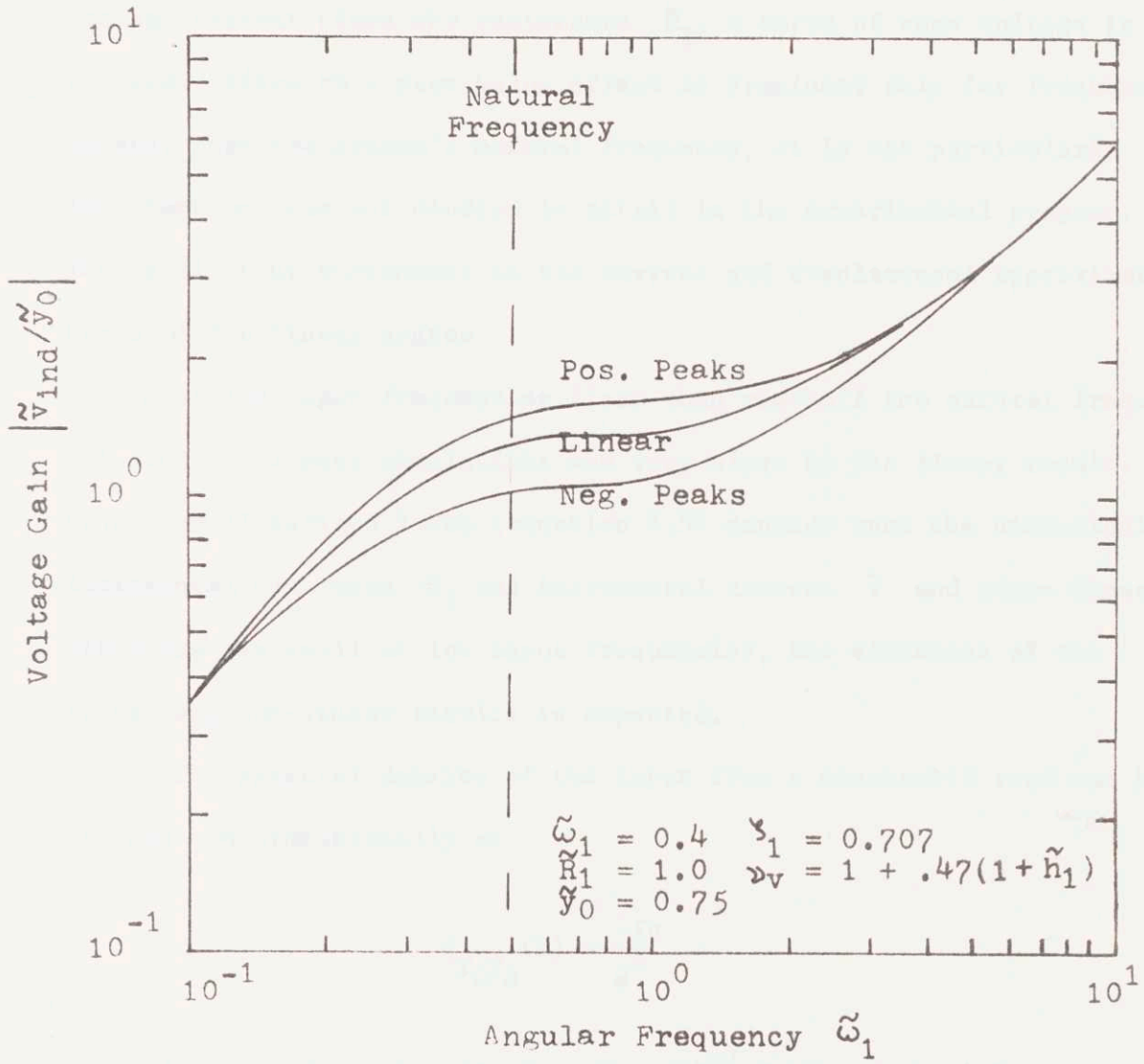


Fig. 8.5. Nonlinear Voltage Bode Plot

larger than the nominal gap. To maintain equilibrium, the average current as shown in Fig. 8.7 must increase and in turn the average voltage increases to overcome ohmic losses. Since the voltage mean value is the average current times the resistance  $\tilde{R}_1$ , a curve of mean voltage is omitted. Since this mean value effect is prominent only for frequencies greater than the system's natural frequency, it is not particularly important and was not studied in detail in the experimental program. The oscillating components of the current and displacement approximate those of the linear system.

At low input frequencies (less than one-half the natural frequency), the non-linear simulations are very close to the linear result. Since the linearized force (equation 6.5) depends upon the dimensionless incremental clearance  $\tilde{h}_1$  and incremental current  $\tilde{I}$  and since these variables are small at low input frequencies, the closeness of the linear and non-linear results is expected.

The spectral density of the input from a stochastic road can be written non-dimensionally as

$$\tilde{\phi}_{\tilde{y}_0\tilde{y}_0}(\tilde{s}) = \frac{-\tilde{A}\tilde{V}}{\tilde{s}^2}$$

where for welded steel rails ( $A = 2\pi \times 10^{-7}$  ft.) and the 1.5 cm nominal clearance and 300 mph speed,  $\tilde{A}\tilde{V} = 0.0044$ . Thus, the rms height of inputs with frequency greater than a given frequency  $\tilde{\omega}$  is:

$$[\text{RMS } \tilde{h}_1]^2 = 2\tilde{A}\tilde{V} \int_{\tilde{\omega}_0}^{\infty} \frac{d\tilde{s}}{\tilde{s}^2} = \frac{2\tilde{A}\tilde{V}}{\tilde{\omega}_0} .$$

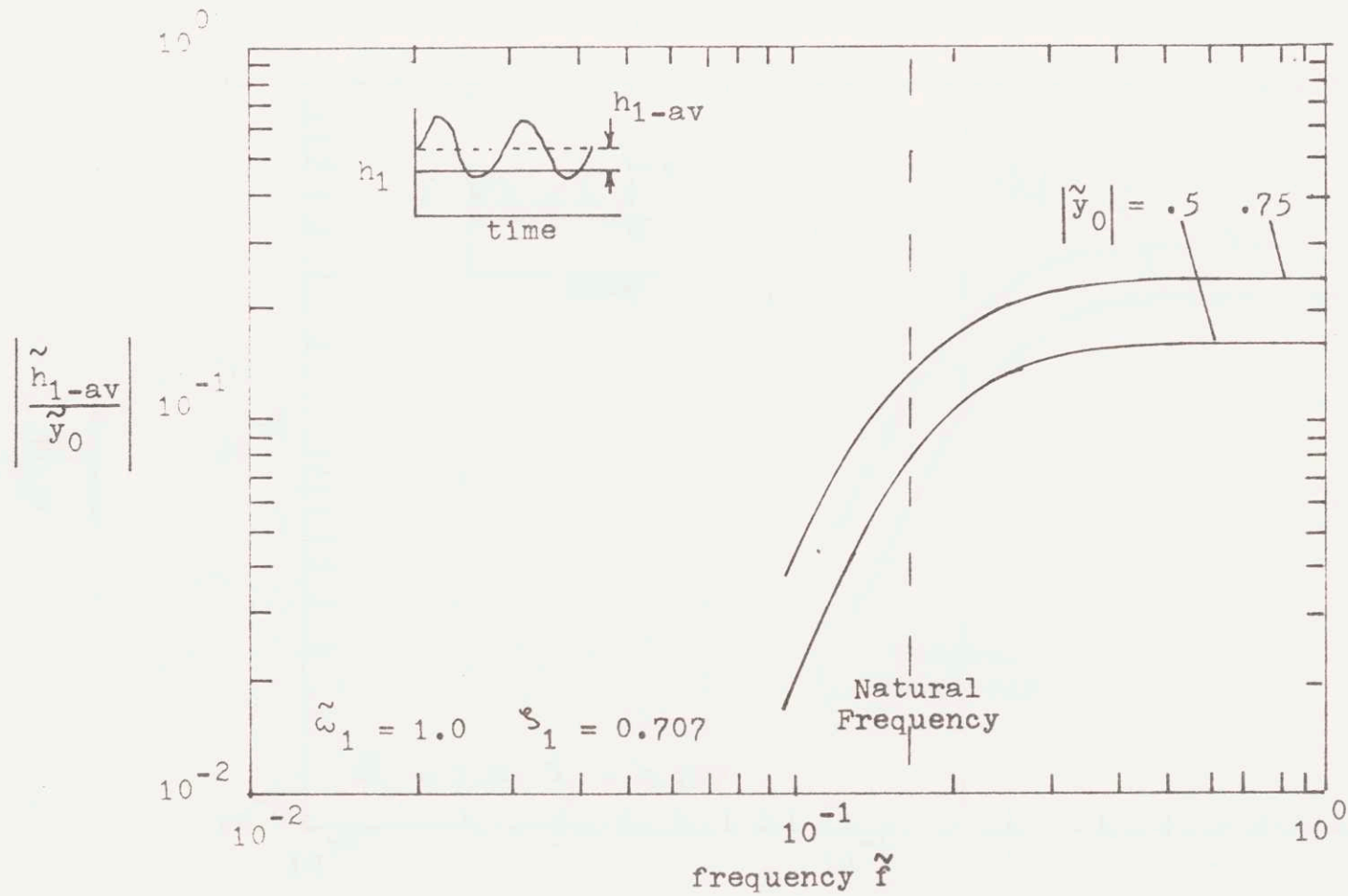


Fig. 8.6. Average Air Gap vs. Frequency

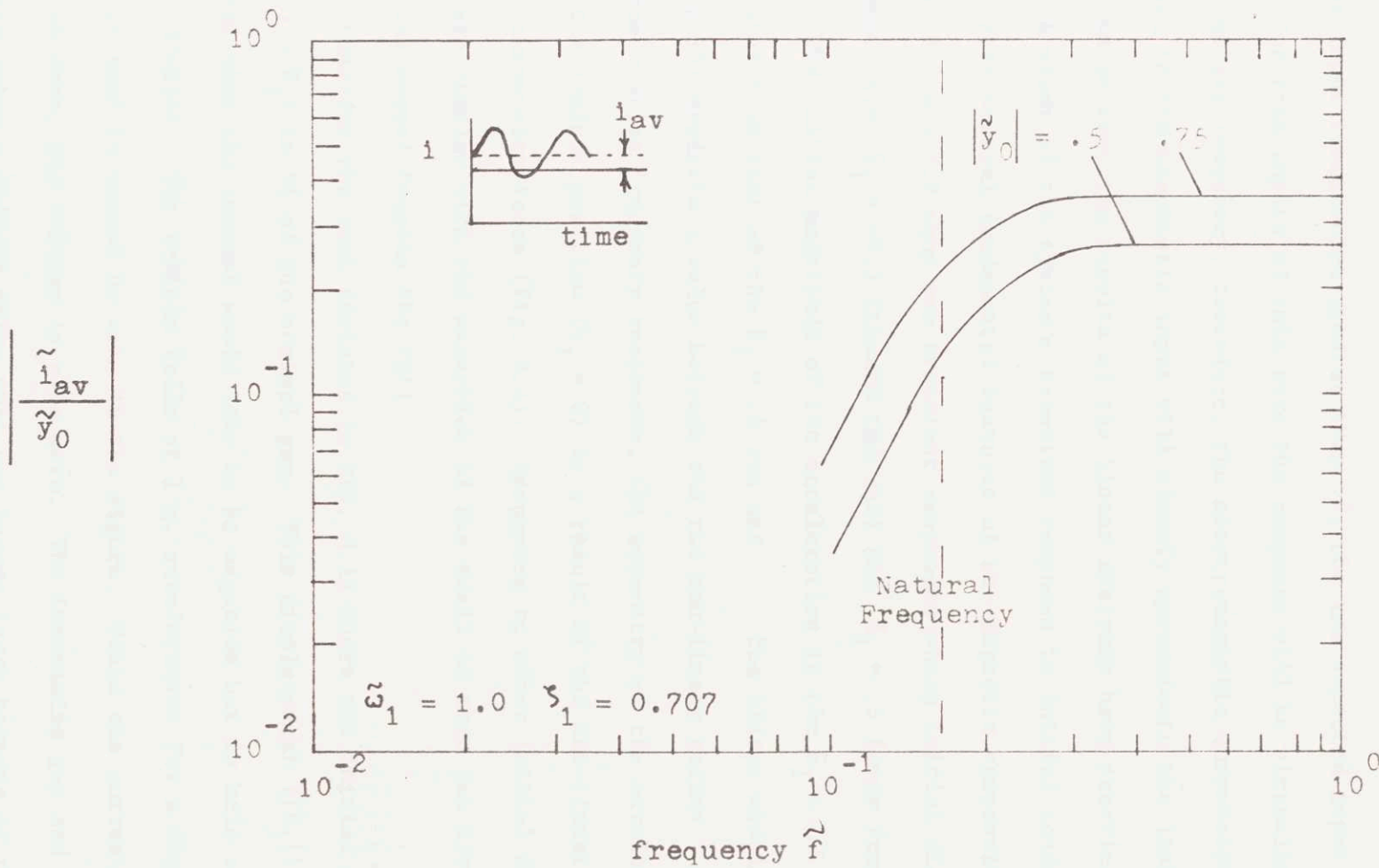


Fig. 8.7. Average Current vs. Frequency

A system with  $\tilde{\omega}_0 = 0.2$  (which corresponds to  $\omega_1 = 1.6$  hz for  $h_{10} = 0.6$  in.) will behave linearly for dimensionless input frequencies less than .2 and for input frequencies greater than .2, the rms expected input is 0.21. For road inputs of this size the response will be virtually linear at any frequency; therefore, the electromagnetic suspension's response to the stochastic input will closely approximate the linear situation so that the results of the linear analyses have practical worth.

A study of the system's transient response to initial conditions illustrates several fundamental features of the magnetic suspension. Figures 8.8 and 8.9 show two transient responses where initial displacements are  $\tilde{h}_1 = -0.5$  (toward the rail) and  $\tilde{h}_1 = .5$  (away from the rail). The initial magnitude of the acceleration in the  $\tilde{h}_1 = -.5$  case is greater than that of the  $\tilde{h}_1 = .5$  run and the linear model (Fig. 8.10) predicts a value between the two non-linear values. As in the acceleration frequency responses, the asymmetry of the accelerations about the nominal position ( $\tilde{h}_1 = 0$ ) is a result of the non-linearities in the suspension force (Fig. 8.1). Responses to other initial displacements are similar with the exception of the small or zero gap situation where the magnet touches the rail.

Consider the test depicted in Fig. 8.11 where the initial clearance ( $1 + \tilde{h}_1$ ) is 5% of the nominal gap. This displacement ( $|\tilde{h}_1|$ ) is so large that the current would like to be negative but is held at zero by the limiter. The vehicle falls at 1 g. acceleration for a duration so short that it cannot be seen in the figure. Since the current is fixed at zero, the voltage is also zero. The increasing gap and downward velocity cause a voltage spike that can become large because of the small gap.

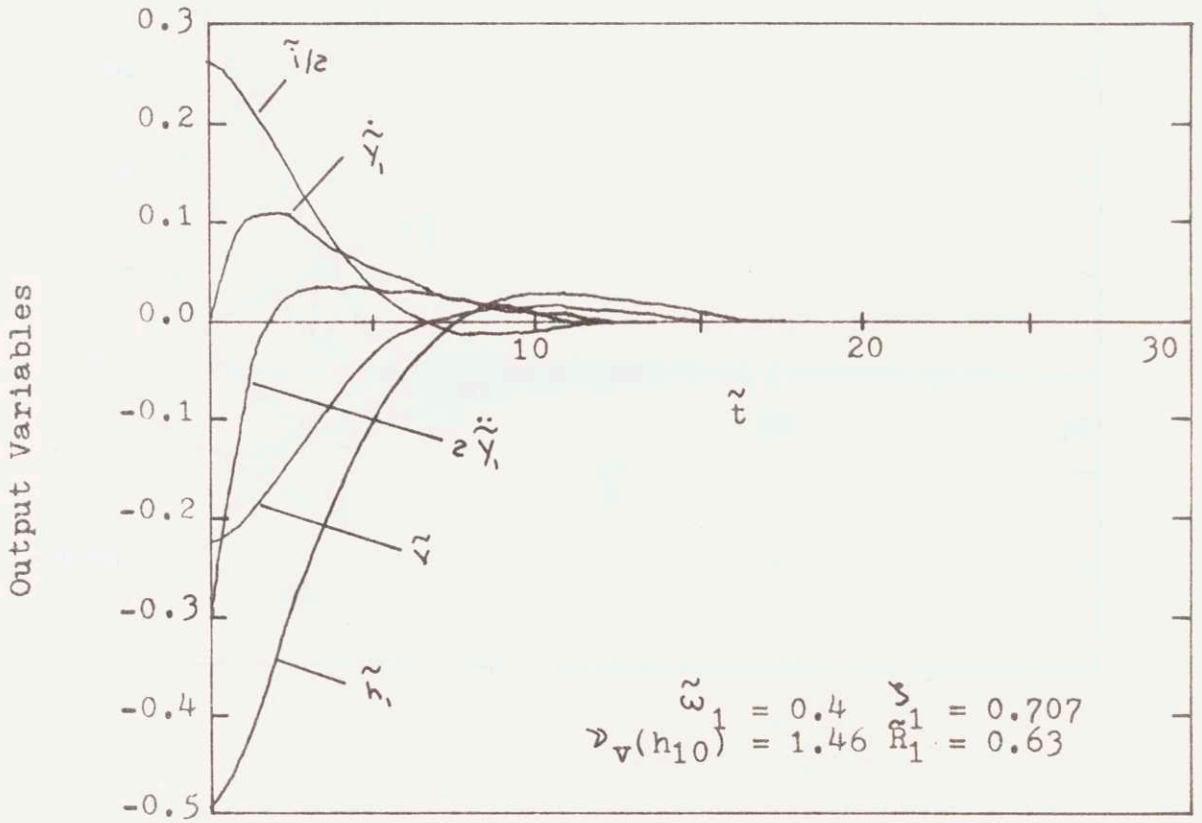


Fig. 8.8 Nonlinear Response to Initial Displacement (at  $t = 0$ ,  $h_1 = -0.5$ ,  $\dot{y}_1 = 0$ )

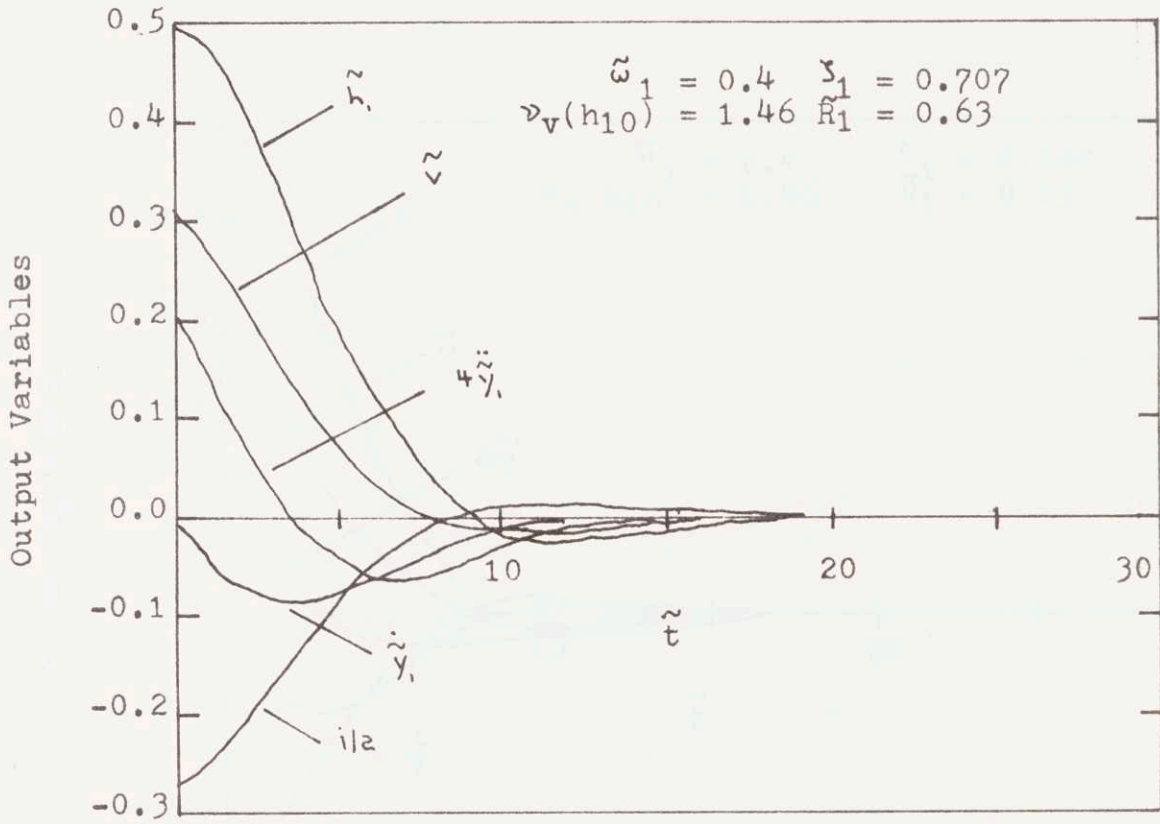


Fig. 8.9. Nonlinear Response to Initial Displacement (at  $\tilde{t} = 0$ ,  $\tilde{h}_1 = 0.5$ ,  $\tilde{y}_1 = 0$ )

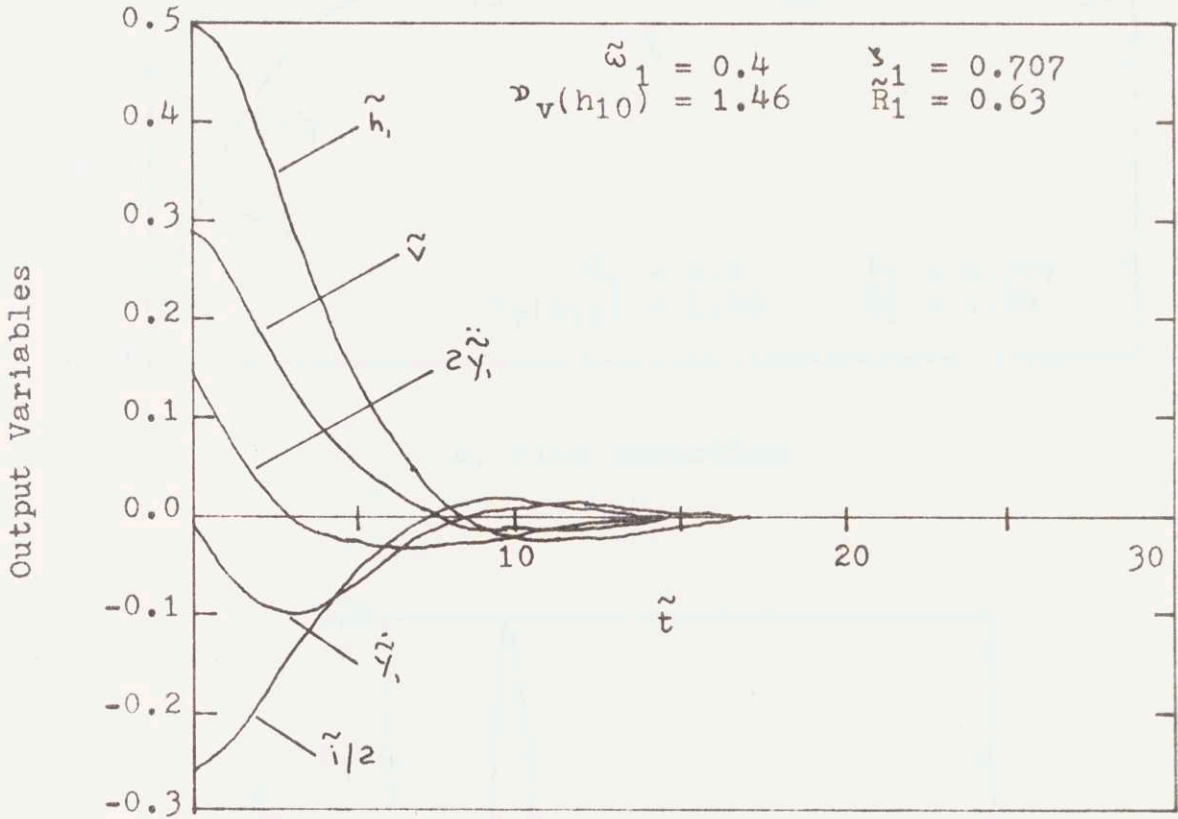
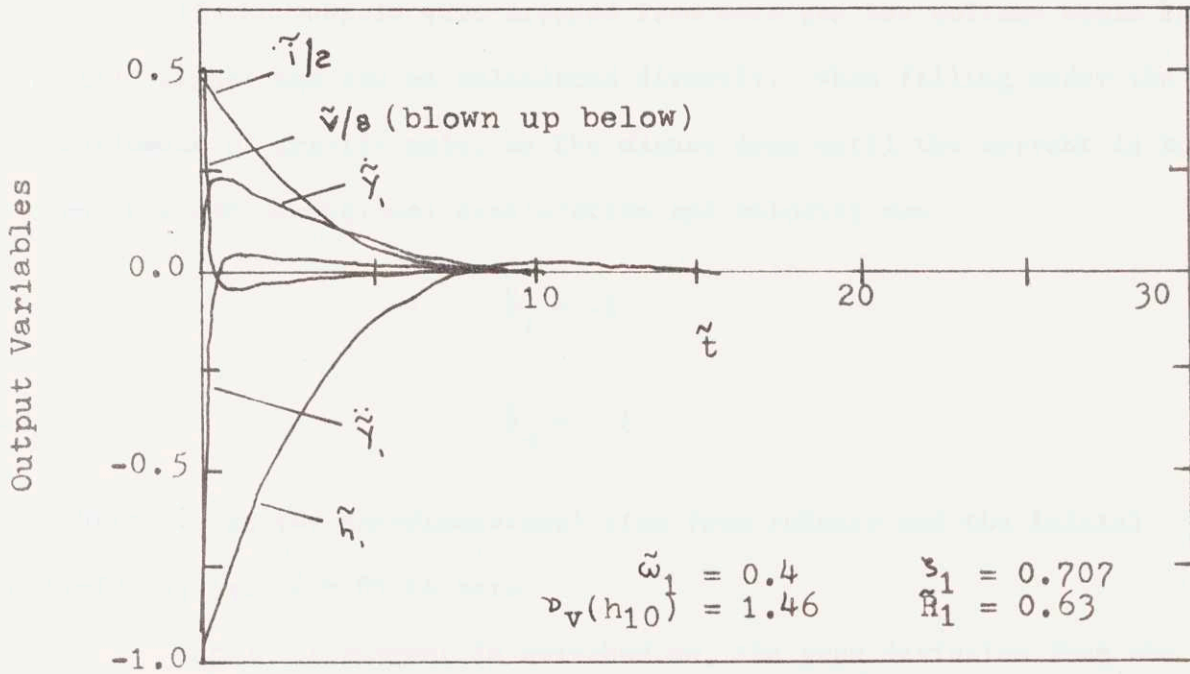
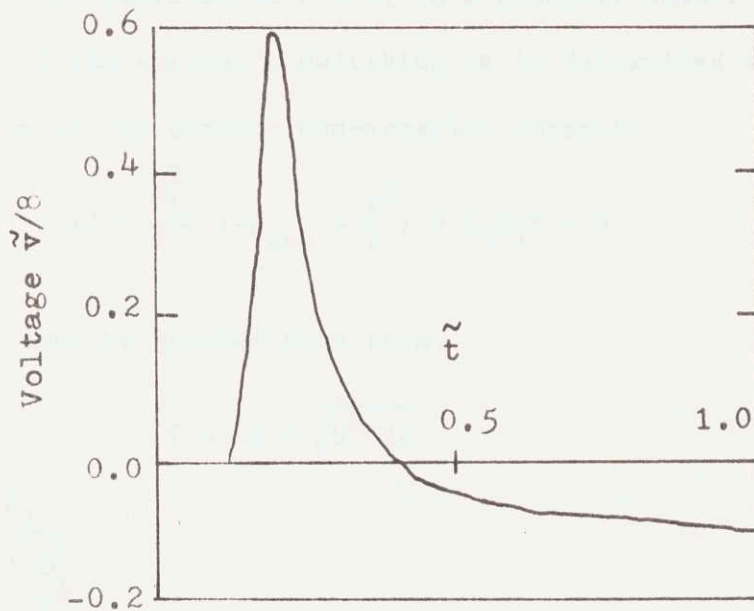


Fig. 8.10. Linear Response to Initial Displacement (at  $\tilde{t} = 0$ ,  $\tilde{\eta}_1 = 0.5$ ,  $\dot{\tilde{y}}_1 = 0$ )



a. Five Variables



b. Expanded Voltage

Fig. 8.11. Nonlinear Response to Initial Displacement  
(at  $\tilde{t} = 0$ ,  $\tilde{h}_1 = -0.95$ ,  $\tilde{y}_1 = 0$ )

If the vehicle were dropped from zero gap the voltage would be still higher and can be calculated directly. When falling under the influence of gravity only, as the magnet does until the current is turned on, the non-dimensional acceleration and velocity are:

$$\ddot{y}_1 = -1$$

$$\dot{y}_1 = -\tilde{t}$$

where  $\tilde{t}$  is the non-dimensional time from release and the initial velocity (at  $\tilde{t} = 0$ ) is zero.

Until the current is switched on, the gaps deviation from the nominal is:

$$\tilde{h}_1 = -\tilde{h}_{t=0} + \frac{\tilde{t}^2}{2}$$

where  $\tilde{h}_{t=0} = 0$ , the position at  $\tilde{t} = 0$ , is a positive number less than one. The time of the current's switching on is determined when the current control law (6.10) demands non-negative current:

$$1 + (1 + \frac{\tilde{\omega}_1^2}{2}) (-\tilde{h}_{t=0} + \frac{\tilde{t}^2}{2}) + \zeta_1 \tilde{\omega}_1 \tilde{t} = 0$$

Since the time must be greater than zero:

$$\tilde{t} = -b + \sqrt{b^2 + 2c}$$

where  $b = \frac{\zeta_1 \tilde{\omega}_1}{1 + \frac{\tilde{\omega}_1^2}{2}}$

$$c = \tilde{h}_{t=0} - \frac{1}{1 + \frac{\tilde{\omega}_1^2}{2}}$$

For the solution to be valid  $c > 0$ .  $c < 0$  implies that current does not equal

## DISCLAIMER NOTICE

Due to the condition of the original material, there are unavoidable flaws in this reproduction. We have made every effort possible to provide you with the best copy available.

Thank you.

**The following pages were not included in the original document submitted to the MIT Libraries.**

**This is the most complete copy available.**

P. 209

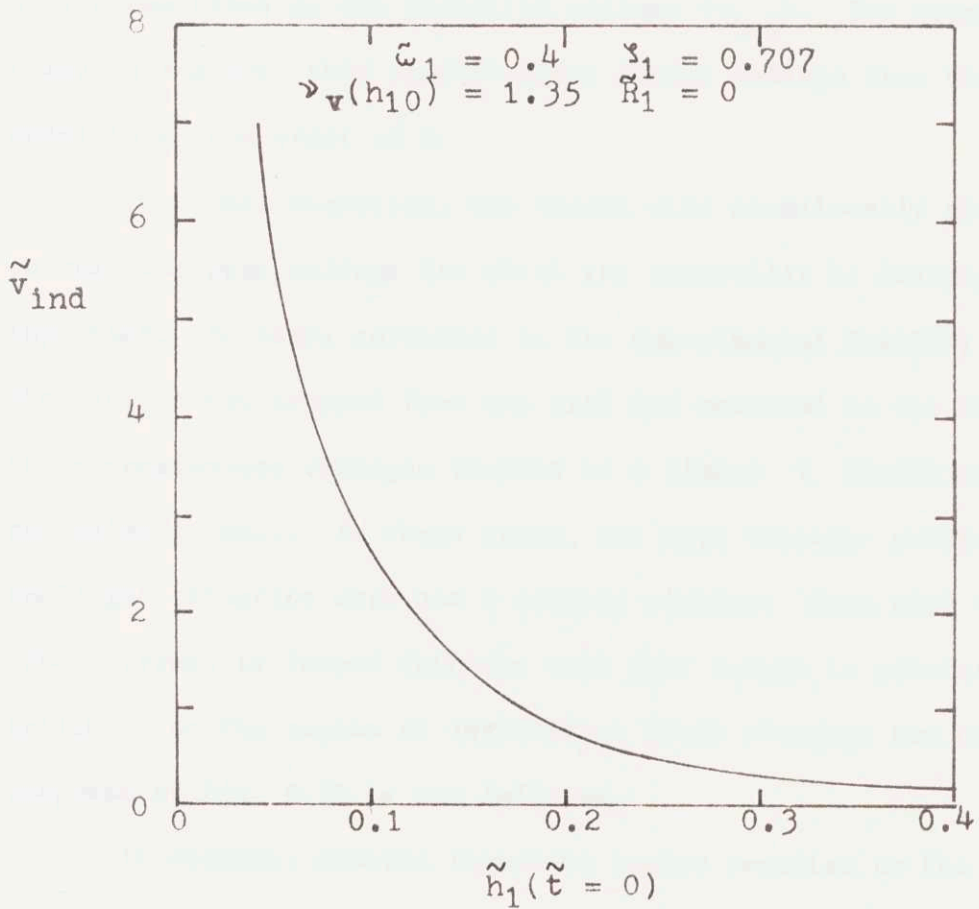


Fig. 8.12. Inductive Voltages from Drop Tests

zero at  $\tilde{t} = 0$ .

For the zero current case, the voltage (8.2) is

$$\tilde{v}_T = \frac{v_v(\tilde{h}_1)}{h_1} \left[ \left(1 + \frac{\tilde{\omega}_1^2}{2}\right) \tilde{h}_1 - \zeta_1 \tilde{\omega}_1 \ddot{\tilde{y}}_1 \right]$$

For  $\tilde{\omega}_1 = 0.4$  and  $\zeta_1 = 0.707$ , the non-dimensional voltage is 26 for a drop from zero nominal gap. Other maximum voltages are plotted in Fig. 8.12. For comparison, in the linearized model traveling over the stochastic roadway, the design voltage for the current control is the ohmic voltage plus three times in the inductive voltage ( $v_{ind}$ ). For practical designs (Table 4 and 13), this dimensionless design voltage from the linearized model is on the order of 2.

In normal operation, the magnet will occasionally strike the rail so that the peak voltage for which the controller is designed becomes important. In tests performed in the experimental facility (Chapter 3), the vehicle was dropped from the rail and returned to the nominal with the dimensionless voltages limited to 4 (lower  $\tilde{v}$  limits could not be conveniently set). In these tests, the high voltages predicted for the small gap situation were not a serious problem. Even with voltage limitation, current is forced into the coil fast enough to prevent the magnet's falling into the region of instability (4.1) although the theoretical response of Fig. 8.11 is not followed.

In summary, several important topics peculiar to the non-linear magnetic suspension have been discussed such as the asymmetry of the acceleration and voltage frequency responses, the non-zero means of the current and displacement frequency responses, and the situation where the magnet falls from contact with the rail. The non-linear analysis has indicated that a linear analysis can provide a very good basis for

the initial design of a closed loop magnetic suspension system; however, once a design is selected, it is advisable to check the linear design with a non-linear simulation to determine the influence of very large excursions from the nominal gap.

Further study is needed to determine the mechanical effects of vehicle rail contact; i.e., the stresses and possible damage to the rail.

9. PASSIVE SECONDARY SUSPENSION

9.1 Linearized Open Loop Equations

The model is extended to include a secondary suspension which consists of a spring and damper in parallel (Fig. 2.8) so that improvements in heave performance can be determined and compared to the system with no secondary. As shown in Chapter 4.3, most electromagnetic suspensions will have a secondary suspension. The secondary suspension configuration of Fig. 2.8 is studied because of its extensive use in current transportation systems. The system is attractive because it consists of purely passive mechanical elements and may be easily implemented. (Active secondary suspensions may have better isolation characteristics than the passive secondary but are more complex.)

With lumped parameters and non-dimensionalizations defined in the previous chapter the linearized open loop equations of motion are

$$\ddot{\tilde{y}}_1 + 2\zeta_2\tilde{\omega}_2\gamma(\dot{\tilde{y}}_1 - \dot{\tilde{y}}_2) + \gamma\tilde{\omega}_1^2(\tilde{y}_1 - \tilde{y}_2) = 2(1 + \gamma)(-\tilde{h}_{1-av} + \tilde{y}) \quad (9.1)$$

$$\ddot{\tilde{y}}_2 + 2\zeta_2\tilde{\omega}_2(\dot{\tilde{y}}_2 - \dot{\tilde{y}}_1) + \tilde{\omega}_2^2(\tilde{y}_2 - \tilde{y}_1) = 0 \quad (9.2)$$

$$\tilde{v} = \tilde{L}_1\tilde{y} - \tilde{h}_{1-av} + \tilde{y}\tilde{R}_1 \quad (9.3)$$

where

$$\tilde{\omega}_2 = \sqrt{\frac{k_2}{m_2} \frac{h_{10}}{g}} = \text{natural frequency of secondary}$$

$$\zeta_2 = \frac{b_2}{2\sqrt{m_2k_2}} = \text{damping ratio of secondary}$$

$$\gamma = \frac{m_2}{m_1} = \text{mass ratio}$$

(9.1) describes the forces on  $m_1$  and (9.2), the forces on  $m_2$ . (9.3) establishes the control voltage.

### 9.2 Equations of Motion with Current Control

The current control law, similar to that of (6.10) is written in non-dimensional form:

$$\ddot{y}_1 = \left[ 1 + \frac{\tilde{\omega}_1^2}{2(1+\gamma)} \right] \tilde{h}_{1-av} - \frac{\zeta_1 \tilde{\omega}_1}{(1+\gamma)} \dot{y}_1 \quad (9.4)$$

where  $\tilde{\omega}_1, \zeta_1 =$  the non-dimensional natural frequency and damping ratio of the primary. As before

$$\tilde{\omega}_1 = \omega_1 \sqrt{h_{10}/g}$$

The transfer function for the absolute displacement of the primary suspension is:

$$\frac{\tilde{y}_1(\tilde{s})}{\tilde{y}_{0-av}(\tilde{s})} = \frac{\sum_{n=1}^5 c_n \tilde{s}^{n-1}}{\sum_{n=1}^5 d_n \tilde{s}^{n-1}} = \frac{\text{NUM}}{\text{DEN}} \quad (9.5)$$

where

$$\begin{aligned} d_5 &= 1.0 \\ d_4 &= (1+\gamma) 2\zeta_2 \tilde{\omega}_2 + 2\zeta_1 \tilde{\omega}_1 \\ d_3 &= (1+\gamma)\tilde{\omega}_2^2 + \tilde{\omega}_1^2 + 4\zeta_1\zeta_2 \tilde{\omega}_1\tilde{\omega}_2 \end{aligned}$$

$$d_2 = 2\zeta_1 \tilde{\omega}_1 \tilde{\omega}_2^2 + 2\zeta_2 \tilde{\omega}_2 \tilde{\omega}_1^2$$

$$d_1 = \tilde{\omega}_1^2 \tilde{\omega}_2^2$$

$$c_4 = c_5 = 0$$

$$c_3 = \tilde{\omega}_2^2$$

$$c_2 = 2\zeta_2 \tilde{\omega}_2 \tilde{\omega}_1^2$$

$$c_1 = \tilde{\omega}_1^2 \tilde{\omega}_2^2$$

In (9.5), the ratio  $c_1/d_1 = 1$  indicates that the magnet follows the rail perfectly for low input frequencies. For  $\gamma = 0$ , the system without secondary can be obtained.

The average clearance is derived from  $\tilde{h}_{1-av} = \tilde{y}_{0-av} - \tilde{y}_1$

$$\frac{\tilde{h}_{1-av}(\tilde{s})}{\tilde{y}_{0-av}(\tilde{s})} = \frac{\sum_{n=1}^5 g_n \tilde{s}^{n-1}}{DEN} \quad (9.6)$$

where

$$g_n = d_n - c_n$$

The displacement between the magnet and the rail at the mid-point of the magnet  $\tilde{h}_{1-p} = \tilde{y}_{0-p} - \tilde{y}_1$  :

$$\frac{\tilde{h}_{1-p}(\tilde{s})}{\tilde{y}_{0-p}(\tilde{s})} = \frac{DEN - NUM F_{mag}(\omega)}{DEN} \quad (9.7)$$

where  $F_{\text{mag}}(\omega)$  is defined in (7.4).

The control current is derived from (9.4), (9.5), and (9.6):

$$\frac{\tilde{i}(\tilde{s})}{\tilde{y}_{0\text{-av}}(\tilde{s})} = \frac{\sum_{n=1}^5 h_n \tilde{s}^{n-1}}{\text{DEN}} \quad (9.8)$$

where

$$h_n = \left[ 1 + \frac{\tilde{\omega}_1^2}{2(1+\gamma)} \right] g_n - \frac{\zeta_1 \tilde{\omega}_1}{1+\gamma} c_{n-1}$$

and undefined coefficients = 0 .

The absolute position of the sprung mass (from (9.2)) is:

$$\frac{\tilde{y}_2(\tilde{s})}{\tilde{y}_{0\text{-av}}(\tilde{s})} = \frac{\sum_{n=1}^5 e_n \tilde{s}^{n-1}}{\text{DEN}} \quad (9.9)$$

where

$$e_5 = e_4 = e_3 = 0$$

$$e_2 = c_2$$

$$e_1 = c_1$$

The numerator of the passenger compartment ((9.9)) is of lower order than that of the magnet (9.5), the basic reason for secondary suspensions.

The clearance between the sprung and unsprung mass is

$$\tilde{h}_2 = \tilde{y}_1 - \tilde{y}_2 \quad \text{so that:}$$

$$\frac{\tilde{h}_2(\tilde{s})}{\tilde{y}_{0-av}(\tilde{s})} = \frac{\sum_{n=1}^5 f_n \tilde{s}^{n-1}}{DEN} \quad (9.10)$$

where

$$f_3 = \omega_1^2$$

$$f_1 = f_2 = f_4 = f_5 = 0$$

The voltage in the control coil is determined from (9.3):

$$\frac{\tilde{v}(\tilde{s})}{\tilde{y}_{0-av}(\tilde{s})} = \frac{\sum_{n=1}^6 p_n \tilde{s}^{n-1}}{DEN} \quad (9.11)$$

where

$$p_n = \tilde{L}_1 h_{n-1} - g_{n-1} + \tilde{R}_1 h_n$$

The real power dissipated by the suspension is:

$$\tilde{P}_R = \frac{P_R}{2mg \sqrt{gh_{10}}} = \frac{\zeta_1 \tilde{\omega}_1^2 \tilde{y}_1^2}{1+\gamma} + \frac{\gamma \zeta_2 \tilde{\omega}_2^2 \tilde{h}_2^2}{1+\gamma} \quad (9.12)$$

This quantity ( $\tilde{P}_R$ ) is negligible compared to the ohmic power and the wind drag. (In sample 8 of Table 13, the real power is only 1 kw compared to 20-50 kw for ohmic losses in the coil and 2600 kw, for wind drag (Appendix 1).

The implications of these relations are discussed in Section 4.3.

## 10. EDDY CURRENTS INDUCED BY VERTICAL MOTION

### 10.1 Introduction

This chapter details a model which estimates the effects of the eddy currents induced by the vehicle's vertical motion. The chapter is arranged as follows:

- (1) An introductory description of the eddy currents induced by vehicle motion is presented.
- (2) The model and underlying assumptions are described.
- (3) The field equations are solved in detail.
- (4) Based on numerical results for the closed form solution, the basic features of the penetration phenomena are described.

From electromagnetic theory, if a closed path is penetrated by a changing magnetic flux, a voltage is induced around that path and associated eddy currents are formed. In the electromagnetic suspension eddy currents are formed by the vertical motion between the magnet and rail and by the vehicle's forward motion.

As the vehicle moves vertically, the changing air gaps and the changing current caused by the controller alter the magnetic fields in the rail over the entire length of the magnet. The changing magnetic fields induce eddy currents which produce a magnetic field that opposes the original field established by the control coil. The net effect of these eddy currents is that the magnetic field from the control coil flows

in a thin sheet near the surface of the material. The thickness of this sheet is called the skin depth or penetration depth. At high frequencies (to be discussed), the eddy currents reduce the flux that enters the rail and introduce a phase lag between the flux in the rail and the control current.

As the vehicle moves forward, the rail section in front of the vehicle contains no flux; however, when the vehicle has moved over the rail a magnetic field is generated in the rail and eddy currents are induced in the rail about the magnet's leading and trailing edge. These eddy currents cause a loss of lift and dissipate power (magnetic drag) which must be overcome by the vehicle's propulsion unit. The effects of eddy currents induced by forward motion on system design are discussed only qualitatively in this thesis in Section 2.3.5 and represent an area in which further research is recommended.

The eddy currents induced by vertical motion are described as shown in Section 2.3.5 by:

$$\nabla^2 \vec{B} = \mu\sigma \frac{\partial \vec{B}}{\partial t} \quad (10.1)$$

where

$\vec{B}$  = magnetic field

$\mu, \sigma$  = permeability and conductivity of medium

This chapter solves this equation in the three regions of the model described in the next section.

## 10.2 Description of Model

The theoretical model described below is used to investigate effects of eddy currents induced by the vehicle's vertical motion. This model allows consideration of magnet and rail material, permeability and conductivity, and two important geometric properties, the air gap and magnet width. Although detailed geometric factors such as the magnet thickness, the pole width, and core length are neglected in the model, the model enables visualization of the fundamental interaction of the fields produced by the control windings and the fields produced by the induced eddy currents and provide guidelines and indicate the operating regions and geometries for which eddy current effects are significant. The theoretical results agree satisfactorily with the experimental observation.

The model and coordinate system are shown in Figures 2.10 and 2.11. The following assumptions are made:

- (1) Since the magnet is long compared to its width

$$\frac{\partial}{\partial x} = 0$$

- (2) The magnet and rail can be considered to be infinite half spaces as shown in Figure 2.10. The magnet's width is considered by representing the windings as a current ( $\vec{K}_s$ ) sheet at  $y = 0$

$$\vec{K}_s = \hat{i} K_s \sin \omega t \sin k z \quad (10.2)$$

$$k = \frac{2\pi}{\lambda_M}$$

where the wavelength of the windings ( $\lambda_M$ ) is derived by considering the magnet-rail configuration as a periodic structure as shown in Figure 2.11; thus,

$$\frac{\lambda_M}{2} = w_1 + 2l_p$$

where

$w_1$  = distance between pole cores

$l_p$  = width of magnet pole face

In (10.2),  $\sin(\omega t)$  represents the change in current with time and  $\sin(kz)$  represents the periodic structure of the magnet.

(3) The magnet (region I) has permeability  $\mu_1$ . Since the magnet can be laminated fully, the magnet conductivity is assumed zero; i.e., no eddy currents form in the magnet. The magnet is assumed laminated but not the rail since it is relatively cheap to laminate a magnet but very expensive to laminate miles of track.

(4) The air gap (region II) has zero conductivity and permeability  $\mu_2$ . The air gap ( $h_1$ ) is assumed uniform and does not vary with time; i.e., in the model, the magnet current is allowed to vary with time to estimate the effects of eddy currents.

(5) The rail (region III) is a thick ferromagnetic conductor with permeability  $\mu_3$  and conductivity  $\sigma$ . Since the solution will depend on a skin depth which is small compared to the rail thickness for practical systems, the thickness of the rail does not enter the analysis.

### 10.3 Mathematical Formulation and Solution

The current sheet (10.2) can be written as

$$\vec{K}_s = \vec{i} K_s [\cos(-\omega t + kz) - \cos(\omega t + kz)] \quad (10.3)$$

where  $\vec{i}$  is a unit vector parallel to the x axis.

Since the equations describing the field are linear, consider temporarily the general complex input for steady state:

$$\vec{K}_s = \vec{i} K_s e^{j(\omega t + kz)} \quad (10.4)$$

where

$$j = \sqrt{-1}$$

The equations of motion in the three regions defined in Figure 2.10 and the boundary conditions between the regions can be written.

In the three regions:

$$\nabla \cdot \vec{B} = 0 \quad (10.5)$$

In the magnet (region I),  $\mu = \mu_1$  and  $\sigma = 0$  so that (10.1)

becomes

$$\nabla^2 \vec{B} = 0 \quad (10.6)$$

Because the system is linear and because the current sheet input is a complex exponential, the magnetic field is also a complex exponential

which is of the general form:

$$B_{1z} = (A e^{ky} + B e^{-ky}) e^{j(\omega t + kz)} \quad (10.7a)$$

$$B_{1y} = j(-A e^{ky} + B e^{-ky}) e^{j(\omega t + kz)} \quad (10.7b)$$

(10.7a) and (10.7b) satisfy the magnetic field equations (10.5) and (10.6) where A and B are complex constants to be determined from the boundary conditions.

In the air gap (Region II),  $\mu = \mu_2$  and  $\sigma = 0$  so that

$$\nabla^2 \vec{B} = 0$$

As in region I, the solution in region II is of the form:

$$B_{2z} = (C e^{ky} + D e^{-ky}) e^{j(\omega t + kz)} \quad (10.8a)$$

$$B_{2y} = j(-C e^{ky} + D e^{-ky}) e^{j(\omega t + kz)} \quad (10.8b)$$

where C and D are to be determined.

In region 3,  $\mu = \mu_3$  and  $\sigma_3 = \sigma$ , so that

$$\frac{1}{\mu_3 \sigma_3} \nabla^2 \vec{B} = \frac{\partial \vec{B}}{\partial t} \quad (10.9)$$

and the solution in region III is of the form:

$$B_{3z} = [E e^{\alpha y} + F e^{-\alpha y}] e^{j(\omega t + kz)} \quad (10.9)$$

$$B_{3y} = \frac{j k}{\alpha} [-E e^{\alpha y} + F e^{-\alpha y}] e^{j(\omega t + kz)} \quad (10.10b)$$

where E and F are to be determined and where  $\alpha$  is determined by substituting (10.10) into the magnetic field equation (10.9):

$$\alpha = k(1 + R_M j)^{1/2} \quad (10.11a)$$

where  $R_M = \frac{\mu_3 \sigma_3 \omega}{k^2}$  is the magnetic Reynolds number.

$\alpha$  may be written as:

$$\alpha = n_1 + j n_2$$

where

$$n_1 = \frac{k}{\sqrt{2}} [(1 + R_M^2)^{1/2} + 1]^{1/2}$$

$$n_2 = \frac{k}{\sqrt{2}} [(1 + R_M^2)^{1/2} - 1]^{1/2}$$

The complex constants A, B, C, D, E, and F which are functions of the input frequency  $\omega$  are evaluated from the following boundary conditions. In the magnet at distances far from the current sheet, the magnetic fields must be finite; therefore:

$$B = 0 \quad (10.12)$$

At  $y=0$ , the boundary between the magnet and the air gap, the flux density that crosses the air gap is continuous:

$$B_{1y} = B_{2y} \quad (10.13a)$$

and the magnetic intensity is discontinuous by the current sheet (for a small path around the boundary Ampere's circuital law must hold).

$$K_s + \frac{B_{1z}}{\mu_1} = \frac{B_{2z}}{\mu_2} \quad (10.13b)$$

In the rail, fields far from the current sheet must be finite; thus,

$$E = 0 \quad (10.14)$$

At  $y = h_1$ , the boundary between the rail and the air gap,

$$B_{2y} = B_{3y} \quad (10.15a)$$

$$\frac{B_{2z}}{\mu_2} = \frac{B_{3z}}{\mu_3} \quad (10.15b)$$

Substitution of (10.7), (10.8), (10.10), (10.12), and (10.14) into (10.13) and (10.15) yields the remaining coefficients:

$$A = \frac{\mu_1 K_s [(1+\zeta)e^{kh_1} - (1-\zeta)e^{-kh_1}]}{\text{DEN}} \quad (10.16a)$$

$$C = \frac{-\mu_1 K_s (1-\zeta)e^{-kh_1}}{\text{DEN}} \quad (10.16n)$$

$$D = \frac{-\mu_1 K_s (1+\zeta)e^{kh_1}}{\text{DEN}} \quad (10.16c)$$

$$F = -\frac{\alpha}{k} \frac{2\zeta \mu_1 K_s}{\text{DEN}} e^{\alpha h_1} \quad (10.16d)$$

where

$$\text{DEN} = -(1+\zeta)(1+\gamma)e^{kh_1} + (1-\zeta)(1-\gamma)e^{-kh_1}$$

and

$$\gamma = \frac{\mu_1}{\mu_2}$$

$$\zeta = \frac{\mu_3}{\mu_2} \left( \frac{k}{\alpha} \right)$$

The above solution is for the complex exponential (10.4) which represents the term  $\cos(\omega t + kz)$  in (10.3). The solution for the  $\cos(-\omega t + kz)$  can be found by replacing  $\omega$  by  $-\omega$  in (10.7) through (10.16). With the input described by (10.2), the magnetic fields in the magnet (region I) are:

$$B_{1z} = -|A| e^{ky} \sin(\omega t + \theta_1) \sin kz \quad (10.17a)$$

$$B_{1y} = |A| e^{ky} \sin(\omega t + \theta_1) \cos kz \quad (10.17b)$$

where  $\theta_1 = \text{ARG}(A) - 180^\circ$

In the air gap (region II)

$$B_{2z} = |C e^{-ky} + D e^{ky}| \sin(\omega t + \theta_{2z}) \sin kz \quad (10.18a)$$

$$B_{2y} = |C e^{-ky} - D e^{ky}| \sin(\omega t + \theta_{2y}) \cos kz \quad (10.18b)$$

where

$$\theta_{2z} = \text{ARG}(C e^{ky} + D e^{-ky})$$

$$\theta_{2y} = \text{ARG}(-C e^{ky} + D e^{-ky})$$

In the rail (region III):

$$B_{3z} = |F e^{-jn_2 y}| e^{-n_1 y} \sin(\omega t + \theta_{3z}) \sin kz \quad (10.19a)$$

$$B_{3y} = + \left| \frac{k}{\alpha} F e^{-jn_2 y} \right| e^{-n_1 y} \sin(\omega t + \theta_{3y}) \cos kz \quad (10.19b)$$

where

$$\theta_{3z} = \text{ARG}(F e^{-jn_2 y})$$

$$\theta_{3y} = \text{ARG}\left(\frac{k}{\alpha} F e^{-jn_2 y}\right)$$

The lift force per unit area on the rail surface  $y = h_1$  is obtained from the Maxwell stress tensor [51]

$$P_L = \frac{1}{2\mu_0} (B_{2y}^2 - B_{2z}^2), \quad y = h_1 \quad (10.20)$$

Along the surface of the rail, the average lift force per unit area is:

$$\frac{P_L}{K_B^2} = \frac{F^2}{8\mu_0} \left[ \left(\frac{k}{\alpha}\right)^2 - \left(\frac{\mu_2}{\mu_3}\right)^2 \right] \quad (10.21)$$

The current density in the rail is obtained from  $\vec{J}_3 = \frac{1}{\mu_3} \nabla \times \vec{B}_3$

$$\left| \frac{\vec{J}_3}{K_s} \right| = \left| \frac{F}{\alpha} (\alpha^2 - k^2) \right| \quad (10.22)$$

The average power dissipated per unit magnet length is obtained from

$$\frac{\vec{P}_3}{l_1 K_s^2} = \frac{|J_3|^2}{2\sigma} \int_{-\infty}^0 e^{2n_1 z} dz \int_0^\lambda \sin^2 kx dx$$

so that the average ohmic power per unit magnet length is

$$\frac{P_3}{l_1 K_s^2} = \frac{|J_3|^2}{8\sigma n_1} \quad (10.23)$$

Since the flux entering the rail is

$$\phi_R = l_1 \int_0^{\lambda/2} B_{3y}(y = h_1) dz$$

For a given configuration the flux that enters the rail is proportional to  $B_{3y}$  at  $y = h_1$ ; that is

$$\phi_R \propto |B_{3y}| \quad (10.24)$$

and the flux lags the control current by  $\theta_{3y}$ .

Similarly, the total flux in the magnet is proportional to  $B_{1y}$  at  $y = 0$ ; that is:

$$\phi_T \propto |B_{1y}| \quad (10.25)$$

and  $\phi_T$  lags the control current by  $\theta_1$ .

#### 10.4 Description of the Penetration Phenomena

Through a numerical example, the qualitative behavior of the circuit can be described. In Table 14, data is presented for a ferromagnetic magnetic magnet and rail. The magnet width (10 inches) and air gap (0.6 in.) correspond to Design 4 of Table 4.

For most frequencies of interest (typically, greater than 0.1 hz.), the exponent  $\alpha$  is:

$$\alpha \approx \frac{1}{\delta} (1 + i)$$

because the magnetic Reynolds number ( $R_M$ ) is much greater than one (at 0.1 hz.,  $R_M = 43$ ). Because  $\alpha$  determines the exponential decay of the fields in the rail (10.10),  $\delta$  (or  $1/n_1$  to be exact) is given the title penetration depth or skin depth; i.e., if the flux density  $B_{3z}(y)$  were equal to  $B_{3z}$  at the surface, all the flux in the rail would be in the skin depth.

At low frequencies (typically until 10 hz.) the flux that penetrates the rail is equal to the flux that penetrates under static conditions despite the concentration of flux in the skin depth. Until 10 hz., the high permeability of the metal relative to the air gap causes the vertical field at the rail-air gap interface ( $B_{3y} = B_{2y}$ ) to be much

greater than the horizontal field ( $B_{2z}$ ); thus, the lift pressure (10.20)

is:

$$P_L = \frac{1}{8\mu_0} [B_{2y}^2 - B_{2z}^2] \approx \frac{B_{2y}^2}{8\mu_0}$$

As frequency increases the flux in the decreasing skin depth is compressed further and some of the flux from the control coil does not enter the rail as seen by the differences between  $|B_{1y}|$  and  $|B_{3y}|$  which begins to appear at 10 hz. As the flux is compressed in the skin depth, the tangential fields at the surface increase until the attractive force becomes repulsive at about  $10^5$  hz.

As a comparison, Table 15 is compiled with the rail's permeability equal to  $\mu_0$ . Because of its higher permeability, the ferromagnetic rail has a higher depth of penetration than the non-magnetic rail. Because its permeability is low, the field at the non-magnetic rail's surface is not perpendicular to the surface and the force is repulsive at low frequencies. When the field from the control coil does not penetrate the rail (high input frequency), the magnetic field in the air does not depend on the properties of the rail and the flux densities in the air gap are identical for the two rails.

With both rails, the phase ( $\theta_{3y}$ ) between the flux that enters the rail and the current sheet approaches 45 degrees. As the magnet's flux is rejected from the rail, the phase ( $\theta_1$ ) between the flux in the magnet and the current sheet shows a lag; however, the phase angle between the magnet's flux and the control current ( $\vec{K}_s$ ) returns to zero.

Table 14

## SAMPLE DATA BASED ON EDDY CURRENT ANALYSIS

FERROMAGNETIC RAIL ( $\mu_3 = 3500$ )

$$\mu_1 = 3500, \mu_2 = \mu_0, \sigma = .25 \times 10^{-7} \text{ (ohm-m)}^{-1}, \frac{\lambda_M}{2} = 0.25 \text{ m}, h_1 = 0.015 \text{ m}$$

F	R <sub>M</sub>	1/n <sub>1</sub>	$\left  \frac{B_{3y}}{K_s} \right $	$\theta_{3y}$	$\left  \frac{B_{1y}}{K_s} \right $	$\theta_1$	$\left  \frac{B_{2z}}{K_s} \right $	$\frac{P_L}{K_s^2}$	$\frac{P_3}{1_1 K_s^2}$
(hz)	(m)	(m)	$\left( \frac{T-m}{amp} \right)$	(deg)	$\left( \frac{T-m}{amp} \right)$	(deg)	$\left( \frac{T-m}{amp} \right)$	$\left( \frac{nt}{amp^2} \right)$	$\left( \frac{watts-m}{amp^2} \right)$
0.100E-01	0.437E-01	0.164E-01	0.660E-05	-0.116E-00	0.672E-05	-0.112E-00	0.399E-08	0.433E-05	0.817E-11
0.110E-01	0.437E-02	0.164E-01	0.657E-05	-0.403E-00	0.668E-05	-0.389E-00	0.124E-07	0.429E-05	0.283E-09
0.120E-01	0.437E-03	0.534E-02	0.647E-05	-0.127E-01	0.659E-05	-0.122E-01	0.386E-07	0.416E-05	0.877E-08
0.999E-01	0.437E-04	0.171E-02	0.616E-05	-0.382E-01	0.628E-05	-0.368E-01	0.116E-06	0.377E-05	0.252E-06
0.999E-02	0.437E-05	0.534E-03	0.530E-05	-0.105E-02	0.544E-05	-0.100E-02	0.317E-06	0.279E-05	0.590E-05
0.998E-03	0.437E-06	0.171E-03	0.356E-05	-0.226E-02	0.371E-05	-0.212E-02	0.672E-06	0.122E-05	0.839E-04
0.998E-04	0.436E-07	0.533E-04	0.167E-05	-0.347E-02	0.183E-05	-0.306E-02	0.994E-06	0.178E-06	0.582E-03
0.998E-05	0.436E-08	0.171E-04	0.610E-06	-0.413E-02	0.790E-06	-0.300E-02	0.115E-05	-0.948E-07	0.246E-02
0.997E-06	0.436E-09	0.533E-05	0.202E-06	-0.438E-02	0.402E-06	-0.203E-02	0.121E-05	-0.141E-06	0.857E-02
0.997E-07	0.436E-10	0.171E-05	0.652E-07	-0.446E-02	0.283E-06	-0.911E-01	0.123E-05	-0.149E-06	0.279E-01
0.996E-08	0.436E-11	0.533E-06	0.200E-07	-0.449E-02	0.249E-06	-0.330E-01	0.123E-05	-0.151E-06	0.891E-01
0.996E-09	0.436E-12	0.171E-06	0.054E-08	-0.450E-02	0.239E-06	-0.103E-01	0.123E-05	-0.151E-06	0.283E-00
0.996E-10	0.435E-13	0.533E-07	0.207E-08	-0.450E-02	0.235E-06	-0.350E-02	0.123E-05	-0.151E-06	0.894E-00

Table 15

## SAMPLE DATA BASED ON EDDY CURRENT ANALYSIS

NON MAGNETIC RAIL ( $\mu_3 = \mu_0$ )

$$\mu_1 = 3500, \mu_2 = \mu_0, \sigma = .25 \times 10^7 \text{ (ohm-m)}^{-1}, \frac{\lambda_M}{2} = 0.25 \text{ m}, h_1 = .015 \text{ m}$$

F	R <sub>M</sub>	1/n <sub>1</sub>	$\left  \frac{B_{3y}}{K_s} \right $	$\theta_{3y}$	$\left  \frac{B_{1y}}{K_s} \right $	$\theta_1$	$\left  \frac{B_{2z}}{K_s} \right $	$\frac{P_L}{K_s^2}$	$\frac{P_3}{1_1 K_s^2}$
(hz)		(m)	$\left( \frac{T-m}{amp} \right)$	(deg)	$\left( \frac{T-m}{amp} \right)$	(deg)	$\left( \frac{T-m}{amp} \right)$	$\left( \frac{nt}{amp^2} \right)$	$\left( \frac{watts-m}{amp^2} \right)$
0.100E-01	0.125E-02	0.796E-01	0.174E-25	-0.333E-01	0.126E-05	-0.271E-01	0.104E-05	0.322E-10	0.430E-12
0.100E-02	0.125E-01	0.796E-01	0.174E-25	-0.302E-02	0.126E-05	-0.246E-02	0.104E-05	0.241E-10	0.337E-10
0.100E-01	0.125E-03	0.796E-01	0.174E-25	-0.302E-01	0.126E-05	-0.244E-01	0.104E-05	-0.799E-09	0.333E-08
0.995E-01	0.125E-01	0.593E-01	0.453E-26	-0.224E-02	0.126E-05	-0.176E-02	0.109E-05	-0.441E-07	0.201E-06
0.995E-02	0.125E-02	0.373E-01	0.336E-26	-0.427E-02	0.529E-26	-0.247E-02	0.119E-05	-0.129E-06	0.134E-05
0.995E-03	0.125E-03	0.171E-01	0.129E-26	-0.441E-02	0.327E-26	-0.135E-02	0.122E-05	-0.147E-06	0.466E-05
0.995E-04	0.125E-04	0.319E-02	0.344E-27	-0.448E-02	0.259E-26	-0.533E-01	0.123E-05	-0.150E-06	0.150E-04
0.995E-05	0.125E-05	0.171E-02	0.117E-27	-0.449E-02	0.242E-26	-0.182E-01	0.123E-05	-0.151E-06	0.478E-04
0.997E-06	0.125E-06	0.319E-03	0.353E-28	-0.452E-02	0.236E-26	-0.588E-02	0.123E-05	-0.151E-06	0.151E-03
0.997E-07	0.125E-07	0.171E-03	0.111E-28	-0.450E-02	0.235E-26	-0.187E-02	0.123E-05	-0.151E-06	0.478E-03
0.996E-08	0.124E-08	0.319E-04	0.353E-09	-0.452E-02	0.234E-26	-0.594E-01	0.123E-05	-0.152E-06	0.151E-02
0.996E-09	0.124E-09	0.171E-04	0.111E-09	-0.452E-02	0.234E-26	-0.188E-01	0.123E-05	-0.152E-06	0.478E-02
0.996E-10	0.124E-10	0.319E-05	0.352E-10	-0.452E-02	0.234E-26	-0.595E-02	0.123E-05	-0.152E-06	0.151E-01

For design purposes and for experimental use, it is convenient to use the ratio of the flux at a given frequency to the flux with zero frequency. Using (10.24), the ratio of the flux magnitudes in the rail is:

$$\frac{|\phi_R(\omega)|}{|\phi_R(0)|} = \frac{|B_{3y}(\omega)|}{|B_{3y}(0)|} \quad (10.27)$$

and the phase between the flux entering the rail and the control current is  $\theta_{3y}$  from (10.19b). Similarly, for the flux entering the magnet,

$$\frac{|\phi_T(\omega)|}{|\phi_T(0)|} = \frac{|B_{1y}(\omega)|}{|B_{1y}(0)|} \quad (10.28)$$

and the phase between the flux and the current is  $\theta_1$  from (10.17).

The static flux can be calculated by using the techniques of Chapter 5. From (5.8) the total flux in the magnet is

$$\phi_T(0) = \frac{v_T \mu_o l_1 l_p (Ni)}{2h_1^2} \quad (10.29)$$

and the flux in the rail is:

$$\phi_R(0) = \frac{v_\partial}{v_T} \phi_T(0)$$

The use of the model for eddy currents induced by vertical motion is suspension design is discussed in Section 2.3.5.

PART III. PRELIMINARY INVESTIGATIONS OF RELATED TOPICS

11. OPTIMAL SUSPENSIONS FOR A HEAVE-PITCH VEHICLE MODEL

11.1 Introduction

This chapter extends the heave motion model to a heave-pitch model. The vehicle is modeled with mass and pitch inertia and with front and rear suspension. The vehicle is allowed both vertical and angular pitch motion as shown in Figure 2.16. Heave-pitch models demonstrate that the front and rear magnets are coupled dynamically by the vehicle's rotational inertia, a significant effect which cannot be derived from the heave only case.

Optimal configurations derived from Wiener filter theory are derived and compared to suspensions designed from heave only considerations to demonstrate the benefits of crossfeedback, the feedback of variables measured at one end of a vehicle into the suspension at the opposite end.

11.2 The Optimal for Heave Pitch Models with Basic Suspensions

To derive an optimal control law for the heave-pitch model, a performance index that includes the expected values of acceleration and displacement at both ends of the vehicle is used:

$$P.I. = E[\ddot{y}_{1F}^2] + \rho_1 E[h_{1F}^2] + \rho_2 E[\ddot{y}_{1R}^2] + \rho_3 E[h_{1R}^2] \quad (11.1)$$

where the subscript F denotes the front and the subscript R denotes the rear and where  $\rho_1$ ,  $\rho_2$ , and  $\rho_3$  are the relative weights of the terms.

Since the analysis is linearized, all variables are incremental. As in Chapter 6, it is assumed the magnets are short compared to the wave lengths of the irregularities (point contact). Since accelerations and displacements will be largest at the vehicle's ends, the derivation will be carried out for the end points. Physically, the magnets should be near the vehicle's ends to increase stability. Although the magnets have finite length so the center of force exerted by the magnet is not at the vehicle's end, the force is considered to act at the end of the vehicle.

As in (2.8), the spectral density of the road input is:

$$\phi_{y_{OF} y_{OF}}(s) = \phi_{y_{OR} y_{OR}}(s) = -\frac{AV}{s^2} \quad (11.2)$$

where

$$(-j\infty < s < +j\infty)$$

The input at the rear is the input at the front offset by a time delay so that

$$y_{OR}(s) = y_{OF}(s) e^{-Ts} \quad (11.3)$$

The cross spectral density that corresponds to the cross correlation

$R[y_{OF}(t) y_{OR}(t-T)]$  is:

$$\phi_{y_{OF} y_{OR}}(s) = -\frac{AV e^{-Ts}}{s^2} \quad (11.4)$$

where  $T = L_V/V =$  vehicle's transit time  
 $L_V =$  the length of the vehicle which is also used as  
the distance between the suspensions  
 $V =$  forward velocity

The transfer function for the displacement at the front is:

$$y_{1F}(s) = G_{FF} y_{OF}(s) + G_{FR} y_{OR}(s)$$

Using (11.3), the transfer function may then be written as:

$$y_{1F}(s) = [G_{FF}(s) + G_{FR}(s)e^{-Ts}] y_{OF}(s) = A_F(s) y_{OF}(s) \quad (11.5a)$$

and a similar relation may be written at the rear.

$$y_{1R}(s) = [G_{RF}(s)e^{Ts} + G_{RR}(s)] y_{OR}(s) = A_R(s) y_{OR}(s) \quad (11.5b)$$

Having written the transfer functions in the form of (11.5),  
Wiener filter theory shows that an optimal suspension for the performance  
index (11.1) with the road input (11.2) can be obtained by optimizing  
independently the following performance indices:

$$PI_F = E[y_{1F}^2] + \omega_F^4 E[h_{1F}^2] \quad (11.6a)$$

$$PI_R = E[y_{1R}^2] + \omega_R^4 E[h_{1R}^2] \quad (11.6b)$$

Thus, the solutions are those of the one degree of freedom situation of Chapter 6 so that the optimal transfer functions are given by (6.11):

$$A_F(s) = \frac{y_{1F}(s)}{y_{OF}(s)} = \frac{\omega_{1F}^2}{s^2 + \sqrt{2} \omega_{1F} s + \omega_{1F}^2} \quad (11.7a)$$

$$A_R(s) = \frac{y_{1R}(s)}{y_{OR}(s)} = \frac{\omega_{1R}^2}{s^2 + \sqrt{2} \omega_{1R} s + \omega_{1R}^2} \quad (11.7b)$$

Note that  $\phi_{y_{OF} y_{OR}}$  was not used so that these relations are independent of the vehicle length and velocity.

If the accelerations and displacements at both ends are to be of equal magnitude

$$\omega_1 = \omega_{1F} = \omega_{1R}$$

so that

$$A_1(s) = A_2(s) = A(s) \quad (11.8)$$

When (11.7) is implemented with a vehicle which may possess a arbitrary mass  $m$  and rotational inertia  $I$  about the center of gravity and when a matrix of the force transfer functions are defined:

$$\begin{bmatrix} F_F(s) \\ F_R(s) \end{bmatrix} = \begin{bmatrix} f_{FF}(s) & f_{FR}(s) \\ f_{RF}(s) & f_{RR}(s) \end{bmatrix} \begin{bmatrix} y_{OF}(s) \\ y_{OR}(s) \end{bmatrix} \quad (11.9)$$

where  $F_i(s)$  is the force at one end ( $F = \text{front}$ ,  $R = \text{rear}$ )

$f_{ij}(s)$  is the transfer function which relates the input at end  $j$  to a force at end  $i$ .

The vehicle's equation of motion may be written for the linear motion in the vertical direction as:

$$F_F(s) + F_R(s) = \frac{m s^2}{2} [y_{1F}(s) + y_{1R}(s)] \quad (11.10)$$

and for rotation about the center of mass as:

$$\frac{L_V}{2} [F_F(s) - F_R(s)] = \frac{I s^2}{L_V} [y_{1F}(s) - y_{1R}(s)] \quad (11.11)$$

where it has been assumed that the center of gravity is midway between the two suspensions and where the angle of rotation is assumed small, a valid assumption since the displacement at an end is of the order of an inch while the vehicle is 50 to 100 feet long.

When (11.5), (11.8), (11.9) are substituted into (11.10) and (11.11):

$$(f_{FF} + f_{RF})y_{OF} + (f_{RR} + f_{FR})y_{OR} = \frac{m s^2}{2} A(s) [y_{OF} + y_{OR}] \quad (11.12)$$

$$(f_{FF} - f_{RF})y_{OF} - (f_{RR} - f_{FR})y_{OR} = \frac{2I s^2}{L_V} A(s) [y_{OF} - y_{OR}]$$

By equating the coefficients of  $y_{OF}(s)$  and  $y_{OR}(s)$ , the force transfer function matrix is obtained where the consequences of the symmetry assumption (11.8) are evident:

$$\begin{aligned}
 f_{FF}(s) &= f_{RR}(s) \\
 f_{FR}(s) &= f_{RF}(s) \\
 f_{FF}(s) &= \left[ \frac{m}{4} + \frac{I}{L_V^2} \right] s^2 A(s) \\
 f_{FR}(s) &= \left[ \frac{m}{4} - \frac{I}{L_V^2} \right] s^2 A(s)
 \end{aligned}
 \tag{11.13}$$

Note that, if  $I = m L_V^2/4$ , the vehicle becomes two point masses over two point suspensions and that the force at one end does not depend on the input to the other; that is, the finite length\* vehicle has become two single degree of freedom suspensions.

The results of this section have not been restricted to electromagnetic suspensions. In the next section, the force matrix will be used to determine the current control laws for the electromagnetic suspensions.

### 11.3 The Optimal Magnetic Suspension

The control law for the optimal suspension in the tractive electromagnetic suspension may be described by writing:

$$A(s) = \frac{\omega_1^2}{s^2 + 2\zeta_1 \omega_1 s + \omega_1^2}
 \tag{11.14}$$

---

\* For a vehicle with uniformly distributed mass,  $I = m L_V^2/12$ .

The linearized force exerted by one suspension (say the front)

is:

$$F_F = -K_2 \Delta h_{1F} + K_1 \Delta i \quad (11.15)$$

where

$$K_1 = \left. \frac{\partial F_F}{\partial i_F} \right|_{\text{OP Point}} = \frac{\mu_o l_{1p} N^2 i_o}{2h_{10}^2}$$

$$K_2 = - \left. \frac{\partial F_F}{\partial h_{1F}} \right|_{\text{OP Point}} = \frac{\mu_o l_{1p} N^2 i_o^2}{2h_{10}^3}$$

The current control law may be written in the form which yields the optimum suspension:

$$\Delta i_F = \left[ \frac{K_2}{K_1} + A_h \right] \Delta h_{1F} - A_y \dot{y}_{1F} + C_h \Delta h_{1R} - C_y \dot{y}_{1R} \quad (11.16)$$

where the A denotes auto feedback; i.e., the variable measured at one end is fed into the controller at the same end and where C denotes cross feedback where the variables measured at one end are fed into the controller at the other end. The feedback constants may be determined by substituting (11.14) into (11.13) and then inserting (11.13) and (11.16) into (11.15) to obtain:

$$y_{OR}(s) \left[ \frac{m}{4} + \frac{I}{2} \right] \frac{s^2 \omega_1^2}{L_V} + y_{OR}(s) \left[ \frac{m}{4} - \frac{I}{2} \right] \frac{s^2 \omega_1^2}{L_V} =$$

$$\{ A_h K_1 s^2 + [2\zeta_1 \omega_1 A_h K_1 - A_y K_1 \omega_1^2] s \} y_{OF}(s) +$$

$$\{ C_h K_1 s^2 + [2\zeta_1 \omega_1 C_h K_1 - C_y K_1 \omega_1^2] s \} y_{OR}(s)$$

Equating the coefficients of  $y_{OF}(s)$  and  $y_{OR}(s)$  to solve for the feedback coefficients yields:

$$\begin{aligned}
 A_h &= \frac{\omega_1^2}{K_1} \left( \frac{m}{4} + \frac{I}{L_v^2} \right) \\
 A_y &= \frac{2\zeta_1 \omega_1}{K_1} \left( \frac{m}{4} + \frac{I}{L_v^2} \right) \\
 C_h &= \frac{\omega_1^2}{K_1} \left( \frac{m}{4} - \frac{I}{L_v^2} \right) \\
 C_y &= \frac{2\zeta_1 \omega_1}{K_1} \left( \frac{m}{4} - \frac{I}{L_v^2} \right)
 \end{aligned}
 \tag{11.17}$$

It is convenient to non-dimensionalize the results using:

$$\frac{mg}{2} = \frac{\mu_o l_1 l_p (Ni_o)^2}{4h_{10}^2}
 \tag{11.18}$$

so that the following ratios are defined:

$$\frac{K_2}{K_1} = \frac{i_o}{h_{10}}$$

$$\frac{m}{K_1} = \frac{i_o}{g}$$

$$\frac{m}{K_2} = \frac{h_{10}}{g}$$

The dimensionless open loop force is:

$$\tilde{F}_F = \frac{F}{mg} = -\tilde{h}_{1F} + \tilde{i}_F \quad (11.19)$$

The dimensionless current control law is:

$$\begin{aligned} \tilde{i}_F = \frac{\Delta i_F}{i_0} = & (1 + \tilde{M} \tilde{\omega}_1^2) \tilde{h}_{1F} - \tilde{M} 2\zeta_1 \tilde{\omega}_1 \dot{\tilde{y}}_{1F} \\ & + \tilde{M}^* \tilde{\omega}_1^2 \tilde{h}_{1R} - \tilde{M}^* 2\zeta_1 \tilde{\omega}_1 \dot{\tilde{y}}_{1R} \end{aligned} \quad (11.20)$$

where

$$\tilde{M} = \frac{1}{4} + \frac{I}{mL_v^2}$$

$$\tilde{M}^* = \frac{1}{4} - \frac{I}{mL_v^2}$$

and as in Chapter 6:

$$\tilde{y}_1 = \frac{\Delta y_1}{h_{10}}, \quad \tilde{h}_1 = \frac{\Delta h_1}{h_{10}}$$

The dimensionless transfer functions for the displacements are the same as (6.11):

$$\frac{\tilde{y}_{1F}(\tilde{s})}{\tilde{y}_{0F}(\tilde{s})} = \frac{\tilde{\omega}_1^2}{\text{DEN}} \quad (11.21)$$

$$\frac{\tilde{h}_{1F}(\tilde{s})}{\tilde{y}_{OF}(\tilde{s})} = \frac{\tilde{s}^2 + 2\zeta_1 \tilde{\omega}_1 \tilde{s}}{\text{DEN}} \quad (11.22)$$

where

$$\text{DEN} = \tilde{s}^2 + 2\zeta_1 \tilde{\omega}_1 \tilde{s} + \tilde{\omega}_1^2$$

The current is a function of two inputs:

$$\tilde{i}_F(\tilde{s}) = \frac{[(1 + \tilde{M}\tilde{\omega}_1^2)\tilde{s}^2 + 2\zeta_1 \tilde{\omega}_1 \tilde{s}] \tilde{y}_{OF}(\tilde{s}) + \tilde{M}^* \tilde{\omega}_1^2 \tilde{s}^2 \tilde{y}_{OR}(\tilde{s})}{\text{DEN}} \quad (11.23)$$

From (5.12), the voltage without ohmic terms is:

$$\begin{aligned} \tilde{v}_{ind}(\tilde{s}) = \frac{v i_o}{mg\sqrt{gh_{10}}} = & \frac{\tilde{s}^3 [v_v (1 + \tilde{M}\tilde{\omega}_1^2) - 1] + \tilde{s}^2 (v_v - 1) 2\zeta_1 \tilde{\omega}_1}{\text{DEN}} \tilde{y}_{OF}(\tilde{s}) \\ & + \frac{v_v \tilde{M}^* \tilde{\omega}_1^2 \tilde{s}^2}{\text{DEN}} \tilde{y}_{OR}(\tilde{s}) \end{aligned} \quad (11.24)$$

where  $v_v$  is the flux leakage coefficient.

Before concluding the optimal suspension analysis of the two degree of freedom electromagnetic suspension, one must determine the response to the stochastic road input defined in (11.2) and (11.4). Since the transfer functions for displacement and acceleration are identical with those of Chapter 6, the results of that section apply.

The current transfer function differs from that of the heave case so that:

$$E[i_{F,R}^2] = \frac{AV}{j} \int_{-j\infty}^{+j\infty} \frac{(1 + \tilde{M} \tilde{\omega}_1^2) \tilde{s} + 2\zeta_1 \tilde{\omega}_1 + \tilde{M}^* \tilde{\omega}_1^2 \tilde{s} e^{-\tilde{T}\tilde{s}}}{\tilde{s}^2 + 2\zeta_1 \tilde{\omega}_1 \tilde{s} + \tilde{\omega}_1^2} ds$$

$$\times \frac{- (1 + \tilde{M} \tilde{\omega}_1^2) \tilde{s} + 2\zeta_1 \tilde{\omega}_1 - \tilde{M}^* \tilde{\omega}_1^2 \tilde{s} e^{+\tilde{T}\tilde{s}}}{\tilde{s}^2 - 2\zeta_1 \tilde{\omega}_1 \tilde{s} + \tilde{\omega}_1^2}$$

(11.25)

when  $\tilde{T}$  is positive the current calculated will be that of the front end while negative  $T$  gives the current at the rear of the vehicle, as dictated by (11.3). For the particular case where  $\zeta = 1/\sqrt{2}$ , the integral can be evaluated by referring to [47] and [55] or by integration in the complex plane so that the expected current for  $\zeta = 1/\sqrt{2}$  squared is then

$$E[i^2] = \frac{\pi AV}{\sqrt{2} \tilde{\omega}_1} [(1 + \tilde{M} \tilde{\omega}_1^2)^2 + 2] + \frac{\pi AV \tilde{M}^{*2} \tilde{\omega}_1^3}{\sqrt{2}}$$

$$+ \sqrt{2} \pi AV \tilde{M}^* \tilde{\omega}_1 e^{-\frac{\tilde{\omega}_1 \tilde{T}}{\sqrt{2}}} \left\{ (1 + \tilde{M} \tilde{\omega}_1^2) \cos \frac{\tilde{\omega}_1 \tilde{T}}{\sqrt{2}} \right.$$

$$\left. + [2 (\text{sgn} \frac{\tilde{\omega}_1 \tilde{T}}{\sqrt{2}}) - 1 - \tilde{M} \tilde{\omega}_1^2] \sin \frac{|\tilde{\omega}_1 \tilde{T}|}{\sqrt{2}} \right\}$$

(11.26)

A sample of current for the heave pitch model is compared to that for a heave only suspension in Figure 11.1. For these calculations, the inertia is modeled as a long thin beam with  $I = mL_V^2/12$ ; thus,  $\tilde{M} = 1/3$  and  $\tilde{M}^* = 1/6$  from (11.20). Also let  $L_V = 100$  ft.,  $V = 300$  mph, and  $A = 6.3 \times 10^{-7}$  ft. Virtually the entire rms value is

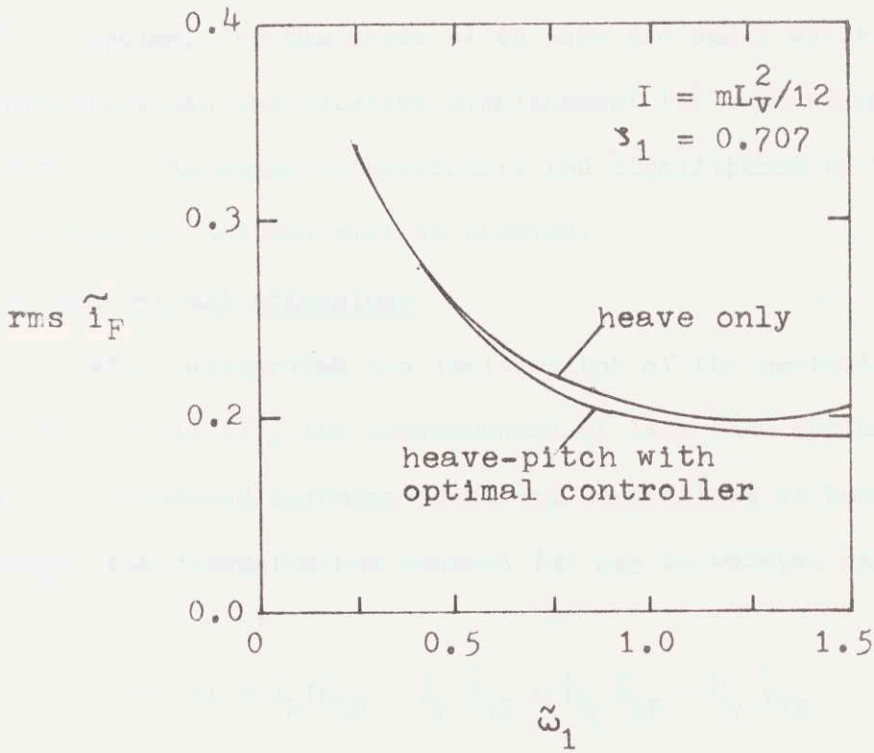


Figure 11.1. Current vs. Frequency: Comparison of Heave and Heave-Pitch Models

made of the first term of (11.26), and most of the current is used to maintain stability while only a small portion is used to give the desired control characteristics. The voltage gives similar results and is omitted from the discussion.

The differences in current between the heave only situation and the optimal for the heave pitch case are small while the acceleration and the relative displacement for both situations are identical. In order to appreciate the significance of these results, non-optimal situations must be studied.

### 11.3 Non-optimal Situations

Before discussing the implications of the optimal control law (11.16) and (11.17), the consequences of less than optimal control laws must be introduced assuming identical suspensions at both ends. In general, the dimensionless control law may be written as:

$$\ddot{y}_F = (1 + \tilde{A}_h)\tilde{h}_{1F} - \tilde{A}_y \dot{\tilde{y}}_{1F} + \tilde{C}_h \tilde{h}_{1R} - \tilde{C}_y \dot{\tilde{y}}_{1R} \quad (11.27)$$

where A denotes auto-feedback (variables from one end are fed into the magnet at that end) and the C denotes cross feedback (variables at a given end are fed into the opposite end's magnet). Interchange R and F for the control at the opposite end. Solve (11.10) and (11.11) simultaneously to obtain  $y_{1F}$ , nondimensionalize, and substitute (11.19) to obtain the open loop equations of motion:

$$\tilde{s}^2 \tilde{y}_{1F} = \tilde{I}(-\tilde{h}_{1F} + \tilde{i}_F) + \tilde{I}^*(-\tilde{h}_{1R} + \tilde{i}_R) \quad (11.28)$$

where

$$\tilde{I} = 1 + \frac{mL_v^2}{4I} \quad \tilde{I}^* = 1 - \frac{mL_v^2}{4I}$$

Note that for point masses  $I = mL_v^2/4$  and the force at the front is decoupled from the motion at the back. Also with point masses,  $\tilde{I} = 2$  so that the heave only situation is regained.

Substitute (11.27) into (11.28) where the current law is similar at both ends to obtain the transfer function for displacement:

$$\begin{aligned} \tilde{y}_{1F}(\tilde{s}) = & \{ \tilde{y}_{0F}(\tilde{s}) [ (\tilde{I}\tilde{A}_h + \tilde{I}^*\tilde{C}_h)\tilde{s}^2 + (\tilde{I}^2 - \tilde{I}^{*2})(\tilde{A}_y\tilde{A}_h - \tilde{C}_y\tilde{C}_h)\tilde{s} \\ & + (\tilde{I}^2 - \tilde{I}^{*2})(\tilde{A}_h^2 - \tilde{C}_h^2) ] \end{aligned} \quad (11.29)$$

$$\frac{+ \tilde{y}_{0R}(\tilde{s}) [ (\tilde{I}\tilde{C}_h + \tilde{I}^*\tilde{A}_h)\tilde{s}^2 + (\tilde{I}^2 - \tilde{I}^{*2})(\tilde{A}_y\tilde{C}_h - \tilde{C}_y\tilde{A}_h)\tilde{s} ]}{\{ \tilde{s}^2 + \tilde{s}(\tilde{I} + \tilde{I}^*)(\tilde{A}_y + \tilde{C}_y) + (\tilde{I} + \tilde{I}^*)(\tilde{A}_h + \tilde{C}_h) \} \{ \tilde{s}^2 + \tilde{s}(\tilde{I} - \tilde{I}^*)(\tilde{A}_y - \tilde{C}_y) + (\tilde{I} - \tilde{I}^*)(\tilde{A}_h - \tilde{C}_h) \}}$$

For our purposes (11.29) need only be studied under two conditions:

- (1) with the optimal control law which has already been investigated; and
- (2) with no crossfeedback.

Without crossfeedback,  $\tilde{C}_h = \tilde{C}_y = 0$  and the vehicle essentially has two identical suspensions at the front and rear which are the optimal suspensions derived on the basis of the heave model. For heave only motion  $\tilde{\omega}_1^2 = 2\tilde{A}_h$  and  $2\zeta_1\tilde{\omega}_1 = 2\tilde{A}_y$  and the absolute acceleration is:

$$\tilde{y}_{1F}(\tilde{s}) = \frac{\tilde{s}^2 \tilde{A}_h \{ \tilde{y}_{0F}(\tilde{s}) [ \tilde{I}\tilde{s}^2 + \tilde{s}(\tilde{I}^2 - \tilde{I}^{*2})\tilde{A}_y + (\tilde{I}^2 - \tilde{I}^{*2})\tilde{A}_h ] + \tilde{y}_{0R}(\tilde{s})\tilde{I}^*\tilde{s}^2 \}}{\text{DEN}}$$

where

$$\text{DEN} = \{\tilde{s}^2 + \tilde{s}(\tilde{I} + \tilde{I}^*)\tilde{A}_y + (\tilde{I} + \tilde{I}^*)\tilde{A}_h\}\{\tilde{s}^2 + \tilde{s}(\tilde{I} - \tilde{I}^*)\tilde{A}_y + (\tilde{I} - \tilde{I}^*)\tilde{A}_h\}$$

$I + I^* = 2$  so that one factor of the denominator does not depend on the rotational inertia; thus, the natural frequency of the heave mode is unchanged by the rotational mode. The natural frequency ( $\tilde{\omega}_R$ ) of the rotational mode is given by:

$$\tilde{\omega}_R = \sqrt{\frac{\tilde{A}_h(\tilde{I} - \tilde{I}^*)}{\tilde{I} + \tilde{I}^*}} = \sqrt{\frac{\tilde{I} - \tilde{I}^*}{\tilde{I} + \tilde{I}^*}} \tilde{\omega}_H$$

where  $\tilde{\omega}_H$  is the natural frequency of the heave mode. If the vehicle is modeled as a long thin beam  $I = mL_V^2/12$  so that  $\tilde{I} = 4$  and  $\tilde{I}^* = -2$  so that  $\tilde{\omega}_R = \sqrt{3} \tilde{\omega}_H$ . The displacement at an end depends on the input at both ends.

The relative displacement between the magnet and rail is:

$$\begin{aligned} \tilde{h}_{1F}(\tilde{s}) = & \{\tilde{y}_{0F}(\tilde{s})[\tilde{s}^4 + 2\tilde{A}_y\tilde{I}\tilde{s}^3 + (\tilde{A}_y^2(\tilde{I}^2 - \tilde{I}^{*2}) + \tilde{I}\tilde{A}_h)\tilde{s}^2 \\ & + \frac{\tilde{A}_y\tilde{A}_h(\tilde{I}^2 - \tilde{I}^{*2})\tilde{s} - \tilde{y}_{0R}(s)\tilde{I}^*\tilde{A}_h\tilde{s}^2}{\text{DEN}} \} \end{aligned} \quad (11.31)$$

The transfer function for the current with no crossfeedback is:

$$\begin{aligned} \tilde{i}_F(\tilde{s}) = & \tilde{y}_{0F}(\tilde{s})\{\tilde{s}^4(1 + \tilde{A}_h) + \tilde{s}^3(2\tilde{A}_y\tilde{I} + \tilde{A}_y\tilde{A}_h\tilde{I}) + \tilde{s}^2[\tilde{A}_h\tilde{I}(1 + \tilde{A}_h) \\ & + \tilde{A}_y^2(\tilde{I}^2 - \tilde{I}^{*2})] + \tilde{s}\tilde{A}_y\tilde{A}_h(\tilde{I}^2 - \tilde{I}^{*2})\} \\ & - \frac{\tilde{y}_{0R}(\tilde{s})\{\tilde{s}^3\tilde{A}_y\tilde{A}_h\tilde{I}^* + \tilde{s}^2\tilde{I}^*\tilde{A}_h(1 + \tilde{A}_h)\}}{\text{DEN}} \end{aligned} \quad (11.32)$$

Finally, the voltage is (without ohmic terms):

$$\begin{aligned}
 \tilde{v}_F &= \frac{v_{ind} i_o}{mg \sqrt{g} h_{10}} \\
 &= \tilde{y}_{OF}(\tilde{s}) \{ \tilde{s}^5 [v_v (1 + \tilde{A}_h) - 1] + \tilde{s}^4 [(v_v - 1) 2\tilde{A}_y \tilde{I} + v_v \tilde{A}_y \tilde{A}_h \tilde{I}] \\
 &\quad + \tilde{s}^3 [(v_v - 1) (\tilde{A}_y^2 (\tilde{I}^2 - \tilde{I}^{*2}) + \tilde{I} \tilde{A}_h) + v_v \tilde{I} \tilde{A}_h^2] \\
 &\quad + \tilde{s}^2 [(v_v - 1) (\tilde{I}^2 - \tilde{I}^{*2}) \tilde{A}_h \tilde{A}_y] \} \tag{11.33} \\
 &\quad - \frac{\tilde{y}_{OR}(\tilde{s}) \{ \tilde{s}^4 v_v \tilde{A}_h \tilde{A}_y \tilde{I}^* - \tilde{s}^3 [v_v \tilde{I}^* \tilde{A}_h (1 + \tilde{A}_h) - \tilde{I}^* \tilde{A}_h] \}}{DEN}
 \end{aligned}$$

The expected values of acceleration, displacement, and current were calculated by integrating their respective integrals in the complex plane with a digital computer program. These results appear in Figure 11.2 for a representative situation where  $L_v = 100$  ft.,  $V = 300$  mph,  $A = 6.3 \times 10^{-7}$  ft.,  $I = mL_v^2/12$  which were the same parameters used for Fig. 11.1. The plotted curves are close to those of the heave only situation and change little with vehicle length or from the front to the rear. Voltages are similar to those determined from the heave only model (Chapter 7).

Figure 2.17 compares the acceleration spectra at the vehicle's end for systems with and without crossfeedback. The indicated natural

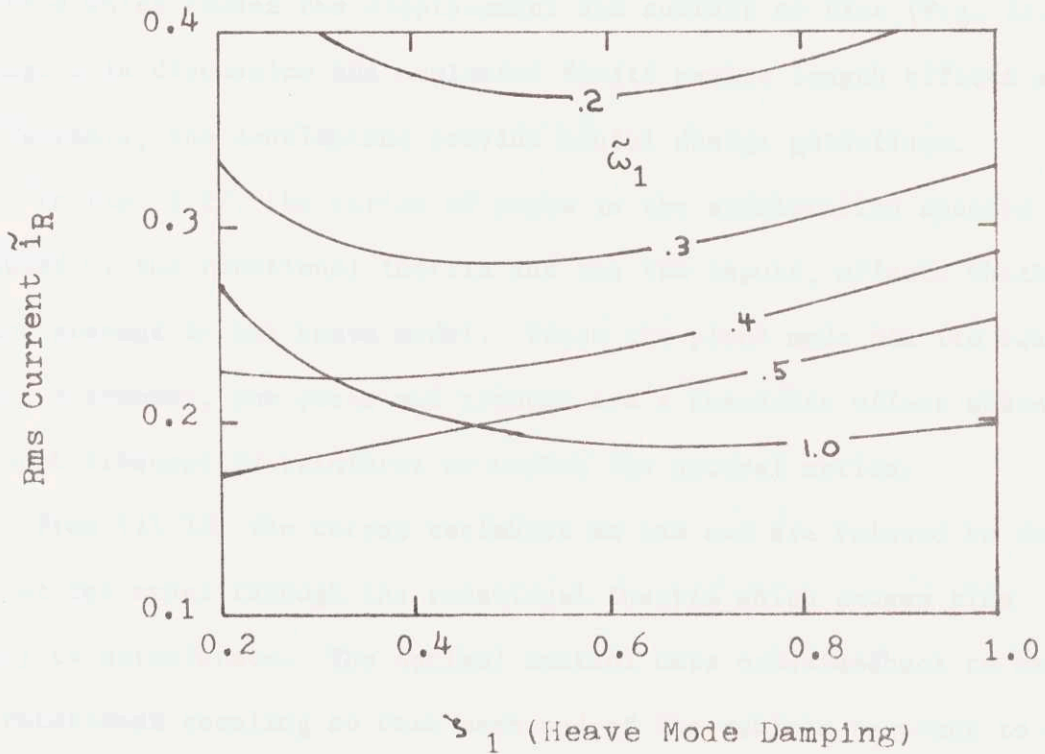
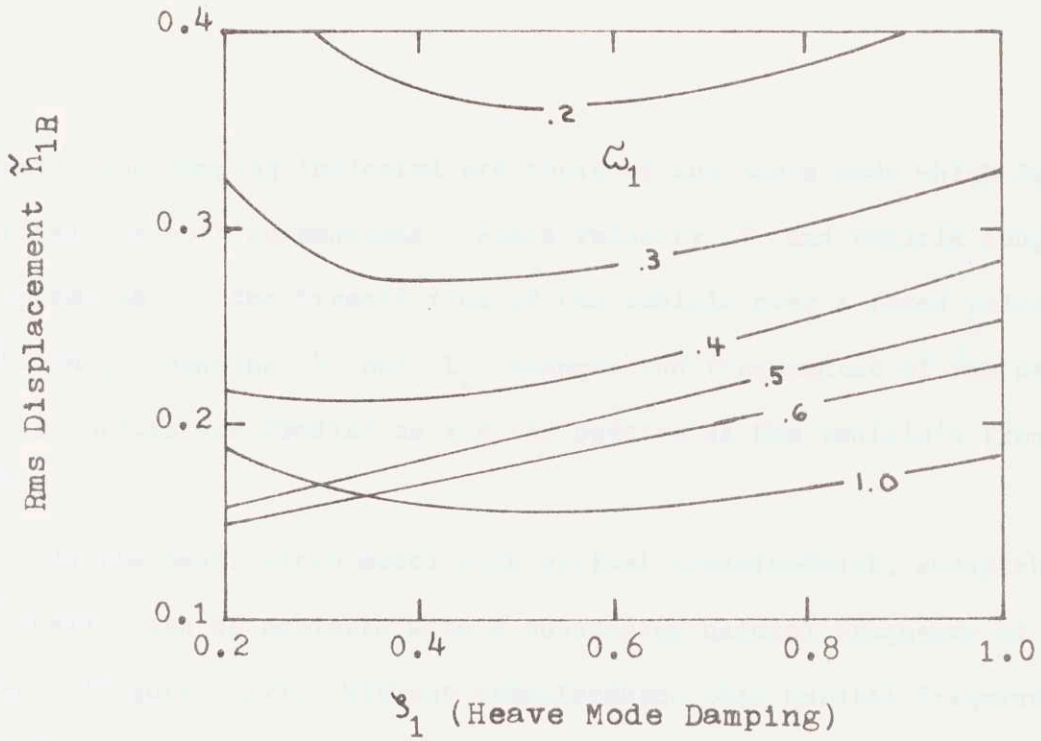


Fig. 11.2. Current and Displacement of Heave-Pitch Model ( $\tilde{I} = 4$ ,  $\tilde{I}^* = -2$ ,  $\tilde{T} = 5.8$ ,  $A = 2\pi \times 10^{-7}$  ft.,  $V = 300$  mph.,  $L_V = 100$  ft.)

frequency and damping indicated are those of the heave mode which is identical for both suspensions. Since velocity  $V$  and vehicle length  $L_v$  appear in  $\tilde{T}$  the transit time of the vehicle over a fixed point in the rail, changing  $V$  and  $L_v$  changes the frequencies of the peaks, but the spectra are similar as are the spectra at the vehicle's front and rear.

In the heave pitch model with optimal crossfeedback, acceptable ride quality can be achieved with a suspension natural frequency of 1.6 hz. (Figure 2.17). Without crossfeedback this natural frequency gives a poor ride at the critical 6 hz., so that an acceptable ride cannot be obtained unless the suspension's heave natural frequency is decreased which causes the displacement and current to rise (Fig. 11.2). Although this discussion has neglected finite magnet length effects and eddy currents, the conclusions provide useful design guidelines.

In Fig. 2.17, the series of peaks in the acceleration spectra is caused by the rotational inertia and the two inputs, effects which are not present in the heave model. Since the pitch mode has its own natural frequency, the peaks and troughs are a resonance effect where the input frequencies reinforce or weaken the natural motion.

From (11.28) the output variables at one end are related to the input at the other through the rotational inertia which causes ride quality to deteriorate. The optimal control uses crossfeedback to cancel this rotational coupling so that each end of the vehicle responds to only the inputs at that end. The optimal control (11.17) allows optimal ride

quality without sacrificing current or displacement. This result is particularly suited to the electromagnetic suspension since the variables must be measured to stabilize the suspension and since electrical signals can be transmitted the length of the vehicle. This improvement of ride quality through crossfeedback is an important asset of electromagnetic suspensions.

The vehicle's center of gravity is unaffected by the rotational coupling. In (11.10)  $1/2(y_{1F} + y_{1R})$  is the c.g.'s displacement so that motion of the center depends only on the sum of the forces. In a linearized situation, the sum of the forces is a function of the average input displacement so that the motion of the center is identical to that of the heave only situation in a stochastic sense.

In summary, the addition of pitch to the heave model couples the behavior of the two ends of the vehicle. If suspensions designed from heave considerations alone are used, the acceleration spectra for the ends of the vehicle have a series of undesirable peaks which are caused by the rotational coupling. This undesirable effect can be countered by reducing the stiffness of the suspension with accompanying penalties in control current and relative displacement or by crossfeedback which feeds the variables measured at one end into the suspension at the other. Crossfeedback which is easily adapted to electromagnetic suspensions eliminates the coupling of the two ends and the accompanying deterioration in ride quality.

## 12. LATERAL MOTION

### 12.1 Introduction

At least two strategies exist for obtaining lateral guidance from an electromagnetic suspension. One technique uses two sets of magnets one for lateral guidance and one for vertical support. The separate magnets give much freedom in the selection of control and suspension dynamics; however, the two sets of magnets increase the total suspension weight and the ohmic and drag power. Also additional sections of rail for the lateral guidance could be required.

This chapter explores the possibility of using the magnets which support the vehicle vertically for laterally guiding the vehicle. Rails designs of previous chapters have allowed for lateral motions and are reasonably shaped for lateral guidance as will be shown. This chapter concludes that the use of the lift magnets for lateral guidance should be given further consideration.

This chapter is divided into two sections:

(1) Experimental measurements are taken to estimate the magnet's approximate lateral stiffness for linearized analyses. Scale laws are developed to relate the experiment to full scale systems.

(2) The performance of full size systems is evaluated from linearized models with stochastic wind and road inputs. The wind input with spatial correlation is developed in Appendix A.4.

## 12.2 Scale Model Tests and Analysis

To enable the experiments to be applied to a full size system, scale laws are developed for the lateral force in static situations.

The following assumptions are used:

- (1) Lateral forces may be determined from [50]

$$F_z = \frac{1}{2} (Ni)^2 \frac{\partial P_T}{\partial g_1} \quad (12.1)$$

where

$F_z$  = force in lateral direction

$g_1$  = lateral position of magnet relative to rail (Fig. 12.1)

$Ni$  = amp turns of control coil

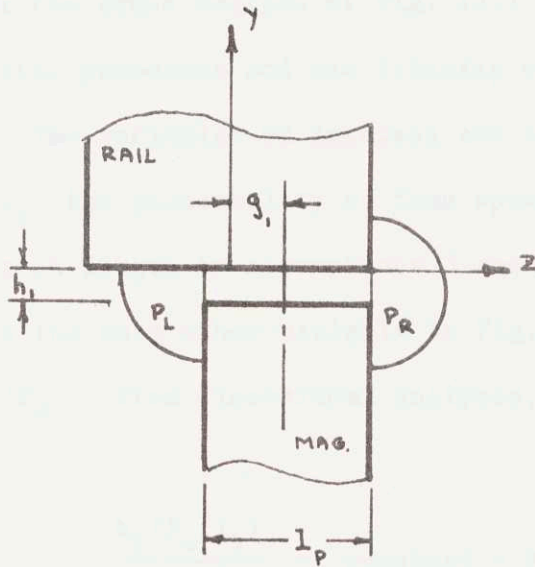
$P_T$  = total permeance of flux paths.

- (2) As long as the magnet is below the rail, the useful permeance (Fig. 12.1) does not change with lateral position; i.e.,

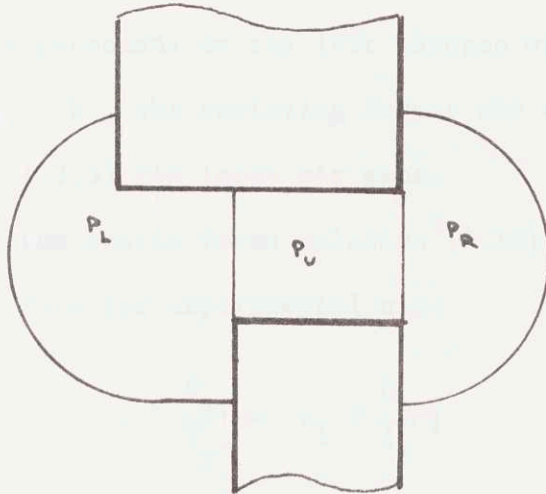
$$\frac{\partial P_u}{\partial g_1} = 0 \quad (12.2)$$

This assumption is shown in Chapter 5 and in [50].

- (3) The magnets are long so that end effects are neglected.
- (4) The reluctance of the iron is negligible compared to that of the air gap.
- (5) The basic cross section is illustrated in Fig. 2.1.
- (6) For magnets where the end effects can be neglected the lateral force per unit magnet length ( $F_z/l_1$ ) is constant with respect to position along the magnet's length.



a. Small Air Gap



b. Large Air Gap

Fig. 12.1. Permeances for Scale Law for Lateral Forces

Consider the cross section of Fig. 12.1 where the air gap is small so that the useful permeance and one fringing permeance ( $P_L$ ) do not change with  $z$ . The variables of interest are the current ( $Ni$ ) by assumption 1,  $\mu_0$  the permeability of free space by assumptions 1 and 4, the force per unit length by assumptions 3 and 6, and  $h_1$  the air gap height which is the only other variable in Fig. 12.1 that can affect the flux path ( $P_R$ ). From dimensional analysis, the dimensionless ratio  $\pi_1$ , is defined:

$$\frac{h_1 (F_z / l_1)}{\mu_0 (Ni)^2} = \text{constant} = \pi_1 \quad (12.3)$$

This relation is studied in the experiment to be described. For large air gaps, the permeance on the left changes with  $z$ . Since  $\partial P_L / \partial g_1 > 0$  while  $\partial P_R / \partial g_1 < 0$ , the restoring forces are expected to be less than predicted by (12.3) for large air gaps.

Using the static force relation (5.10), (12.3) is written in a convenient form for experimental use:

$$\frac{F_z}{F_y} = \pi_1 \left( \frac{h_1}{l_p} \right) \quad (12.4)$$

Both the experiment and the full scale prototypes of Chapter 4 are designed so that the ratio of nominal gap to magnet rail overlap ( $l_2 - l_p = 2h_{10}$  from Fig. 2.1) is constant; i.e.,

$$\frac{l_2 - l_p}{h_{10}} = 2$$

Since lateral force does not depend on the useful permeance (assumption 2), (12.3) can be used to convert experimental measurements to full scale designs as long as the fringing flux paths are geometrically similar; that is, for comparable positions:

$$\pi_2 \left( \frac{h_1}{h_{10}}, \frac{g_1}{h_{10}} \right) = \left[ \frac{h_1 (F_z / l_1)}{\mu_o (Ni)^2} \right]_m = \left[ \frac{h_1 (F_z / l_1)}{\mu_o (Ni)^2} \right]_p \quad (12.5)$$

where the subscript  $m$  refers to the experimental model and  $p$  to the full scale prototype.

The test facility described in Chapter 3 was used to measure lateral forces. The transducer for lateral forces is connected between the magnet and the body of the vehicle as shown in Fig. 3.6. Strain gages are mounted on the transducer's vertical beams which flex in parallel as cantilevers so that the uniform air gap is maintained and the proper static stiffness is achieved. Four strain gages are mounted, one on each side of the two beams so that a full bridge is realized. This transducer is much stiffer in the vertical direction than in the horizontal direction and the strain gages are mounted so that the bridge remains balanced when vertical forces are applied; thus, only horizontal forces are measured. As a further precaution, all tests were run with the same vertical force.

Although the rail could be displaced laterally, the facility was not equipped to measure lateral displacements with high accuracy; therefore, all force measurements were done where the edge of the rail coincided with that of the magnet.

For all measurements, the vehicle was suspended while the magnets were controlled in the closed loop so that the vertical force was the weight of the vehicle (13.3 lbf). The bridge was excited and balanced by a Sanborn 321 recorder.

The lateral forces were measured at both edges as a function of gap height. These results are plotted in Fig. 12.2 as  $F_z/F_y$  versus  $h_1$ .  $F_z$  is stabilizing; i.e.,  $F_z$  pushes the magnet to  $g_1 = 0$ . The linear result predicted by (12.3) is valid for  $h_1/h_{10} < 1/2$  after which the lateral force increases at a rate less than the linear law predicts as discussed.

The lateral stiffness which is used in the dynamic analysis is estimated from the linearized force:

$$F_z = \left. \frac{\partial F_z}{\partial h_1} \right|_{OP} \Delta h_1 + \left. \frac{\partial F_z}{\partial g_1} \right|_{OP} \Delta g_1$$

where the operating point is  $h_1 = h_{10}$  and  $g_1 = 0$ . For the magnet centered below the rail  $g_1 = 0$  and  $F_z = \partial F_z / \partial h_1 = 0$ . Since lateral forces were measured only at the magnet's edge, an approximate stiffness is obtained from

$$k_L = \frac{F_z \Big|_{g_1 = h_1 = h_{10}}}{h_{10}} \quad (12.6)$$

With the nominal vertical force equal to the vehicle's weight ( $mg$ ). Using (5.10) rewrite (12.5) as

$$\pi_2 \left( \frac{h_1}{h_{10}}, \frac{g_1}{h_{10}} \right) = \frac{F_z}{F_y} \frac{l_p}{h_1} \quad (12.7a)$$

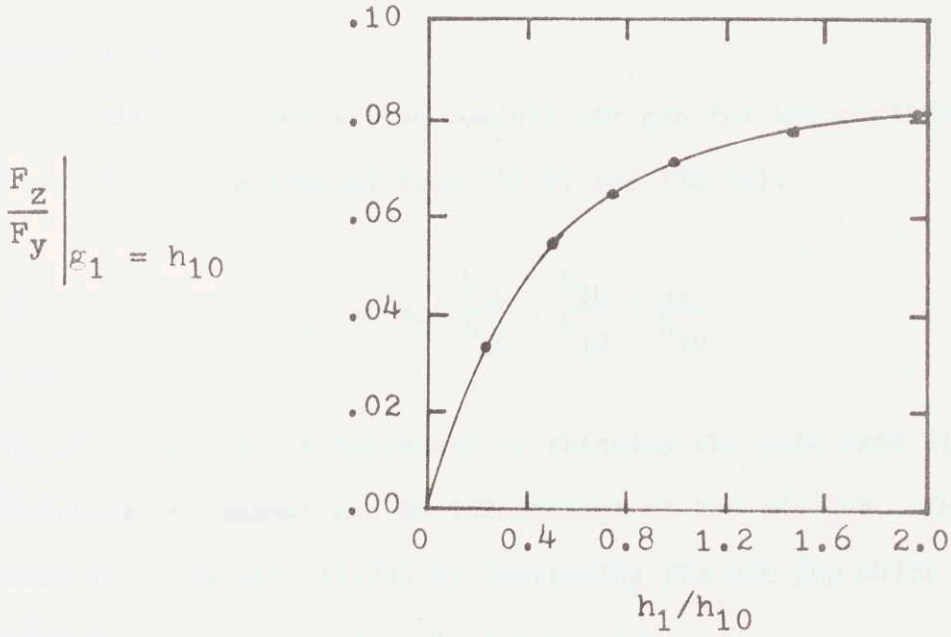


Fig. 12.2. Lateral Force Measurements  
(Line is fit to experimental  
points.)

For the experiment  $F_z/mg = 0.072$  from Figure 12.2 for  $l_p/h_1 = 4.2$  at  $h_1 = h_{10}$  and  $g_1 = h_{10}$ . Thus,  $\pi\left(\frac{h_{10}}{h_{10}}, \frac{h_{10}}{h_{10}}\right) = 0.3$ . For full scale designs, such as design 2 of Table 3,  $h_1/l_p = 0.45$  so that the maximum lateral force at the nominal air gap is 0.14 mg a value which places lateral guidance by the fringing fields into the realm of possibility.

The stiffness at the nominal air gap for the configuration of Figure 2.1 is determined from (12.6) and (12.7a):

$$k_L = \pi_2\left(\frac{h_{10}}{h_{10}}, \frac{h_{10}}{h_{10}}\right) \frac{mg}{h_{10}} \quad (12.7b)$$

The stiffness can be increased by thinning the pole face ( $l_p$ ) which lengthens the magnet and is independent of the air gap. The maximum force is increased (12.7a) by increasing the air gap which increases the maximum  $g_1$  because  $l_2 = l_p + 2 h_{10}$ .

In the linearized analysis of Section 12.3, the linearized stiffness will be described by (12.6). Since the linearization is done for  $g_1 = 0$  and since the lateral force is zero for all  $h_1$  when  $g_1 = 0$  the linearization will neglect the possibly important effects which result from the lateral force's dependence on the air gap  $h_1$ . It is recommended that lateral force measurements be made as a function of lateral displacement and air gap.

### 12.3 Linearized Model for Lateral Motion

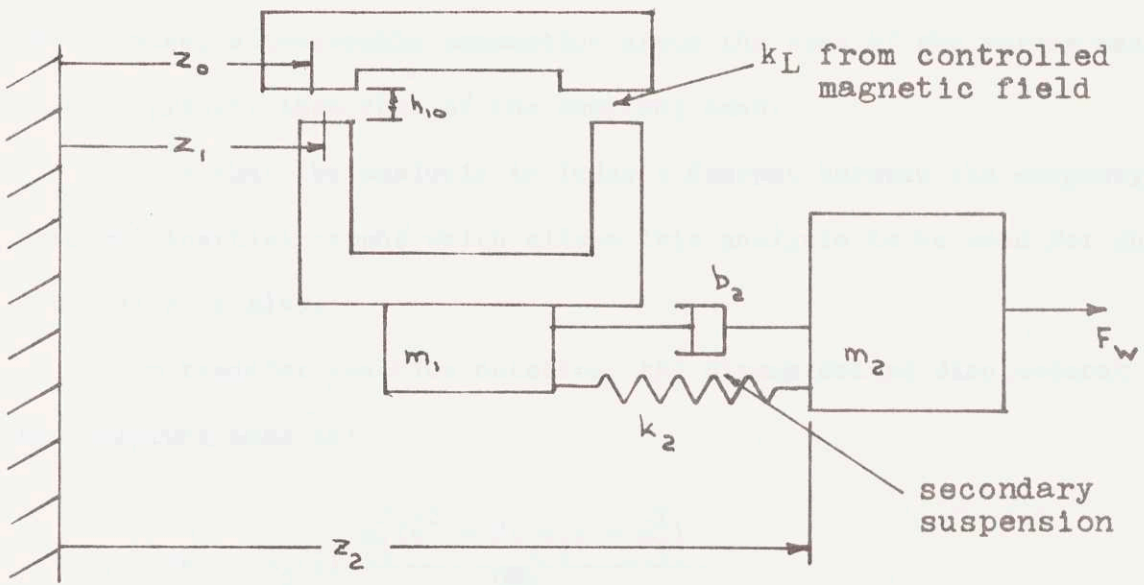
Using the linearized stiffness determined in the previous section, the performance of a full size vehicle operating in the lateral mode is

investigated. Two inputs to the lateral motion will be considered. In addition to the stochastic rail input which is similar to that of the vertical motion, the lateral suspension must counter winds which force the vehicle with both steady and stochastic components. This chapter:

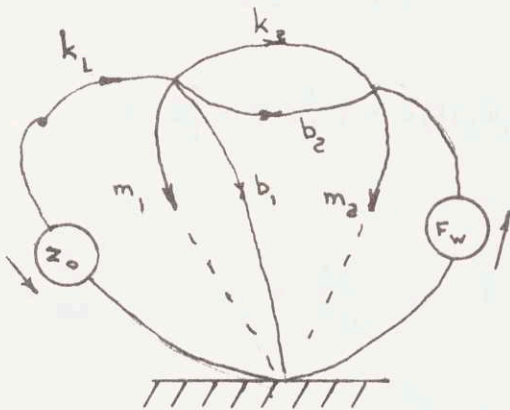
- (1) Develops a linearized model for lateral motion.
- (2) Describes wind and road inputs.
- (3) Investigates performance of a typical system with passive secondary suspension.

The transfer function of an electromagnetic suspension which operates in the lateral mode and is forced by wind and road inputs is developed. Since lift forces do not depend on lateral position as long as the magnet is below the pole face of the rail and since the linearized lateral force is zero for all air gaps when the magnet is centered with respect to the rail ( $g_1 = 0$ ), the magnet motions in the lateral and vertical modes are decoupled in a linearized analysis (although coupled in a non-linear analysis since lateral force depends on the air gap when magnet is not centered below rail). As in the vertical motion situation, it is assumed that eddy current effects are negligible; thus, eddy currents induced by the lateral motion will cause little if any damping so that the primary suspension is modeled with no damping ( $b_1 = 0$ ) and a linear spring  $k_1$  which is described by (12.7b). Since the primary suspension has no damping, the lateral suspension must include a secondary suspension. As in Chapters 2 and 9, the secondary suspension is assumed to be a spring in parallel with a dashpot as shown in Figure 12.3.

As shown in Figure 12.3, assume that the wind acts only on the



a. Schematic



b. Linear Graph

Fig. 12.3. Lateral Motion with Passive Secondary Suspension

sprung mass, a reasonable assumption since the area of the sprung mass is much greater than that of the unsprung mass.

Note that the analysis includes a dashpot between the unsprung mass and inertial ground which allows this analysis to be used for the vertical mode also.

In transfer function notation, the dimensionless displacement of the unsprung mass is:

$$\begin{aligned} \tilde{z}_1(\tilde{s}) = \tilde{z}_0(\tilde{s}) & \frac{\tilde{\omega}_1^2(\tilde{s}^2 + 2\zeta_2\tilde{\omega}_2\tilde{s} + \tilde{\omega}_2^2)}{\text{DEN}} \\ & + \tilde{F}_w(\tilde{s}) \frac{(2\zeta_2\tilde{\omega}_2\tilde{s} + \tilde{\omega}_2^2)(\gamma + 1)}{\text{DEN}} \end{aligned} \quad (12.8)$$

where

$$\begin{aligned} \text{DEN} = \tilde{s}^4 + \tilde{s}^3(2\zeta_2\tilde{\omega}_2 + 2\zeta_1\tilde{\omega}_1 + \gamma 2\zeta_2\tilde{\omega}_2) + \tilde{s}^2(4\zeta_1\zeta_2\tilde{\omega}_1\tilde{\omega}_2^2 + \tilde{\omega}_1^2 \\ + \tilde{\omega}_2^2 + \gamma\tilde{\omega}_2^2) + \tilde{s}(2\zeta_1\tilde{\omega}_1\tilde{\omega}_2^2 + 2\zeta_2\tilde{\omega}_2\tilde{\omega}_1^2) + \tilde{\omega}_1^2\tilde{\omega}_2^2 \end{aligned}$$

where

$$\tilde{F}_w = \frac{F_w}{mg}, \quad \tilde{z}_1 = \frac{\Delta z}{h_{10}}, \quad \tilde{t} = t\sqrt{g/h_{10}}, \quad \tilde{z}_0 = \frac{\Delta z_0}{h_{10}}$$

$$m = m_1 + m_2 \quad \gamma = \frac{m_2}{m_1}$$

$$\tilde{\omega}_1 = \sqrt{k_L/m_1 h_{10}/g}, \quad \omega_2 = \sqrt{k_2/m_2 h_{10}/g}$$

$$2\zeta_1\tilde{\omega}_1 = \frac{b_1}{m_1} \sqrt{\frac{h_{10}}{g}} = 0, \quad 2\zeta_2\tilde{\omega}_2 = \frac{b_2}{m_2} \sqrt{\frac{h_{10}}{g}}$$

The absolute displacement of the secondary

$$\begin{aligned} \tilde{z}_2 = \tilde{z}_0(s) & \frac{(2\zeta_2 \tilde{\omega}_2 \tilde{s} + \tilde{\omega}_2^2) \tilde{\omega}_1^2}{\text{DEN}} \\ & + \tilde{F}_w(\tilde{s}) \frac{(1+\gamma) [\tilde{s}^2/\gamma + \tilde{s}(2\zeta_2 \tilde{\omega}_2 + 2\zeta_1 \tilde{\omega}_1/\gamma) + \tilde{\omega}_2^2 + \tilde{\omega}_1^2/\gamma]}{\text{DEN}} \end{aligned} \quad (12.9)$$

The relative displacement between the rail and the magnet is given by  $\tilde{g}_1 = \tilde{z}_0 - \tilde{z}_1$  and the relative displacement between the magnet and the secondary is given by  $\tilde{g}_2 = \tilde{z}_1 - \tilde{z}_2$ . As for heave motion, the rail inputs are modeled as a stochastic process with zero mean and the spectral density of irregularities ( $z_0$ ) is given by

$$\phi_{z_{OL} z_{OL}}(s) = \phi_{z_{OR} z_{OR}}(s) = - \frac{AV}{s^2} \quad (12.10)$$

where the subscript L and R denote left and right, respectively. To completely define the road input a correlation between the two rails must be defined. Intuitively, for irregularities of long wave length, the two rails will be parallel; that is, the correlation will be perfect. We shall neglect any skewness of the rail which can only occur for very short wave lengths, so that only one rail input need be considered. This assumption is similar to omitting roll from the vertical models as is done in Chapters 6 and 11. As in previous chapters, welded rails with  $A = 6.3 \times 10^{-7}$  ft. and vehicle speed of 300 mph are assumed.

The prevailing winds will load the vehicle with a lateral force that must be balanced or absorbed by the suspension. From [43], the

probable vehicle can be modeled as body of revolution since, for revenue traffic, the vehicle can be expected to be on the order of 100 feet long, 10 feet wide, and 10 feet high. The wind force in the lateral direction is then given by

$$F_w = \frac{1}{2} \rho c_d A_L V_r^2 \quad (12.11)$$

where

$V_r$  = component of wind velocity perpendicular to direction of motion and parallel to surface.

$A_L$  = area of cross section projected toward V

$\rho$  = density of the atmosphere

$c_d$  = drag coefficient

Note that (12.11) states that the force is proportional to the total wind velocity ( $V_T$ ) relative to the vehicle squared when this quantity is multiplied by the sine of the angle of attack ( $\theta$ ) squared

$$F_w \propto (V_T \sin\theta)^2$$

Many mathematical theories for small angle of attack predict that the force should be proportional to the sine and not the sine squared.

However, for thin bodies of revolution and for the angles of attack under consideration ( $\theta = \sin^{-1} 36/300 = 7^\circ$ ), [63] shows that the lift is proportional to a quantity which contains terms proportional to both the sine and sine squared. For this situation, [63] suggests  $c_d = 0.8$  as a reasonable drag coefficient.

The wind can be considered to consist of a steady and oscillating component

$$V_r = V_0 + \Delta V_r \quad (12.12)$$

which can be squared and the  $(\Delta V_r)^2$  neglected

$$V_r^2 \approx V_0^2 + 2V_0 \Delta V_r$$

The steady component of the wind force is calculated directly from (12.11) while the spectral density of the oscillating force can be written as:

$$\phi_w(s) = (\rho c_d A_L V_0)^2 \phi_{\Delta V_r}(s)$$

where we have assumed that the velocity is constant over the cross section A.

From [55], [61] and [62], the spectral density of  $\Delta V_r$  at a point at the surface of the earth

$$\phi_{\Delta V_r}(s) = (\text{rms } \Delta V_r)^2 \frac{\nu}{\pi(-s^2 + \nu^2)} \quad (12.13)$$

where  $\nu$  is a characteristic frequency and the spectrum extends from  $-j\infty$  to  $+j\infty$ . [61] suggests a slightly different, more complicated form for (12.13); however, for the data presented in that reference, the above spectral density is suitable.

For the design examples which follow, the wind spectral density (12.13) will be employed; however, the vehicle's finite length filters the wind just as the magnet filters the road input (Chapter 2.3.3 and 7).

The effects of the vehicle's length as a filter is evaluated in Appendix A.4 where it is shown that, for 300 mph vehicle speeds and 100 ft vehicle lengths, the filtering of the wind can be ignored.

For the numerical examples, select  $V_0 = 36$  mph and rms  $\Delta V_r = 9$  mph, which is a worst design case that covers all but a few minutes per year [40]. The density of air at 1 atmosphere and 20°C is 0.075 lbm/ft. The break frequency  $\nu$  for design purposes has not been agreed upon. [55] simply states that  $\nu$  ranges from .5 to 3 sec<sup>-1</sup> and uses 1.0 sec<sup>-1</sup> for a design example while [61] suggests that  $\nu = V_T/L$  where  $V_T$  is total velocity of wind relative to the vehicle and  $L$  is the scale of turbulence which is a characteristic of the wind. At 300 mph, with  $L = 1000$  ft., which [61] suggests as a typical value,  $\nu = 0.45$  sec<sup>-1</sup>. [61] also mentions that on occasion  $L$ 's as low as 200 ft have been measured so that  $\nu = 2.5$  sec<sup>-1</sup> is also possible. This work plots the design data for  $\nu = 0.5, 1.5,$  and  $3.0$  sec<sup>-1</sup> ( $\tilde{\nu} = 0.02, 0.06$  and  $0.12$ ). For estimation assume that the vehicle is 100 feet long and 10 feet high with drag coefficient = 0.8 as mentioned earlier. With proper streamlining, these values will probably be conservative. For an 88,000 lb vehicle, these values yield a steady wind force component of 0.03 mg and an rms fluctuating wind force of 0.015 mg. These figures compare to the 0.14 mg maximum that can be developed by the fringing fields of the vertical magnets (Chapter 12.2). These crude figures do not eliminate the use of the fringing fields for lateral guidance.

Table 16

Parameter Values for Sample Designs for Lateral Motion

primary natural frequency ( $f_1$ )	4.0 hz.
primary damping ratio ( $\zeta_1$ )	0.0
secondary natural frequency ( $f_2$ )	1.0 hz.
secondary damping ratio ( $\zeta_2$ )	0.25
sprung to unsprung mass ratio ( $\gamma$ )	5.0
air gap ( $h_{10}$ )	0.6 in.
magnet length ( $l_1$ )	30.0 ft.
vehicle weight (m)	88,000 lbf.
road roughness (A)	$6.3 \times 10^{-7}$ ft.
forward velocity (V)	300 mph.
steady lateral wind force	.03 mg
oscillating rms lateral wind force	.015 mg
characteristic wind frequency ( $\nu$ )	0.5, 1.5, and 3.0 hz.

The equations of motion (12.8) and (12.9) with the spectral densities for the wind and road inputs (12.10) and (12.13) are used to construct sample design curves by the techniques of (4.11) and (4.12). Magnet design 2 of Table 4 was selected since it is a realistic sample. The mass ratio ( $\gamma$ ) is five and the pole width ( $l_p$ ) of the magnet is 1.38 in. for an air gap of 0.6 in. and magnet length ( $l_1$ ) of 30 ft. Referring to (12.7b) and (12.8) the dimensionless natural frequency  $\tilde{\omega}_1$  is approximately one ( $\tilde{\omega}_1 \approx 1$ ) which corresponds to 4 hz. As discussed, the damping ratio  $\zeta_1 = 0$ . The natural frequency of the secondary suspension is 1 hz. ( $\tilde{\omega}_2 = 0.25$ ) and the damping ratio ( $\zeta_2$ ) is 0.25 as concluded in Chapter 4.2.

The quantities used in the sample design are summarized in Table 16.

The responses to the wind and road inputs are determined separately. Since wind and road inputs are uncorrelated, the spectral densities and the rms values which result from both inputs operating simultaneously is determined from the response to the individual inputs by:

$$z_{wR}^2 = z_w^2 + z_R^2 \quad (12.14)$$

where

$z_{wR}$  is the response to the combined input

$z_w, z_R$  are responses to the wind and road, respectively.

Figure 12.4 displays the systems square root acceleration spectrum. In Figure 12.4a, the response to the road inputs was

determined with the finite magnet length assumption of Chapter 7. The DOT specifications are used for comparison. The zero damping of the primary still allows a suitable ride for the system.

Figure 12.4b displays the response to the wind input for three characteristic wind frequencies which correspond to  $v = 0.5, 1.5$  and  $3$  hz. Although the rms wind velocity  $\Delta V_r$  is identical, the higher  $v$ 's raise the input spectrum at the critical  $1$  hz. Without considering the road, the ride is acceptable in all cases. The spectrum at  $1$  hz. for the situation where both the wind and road are acting may be derived from (12.14) and summarized as follows:

$v$ (sec <sup>-1</sup> )	$\ddot{z}_{2R}$ (1 hz)	$\ddot{z}_{2w}$ (1 hz)	$\ddot{z}_{2Rw}$
.5	.021	.007	.022
1.5	.021	.012	.024
3.0	.021	.017	.027

Although the results are acceptable for each  $v$ , the effects of  $v$  are clearly evident and affect the maximum roughness of the road which can be permitted.

Figure 12.5 displays the rms acceleration of the primary ( $\ddot{z}_1$ ) versus the natural frequency of the primary based on the point contact model.

In Figure 12.6, the rms acceleration of the secondary ( $\ddot{z}_2$ ) is plotted based on the point contact assumption. The effects of this curve

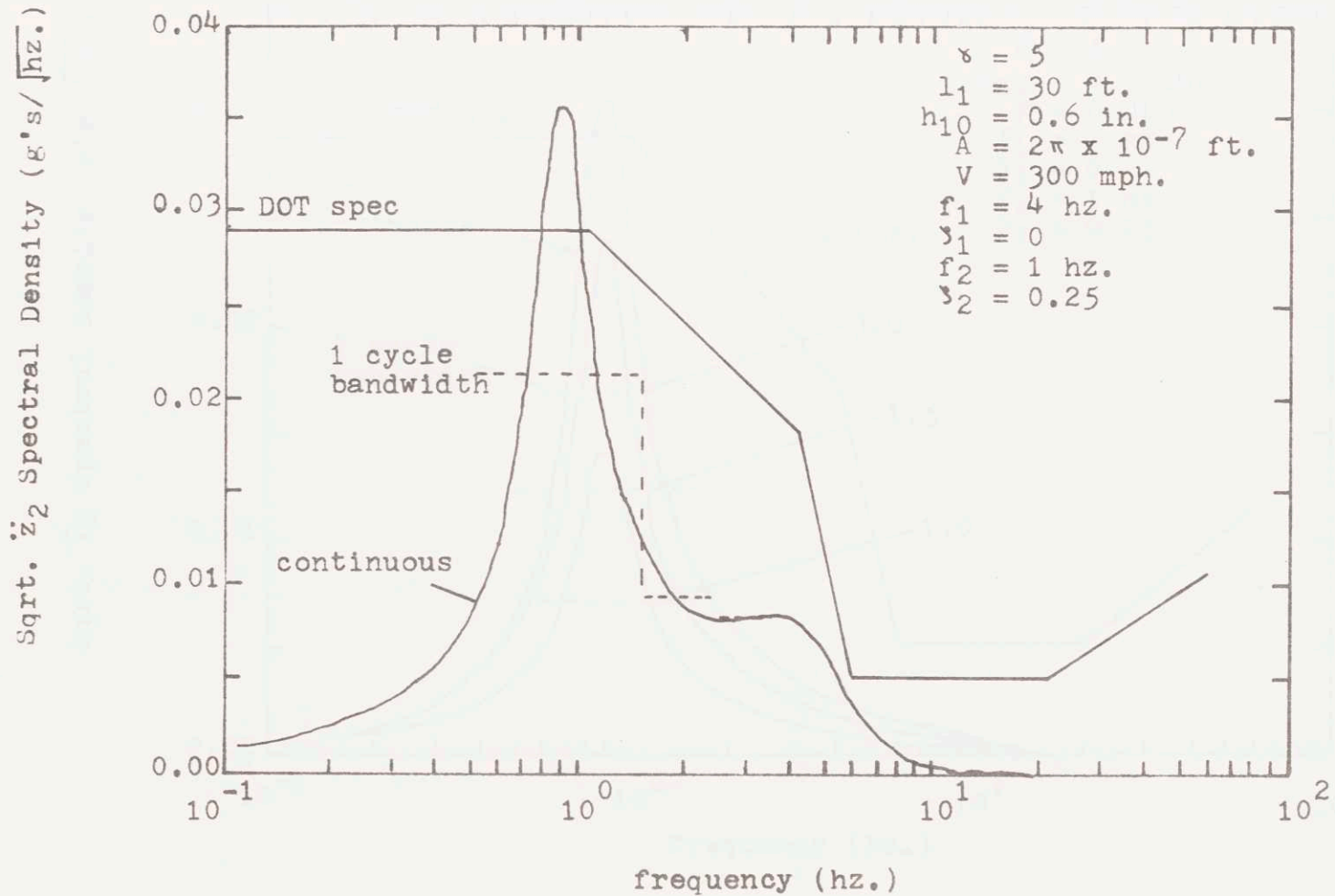


Fig. 12.4a. Passenger Comfort: Acceleration Spectral Density from Road Input to Lateral Mode

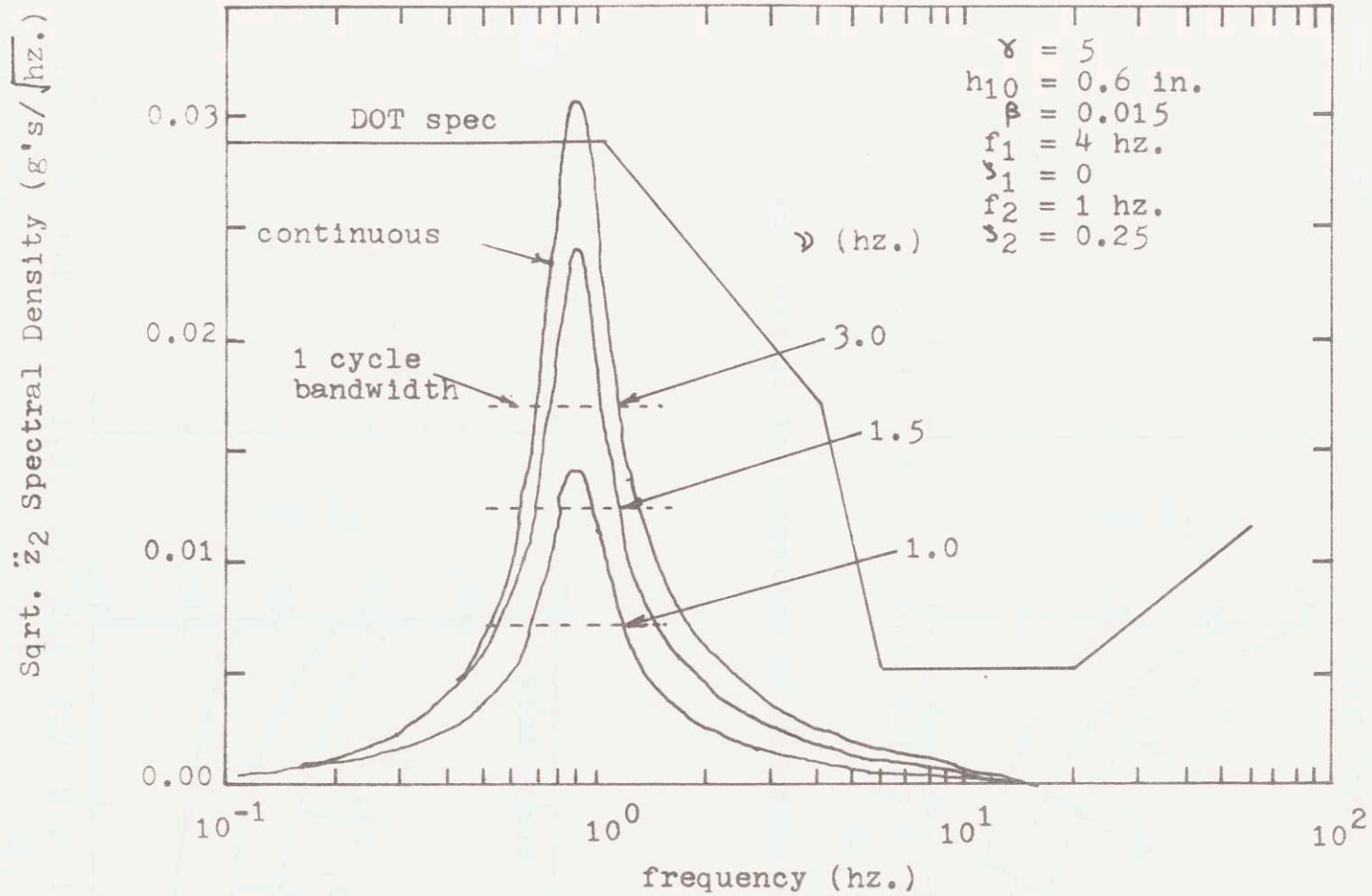


Fig. 12.4b. Passenger Comfort: Acceleration Spectral Density from Wind Input to Lateral Mode

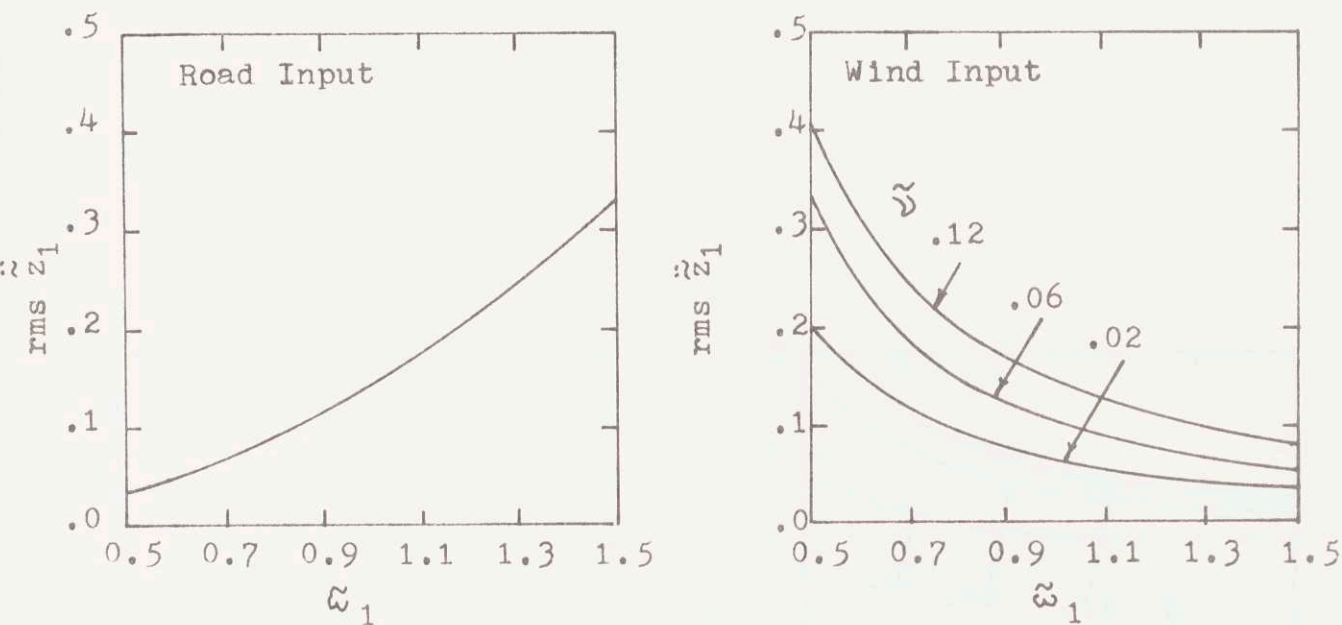


Fig. 12.5. Rms Lateral Acceleration of Unsprung Mass

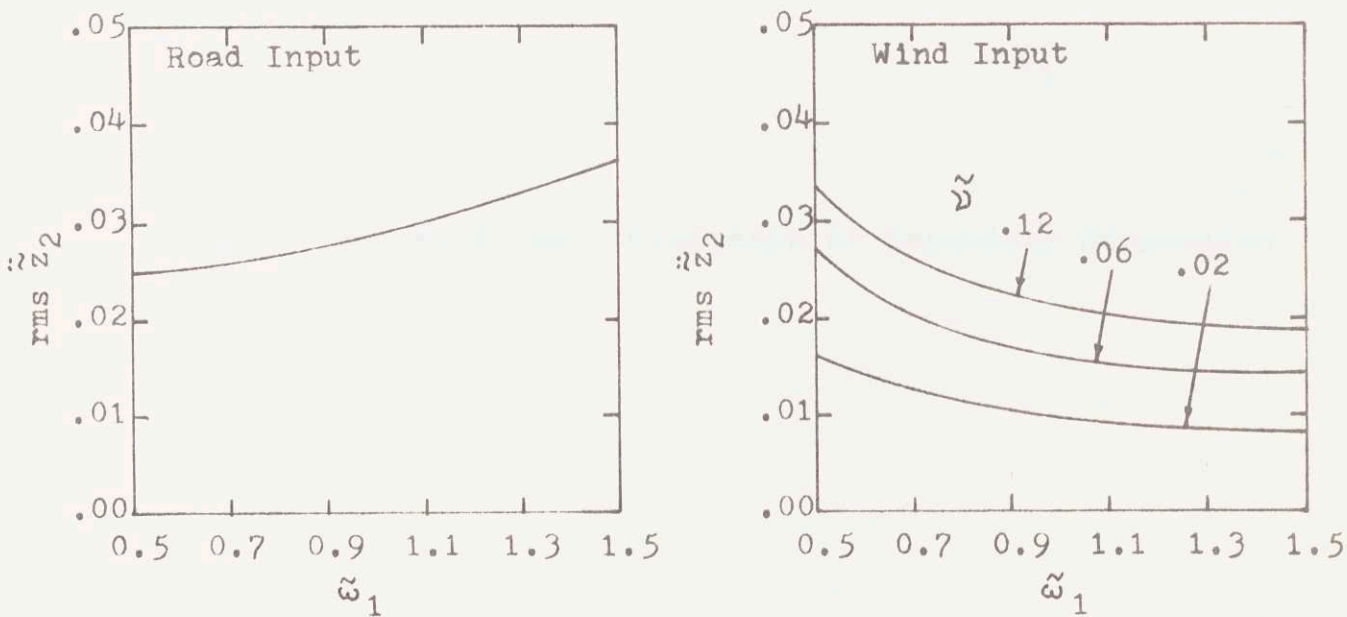


Fig. 12.6. Rms Lateral Acceleration of Sprung Mass

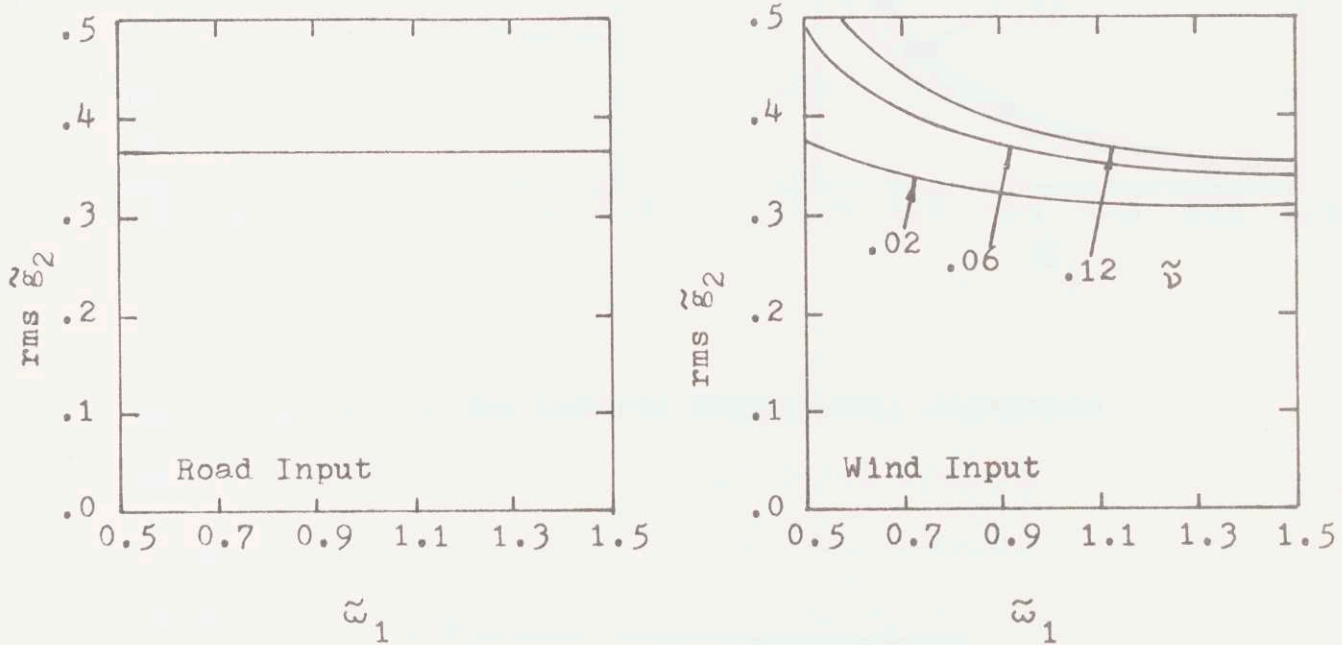


Fig. 12.7. Rms Lateral Clearance of Secondary Suspension

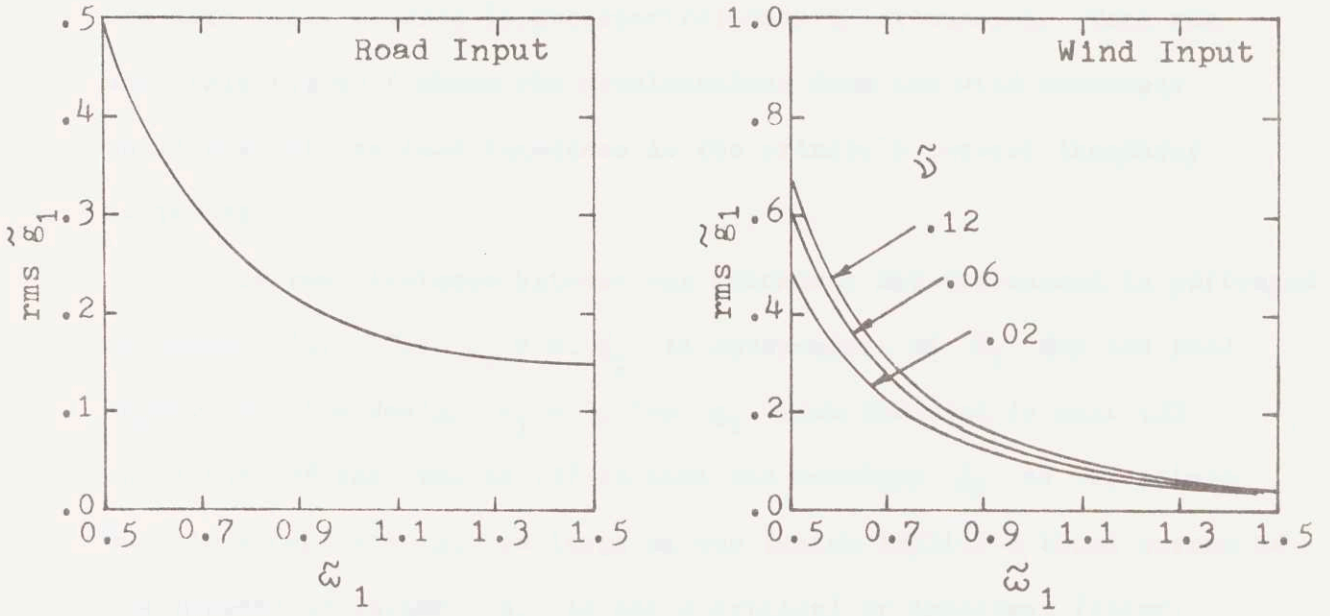


Fig. 12.8. Rms Lateral Magnet-Rail Clearance

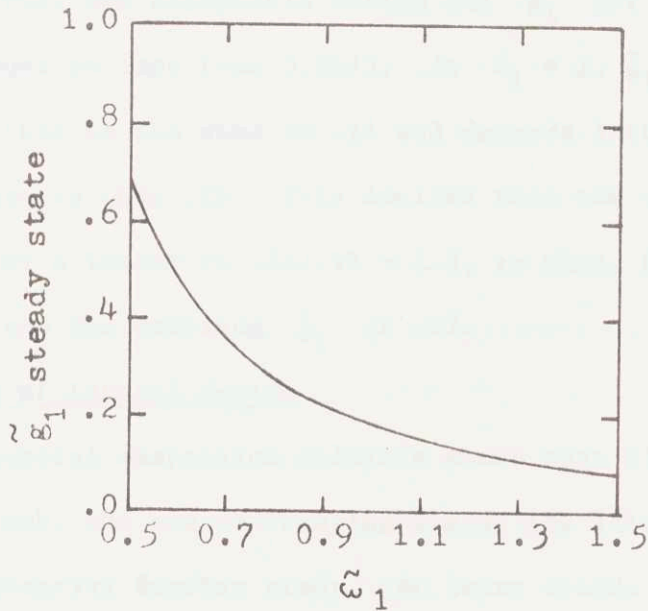


Fig. 12.9. Lateral Magnet-Rail Clearance with Steady Wind

are more fully covered in the spectral density discussion. Note the unfavorable tradeoff where the accelerations from the wind decreases while that of the road increases as the primary's natural frequency increases.

The rms clearance between the secondary and the magnet is portrayed in Figure 12.7. For  $\zeta_1 = 0$ ,  $\tilde{g}_2$  is independent of  $\tilde{\omega}_1$  for the road input. For the design  $\tilde{\omega}_1 = 1$ , the  $g_2$  from the wind is near .35 while that of the road is .37 so that the combined  $\tilde{g}_2$  is .5. Since one can accept rms  $g_2$  as large as one (which implies a total stroke of 3.6 inches) or larger,  $\tilde{g}_2$  is not a critical or important factor.

Figure 12.8 depicts the relative clearance between the magnet and the rail for the oscillating portion of the road and wind inputs, while Figure 12.9 displays the response to the steady portion of the wind input. For the worst case steady wind, the displacement for  $\tilde{\omega}_1 = 1$  is .18 inches; thus, for acceptable design rms  $\tilde{g}_1$  for combined wind and road inputs must be less than  $0.82/3$ . At  $\tilde{\omega}_1 = 1$ ,  $\tilde{g}_1$  for the road input is .19 while that of the wind is .11 and depends little on  $v$ ; thus the combined figure is then .22. This implies that the road input could be increased to by a factor of  $.25/.19 = 1.3$ , so that  $\tilde{g}_1$  from the wind alone is .25 and the combined  $\tilde{g}_1$  is .27.

#### 12.4 Summary of Lateral Motion

This lateral suspension analysis shows that with welded steel rails at 300 mph, the use of fringing fields for lateral guidance has promise and deserves further study. At lower speeds rougher roads can

be used as described in Chapter 4.3. In addition the wind input is filtered more so that the oscillating wind effects the vehicle's acceleration and displacement less.

The following general conclusions can be drawn:

(1) To develop lateral forces of sufficient magnitude, the system design should seek thin (which implies long) magnets.

(2) The lateral rail roughness is more stringent than the horizontal roughness requirements because:

(a) In the lateral situation, there is less freedom in selecting system parameters.

(b) Allowance must be made for the effects of external winds.

Further work is required before this lateral suspension using fringing fields can be evaluated. Models and simulations which allow both vertical and horizontal motion and realistically model the lateral force's dependence on both horizontal and vertical position must be developed. Improved shaping of the pole faces and the rail magnet configuration might allow larger lateral forces to be developed. The effects of eddy currents induced in the rail should be studied.

As in the vertical situation, more complex secondary suspensions might improve the system's performance. The questions of the proper wind parameters must be resolved.

In summary, the use of the lifting magnet's fringing fields for lateral guidance has not been eliminated but further work is needed before a comprehensive evaluation can be performed.

## PART IV. CONCLUSIONS AND RECOMMENDATIONS

### 13. CONCLUSIONS AND RECOMMENDATIONS

This thesis is divided into the following sections:

(1) Analysis (Chapters 2 and 5 through 10) and experimental verification (Chapter 3) of models which describe heave motion of an electromagnetic suspension.

(2) Preliminary studies of heave-pitch models (Chapter 11), and lateral guidance (Chapter 12).

(3) Design of full size systems (Chapter 4).

For electromagnetic suspensions operating in the heave mode, lumped parameter models were formed for the force-current-gap relationships, leakage fluxes, eddy currents, finite magnet length, and feedback controls and were experimentally verified. Compared to models which neglect fringing and leakage flux, magnetic flux leakage reduces the magnet's maximum lift (typically by a factor of 5 to 10) and increases the required control voltage (typically by a factor of 3 to 6). The magnet's length filters road irregularities so that high frequency inputs to the suspension are reduced. For the practical systems studied (for example, an air gap of 0.6 inches and magnet width of less than 10 inches), eddy currents induced by heave motion have little effect on system dynamics and can be neglected. The model identifies current control with feedback of the average relative displacement and absolute velocity as a rational control strategy.

The model for heave motion has been experimentally verified with a magnetic suspension which was scaled geometrically and dynamically to

represent full size systems. Both static tests of force-current-gap relations and dynamic tests using a ferromagnetic rail attached to a shaker programmed to simulate road inputs were performed. Agreement between the lumped models and the experimental data was good.

To evaluate the capabilities of magnetic suspensions more fully, preliminary investigations of heave-pitch models, and lateral guidance were conducted.

Models with heave and pitch degrees of freedom show that ride quality in electromagnetic suspensions is improved by crossfeedback (the feeding back of variables measured at one end into the suspension at the vehicle's other end) which isolates motion at the vehicle's ends from inputs at the opposite ends.

The fringing fields of the lifting magnets have promise for lateral guidance of the vehicle and deserve further investigation. Long magnets (30 ft.) permit enough lateral force to be developed so that additional magnets for lateral guidance may not be required.

The heave models are used to generate guidelines and sample designs for full scale systems. Air gaps of .4 to .6 inches are feasible. As indicated in Tables 5 and 14, road roughness (A) of  $1.5 \times 10^{-6}$  (welded rail) ft. at 300 mph. and of  $7 \times 10^{-6}$  (runway) at 100 mph. are possible with simple secondary suspensions and magnets which are 10-15% of the vehicle's total weight.

Road roughness is limited by passenger comfort and rail clearance. Since the acceleration of the upsprung mass ( $\ddot{y}_1$ ) and the clearance between

the magnet and sprung mass ( $\Delta h_2$ ) have considerable leeway, improved suspensions could permit still greater road roughness or improved ride quality.

To further evaluation and design of electromagnetic suspensions the following extensions to this thesis are recommended:

(1) The permissible limits of magnet rail contact should be studied so that constraints on vehicle motion can be rigorously defined.

(2) Alternate magnet-rail configurations should be studied; for example, this thesis has made the rail pole width ( $l_2$ ) greater than that of the magnet ( $l_p$ ). The situation where the magnet's pole width is greater than the rail's should be investigated.

(3) The model of eddy currents induced by vertical motion can be improved by including the magnet's window. The effects of eddy currents should be included in the vehicle's equations of motion so that tradeoffs between track dimensions and vehicle performance can be evaluated.

(4) Analytical and experimental evaluation of the eddy current effects induced by the forward motion are needed.

(5) The heave-pitch model should be extended to include secondary suspensions.

(6) Detailed investigation of lateral guidance is required for realistic evaluation of system capabilities.

(7) Alternate control laws for the electromagnetic suspension and alternate secondary suspensions should be investigated. Active secondary suspensions and magnet control laws which include the motion of the secondary suspension could improve the system's performance.

REFERENCES

1. ---, "54 Years Ago," Hovering Craft and Hydrofoil, Vol. 3, No. 8, May 1964, p. 20.
2. ---, "Floating Commuter Cars Ride Magnetic Highway," Machine Design, Vol. 37, No. 4, 1965, p. 12.
3. N. P. Chironis, "Supermagnetism Supports Train at Airliner Speed," Product Engineer, Vol. 38, January 16, 1967, p. 32.
4. H. T. Coffey, F. Chilton, T. W. Barbee, Jr., "Suspension and Guidance of Vehicles by Superconducting Magnets," J. Applied Physics, Vol. 40, 1969, p. 216.
5. P. J. Geary, Magnetic and Electric Suspensions, British Scientific Research Association, South Hill, England, 1964.
6. C. A. Guderjahn, S. L. Wipf, "Magnetic Suspensions and Guidance for High Speed Trains by Means of Superconducting Magnets and Eddy Currents," Advances in Cryogenic Engineering, Vol. 15, K. D. Timmerhaus, Ed., Plenum Press, N. Y., 1970.
7. C. A. Guderjahn, S. L. Wipf, H. J. Fink, R. W. Boom, K. E. MacKenzie, D. Williams, T. Downey, "Magnetic Suspensions and Guidance for High Speed Rockets by Superconducting Magnets," J. Applied Physics, Vol. 40, 1969, p. 2133.
8. L. Hannakam, "Wirbelströme in Dunnen Leitenden Platten infolge Stromdurch Flossener Leiter," Elektrotechnik Zeitschrift A, 1965, p. 427.
9. C. Kerr, R. Olsen, "A Highway without Wheels Employing a Permanent Magnet Suspension and Linear Motor Propulsion," Westinghouse Internal Paper, August 1961.
10. E. C. Okress, S. M. Wroughton, G. Coments, P. H. Brace, J. C. R. Kelly, "Electromagnetic Levitation of Solid and Molten Metals," J. Applied Physics, Vol. 23, No. 5, 1952, p. 545.
11. G. R. Polgreen, "Transportation Possibilities with Magnetic Suspension," Electrical Times, Vol. 148, August 26, 1965, p. 298.
12. G. R. Polgreen, New Applications of Modern Magnets, MacDonald and Co., London, 1966.
13. J. R. Powell, G. R. Danby, "High Speed Transport by Magnetically Suspended Trains," ASME paper 66-WA/RR-5.

14. J. R. Powell, "The Magnetic Road: A New Form of Transport," ASME Paper 63-RR-4, ASME Railroad Conference, April 23-25, 1963.
15. J. R. Powell, G. R. Danby, "Dynamically Stable Cryogenic Magnetic Suspension for Very High Velocity Transportation Systems," Recent Advances in Engineering Science, A. C. Erringen, Ed., Gordon and Breach Science Publishers, N. Y., 1970.
16. J. R. Powell, G. R. Danby, "Magnetically Suspended Trains: The Application of Superconductors to High Speed Transport," Cryogenics and Industrial Gases, Vol. 19, October 1969, p. 11.
17. J. R. Reitz, "Forces on Moving Magnets due to Eddy Currents," J. Applied Physics, Vol. 41, 1970, p. 2067.
18. R. H. Borcherts, L. C. Davis, J. R. Reitz, D. F. Wilkie, "Baseline Specifications for a Magnetically Suspended High-Speed Vehicle," Proceedings of IEEE, Vol. 61, No. 5, May 1973, p. 579.
19. R. D. Thornton, "Design Principles for Magnetic Levitation," Proceedings of IEEE, Vol. 61, No. 5, May 1973, p. 586.
20. Y. Iwasa, "Magnetic Shielding for Magnetically Levitated Vehicle," Proceedings of IEEE, Vol. 61, No. 5, May 1973, p. 598.
21. S. A. Nasar, E. Del Cid, Jr., "Propulsion and Levitation Forces in a Single Sided Linear Induction Motor for High Speed Ground Transportation," Proceedings of IEEE, Vol. 61, No. 5, May 1973, p. 638.
22. J. A. Ross, "ROMAG Transportation System," Proceedings of IEEE, Vol. 61, No. 5, May 1973, p. 617.
23. E. Ohno, M. Iwamoto, and T. Yamada, "Characteristics of Superconductive Magnetic Suspension and Propulsion for High Speed Trains," Proceedings of IEEE, Vol. 61, No. 5, May 1973, p. 579.
24. ---, "Transrapid," Krauss-Maffei, Munich, Germany, 1972.
25. G. Bohn, P. Romstedt, W. Rothmayer, P. Schwarzler, "A Contribution to Electromagnetic Levitation Technology," Krauss-Maffei, Munich, Germany, 1972.
26. S. G. Meisenholder, T. C. Wang, Dynamic Analysis of an Electromagnetic Suspension System for a Suspended Vehicle System, TRW Systems Group, Redondo Beach, Cal., January 1972.

27. D. R. Merritt, Optimal Design of High Speed Magnetically Suspended Trains, S. B. Thesis, M. I. T. Dept. of E. E., 1970.
28. J. R. Reitz, R. H. Borcherts, L. C. Davis, D. F. Wilkie, Technical Feasibility of Magnetic Levitation as a Suspension System for High Speed Ground Vehicles, Ford Motor Co., Dearborn, Mich., February 1972.
29. J. B. Muhlenberg, J. D. Dukowicz, O. C. Frah, S. D. Rajan, N. S. Sussman, "Comparative Analysis of Non Contacting Suspensions for High Speed Ground Vehicles," Mitre Corp., 1972.
30. D. Williams, Jr., "Magnetically Suspended Rocket Sleds," Sandia Corp., Albuquerque, N. M., January 1969 (Clearinghouse PB 182 753).
31. H. T. Coffey, E. Chilton, L. O. Hoppie, The Feasibility of Magnetically Levitating High Speed Ground Vehicles, Stanford Research Institute, Menlo Park, Cal., 1972.
32. ---, "High Speed Rail Systems," TRW Systems Group, Redondo Beach, Cal., 1970 (Clearinghouse PB 192 506).
33. ---, "Supporting Studies for HSGT System Reports," TRW Systems Group, Redondo Beach, Cal., 1970 (Clearinghouse PB 193 145).
34. D. M. Baumann, G. B. K. Meacham, "Preliminary Design and Test of Linear Induction Traction Motors and Suspension Systems," M. E. Dept., Engineering Projects Lab., M. I. T., Cambridge, Mass., November 1966 (Clearinghouse PB 173 686).
35. D. F. Wilkie, R. H. Borcherts, Dynamic Characteristics and Control Requirements for Electromagnetic Suspensions, Scientific Research Staff, Ford Motor Co., 1973.
36. R. M. Katz, V. C. Nene, R. J. Raverno, C. A. Skalski, Performance of Magnetic Suspensions for High Speed Vehicles Operating over Flexible Guideways, Mitre Corp., McLean Va., 1973.
37. D. A. Hullender, D. N. Wormley, H. H. Richardson, A Preliminary Study of Air Cushion Vehicle Suspensions, Engineering Projects Lab., M. E. Dept., M. I. T., Cambridge, Mass., June 15, 1970.
38. D. A. Hullender, On the Active Control of the Heave Dynamics of Fluid Suspensions, Ph. D. Thesis, M. E. Dept., M. I. T., Cambridge, Mass., August 1969.
39. L. M. Sweet, Optimal Linear Feedback and State Variable Estimation for Tracked Air Cushion Vehicle Suspensions, Master's

- thesis, M. E. Dept., M. I. T., Cambridge, Mass., June 1971.
40. ---, A Cost Comparison of Three Tracked Air Cushion Vehicle Configurations, Tracked Hovercraft Limited, London, England, July 1970.
  41. E. K. Bender, Optimization of the Random Vibration Characteristics of Vehicle Suspensions, Sc. D. thesis, M. E. Dept., M. I. T., Cambridge, Mass., 1968.
  42. E. K. Bender, I. L. Paul, Analysis of Optimum and Preview Control of Active Vehicle Suspensions, Engineering Projects Lab., M. E. Dept., M. I. T., Cambridge, Mass., September 1, 1967 (Clearinghouse PB176137).
  43. I. L. Paul, E. K. Bender, Active Vibration Isolation and Active Vehicle Suspension, Engineering Projects Lab., M. E. Dept., M. I. T., Cambridge, Mass., November 1, 1966 (Clearinghouse PB 173 648).
  44. G. H. Tidbury, Ed., Advances in Automobile Engineering (Part III), Pergamon Press, Oxford, England, 1965.
  45. A. K. Trikha, Optimization of Vibration Isolaters Subject to Random Input, Sc. D. thesis, M. E. Dept., M. I. T., Cambridge, Mass., June 1969.
  46. B. D. van Deusen, A Statistical Technique for the Dynamic Analysis of Vehicles Traversing Rough Yielding and Non Yielding Surfaces, NASA CR-659, March 1967.
  47. D. P. Welch, Optimization of Suspension Dynamics for a Finite Length Vehicle, Master's thesis, M. E. Dept., M. I. T., Cambridge, Mass., May 1970.
  48. J. W. Young, Optimization of Vehicle Suspensions Subject to Multiple Inputs, Master's thesis, M. E. Dept., M. I. T., Cambridge, Mass., August 1970.
  49. W. A. Ribich, K. M. Captain, H. H. Richardson, An Analysis of Finite Fluid Suspension Pad Length of the Dynamics of a Vehicle on an Irregular Guideway, Engineering Projects Lab., M. E. Dept., M. I. T. Cambridge, Mass., September 1967 (Clearinghouse PB 176 135).
  50. H. C. Roters, Electromagnetic Devices, J. Wiley and Sons, N. Y., 1941.

51. H. H. Woodson, J. R. Melcher, Electromechanical Dynamics, J. Wiley and Sons, N. Y., 1967.
52. S. H. Crandall, D. C. Karnopp, E. F. Kurtz, D. C. Pridmore-Brown, Dynamics of Mechanical and Electromechanical Systems, McGraw-Hill, New York, 1968.
53. E. E. Staff, M. I. T., Magnetic Circuits and Transformers, J. Wiley and Sons, 1943.
54. A. E. Bryson, Y. C. Ho, Applied Optimal Control, Blaisdell Publishing Co., Waltham, Mass., 1969.
55. G. C. Newton, L. A. Gould, J. F. Kaiser, Analytical Design of Feedback Controls, J. Wiley and Sons, N. Y., 1959.
56. A. P. Sage, Optimum Control Systems, Prentice-Hall, Englewood Cliffs, N. J., 1968.
57. R. Rudenberg, Transient Performance of Electric Power Systems, M. I. T. Press, Cambridge, Mass., 1970.
58. D. T. Thomas, Engineering Electromagnetics, Pergamon Press, N. Y., 1972.
59. ---, "Prelaunch Ground Wind Loads," NASA SP 8008, November 1965.
60. ---, The Role of Simulation in Space Technology, Part C, Va. Poly. Inst., 1965.
61. P. B. MacReaddy, "Structure of Atmospheric Turbulence," J. of Meteorology, Vol. 10, p. 434-449, 1953.
62. H. Press, M. T. Meadows, I. Hadlock, "A Reevaluation of Data of Atmospheric Turbulence and Airplane Gust Loads for Application in Spectral Calculations," NACA Report 1272, Langley Aeronautic Laboratory, 1956.
63. B. Thwaites, Incompressible Aerodynamics, Oxford U. Press, Oxford, England, 1960.
64. ---, ASM Metals Handbook, 8th Edition, Vol. 1, Metals Park, 1961.
65. F. Steinmann, Experiments on the Heave Dynamics of Fluid Suspensions, Master's thesis, M. E. Dept., M. I. T., Cambridge, Mass., May 1969.
66. D. N. Wormley, Dynamic Characteristics of Externally Pressurized Thrust Bearings, Master's thesis, M. E. Dept., M. I. T., Cambridge, Mass., 1964.

67. K. Yokose, "On the Measuring Method of the Creep Force between Wheel and Rail," Quarterly Reports of the Tokyo Railway Tech. Research Inst., Vol. 14, No. 1, p. 43-47, 1973.
68. H. T. Coffey, J. D. Colton, and K. D. Mahrer, Study of a Magnetically Levitated Vehicle, U. S. Dept. of Transportation Report DOT-FR-73-24, February 1973.
69. J. R. Reitz, L. C. Davis, "Force on a Rectangular Coil Moving Above a Conducting Slab," J. Appl. Physics, Vol. 43, 1972, p. 1547.
70. J. R. Reitz, R. H. Borcherts, L. C. Davis, T. K. Hunt, D. F. Wilkie, Preliminary Design Studies of Mag. Suspensions for High Speed Ground Transportation, Ford Motor Co., 1973.
71. R. M. Katz, V. D. Nene, R. J. Ravera, C. A. Skalski, Performance of Magnetic Suspensions Operating over Flexible Guideways, Mitre Technical Report, July 10, 1973.
72. I. A. Alston, J. M. Clark, J. T. Hayden, "Magnetic Suspension and Guidance of High Speed Vehicles," High Speed Ground Transportation Journal, Vol. 7, No. 7, Summer 1973, p. 215.

APPENDICES

A.1 Estimated Wind Drag

The power necessary to overcome wind drag is estimated from [63]:

$$P_w = \frac{1}{2} \rho c_d A_c V^3$$

where (values used for design estimates are in parentheses)

- $\rho$  = density of ambient atmosphere (0.075 lbm/ft<sup>3</sup>)
- $A_c$  = cross sectional area of vehicle (50 ft<sup>2</sup>)
- $c_d$  = drag coefficient ([63] suggests .5 for streamlined designs)
- $V$  = vehicle's forward velocity

The wind drag at 100 and 300 mph. is approximately 100 and 3000 kw.

A.2 Magnet Permeances with End Effects

With reference to Figure 5.3, the permeance of four corners is:

$$4(P_3 + P_4) = 4(0.308 \mu_o h_1 + .5 \mu_o t_p) \tag{A.2.1}$$

where

$t_p$  = region over which leakage occurs as shown in Figure 5.3.

The numerical subscripts of the permeance correspond to flux paths indicated in Figure 5.3.

The fringing from the sides and ends is determined by considering paths 1 and 2 where a pole has two faces and two ends and where a magnet has two flux paths:

$$\begin{aligned}
 & 2(P_1 + P_2)_{\text{sides}} + 2(P_1 + P_2)_{\text{ends}} = \\
 & [0.52 \mu_o l_1 + \frac{2\mu_o l_1}{\pi} \ln(1 + \frac{t_p}{h_1})] \\
 & [0.52 \mu_o l_p + \frac{2\mu_o l_p}{\pi} \ln(1 + \frac{t_p}{h_1})] \tag{A.2.2}
 \end{aligned}$$

[50] and [53] suggest that the region of leakage  $t_p$  is equal to the air gap  $h_1$  unless the geometry demands  $t_p < h_1$ ; thus, addition of (A.2.1) and (A.2.2) gives the fringing permeance

$$2P_F = 1.92 \mu_o (l_1 + l_p) + 3.23 \mu_o h_1 \tag{A.2.3}$$

For  $l_p + l_1 \gg h_1$ , the fringing permeance is independent of  $h_1$  a result which is supported by the experimental evidence of Chapter 3.

The leakage permeance is determined from the flux path model of Figure 5.4.

$$\begin{aligned}
 2P_L = (P_1)_{\text{leak}} + (P_5 + P_6) &= (w_3 - h_1) \mu_o [ \frac{l_1}{w_1} \\
 &+ 2( \frac{1}{\pi} \ln \{ 1 + \frac{2 l_p}{w_1} \} + .26) ] \tag{A.2.4}
 \end{aligned}$$

where two ends and leakage across the pole cores has been included. As noted in Chapter 5, this permeance is less than 100% effective since the leakage flux is not driven by the full magnetomotive potential  $Ni_o$ .

From (5.1), the useful permeance is:

$$P_u = \frac{\mu_o l_1 l_p}{2h_1}$$

From (5.2), the leakage coefficient is:

$$v_L = \frac{P_L}{P_u}$$

And from (5.5), the total flux coefficient is:

$$v_T = \frac{P_u + P_L + P_F}{P_u}$$

For the experimental model of Chapter 3:

$$l_1 = 3.00 \text{ in.}$$

$$l_p = 0.42 \text{ in.}$$

$$w_1 = 1.00 \text{ in.}$$

$$w_3 = 0.85 \text{ in.}$$

For small clearances,  $h_1$  may be neglected with respect to  $l_1 + l_p$  in (A.2.3) and  $h_1$  may be neglected with respect to  $w_3$  in (A.2.4).

Thus, for the experimental magnet of Chapter 3, the total flux coefficient is:

$$v_T = 1 + 8h_1 \tag{A.2.5}$$

The leakage coefficient is:

$$v_L = 1 + 2.6 h_1 \tag{A.2.6}$$

The theoretical coefficients (A.2.5) and (A.2.6) are compared to experimental evidence in Figure 3.9.

### A.3 Conversion of Voltage Control to Current Control

Figure A.3.1 shows the circuit required to change a voltage controller to a current controller. The voltage source which is to be converted is represented by:

$$V_o = -G V_I$$

where

$G$  is the gain of the voltage control

$V_o$  = output voltage

$V_I$  = input voltage

The voltage  $V_o$  is to be controlled so that the current ( $i$ ) through the load impedance which is represented by a resistor  $R_L$  and inductor  $L$  is proportional to the input voltage  $V_{IN}$ . The conversion to voltage control is made by placing a sensing resistor ( $R_s$ ) in series with the load. The voltage ( $V_s$ ) across the sensing resistor is proportional to the current  $i$  for control resistor ( $R_c$ ) much greater than  $R_s$ . The operational amplifier supplies the large gains ( $-K$ ) which eliminate the load from the control equation.

The op amp is modeled as an inverting amplifier (Gain =  $-K$ ) with an infinite input impedance so that

$$\frac{V_s - V_I}{R_c} = \frac{V_I - V_{IN}}{R_I}$$

where  $V_{IN}$  is the input voltage which system design seeks to make proportional to the load current.

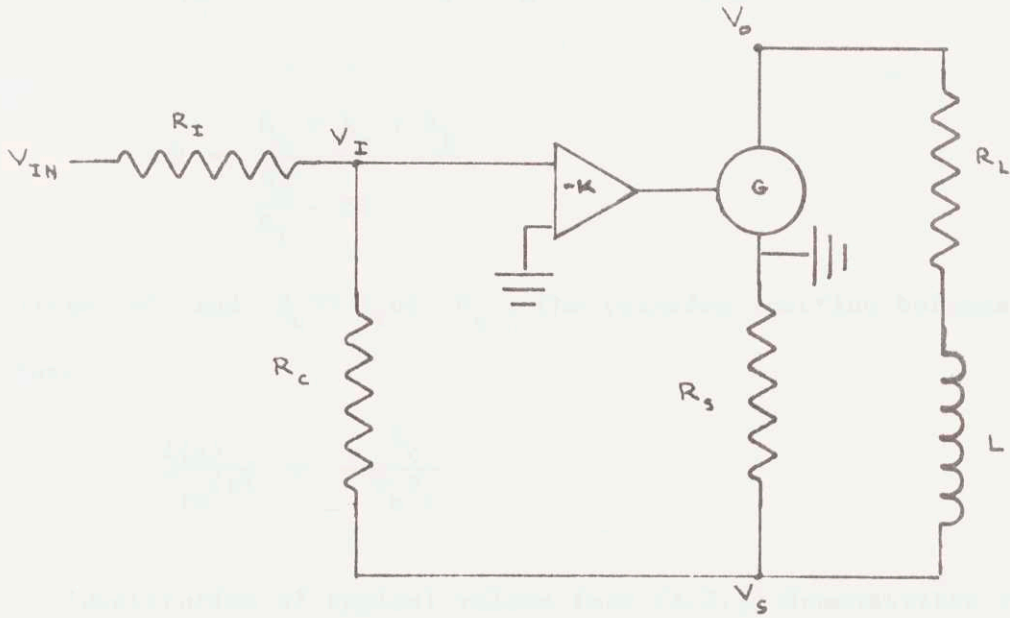


Fig. A.3.1. Circuit to Convert Voltage Control to Current Control

The transfer function between the load current and the input voltage is:

$$\frac{i(s)}{V_{IN}(s)} = \frac{-\frac{R_s}{R_I} IR + R_s + R_c}{+ IR [R_s + R_L + sL] - R_s R_I} \quad (A.3.1)$$

where

$$IR = \frac{R_s + R_c + R_I}{\frac{R_s}{R_I} - KG}$$

For large KG and  $R_s \ll R_I$  or  $R_c$ , the transfer function becomes a constant:

$$\frac{i(s)}{V_{IN}(s)} = -\frac{R_c}{R_s R_I} \quad (A.3.2)$$

Substitution of typical values into (A.3.1) demonstrates that the ideal current control (A.3.2) is feasible. For an example, select static design 2 of Table 4 for which

$$\frac{L}{R_L} = .33 \text{ sec}$$

$$Ni_o = 1.49 \times 10^4 \text{ amp turn}$$

$$\frac{R_L}{N^2} = 8.69 \times 10^{-5} \frac{\Omega}{\text{turn}^2}$$

where N number of turns in control coils.

$i_o$  = current at nominal position

With  $N = 300$  turns

$$i_o = 50 \text{ amps}$$

$$R_L = 7.8 \text{ ohms}$$

$$L = 2.6 \text{ H}$$

Choose the following values for the resistors in the control circuit:

$$R_s = .2 \text{ ohms}$$

$$R_c = R_I = 2 \times 10^3 \text{ ohms}$$

The ideal control (A.3.2) is then

$$i = (3.33 \frac{\text{amp}}{\text{volt}}) V_{IN}$$

A 15 volt input signal  $V_{IN}$  is required to maintain the 50 amps nominal current ( $i_o$ ).

For the maximum input frequency select 10 hz for which Figure 4.7 to 4.18 show that the road input is small because of the magnet's finite length filtering.

Let  $KG = 3 \times 10^4$  volt/volt a value which is attained by single stage operational amplifiers.

The system transfer function (A.3.1) is then

$$\frac{j(62.8j)}{V_{IN}(62.8j)} = \frac{2 \times 10^3}{22j + 600} \frac{\text{amp}}{\text{volt}}$$

where

$$j = \sqrt{-1}$$

which equals in polar notation.

$$\frac{i(62.8j)}{V_{IN}(62.8j)} = -6.33 \frac{\text{amp}}{\text{volt}} e^{-j2^\circ}$$

Since the phase shift is only  $2^\circ$  at the highest operating frequency, the conversion of voltage controllers to current controllers is feasible.

#### A.4 The Vehicle Length's Filtering of the Wind

The spectral density of the wind's oscillating component is given

by:

$$\psi_{\Delta V_r}(s) = \frac{(\text{rms } \Delta V_r)^2 v}{\pi(-s^2 + v^2)} \quad (12.13)$$

The oscillating wind component  $\Delta V_r$  is not uniform over space; therefore, a cross correlation between separate points is used to obtain a spectral density for the wind averaged along the length of the vehicle. From the average  $\Delta \dot{v}_r$ , an estimate of the oscillating wind force can be obtained.

The wind's cross spectral density between two points  $x_1$  and  $x_2$  can be written as:

$$\phi_{12}(s) = \phi_{\Delta V_r}(s) e^{\frac{-k_w |x_1 - x_2|}{\lambda}} \quad (A.4.1)$$

In [59] and [60], the spectrum was used for a vertical rocket on the launch pad where  $k_w$  was taken as 4 and  $\lambda$  is the wave length of the wind gusts which can be converted into an input frequency through:

$$\omega = \frac{2\pi V_T}{\lambda}$$

where

$V_T$  = total velocity of wind relative to vehicle

Another method of obtaining the cross spectrum converts (12.13) into the correlation:

$$E[\Delta V_r(t) \Delta V_r(t+\tau)] = (\text{RMS } \Delta V_r)^2 e^{-v|\tau|} \quad (\text{A.4.2})$$

where  $\tau$  is the time between measurements. This time can be converted into a distance by

$$\tau = \frac{x_1 - x_2}{V_T}$$

With the characteristic frequency  $v$  equal to  $V_T/L$  from [61] the correlation becomes:

$$E[\Delta V_r(t) \Delta V_r(t+\tau)] = (\text{RMS } \Delta V_r)^2 e^{-\frac{|x_1 - x_2|}{L}}$$

[61] and [62] state that these wind eddies obey isotropy laws which imply that the correlation for  $\Delta V_r$  is valid independent of the direction over which  $|x_1 - x_2|$  is taken as long as the distance lies in a horizontal plane. For a given frequency, the scale of turbulence is the wavelength. Comparison of (A.4.1) and (A.4.2) suggests that  $k_w = 1$  in (A.4.1) for correlations in the horizontal plane. Since the mentioned references differentiate between horizontal and vertical,  $k_w = 1$  is used for the discussions that appear in this section.

The cross spectral density can be used to determine the average  $\Delta V_r$  and, hence, the average oscillating wind force on the vehicle. The average square of the winds is given by weighting the lengths of finite sections and the magnitudes of the winds as sketched in Figure A.4.1. Note that it has been assumed that equal weights may be given to each point on the vehicle. Because of vehicle geometry the weighting may be a function of position.

$$[(\Delta V_r)^2]_{av} = \frac{1}{L_v^2} (w_1 \Delta x_1 + w_2 \Delta x_2 + \dots + w_n \Delta x_n)^2$$

The spectral density of the average is derived in a straightforward manner using (A.4.1):

$$\phi_{\Delta V_r}(s) \Big|_{av} = \frac{\phi_{\Delta V_r}(s)}{L_v^2} \sum_{j=1}^n \sum_{i=1}^n e^{-\frac{k_w |x_i - x_j|}{\lambda}} \Delta x_i \Delta x_j$$

The summations are changed to integrals by allowing the finite elements to become infinitesimally tiny:

$$\phi_{\Delta V_r}(s) \Big|_{av} = \frac{\phi_{\Delta V_r}(s)}{L_v^2} \int_0^{L_v} \int_0^{L_v} e^{-\frac{|x_i - x_j| k_w}{\lambda}} dx_i dx_j$$

Performing the integration yields the filtering effect of the finite length to the wind input so that the spectral density of the average wind force is:

$$\phi_w(s) = \frac{B^2 v F_L}{\pi(-s^2 + v^2)}$$

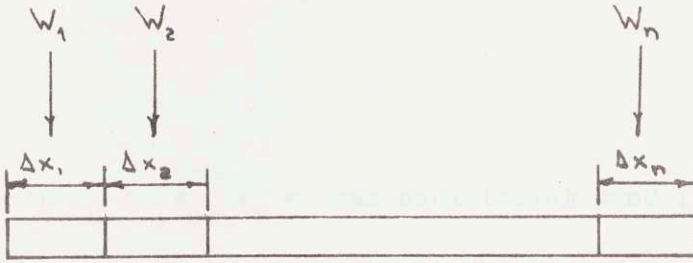


Fig. A.4.1. Averaging of Wind Force along Vehicle

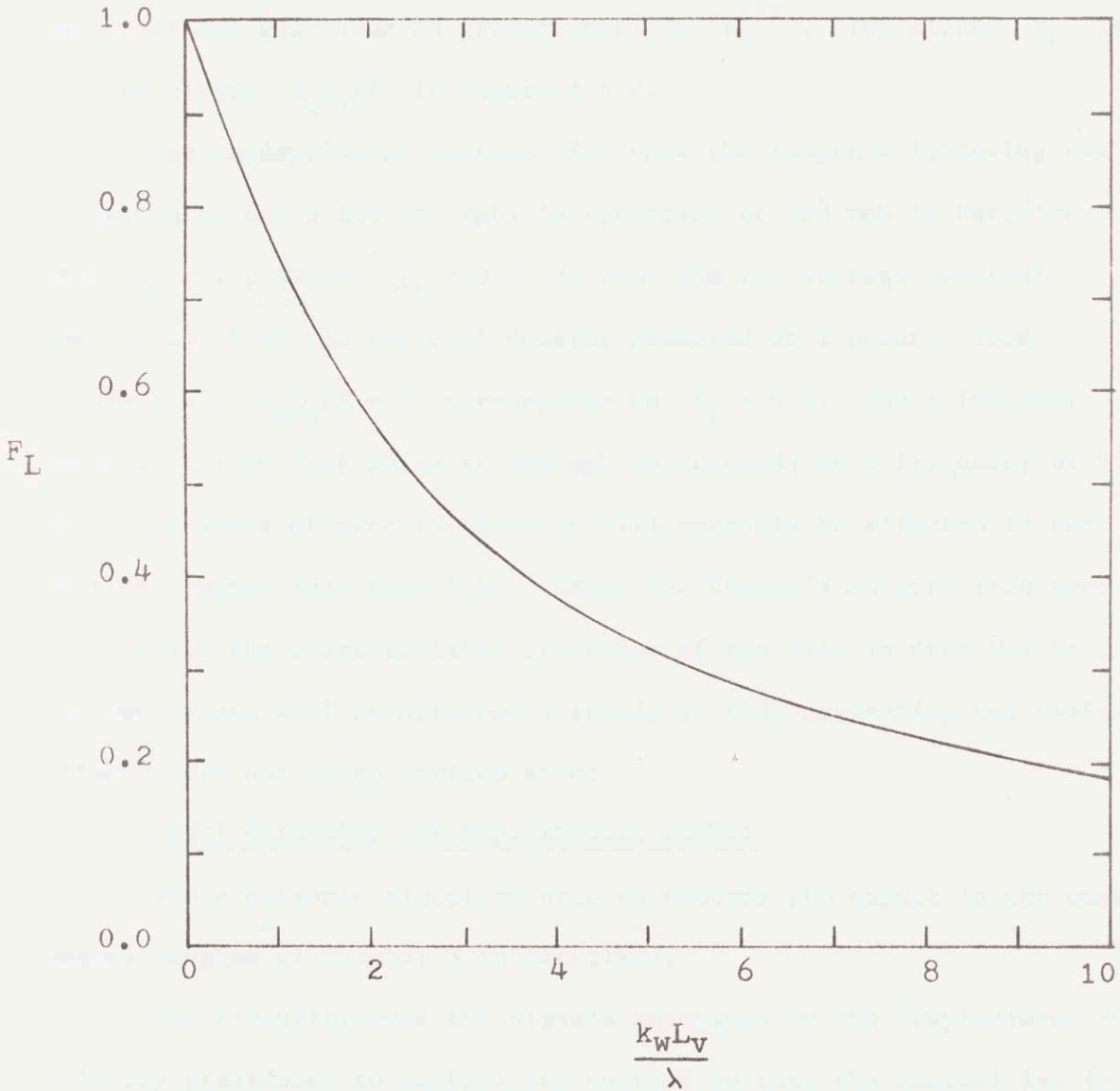


Fig. A.4.2. Finite Length Filtering

where

$$B = \rho c_d A V_{O \wedge R}^{rms} \Delta V_r = \text{rms oscillating wind force} \quad (\text{A.4.3})$$

where the finite length filtering is:

$$F_L = 2 \left( \frac{\lambda}{k_w L_v} \right)^2 \left( e^{-\frac{k_w L_v}{\lambda}} + \frac{k_w L_v}{\lambda} - 1 \right)$$

Note that the rms value is proportional to  $F_L^{1/2}$ . The filter  $F_L$  is plotted versus  $k_w L_v / \lambda$  in Figure A.4.2.

The assumption of Section 12.3 that the length's filtering can be neglected for a 100 ft. vehicle operating at 300 mph is verified. With  $k_w = 1$ , select  $F_L = 0.6$  so that the rms average spectral density is .8 of the spectral density measured at a point. From Figure A.4.2  $k_w L_v / \lambda = 2$  corresponds to  $F_L = 0.6$ . For a 100 foot vehicle,  $\lambda = 50$  feet which at 300 mph corresponds to a frequency of 9 hz. Thus, any plots of spectral density will scarcely be affected in the critical region less than 6 hz. Since the system's natural frequency is 4 hz. while the characteristic frequency of the wind is near 0.5 hz., the rms values will be affected slightly so that neglecting the filtering effects does not cause serious error.

#### A.5 Control Circuitry for Experimental Magnet

The electronic circuitry used to control the magnet in the experimental program of Chapter 3 is described.

The circuitry uses the signals generated by the displacement and velocity transducer to control the current so that the control law (3.3)

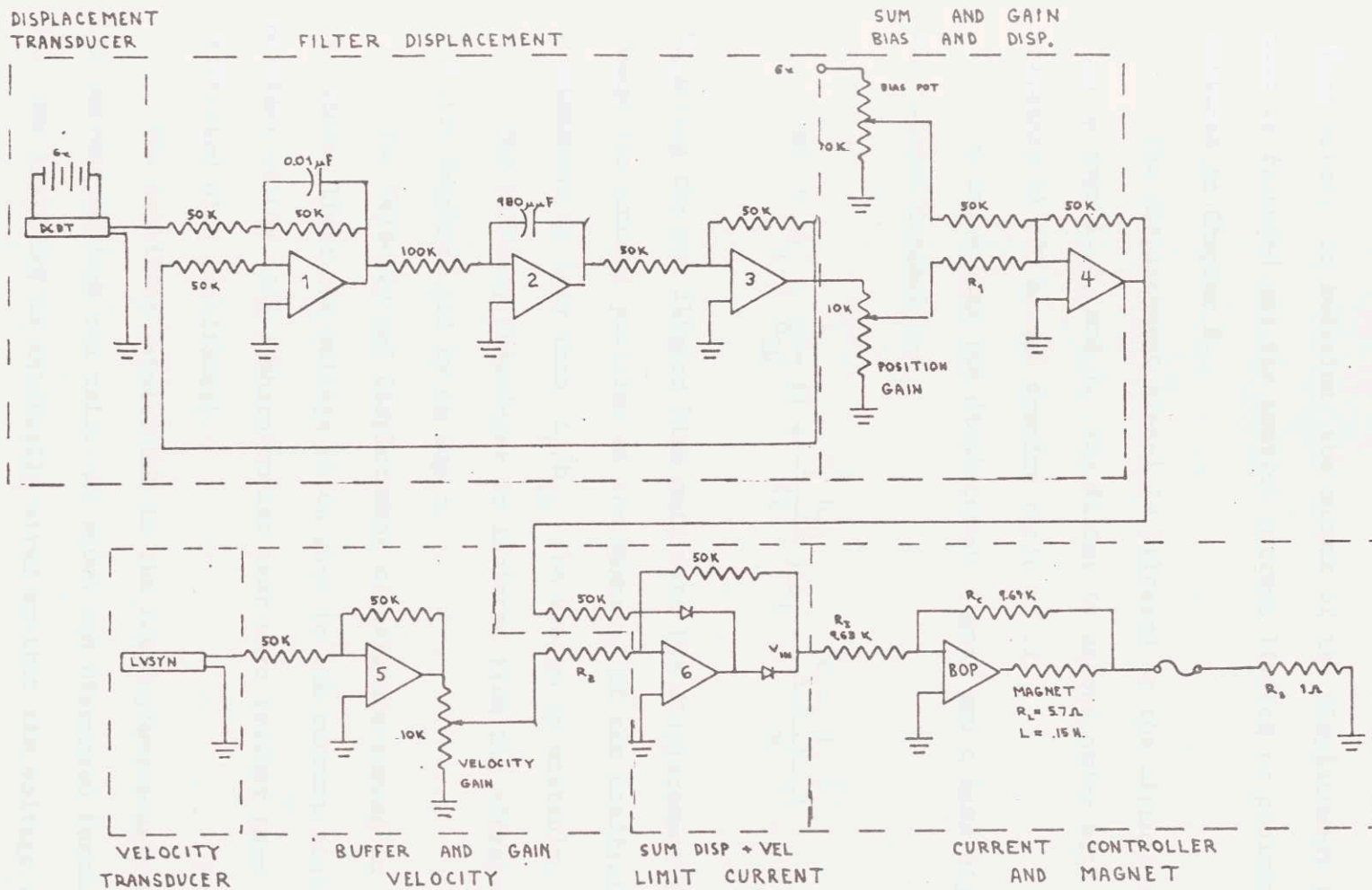


Fig. A.5.1. Circuit Diagram of Magnet Control

is effected. In addition, the output of the displacement transducer must be filtered and the control current limited to positive values as outlined in Chapter 8.

The displacement signal is filtered by the circuit associated with op amps 1, 2, and 3. The filter is second order with a natural frequency of 800 hz and damping ratio of .2.

Op amp 4 sums the displacement signal and a bias signal. The dimensional current is:

$$\Delta i = i_o + \frac{i_o}{h_{10}} \left( 1 + \frac{\omega_1^2 h_{10}}{2g} \right) \Delta h_1 - \frac{\zeta_1 \omega_1 i_o}{g} \dot{y}_1$$

Adjusting the pot labeled bias acts with the displacement feedback to change the nominal position of the magnet. If the coefficient of the displacement is less than  $i_o/h_{10}$  the system is unstable.

The velocity transducer is isolated from the effects of the velocity feedback pot by op amp 5.

The velocity and displacement signals are summed in op amp 6 where the diodes limit the voltage which goes to the current controller to positive values with a sharp corner near zero (rather than the .6 volts associated with the diodes).

The amplifier labeled BOP is the Kepco power supply which drives the current through the coil. As shown and discussed further in Appendix A-3, the amplifier is externally wired so that the voltage control is converted to a current controller which obeys

$$i = -\frac{R_c}{R_s R_I} V_{IN}$$

For the values shown the gain of the current controller is  $G_I = 1$  amp/volt. If the current exceeds the desired value (5 amps for this supply), a fuse opens the circuit so that the sensing resistance ( $R_s$ ) becomes infinite and the supply becomes a voltage control and the currents decrease rapidly. Further protection is provided by the circuit breakers of the BOP.

The feedback coefficients are set by adjusting the displacement and velocity pots and by changing the resistors  $R_1$  and  $R_2$ . For the tests which were conducted, the setting of the resistors and pots are listed in Table A.1. Note that the settings are nominal for the 4 hz situation. Let  $k_y$  be the coefficient of the relative displacement. The dimensionless natural frequency is then:

$$\tilde{\omega}_1 = [2(k_y - 1)]^{1/2}$$

For  $\tilde{\omega}_1 = 0.4$ ,  $k_y$  should be 1.08; however, if  $k_y$  is set incorrectly which is possible, because the output of the DCDT can change as the battery charge diminishes or because the resistance of a component differed from the value of the calculations, the natural frequency can change greatly. For example, if  $k_y = 1.10$  rather than 1.08, the natural frequency is 0.45 rather than 0.4 a 13% error. In the tests, where  $\tilde{\omega}_1 = 0.4$  (4hz), the displacement feedback was set approximately according to Table A.1 and then calibrated by setting the damping to low values and performing a transient response to initial displacement. The actual natural frequency was then compared to the desired natural frequency. For natural frequencies of 10 and 15 hz ( $\tilde{\omega}_1 = 1.0$  and 1.5), settings based

Table A.1

EXPERIMENTAL NATURAL FREQUENCIES, DAMPING AND POT SETTING

$f_1$	$\tilde{\omega}_1$	$\zeta_1$	DISP POT	$R_1$	VELOCITY POT	$R_2$
4	.4	.707	0.625	50 k	0.705	50 k
10	1.0	0.2	0.846	50 k	0.249	25 k
		0.707	0.846	50 k	0.891	25 k
		2.0	0.846	50 k	0.978	9.8 k
15	1.5	0.707	0.641	25 k	1.0	19.6 k

on theory were accurate. With the correct natural frequencies, the damping ratios were accurately determined for frequencies from 4 to 15 hz.

A.6 Computer Programs

The principal Fortran programs which were used in compiling the sample designs of Sections 2.5, 4.3, and Chapters 6 and 10 are listed with comments and sample output. The included programs are:

- (1) Static design of magnet and rail.
- (2) Heave motion with current control which feeds back average relative displacement and absolute velocity, finite magnet length, and passive secondary suspension.
- (3) Eddy current effects induced by AC current sheet.

In the static design program which is derived from Section 4.3, the designer selects material properties for the rail, core, and coil,

the maximum temperature rise in the magnet, the heat transfer coefficient between the magnet and the atmosphere, the coil's packing factor, and the vehicle's weight. After the pole width of the magnet and the distance between the pole cores are selected (the program allows automatic iteration of these variables), the program iterates the length of the pole core until the temperature constraint is satisfied. Additional output variables such as magnet weight, dissipated ohmic power, and track weight are determined.

The inputs to the heave motion program which is derived from the analyses of Chapters 5 through 7 and 9 include the ratio of the vehicle's sprung to unsprung mass, the road roughness, the forward velocity, and the magnet's length and leakage coefficient. Dimensionless natural frequencies and damping ratios of the primary and secondary suspension can be selected or iterated automatically. The system's eigenvalues are determined with the IBM scientific subroutine POLRT. The transfer functions for the output variables are calculated in the main program and the root mean squares of the output variables are determined by the subroutines MILLY, JUDY, YPT, and SYLVY. To enable plotting of spectral densities by routines that do Bode plots, the transfer functions for acceleration are printed with the output.

The program for eddy current effects induced by an AC current sheet (based on the analysis of Chapter 10) requires the following inputs: the relative permeabilities of the three regions diagrammed in Figure 2.10; the conductivity of region III; the air gap; and the magnet's width. For a given input frequency, the program calculates magnitude and phase of

the fields perpendicular to the surface of the magnet (region I) and of the rail (region III) and calculates power dissipated by eddy currents in the rail, lift pressure, and penetration depth in the rail. All output quantities are normalized with respect to the magnitude of the current sheet. To allow tabulation of data, the program allows for automatic iteration of the input frequency.

```

C
C STATIC DESIGN OF MAGNET AND RAIL
C
C INPUT VARIABLES
C L1 = POLE FACE WIDTH (INCHES)
C W1, W1 = WINDOW WIDTH (INCHES)
C H, H1 = WINDOW HEIGHT (INCHES)
C DL, DW, DH = INCREMENTS FOR ITERATIONS
C DTMAX = MAXIMUM TEMPERATURE RISE (DEG C)
C BSATC = SATURATION FLUX OF CORE (TESLA)
C BSATR = SATURATION FLUX OF RAIL (TESLA)
C RO = RESISTIVITY OF COIL (OHM-IN)
C ROR = RESISTIVITY OF THE RAIL (OHM-IN)
C DCORE, DRAIL, DCOIL ARE DENSITIES (PCI)
C MG = TOTAL VEHICLE WEIGHT (LBF)
C ERR = SAFETY FACTOR
C YO = AIR GAP (INCHES)
C PF = PERMEANCE OF FRINGING FIELD (NON-DIMENSIONAL)
C F = COIL PACKING FACTOR (NON-0)
C K = HEAT TRANSFER COEF (WATTS-DEG C/SQ IN)

C IREP CONTROLS ENTRY OF NEXT DATASET
C
C INTEGER, OUT
C REAL L1, MG, W1, W1, H, H1, MU, NI, MU, K, LENG, LCOIL, LRAIL
C DATA IN, OUT/8, 5/
C DATA RVRT, MU, PI/58.0, 1.256E-6, 3.14159/
1 READ(1,2) IREP, IL, IW, IH, L1, W1, H1, DL, DW, DH, Z, MG, YO, ERR,
DCORE, DRAIL, DCOIL, PF, BSATC, BSATR, RO, ROR, F, K, DTMAX
2 FORMAT (3I2, I4, 7F10.6/F10.2, 6F10.6/2F10.6, 2E10.3, 3F10.6)
WRITE(OUT,3) Z, YO, ERR, DCORE, DRAIL, DCOIL, PF, BSATC, BSATR,
1 RO, F, K, DTMAX
3 FORMAT(1H0, ' Z = ', F6.4, ' INCHES', 8X, 'GAP = ', F6.4, ' INCHES',
16X, 'SAFETY = ', F6.4, ' DCORE = ', F6.4, ' PCI', 7X, 'DRAIL = ', F6.4,
2' PCI', 7X, 'DCOIL = ', F6.4, ' PCI'/' F PERM = ', F6.4, 10X, 'BSAT CORE

```

```

3= 1,F6.4,' T',5X,'RAIL BSAT = ',F6.4,' T'/' COIL RESISTIVITY = ',
4E12.3,' OHM-IN',12X,' PACKING FACTOR = ',F8.6/' K' = ',F9.6,
5' WATTS-DEG C/SQ IN',19X,'MAX TEMP = ',F10.4,' DEG C')
WRITE(OUT,44) ROR, MG
44 FORMAT(' RAIL RESISTIVITY = ',E12.3,' OHM-IN',12X,
1' TOTAL VEHICLE WEIGHT', F10.2,' LBF'//)
MG = 0.25*MG
C ITERATE THE POLE WIDTH
DO 4 ILSE = 1,IL
W = W1
C DETERMINE FRINGING FLUX COEFFICIENT
PU = L1/YO
NUF = PF/PU
C ITERATE THE WINDOW WIDTH
DO 5 JOEY = 1,IW
H = H1
C ITERATE THE WINDOW HEIGHT
DO 6 JAMES = 1,IH
C DETERMINE TOTAL FLUX LEAKAGE COEFFICIENT AT TWICE NOMINAL GAP
PL = (H-YO)/W
NUL = PL/PU
NUT = 1.+2.*(NUL+NUF)
C DETERMINE MAGNET'S LENGTH
BO = BSATC / (NUT*ERR)
S = 30*BO*PCVRT
LENG = MG / (2.*S*L1)
C DETERMINE OHMIC HEATING
LCOIL = 2.*(LENG + L1+PI*W*0.25)
ACoil = W*(H-Z)*F
NI = 0.2508*YO*BO/MU
RCOIL = RO*LCCIL/ACoil
Q = RCOIL*NI*NI
C DETERMINE AREA FOR HEAT DISSIPATION
ADIS = 4.*(L1+W+H)*LENG + 4.*H*L1+2.*L1*(2.*L1+W) +
14.*L1*W+PI*W*W+2.*(H-Z)*PI*W

```

```

      T = Q/(K*ADIS)
C IF TEMPERATURE RESTRAINT IS SATISFIED, DESIGN IS COMPLETED
      IF(T=DTMAX) 7,7,8
      8 H = H+DH
      6 CONTINUE
C DO AUXILIARY VARIABLES THAT DEPEND ON MAGNET RAIL DESIGN
C CALCULATE WEIGHTS OF MAGNETS AND RAIL
      7 WCORE = DCORE*LENG*(W*L1+2.*L1*(H+L1))
      WCOIL = DCOIL*ACOIL*LCOIL
      WTOT = 4.*(WCORE+WCOIL)
      TRAIL = ((1.+2.*NUF)/NUT)*(BSATC/BSATR)*L1
      LRAIL = L1+2.*YO
      WRAIL = 126720.*DRAIL*(2.*LRAIL*(TRAIL+YO)+ TRAIL*(W-2.*YO))
C TOTAL LEAKAGE COEF.
      NUT = 1.+NUL+NUF
      LCOIL = LCOIL/12.
      LENG = LENG/12.
      ADIS = ADIS/144.
      Q = Q/250.7
      WRITE(OUT,10) L1,W,H,LENG,BO,S,NI,RCOIL,Q,NUF,NUL,NUT
10  FORMAT(' L1 = ',F8.5,6X,' W = ',F8.5,8X,' H = ',F8.5,7X,' LENG = ',
1  F10.5,' FT',5X,' BO = ',F10.6,' TESLA',4X,' P = ',F10.6,' PSI'/
2  ' NI = ',F10.2,' AMP-T',4X,' RCOIL = ',F12.10,' OHM Q = ',
3  F10.4,' KW'/) NUF = ',F10.6,9X,' NUL = ',F10.6,9X,' NUT = ',
4  F10.6)
      WRITE(OUT,11) LCOIL,T,ADIS,TRAIL,WRAIL,WCORE,WCOIL,WTOT
11  FORMAT(' LCOIL = ',F10.6,' FT',4X,' T = ',F10.4,' DEG C',5X,
1  ' ADIS = ',F10.4,' SQ FT'/) TRAIL = ',F8.5,' IN',6X,' WRAIL = ',
2  E12.3,' LB/MILE'/) WCORE = ',F10.2,' LBF',4X,' WCOIL = ',F10.3,
3  ' LBF',4X,' WTOT = ',F10.2,' LBF'/)
      N = W + DW
      5 CONTINUE
      L1 = L1 + DL
      4 CONTINUE
C IS THERE ANOTHER DATA SET?

```

IF(IREP) 14,1,14  
14 CALL EXIT

END

0002010120	1.0	5.0	1.0	0.5	0.0	0.1	0.2
88002.	0.6	1.0	0.28	0.27	0.10	1.92	
2.3	1.6	1.6E-6	1.6E-5	0.7	0.009	140.0	

Z = 7.2000 INCHES      GAP = 2.6000 INCHES      SAFETY = 1.0000  
 DCORE = 0.2800 PCI      RAIL = 2.2700 PCI      DCOIL = 0.1000 PCI  
 F PERM = 1.9200      BSAT CORE = 2.3000 T      RAIL BSAT = 1.6000 T  
 COIL RESISTIVITY = 0.164E-05 OHM-IN      PACKING FACTOR = 0.700000  
 K = 2.00900 WATTS-DEG C/SQ IN      MAX TEMP = 140.0000 DEG C  
 RAIL RESISTIVITY = 0.164E-04 OHM-IN      TOTAL VEHICLE WEIGHT 88000.00LBF

L1 = 1.00000      W = 5.00000      H = 3.79998  
 LENG = 40.53847 FT      BO = 2.564834 TESLA      P = 18.504135 PSI  
 NI = 1377.011 AMP-T      RCOIL = 0.0221522262 OHM Q = 114.4040 KW  
 NUF = 1.151999      NUL = 2.383998      NUT = 2.535997  
 LCOIL = 99.898071 FT      T = 134.9783 DEG C      ADIS = 163.4979 SQ FT  
 TRAIL = 1.16638 IN      WRAIL = 0.418E 06 LB/MILE  
 WCORE = 2430.15 LBF      WCOIL = 1510.452 LBF      WTOT = 15762.43 LBF

L1 = 1.50000      W = 5.20000      H = 4.99998  
 LENG = 2.90862 FT      BO = 0.709878 TESLA      P = 29.227722 PSI  
 NI = 1726.97 AMP-T      RCOIL = 0.0020488250 OHM Q = 57.9589 KW  
 NUF = 0.768000      NUL = 0.351998      NUT = 2.119997  
 LCOIL = 42.721725 FT      T = 135.8068 DEG C      ADIS = 82.3254 SQ FT  
 TRAIL = 1.68773 IN      WRAIL = 2.642E 06 LB/MILE  
 WCORE = 1896.82 LBF      WCOIL = 861.266 LBF      WTOT = 11032.36 LBF

C  
 C ELECTROMAGNETIC SUSPENSION WITH PASSIVE SECONDARY SUSPENSION  
 C  
 C CURRENT CONTROL WITH FEEDBACK OF AVERAGE RELATIVE DISPLACEMENT AND  
 C ABSOLUTE VELOCITY  
 C  
 C  
 C CALCULATE RMS VALUES WITH FINITE MAGNET LENGTH  
 C  
 C ALL QUANTITIES ARE NON-DIMENSIONAL  
 C DW = VOLTAGE INTEGRATION INCREMENT  
 C NPTS = NUMBER OF POINTS IN VOLTAGE INTEGRATION  
 C NPTS\* = NUMBER OF POINTS IN INTEGRATION  
 C DW\* = INTEGRATION INCREMENT  
 C  
 C W1 = NATURAL FREQUENCY OF PRIMARY  
 C W2 = NATURAL FREQUENCY OF SECONDARY  
 C Z1 = DAMPING RATIO OF PRIMARY  
 C Z2 = DAMPING RATIO OF SECONDARY  
 C DZ1, DZ2, DW1, DW2 = INCREMENTS OF ITERATION  
 C  
 C L = LENGTH OF THE MAGNET  
 C L1 = DIMENSIONLESS SELF INDUCTANCE OF CONTROL WINDINGS  
 C  
 C GAMMA = RATIO OF SECONDARY TO PRIMARY MASS  
 C AV = ROAD ROUGHNESS PARAMETER  
 C V = FORWARD VELOCITY OF VEHICLE  
 C  
 C POLYNOMIALS ARE WRITTEN AS FOLLOWS WHERE C DENOTES COEFFICIENT MATRIX,  
 C N, THE ORDER OF THE POLYNOMIAL, AND X THE VARIABLE SO THAT Y IS WRITTEN  
 C AS A POLYNOMIAL IN X  
 C  $Y = C(N+1)*X**N + \dots + C(2)*X + C(1)$   
 C  
 C IREP CONTROLS ENTRY OF NEXT DATASET  
 C

```

INTEGER OUT
REAL L,L1,K1,K2,IR,NUM
DIMENSION D(5),S(5),F(5),H(6),EM(6),WN(5),ZZ(5),G(5)
COMMON VL,AV, VV(501)
DATA IN,OUT/8,5/
DATA PI/3.14159/
1 READ(IN,2) IREP,IZ11,IW11,IZ21,IW21,NPTSW, NPTS,DWW,DW,
  IZ11,W11,Z21,W21,DZ1,DW1,DZ2,DW2, GAMMA,L,L1,AV,V
2 FORMAT(5I2,2I4,F12.5,F10.5/8F10.5/5F10.6)
  *WRITE(OUT,3) GAMMA,AV,V,L,L1,DW,NPTS,DWW,NPTSW
3 FORMAT(1H1,'GAMMA = ',F9.5,5X,'AV = ',F10.7,5X,'V = ',F10.4/
  1' L = ',F10.4,6X,' L1 = ',F9.6/' DW = ',F10.5,5X,'NPTS = ',I4/
  2' DWW = ',F10.5,4X,'NPTSW = ',I4/)
C CONSTANT IN CALCULATION
  VL = 2.*V/L
  W2 = W21
C ITERATE NATURAL FREQUENCY OF SECONDARY
  DO 10 IKE = 1,IW21
    Z2 = Z21
C ITERATE DAMPING RATIO OF SECONDARY
  DO 11 IZZY = 1, IZ21
    W1 = W11
C ITERATE NATURAL FREQUENCY OF PRIMARY
  DO 12 JOHN = 1,IW11
    Z1 = Z11
C ITERATE DAMPING RATIO OF PRIMARY
  DO 13 JANE = 1,IZ11
C CONVERT NATURAL FREQUENCIES AND DAMPINGS TO SPRINGS AND DAMPERS
  K1 = W1*W1
  K2 = W2*W2
  B1 = 2.*W1*Z1
  B2 = 2.*W2*Z2
C DETERMINE THE DENOMINATOR POLYNOMIAL
  D(1) = K1*K2
  D(2) = B1*K2+B2*K1

```

```

D(3) = B1*B2+(1.+GAMMA)*K2+ K1
D(4) = B2*(1.+GAMMA) + B1
D(5) = 1.0
WRITE(OUT,15) W2,Z2,W1,Z1,(D(I), I = 1,5)
15 FORMAT(/' W2 = ',F10.6, ' Z2 = ',F10.6, ' W1 = ',F10.6,
1' Z1 = ',F10.6/' DENOM POLY',3X,5F10.5)
C FIND EIGENVALUES OF DENOMINATOR
C POLRT IS AN IBM SCIENTIFIC SUBROUTINE
C S IS REAL PART OF ROOT, F IS IMAGINARY PART OF ROOT
C H IS WORK VECTOR
C IER IS ERROR CODE
CALL POLRT (D,H,4,S,F,IER)
IF(IER) 40,41,40
40 WRITE(OUT,28) IER
28 FORMAT(//' IER = ',I2//)
GO TO 23
C CONVERT ROOTS TO POLAR NOTATION
41 DO 14 JEFF = 1,4
IF(ABS(F(JEFF))-0.0001) 30,30,31
31 AN(JEFF) = SQRT(F(JEFF)*F(JEFF)+S(JEFF)*S(JEFF))
ZZ(JEFF) = ABS(S(JEFF)/WN(JEFF))
GO TO 14
30 AN(JEFF) = 100000.
ZZ(JEFF) = 100000.
14 CONTINUE
WRITE(OUT,16) (S(I),F(I),WN(I),ZZ(I), I = 1,4)
16 FORMAT(' EIGENVALUES',6X,'REAL',5X, 'IMAGINARY',6X,'WN',10X,'ZZ'/
1(15X,F10.6,2X,F10.6,2X,F10.6,2X,F10.6))
C DETERMINE ACCELERATION OF UNSPRUNG MASS
23 S(5) = 0.0
S(4) = K1
S(3) = K1*B2
S(2) = D(1)
S(1) = 0.0
CALL SYLVY(S,D,NPTSW,DWW,AR1)

```

```

C DETERMINE POWER EXTRACTED BY THE MAGNET
  DO 91 K = 1,4
  91 ZZ(K) = S(K+1)
  ZZ(5) = 0.0
  CALL SYLVY(ZZ,D,NPTSW,DWW,V1)
  P1 = 0.5*B1*V1*V1/(1.+GAMMA)
C DETERMINE THE ACCELERATION OF SPRUNG MASS
  AN(1) = 0.0
  AN(2) = S(2)
  AN(3) = S(3)
  AN(4) = 0.0
  AN(5) = 0.0
  WRITE(OUT,75) (S(I), I = 1,5)
  75 FORMAT(' A1 ',5(E12.4,2X))
  WRITE(OUT,76) (WN(I), I = 1,5)
  76 FORMAT(' A2 ',5(E12.4,2X))
  CALL SYLVY(WN,D,NPTSW,DWW,AR)
C THE HEIGHT OF THE SUSPENSION
  F(1) = 0.0
  F(2) = K1
  F(3) = 0.0
  F(4) = 0.0
  F(5) = 0.0
  CALL SYLVY(F,D,NPTSW,DWW,YSR)
  DO 90 K = 2,5
  90 ZZ(K) = F(K-1)
  ZZ(1) = 0.0
  CALL SYLVY(ZZ,D,NPTSW,DWW,V2)
  P2 = 0.5*B2*V2*V2*GAMMA/(1.+GAMMA)
C DETERMINE THE AVERAGE ROAD CLEARANCE
  DO 101 J = 1,3
  101 G(J) = D(J+1) - S(J+2)
  G(4) = D(5)
  G(5) = 0.0
  CALL SYLVY(G,D,NPTSW,DWW,YR)

```

```

C DETERMINE THE ROAD CLEARANCE AT A POINT
DO 124 J = 1,4
104 EM(J) = 5(J+1)
EM(5) = 4.2
C YPT PERFORMS NUMERICAL INTEGRATION TO DETERMINE CLEARANCE AT POINT
CALL YPT(EM,D,NPTSW,DWW,YP)
C DETERMINE THE CONTROL CURRENT
A = 1. + 2.5 *K1/(1.+GAMMA)
B = 2.5*B1/(1.+GAMMA)
DO 122 N = 1,3
102 H(N) = A*G(N)-B*S(N+1)
H(4) = 4*G(4)
H(5) = 0.2
CALL SYLVY(H,D,NPTSW,DWW,IR)
C TOTAL REAL POWER DISSIPATED
P = P1 + P2
C DETERMINE VOLTAGE
DO 123 J = 2,5
103 S(J) = L1*H(J-1)-G(J-1)
S(1) = 2.2
CALL SYLVY(S,D,NPTS,DW,VR)
PA = IR*VR
WRITE(OUT,25)AR1,AR,YR,YP,YSR,IR,VR
25 FORMAT(' RMSAC1',4X,'RMSAC2',4X,'RMSYAV',5X,'RMSYP',5X,'RMSZ',
15X,'RMSI1',5X,'RMSV1',1X,7(F8.5,2X))
WRITE(OUT,26) P1,P2,P,PA
26 FORMAT(7X,'P1',8X,'P2',5X,'PTOT',8X,'PA'/1X,4(F8.5,2X))
C INCREMENT VARIABLES FOR NEXT CALCULATION
Z1 = Z1 +DZ1
13 CONTINUE
W1 = W1 + DW1
12 CONTINUE
Z2 = Z2 + DZ2
11 CONTINUE
W2 = W2 + DW2

```

```
10 CONTINUE
C SHOULD A NEW DATA SET BE ENTERED?
  IF (IREP) 5,1,5
  5 CALL EXIT
  END
```

---

```
      SUBROUTINE MILLY(N,DW,VR)
C MILLY PERFORMS INTEGRATION ON VECTOR VV BY SIMPSON'S RULE
C AV = COEFFICIENT OF INTEGRAND
C N = NUMBER OF TERMS IN VV
C DW = FREQUENCY INCREMENT FOR INTEGRATION
C VR = RMS RESULT
      COMMON VL,AV, VV(501)
      NOEL = N-1
      VSG = 2.0
      DO 29 JJ = 2,NOEL,2
29 VSG = VSG+VV(JJ-1)+4.*VV(JJ)+VV(JJ+1)
      VSG = VSG*AV*DW/1.5
      VR = SQRT(VSG)
      RETURN
  END
```

---

```
      SUBROUTINE JUDY (S,F)
C JUDY SQUARES POLYNOMIAL S FOR EFFICIENT CALCULATIONS
      DIMENSION F(5), S(5)
      F(1) = S(1)*S(1)
      F(2) = S(2)*S(2)-2.*S(1)*S(3)
      F(3) = S(3)*S(3)-2.*S(2)*S(4)+2.*S(1)*S(5)
      F(4) = S(4)*S(4)-2.*S(3)*S(5)
      F(5) = S(5)*S(5)
      RETURN
  END
```

---

```
      SUBROUTINE YPT(C,D,N,DW,Y)
C YPT SETS UP MATRIX FOR INTEGRATION OF RMS DISPLACEMENT AT A POINT
C C = NUMERATOR OF ABSOLUTE POSITION OF MAGNET
C D = DENOMINATOR OF SYSTEM'S TRANSFER FUNCTIONS
C DW = FREQUENCY INCREMENT FOR INTEGRATION
```

```
C N = NUMBER OF POINTS IN VECTOR VV WHICH HOLDS INTEGRATION POINTS
C VV = VECTOR OF INTEGRATION
C FPAO = FINITE MAGNET LENGTH FILTER
      COMPLEX NUM,DEN, WW
      REAL C(5), D(5)
      COMMON VL, AV, VV(521)
      VV(1) = (D(2)-C(2))/D(1)
      W = 0.
      DO 1 I = 2, N
      FPAO = (VL/W)*SIN(W/VL)
      NUM = (P.,0.)
      DEN = (Q.,0.)
      WW = (1.,0.)
      DO 2 J = 1, 5
      NUM = NUM + (D(J)-C(J)*FPAO)*WW
      DEN = DEN + D(J)*WW*W*(0.,1.)
      WW = WW*W*(0.,1.)
2 CONTINUE
      S = CABS(NUM/DEN)
      VV(I) = S*Q
      W = W + DW
1 CONTINUE
      CALL MILLY(N,DW,Y)
      RETURN
      END
      SUBROUTINE SYLVY(C,D,N,DW,Y)
C SYLVY SETS UP VV VECTOR FOR INTEGRATION
C C = NUMERATOR OF INTEGRAND
C D = DENOMINATOR OF INTEGRAND
C FPAO = FINITE MAGNET LENGTH FILTER
C N = NUMBER OF TERMS IN INTEGRAND VECTOR VV
C DW = FREQUENCY INCREMENT
      REAL C(5), D(5), CC(5), DD(5), NUM
      COMMON VL, AV, VV(501)
      CALL JUDY(C,CC)
```

```

CALL JUDY(D,DD)
VV(1) = CC(1)/DD(1)
W = DW
DO 2 I = 2, N
FPAD = (VL/W)*SIN(W/VL)
WW = W*W
NUM = CC(1)
DEN = DD(1)
DO 1 J = 2,5
NUM = NUM + CC(J)*WW
DEN = DEN + DD(J)*WW
** = WW*W*W
1 CONTINUE
VV(I) = (NUM/DEN)*FPAD*FPAD
W = W + DW
2 CONTINUE
CALL MILLY(N,DW,Y)
RETURN
END
000102-10172210101  0.1      0.2
0.707      1.25      2.25      0.25      0.0      0.625      0.0      0.0
5.0      677.0      2.18      0.00443  350.0

```

GAMMA = 5.000000 AV = 2.0044300 V = 350.0000  
 L = 600.0000 L1 = 2.179999  
 DW = 0.200000 NPTS = 101  
 DWA = 2.100000 NPTSA = 201

W2 = 2.252000 Z2 = 2.252000 W1 = 1.250000 Z1 = 0.707000  
 DENOM POLY 0.29756 0.32578 2.15844 2.51750 1.00000

EIGENVALUES REAL IMAGINARY WN ZZ  
 -0.247313 -0.223177 0.228262 0.209903  
 -0.247313 0.223177 0.228262 0.209903  
 -1.210337 -0.638865 1.369042 0.884441  
 -1.210337 0.638865 1.369042 0.884441

A1 0.0000E 00 0.9756E-01 0.1953E 00 0.1563E 01 0.0000E 00  
 A2 0.2000E 00 0.9756E-01 0.1953E 00 0.0000E 00 0.0000E 00  
 RMSAC1 RMSAC2 RSYAV RNSYP RMSZ RMSI1 RMSV  
 0.26076 0.02103 0.14907 0.16891 0.27942 0.15752 0.15264  
 P1 P2 PTOT PA  
 0.24100 0.20046 0.22146 0.22404

W2 = 2.252000 Z2 = 2.252000 W1 = 1.875000 Z1 = 0.707000  
 DENOM POLY 2.21973 4.50516 4.22203 3.40125 1.00000

EIGENVALUES REAL IMAGINARY WN ZZ  
 -0.254538 -0.234029 0.240300 0.226957  
 -0.254538 0.234029 0.240300 0.226957  
 -1.646088 -1.046703 1.950690 0.843849  
 -1.646088 1.046703 1.950690 0.843849

A1 0.0000E 00 0.2197E 00 0.4395E 00 0.3516E 01 0.0000E 00  
 A2 0.0000E 00 0.2197E 00 0.4395E 00 0.0000E 00 0.0000E 00  
 RMSAC1 RMSAC2 RSYAV RNSYP RMSZ RMSI1 RMSV  
 0.29267 0.02346 0.10277 0.12716 0.29843 0.11248 0.14851  
 P1 P2 PTOT PA  
 0.24213 0.04067 0.20281 0.01670

C  
C EDDY CURRENT EFFECTS FROM AC CURRENT SHEET  
C  
C REGION I: INFINITE HALF SPACE, ZERO CONDUCTIVITY  
C REGION II: AIR GAP, ZERO CONDUCTIVITY  
C REGION III: INFINITE HALF SPACE, CONDUCTIVITY S

C ALL UNITS ARE MKS

C INPUT VARIABLES

C U1 = RELATIVE PERMEABILITY OF REGION I  
C U2 = RELATIVE PERMEABILITY OF REGION II  
C U3 = RELATIVE PERMEABILITY OF REGION III  
C S = CONDUCTIVITY OF REGION III  
C L = MAGNET WIDTH  
C G = AIR GAP  
C FREQ1 TO FREQ2 = RANGE OF FREQUENCIES (HZ)  
C N = NUMBER OF FREQUENCY INCREMENTS

C IREP CONTROLS ENTRY OF NEXT DATASET

C INTEGER OUT  
C REAL L,K,N1,N2 ,LIFT  
C COMPLEX A,Z,DEN,E,G , CMLPX,CLOG, CONJG,F,JJ,BB  
C DATA IN,OUT/8,5/  
C DATA PI, CNOT/3.1416,1.256E-6/  
8 READ(IN,3) IREP,N,FREQ1, FREQ2,U1,U2,U3,S,L,G  
3 FORMAT(I2,I4, 2E14.3/6E12.3)  
C WRITE(OUT,11) U1,U2,U3, S,L,G  
11 FORMAT(14I,4X,'U1', 10X,'U2', 10X,'U3', 10X,'S', 11X,'L', 11X,'G'/  
15(E12.3,2X)/)  
12 FORMAT(4X,'F',12X,'RM', 9X,'DEL', 8X,'B3Y', 8X,'T3Y',8X,  
1'B1Y', 8X,'T1Y', 8X,'B2Z', 7X,'LIFT', 6X,'POWER')  
C WRITE(OUT,12)  
C K = PI/L

```

C CONVERT RELATIVE PERMEABILITIES TO ABSOLUTE
  U1 = UNOT*U1
  U2 = UNOT*U2
  U3 = UNOT*U3
C SET UP LOGARITHMIC FREQUENCY INCREMENTS
  NPTS = N + 1
  FREQ1 = 2.*PI*FREQ1
  FREQ2 = FREQ2*2.*PI
  F1LOG = ALOG(FREQ1)/2.303
  F2LOG = ALOG(FREQ2)/2.303
  DFLOG = (F2LOG-F1LOG)/FLOAT(N)
C DO CALCULATIONS FOR EACH FREQUENCY
  DO 44 J = 1, NPTS
C W = ANGULAR FREQUENCY
  W = 2.*PI**F1LOG
C RM = MAGNETIC REYNOLDS NUMBER
  RM = U3*S**W/(K*K)
  RW = SQRT(1.+RM*RM)+1.
C N1, N2 = REAL AND IMAGINARY PARTS OF INVERSE OF SKIN DEPTH
  N1 = 2.787*SQRT(RW)*K
  RW = SQRT(1.+RM*RM)-1.
  N2 = 2.787*SQRT(RW)*K
C A = COMPLEX INVERSE OF SKIN DEPTH
  A = CMPLX(N1,N2)
  GAM = U1/U2
  Z = (U3/U2)*(K/A)
  DEN = -(1.+GAM)*(1.+Z)*EXP(K*G) + (1.-Z)*(1.-GAM)*EXP(-K*G)
C E = COMPLEX FLUX DENSITY PERP. TO INTERFACE OF REGIONS II AND III
  E = -2.*Z*U1/DEN
C F = COMPLEX FLUX DENSITY PARALLEL TO INTERFACE OF REGIONS II AND III
  F = E/Z
  B2Z = CABS(F)
C KS = AMPLITUDE OF CURRENT SHEET
C B3Y = MAGNITUDE OF FLUX DENSITY NORMALIZED WRT KS
  B3Y = CABS(E)

```

```

C T3Y = PHASE ANGLE BETWEEN FLUX INTO RAIL AND INPUT CURRENT
  T3Y = AIMAG(CLOG(E))*57.3
C LIFT = LIFT/AREA NORMALIZED WRT KS*KS
  Q = E*CONJG(E)-F*CONJG(F)
  LIFT = (1./(8.*U2))*REAL(Q)
C POWER = AVERAGE OHMIC POWER IN REGION III
C NORMALIZED WRT KS*KS*(MAGNET LENGTH)
  UJ = E*(A*A-K*K)/(U3*K)
  Q = UJ*CONJG(UJ)*L/(4.*S*N1)
  POWER = REAL(Q)
C B1Y = MAGNITUDE OF FLUX DENSITY PERP. TO INTERFACE OF REGION I AND II
C NORMALIZED WRT KS
  BB = U1*((1.+Z)*EXP(K*G)-(1.-Z)*EXP(-K*G))
  BB = -BB/DEN
  B1Y = CABS(BB)
C T1Y = PHASE ANGLE BETWEEN B1Y AND CONTROL CURRENT
  T1Y = AIMAG(CLOG(BB))*57.3
C DEL = SKIN DEPTH
  DEL = 1./N1
  A = W/6.283
  WRITE(OUT,6) W, RM, DEL, B3Y, T3Y, B1Y, T1Y, B2Z, LIFT, POWER
  6 FORMAT(10(E10.3,1X))
  F1LOG = F1LOG + DFLOG
  40 CONTINUE
C IS THERE ANOTHER DATASET?
  IF(IREP) 8,9,8
  9 CALL EXIT
  END
050012 1.0E-2      1.0E10
3.5E3      1.0E0      3.5E3      0.25E7      2.5E-1      1.5E-2

```

U1	U2	U3	S	L	G					
0.350E 04	0.102E 21	2.352E 04	2.250E 07	0.250E 00	0.150E-01					
F	RM	DEL	B3Y	T3Y	B1Y	T1Y	B2Z	LIFT	POWER	
0.100E-01	0.437E 01	0.480E-21	2.660E-05	-0.116E 00	2.672E-05	-0.112E 00	0.399E-08	0.433E-05	0.817E-11	
0.120E 00	0.437E 02	0.160E-21	2.657E-05	-0.403E 00	2.668E-05	-0.389E 00	0.124E-07	0.429E-05	0.283E-09	
0.120E 01	0.437E 23	0.530E-22	2.647E-05	-0.127E 01	2.659E-05	-0.122E 01	0.386E-07	0.416E-05	0.877E-08	
0.999E 21	0.437E 24	0.17 E-22	2.616E-05	-0.382E 01	2.628E-05	-0.368E 01	0.116E-06	0.377E-05	0.252E-06	
0.999E 02	0.437E 25	0.530E-23	2.530E-05	-0.105E 02	2.544E-05	-0.100E 02	0.317E-06	0.279E-05	0.590E-05	
0.998E 03	0.437E 26	0.170E-23	2.356E-05	-0.226E 02	2.371E-05	-0.212E 02	2.672E-06	0.122E-05	0.839E-04	
0.998E 24	0.436E 27	0.530E-24	2.167E-05	-0.347E 02	2.183E-05	-0.326E 02	2.994E-06	0.178E-06	0.582E-03	
0.998E 05	0.436E 28	0.17 E-24	2.612E-05	-0.413E 02	2.790E-06	-0.323E 02	0.115E-05	-0.948E-07	0.246E-02	
0.997E 06	0.436E 29	0.530E-25	0.202E-05	-0.438E 02	2.402E-06	-0.223E 02	0.121E-05	-0.141E-06	0.857E-02	
0.997E 07	0.436E 10	0.170E-25	2.652E-07	-0.446E 02	2.283E-06	-0.911E 01	0.123E-05	-0.149E-06	0.279E-01	
0.996E 08	0.436E 11	0.530E-25	2.200E-27	-0.449E 02	2.249E-06	-0.333E 01	0.123E-05	-0.151E-06	0.891E-01	
0.996E 09	0.436E 12	0.171E-25	2.054E-28	-0.450E 02	2.239E-06	-0.123E 01	0.123E-05	-0.151E-06	0.283E 00	
0.996E 10	0.435E 13	0.530E-27	2.227E-23	-0.450E 02	2.235E-06	-0.353E 00	0.123E-05	-0.151E-06	0.894E 20	

BIOGRAPHICAL SKETCH

Marc Steven Weinberg was born in Boston, Mass., August 9, 1948 to Joseph and Sylvia Weinberg. The author attended the Boston Public Schools and graduated from Boston Latin School, June, 1966. The author was an Eagle Scout and a National Merit Finalist. In September 1966, the author entered M.I.T. where he received the S.B. and S.M. in Mechanical Engineering in June 1971 after participating in the Honors program. The author worked three summers as a machinist, technician and engineering aide at the C.S. Draper Laboratories where he produced several in-house documents. A summer was spent with the Division of Sponsored Research at M.I.T. The Mechanical Engineer was received in January 1973.

In June 1971, the author married Judith Faye Omansky.

The author is a member of Tau Beta Pi, Pi Tau Sigma, and Sigma Xi.